



**ANTONIA STRÜBIG**

**FINGER ON THE TRIGGER**  
-  
**SUSY IN THE FOCUS**

**LEARNING FROM RUN I LHC DATA TO  
IMPROVE SUPERSYMMETRY SEARCHES WITH  
JETS AND MISSING TRANSVERSE ENERGY  
WITH ATLAS AT THE 13 TEV LHC**





## **FINGER ON THE TRIGGER - SUSY IN THE FOCUS**

**Learning from Run I LHC data to improve Supersymmetry  
searches with jets and missing transverse energy with ATLAS at  
the 13 TeV LHC**





# **FINGER ON THE TRIGGER - SUSY IN THE FOCUS**

## **Learning from Run I LHC data to improve Supersymmetry searches with jets and missing transverse energy with ATLAS at the 13 TeV LHC**

### **Proefschrift**

ter verkrijging van de graad van doctor  
aan de Radboud Universiteit Nijmegen  
op gezag van de rector magnificus prof. dr. J.H.J.M. van Krieken,  
volgens besluit van het college van decanen

in het openbaar te verdedigen op woensdag 30 mei 2018 om 10:30 uur precies

door

**ANTONIA HANNA STRÜBIG**

geboren op 14 december 1985  
te Hamburg, Duitsland

Promotor	Prof. dr. O. Igonkina
Copromotor	Dr. S. Caron
Manuscriptcommissie	Prof. dr. N. de Groot (Voorzitter) Prof. dr. W. J. P. Beenakker (Universiteit van Amsterdam) Prof. dr. ir. P. J. de Jong (Universiteit van Amsterdam) Prof. dr. G. Raven (Vrije Universiteit Amsterdam) Prof. dr. A. J. Barr (University of Oxford)

©Antonia Hanna Strübig 2018

Finger on the trigger - SUSY in the focus, Learning from Run I LHC data to improve Supersymmetry searches with jets and missing transverse energy with ATLAS at the 13 TeV LHC Thesis, Radboud University Nijmegen

Cover design by A. Strübig and L. D'Ascoli

This work is part of the research program of the *Stichting voor Fundamenteel Onderzoek der Materie* (FOM), which is financially supported by the *Nederlandse Organisatie voor Wetenschappelijk Onderzoek* (NWO).



# Contents

<b>1</b>	<b>Introduction</b>	<b>1</b>
<b>2</b>	<b>The Standard Model of particle physics and Supersymmetry</b>	<b>3</b>
2.1	The Standard Model of particle physics . . . . .	3
2.1.1	Particle content . . . . .	3
2.1.2	Electroweak theory . . . . .	5
2.1.3	Quantumchromodynamics . . . . .	8
2.1.4	Particle physics at Hadron Colliders . . . . .	9
2.2	Open questions of the Standard Model . . . . .	10
2.2.1	Hierarchy problem . . . . .	10
2.2.2	Unification of couplings . . . . .	11
2.2.3	Dark Matter . . . . .	11
2.2.4	Gravity . . . . .	12
2.3	Supersymmetry . . . . .	12
2.3.1	Constrained models . . . . .	18
2.3.2	Simplified models . . . . .	18
2.3.3	Phenomenological MSSM . . . . .	19
2.3.4	Experimental constraints . . . . .	19
<b>3</b>	<b>The LHC and the ATLAS detector</b>	<b>21</b>
3.1	The Large Hadron Collider . . . . .	21
3.1.1	Experiments at the LHC . . . . .	23
3.1.2	Pre-acceleration chain . . . . .	23
3.1.3	Machine design . . . . .	24
3.2	The ATLAS detector . . . . .	27
3.2.1	Detector layout . . . . .	27
3.2.2	Magnet system . . . . .	28
3.2.3	Inner detector . . . . .	30
3.2.4	Calorimeters . . . . .	33
3.2.5	Muon spectrometer . . . . .	35
3.2.6	Trigger and data acquisition . . . . .	37
3.2.7	Detector performance . . . . .	41
<b>4</b>	<b>Manual for trigger operation</b>	<b>43</b>
4.1	Challenges for trigger operation . . . . .	43

4.2	Menu design . . . . .	46
4.2.1	Trigger rate predictions . . . . .	49
4.3	Trigger software release . . . . .	50
4.4	Daily operation . . . . .	51
4.4.1	Possible situations during daily operations . . . . .	53
4.4.2	Data quality . . . . .	55
<b>5</b>	<b>Rethinking transverse missing energy triggers</b>	<b>59</b>
5.1	Transverse missing energy triggers for Run II . . . . .	59
5.2	Transverse missing energy trigger at Level 1 . . . . .	60
5.3	Pile-up corrected $E_T^{\text{miss}}$ . . . . .	60
5.3.1	The Kalman filter technique . . . . .	62
5.3.2	Kalman filter $E_T^{\text{miss}}$ . . . . .	62
5.3.3	Performance of $E_{T\text{KF}}^{\text{miss}}$ . . . . .	63
5.4	Transverse missing energy trigger at HLT . . . . .	67
5.4.1	$E_T^{\text{miss}}$ trigger performance . . . . .	68
<b>6</b>	<b>Event reconstruction</b>	<b>71</b>
6.1	Tracking and Vertices . . . . .	71
6.2	Jets . . . . .	73
6.2.1	Jet energy calibration . . . . .	74
6.2.2	Heavy flavoured jets . . . . .	75
6.3	Missing transverse energy . . . . .	76
6.4	Leptons and Photons . . . . .	78
6.4.1	Electrons . . . . .	78
6.4.2	Photons . . . . .	80
6.4.3	Muons . . . . .	81
<b>7</b>	<b>The MSSM-15 in the light of Run I data</b>	<b>85</b>
7.1	Approach to the MSSM-15 . . . . .	85
7.2	Scanning algorithm . . . . .	87
7.3	Experimental constraints . . . . .	88
7.4	Implementation of the ATLAS search constraints . . . . .	90
7.4.1	The likelihood function . . . . .	91
7.4.2	Simulation of signal efficiency . . . . .	93
7.4.3	Validation of efficiencies . . . . .	94
7.5	Results . . . . .	97
7.5.1	Profile likelihood excluding LHC data . . . . .	97
7.5.2	Dark matter composition . . . . .	99
7.5.3	Impact of LHC Higgs properties and ATLAS SUSY searches . . . . .	100
7.6	Conclusions for future searches . . . . .	102
7.A	Validation results of ATLAS searches implementation . . . . .	104



<b>8 Search for supersymmetry with jets and missing transverse energy</b>	<b>109</b>
8.1 Analysis strategy . . . . .	110
8.2 Data set and Monte Carlo samples . . . . .	111
8.2.1 Signal samples . . . . .	112
8.2.2 Background samples . . . . .	113
8.3 Event selection and Signal regions . . . . .	114
8.3.1 Object selection . . . . .	114
8.3.2 Event pre-selection . . . . .	116
8.3.3 Signal regions . . . . .	118
8.4 Backgrounds and Systematics . . . . .	121
8.4.1 Background sources . . . . .	122
8.4.2 Control regions . . . . .	122
8.4.3 Validation regions . . . . .	126
8.4.4 Systematic uncertainties . . . . .	127
8.5 Results . . . . .	129
8.A Boosted boson studies . . . . .	135
8.B RJR based signal regions . . . . .	141
8.C Trigger studies . . . . .	142
<b>9 Conclusions</b>	<b>145</b>
<b>Bibliography</b>	<b>149</b>
<b>List of Figures</b>	<b>165</b>
<b>List of Tables</b>	<b>171</b>
<b>Summary</b>	<b>173</b>
<b>Samenvatting</b>	<b>175</b>
<b>Curriculum vitae</b>	<b>177</b>
<b>Acknowledgements</b>	<b>179</b>





## CHAPTER 1

# Introduction

From early days of human development, mankind always aspired to understand its surrounding world - from the largest scales found in the universe to the tiniest particles, elementary building blocks of matter. Our current understanding of particle physics is described by the Standard Model. Particles predicted by the Standard model have been discovered over the past years since the development of the theory. Its latest success is the discovery of the Higgs Boson at the Large Hadron Collider in 2012.

Despite its stunning predictive capabilities, the Standard Model leaves some open questions. One deficit is that it describes only about 5% of the matter and energy in the universe without any explanation of the remaining 95% - so called dark matter and dark energy. Even in the description of known matter remain some unsolved problems. An elegant solution to these problems is proposed by introducing Supersymmetry. Supersymmetry postulates a partner particle for each existing particle with the same properties except the spin. It also includes a good candidate for dark matter. By doubling the number of elementary particles, Supersymmetry provides a whole zoo of new particles, they only need to be found. The theory behind the Standard Model and Supersymmetry is described in Chapter 2.

Supersymmetry is an intriguing extension of the Standard Model and the postulated new particles have been searched for by several large collider experiments, starting with the Super Proton Synchrotron at CERN in the 1980's, which was superseded by the Large Electron Positron collider, and then followed by the Tevatron at Fermilab, to nowadays Large Hadron Collider (LHC) at CERN. The LHC is designed to collide protons at a center-of-mass energy of  $\sqrt{s} = 14$  TeV. Its operation started in 2009 with  $\sqrt{s} = 7$  TeV and  $\sqrt{s} = 8$  TeV during Run I, reaching  $\sqrt{s} = 13$  TeV with the beginning of Run II in 2015. Four different detectors are located around the LHC ring recording the proton collisions, one of them is the ATLAS experiment, a general purpose detector with the main goal of researching the Standard Model and its possible extensions. Chapter 3 describes the LHC and the ATLAS detector in greater detail, Chapter 6 the event reconstruction.

An important part for the data taking is the trigger system that selects the events that are going to be recorded and which events are discarded. The operation of the trigger system is described in Chapter 4. For Supersymmetry especially, the missing transverse energy  $E_T^{\text{miss}}$  triggers play an important role as the final state includes the lightest supersymmetric particle, a weakly interacting particle leaving the detector. It is therefore worth striving to improve the selection efficiency for events containing  $E_T^{\text{miss}}$ . The development of a new  $E_T^{\text{miss}}$  trigger is presented in Chapter 5 together with the general performance of the  $E_T^{\text{miss}}$  triggers

in Run II.

As previous experiments, including the LHC during Run I, failed to find Supersymmetry, their results should be used to define areas in the vast supersymmetric parameter space that are still compatible with the current observations. This can be done by performing a fit of a general phenomenological model of Supersymmetry by taking all existing measurements into account, including relevant results from astro physical experiments. The fits are discussed in Chapter 7 and their implications on the detection prospects at current experiments. The current best expected values for the mass spectra can further be used to improve on the existing search strategies and identify areas of parameter space overlooked to date.

At the point of writing  $36.1 \text{ fb}^{-1}$  at  $\sqrt{s} = 13 \text{ TeV}$  have been recorded and analyzed in Run II by the ATLAS experiment but Supersymmetry remains elusive. One of the most sensitive analyses for the early  $\sqrt{s} = 13 \text{ TeV}$  data is the search for strong production of squarks and gluinos decaying to  $E_T^{\text{miss}}$ , jets and no leptons. Its universal design makes it sensitive to any physics beyond the Standard Model as the strong production cross sections dominates for comparatively small data sets. The analysis of the Run II data taken until summer 2016 is presented in Chapter 8.

With its design goal of delivering  $300 \text{ fb}^{-1}$  at  $\sqrt{s} = 14 \text{ TeV}$ ,  $3000 \text{ fb}^{-1}$  with the planned high-luminosity upgrade, the LHC will provide opportunities for years to come to search for Supersymmetry and other new phenomena.

## CHAPTER 2

# The Standard Model of particle physics and Supersymmetry

THE most powerful description of the underlying principles of particle physics is the Standard Model of particle physics. Although the Standard Model can explain most phenomena, there are still some unresolved questions which could be answered by an extension of the Standard Model. For many years one of the favored extensions has been Supersymmetry - a main search focus for experiments all around the world. Though the increasingly stringent limits by recent experimental results put Supersymmetry under pressure it remains a good candidate for solving the outstanding problems of the Standard Model.

This chapter will give an overview of the underlying principles of both the Standard Model and its supersymmetric extension, it will discuss how Supersymmetry complements the Standard Model and its phenomenology at hadron colliders.

### 2.1 The Standard Model of particle physics

The Standard Model [1–7] is the current most accurate description of particle physics. It is a quantum field theory (QFT) that describes every elementary particle as a field in space time. The Standard Model fulfills several important requirements to be a valid model. It describes all observed elementary particles and their interactions. It is invariant under Lorentz transformations and under local transformations of the underlying gauge group  $SU(3)_C \times SU(2)_T \times U(1)_Y$  as well as it is renormalisable.

In this work only a short summary of the Standard Model of particle physics will be given. There are many elaborated introductions to it in the literature for reference, e.g. [8–10].

#### 2.1.1 Particle content

The elementary particles described by the Standard Model can be divided into two categories, fermions - matter carrying particles and bosons - force carrying particles that mediate the interactions between fermions. All particles with their quantum numbers are listed in Table 2.1.

Fermions are particles which carry spin 1/2 (or more general uneven spin). One can further distinguish between quarks and leptons with the best known example for a lepton the electron. Unlike leptons which only interact through electro-magnetic and weak forces quarks

	Generation			Spin	Electric charge	SU(3) <sub>C</sub>	SU(2) <sub>T</sub>	U(1) <sub>Y</sub>
	I	II	III					
Leptons	$e$	$\mu$	$\tau$	$\frac{1}{2}$	-1	$\mathbf{1}_R, \mathbf{1}_L$	$\mathbf{1}_R, \mathbf{2}_L$	$-2_R, -1_L$
	$\nu_e$	$\nu_\mu$	$\nu_\tau$	$\frac{1}{2}$	0	$\mathbf{1}$	$\mathbf{2}_L$	-1
Quarks	$u$	$c$	$t$	$\frac{1}{2}$	$+\frac{2}{3}$	$\bar{\mathbf{3}}_R, \mathbf{3}_L$	$\mathbf{1}_R, \mathbf{2}_L$	$\frac{4}{3}_R, \frac{1}{3}_L$
	$d$	$s$	$b$	$\frac{1}{2}$	$-\frac{1}{3}$	$\bar{\mathbf{3}}_R, \mathbf{3}_L$	$\mathbf{1}_R, \mathbf{2}_L$	$-\frac{2}{3}_R, \frac{1}{3}_L$
Gauge bosons	$\gamma$			1	0	$\mathbf{1}$	$\mathbf{3}$	0
	$g$			1	0	$\mathbf{8}$	$\mathbf{1}$	0
	$Z^0$			1	0	$\mathbf{1}$	$\mathbf{1}$	0
	$W^\pm$			1	$\pm 1$	$\mathbf{1}$	$\mathbf{3}$	0
	$H$			0	0	$\mathbf{1}$	$\mathbf{2}$	1

**Table 2.1:** Particle content of the Standard Model (the corresponding anti-particles are unlisted).  $R, L$  indicate the values for right- and lefthanded particles.  $Y$  is the hypercharge.

carry an additional “color” charge, hence they underlie the strong interaction.

Fermions are organized in three generations where the second and third generation have the same quantum numbers as the first except that they have different masses:  $m_{1st} < m_{2nd} < m_{3rd}$ .

The first generation consists of the electron  $e$  with electric charge<sup>1</sup> -1, the electrically neutral electron neutrino  $\nu_e$ , and two quarks, the up quark  $q_u$  (or  $u$ ) with electric charge  $+\frac{2}{3}$  and the down quark  $q_d$  ( $d$ ) with electric charge  $-\frac{1}{3}$ . The leptons are completed by the muon  $\mu$  and the tau  $\tau$  and their associated neutrinos. The second generation of quarks contains the strange  $s$  and the charm quark  $c$ , the third generation quarks are called top  $t$  and bottom  $b$ .

All visible mass in our universe solely consists out of the first generation of fermions: the up and down quark form nucleons and together with the electrons atoms are formed. The second and third generation fermions are unstable and decay with varying average lifetimes. For each particle there exists an anti-particle which carries all the same quantum numbers except for electric charge. The electric charge of the anti-particle is simply the opposite of the particle charge. To simplify further descriptions, the anti-particles will not be mentioned explicitly anymore.

The bosons are the “messenger” particles of the fundamental forces implemented in the Standard Model, they carry integer spin. The underlying gauge symmetry in the Standard Model is  $SU(3)_C \times SU(2)_T \times U(1)_Y$

- The photon  $\gamma$  is the gauge mediating particle of the electro-magnetic force. It is massless and has spin 1. All electrically charged particles can interact with it.
- The weak force is mediated by the  $W^\pm$  and  $Z^0$  bosons (the superscript denotes the electric charge). The  $Z^0$  has a mass of 91.2 GeV and the  $W^\pm$  a mass of 80.4 GeV [11].

<sup>1</sup>In this thesis electric charge is given in units of  $e = 1.602 \cdot 10^{-19}$  C, the absolute value of the electron charge.

The weak force is effective for all particles.

- A color octet of massless gluons mediates the strong force, which acts on all particles carrying color charge. So the gluons not only interact with the quarks but also with themselves. This special feature of the strong force causes quarks and gluons to be confined in bound states, the so-called hadrons, and not to be observed as free particles. The self-coupling of the gluons results in the strong force being proportional to  $r$ , the distance between the interacting particles.
- The messenger particle of the gravitational force (the "graviton") has not been discovered yet and gravity is not described by the Standard Model.

The messenger particles (gauge bosons) in the Standard Model are spin 1 bosons, therefore associated theories are gauge invariant [12]. Gauge invariance requires that all spin 1 bosons are massless, which is obviously not true for the gauge bosons of the weak force. This requirement becomes even more stringent by the demands of electroweak symmetry-breaking, not only the gauge bosons but also all fermions have to be massless. So the question is, how do the fundamental particles gain mass? The Higgs mechanism gives an elegant answer [5, 6, 13]. It postulates a scalar field. The fundamental particles acquire mass by the interaction with that field. The physical particle associated with this scalar field is the electric neutral Higgs boson with spin 0. The Higgs boson interacts with all massive particles. The Yukawa couplings of the Higgs cannot be predicted, but are proportional to the mass  $m$  of the interacting particle (proportional to  $m^2$  for  $W/Z$  bosons)[8].

After being predicted in the mid-sixties of the 20th century its discovery by the ATLAS [14] and CMS [15] in 2012 was the latest confirmation of the Standard Model. The latest measurements give a Higgs mass of  $125.09 \pm 0.21$  (stat.)  $\pm 0.11$  (syst.) GeV [16].

### 2.1.2 Electroweak theory

The combination of the electrodynamic and the weak force is described in the electroweak (EW) theory. The EW theory was conceived by Glashow, Salam and Weinberg [1–3]. Its largest success was the predicted discovery of the  $W^\pm$  and  $Z^0$  bosons in 1983 at the SPS collider [17–20].

The EW theory is invariant under transformations of the local gauge symmetry  $SU(2)_T \times U(1)_Y$  with  $Y$  the weak hypercharge and  $T$  the weak isospin. The gauge bosons of the weak force only couple to left-handed particles. This is reflected in the description of the fermions by the chirality eigenstates  $\psi_L$  and  $\psi_R$ :

$$\psi = P_L \psi + P_R \psi = \frac{1}{2} (1 - \gamma^5) \psi + \frac{1}{2} (1 + \gamma^5) \psi = \psi_L + \psi_R \quad (2.1)$$

with  $\psi$  a four component bi-spinor describing a massless fermion field and  $\gamma^5$  the product of the four Dirac matrices  $\gamma^\mu$ .

The left-handed fermions are arranged in weak isospin doublets

$$L = \begin{pmatrix} \nu_L \\ e_L \end{pmatrix} \text{ and } Q = \begin{pmatrix} u_L \\ d_L \end{pmatrix} \quad (2.2)$$

while the right-handed fermions are arranged in singlets  $e_R$  and  $u_R, d_R$  (the second and third generation follow the same pattern). Note that the right-handed neutrinos are not included in the singlets. The singlets have zero weak isospin and do therefore not interact under  $SU(2)_T$ .

Four gauge fields correspond to the  $SU(2)_T \times U(1)_Y$  symmetry,  $W_\mu^1, W_\mu^2$  and  $W_\mu^3$  of the  $SU(2)_T$  group and  $B_\mu$  of the  $U(1)_Y$  group. The Lagrangian is given by

$$\mathcal{L}_{EW} = \sum_f \bar{\psi}_f i \mathcal{D} \psi_f - \frac{1}{4} W_{\mu\nu}^j W_j^{\mu\nu} - \frac{1}{4} B_{\mu\nu} B^{\mu\nu}, \quad (2.3)$$

with  $\mathcal{D}$ , the covariant derivative  $D_\mu$  contracted with the  $\gamma^\mu$  matrices and the sum running over all fermion fields  $f$ , the summation over the index  $j$  is implied. The interaction terms of the gauge bosons then are

$$W_{\mu\nu}^i = \partial_\mu W_\nu^i - \partial_\nu W_\mu^i - g_1 \epsilon_{ijk} W_\mu^j W_\nu^k, \quad (2.4)$$

$$B_{\mu\nu} = \partial_\mu B_\nu - \partial_\nu B_\mu, \quad (2.5)$$

where  $\epsilon_{ijk}$  is the Levi-Civita symbol. The covariant derivative is given by

$$D_\mu = \partial_\mu + \frac{1}{2} i g_1 \sigma^i W_\mu^i P_L + \frac{1}{2} i g_2 Y B_\mu \quad (2.6)$$

with  $g_1$  and  $g_2$  the coupling constants of the  $W$  and  $B$  fields respectively. The generators of the  $SU(2)$  and  $U(1)$  symmetries are the Pauli matrices  $\sigma^i$  and the weak hypercharge  $Y$ . The left-handedness of the weak interaction is observed by adding the projection operator  $P_L$ .

### Electroweak symmetry breaking

The four gauge bosons of electroweak interaction as in Eq. 2.3 are massless in contradiction with the experimental measurement of the  $W^\pm$  and  $Z^0$  boson masses. Furthermore local gauge invariance forbids the explicit introduction of a mass term in the Lagrangian of the form  $\frac{1}{2} m^2 W_\mu^i W^{\mu i}$ . The solution to the problem is spontaneous symmetry breaking as proposed in the Brout-Engler-Higgs mechanism [5, 6, 13].

The symmetry in the electroweak sector is broken by the introduction of isospin doublet of a complex scalar field  $\phi$  with non-zero vacuum expectation value. It is added to the Lagrangian with the term

$$\mathcal{L}_H = D_\mu \phi^\dagger D^\mu \phi - \mu^2 (\phi^\dagger \phi) - \lambda (\phi^\dagger \phi)^2. \quad (2.7)$$

A non-zero vacuum expectation value (VEV) of the Higgs field  $\phi$  is ensured by requiring  $\mu^2 < 0$  and  $\lambda > 0$  resulting in a minimum at

$$v = \pm \sqrt{\frac{\mu^2}{\lambda}} \quad (2.8)$$

and the ground state of the scalar field can be given by

$$\langle \phi \rangle = \begin{pmatrix} 0 \\ v/\sqrt{2} \end{pmatrix}. \quad (2.9)$$

The symmetry breaking generates three new massive and one massless gauge boson that are combinations of the original gauge bosons  $W_\mu^i$  and  $B_\mu$ :

$$W_\mu^\pm = \frac{1}{\sqrt{2}}(W_\mu^1 \mp iW_\mu^2) \quad (2.10)$$

$$Z_\mu^0 = \frac{1}{\sqrt{g_1^2 + g_2^2}}(g_1 W_\mu^3 - g_2 B_\mu) \quad (2.11)$$

$$A_\mu = \frac{1}{\sqrt{g_1^2 + g_2^2}}(g_2 W_\mu^3 + g_1 B_\mu). \quad (2.12)$$

The mixing of the original gauge bosons is normally expressed via the weak mixing angle  $\theta_W$ :

$$\sin \theta_W = \frac{g_2}{\sqrt{g_1^2 + g_2^2}} \text{ and } \cos \theta_W = \frac{g_1}{\sqrt{g_1^2 + g_2^2}}. \quad (2.13)$$

The Lagrangian of the redefined gauge fields has mass terms for the  $W$  and  $Z$  bosons with the values  $m_W = g_1 \cdot v/2 = m_Z \cos \theta_W$  but no mass term for the photon. A byproduct of the spontaneous symmetry breaking is a new massive scalar particle, the Higgs boson, with mass  $m_H = \sqrt{2\lambda}v$ . Its coupling strength to other particles depends on their mass.

### Fermion masses

Not only massive gauge bosons but also fermion masses are introduced by spontaneous symmetry breaking. Before the symmetry breaking fermionic mass terms were forbidden as they would have violated the local  $SU(2)$  gauge invariance. With the newly introduced scalar field Yukawa couplings can be added to the Lagrangian:

$$\mathcal{L}_{\text{Yukawa}} = \sum_{\text{generations}} \left[ -\lambda_e \bar{L} \phi e_R - \lambda_d \bar{Q} \phi d_R - \lambda_u \epsilon^{ab} \bar{Q}_a \phi_b^\dagger u_R + h.c. \right], \quad (2.14)$$

with  $\epsilon^{ab}$  the asymmetric  $SU(2)$  tensor,  $\epsilon^{12} = 1$  and  $\lambda_f$  a coupling constant. From 2.14 mass terms of the form

$$m_f = \frac{1}{\sqrt{2}} \lambda_f v \quad (2.15)$$

arise with the corresponding interaction term in the Lagrangian:



$$\mathcal{L}_{Yukawa} = - \sum_f \frac{\lambda_f}{\sqrt{2}} \bar{f} f H. \quad (2.16)$$

The value of  $\lambda_f$  is completely arbitrary. It is therefore not possible to deduct the Higgs mass from the fermion masses and vice versa.

Here  $\lambda_f$  is a diagonal matrix which holds as long as the fermions are represented in their mass eigenstate basis. The mass eigenstates are not identical to the weak isospin eigenstates, the Cabibbo-Kobayashi-Maskawa (CKM) matrix [21, 22] is introduced to translate between the two states. In the weak isospin eigenstate basis  $\lambda_f$  has off-diagonal terms. As a result interactions with the  $W^\pm$  can change the flavour states.

### 2.1.3 Quantumchromodynamics

Similar to the weak force that is described by the SU(2) gauge group, there is a gauge group for the strong force - SU(3) [4, 7]. The theory describing the strong interactions and its particles is Quantumchromodynamics (QCD). The quarks can be arranged in colour triplets of Red, Green and Blue. The force carrying particle of the strong force is the gluon which carries colour charge itself which leads to self-coupling of gluons. The gluons are arranged in a colour octet.

The Lagrangian of QCD is written as

$$\mathcal{L}_{QCD} = \sum_q \bar{\psi}_{q,i} (i \not{D}_{ij} - m_q \not{\partial}_{ij}) \psi_{q,j} - \frac{1}{4} G_{\mu\nu}^a G^{a\mu\nu}, \quad (2.17)$$

with  $q$  the quark flavors and the summation over  $i$  and  $j$  running over all three colour charges. The covariant derivative  $D_\mu$  contracted with the  $\gamma^\mu$  matrices is given by

$$i \bar{\psi}_{q,i} \not{D}_{ij} \psi_{q,i} = i \bar{\psi}_{q,i} \gamma^\mu (\partial_\mu + i g_s G_\mu^a T^a) \psi_{q,i} \quad (2.18)$$

where  $g_s$  is the strong coupling,  $G_\mu^a$  is the vector field of the gluons with  $a = 1 \dots 8$  and  $T^a$  are the generators of SU(3). One notation relates  $T^a$  to the Gell-Mann matrices:  $T^a = \lambda^a/2$ .  $G_{\mu\nu}^a$  is the field strength of the gluon field:

$$G_{\mu\nu}^a = \partial_\mu G_\nu^a - \partial_\nu G_\mu^a - g_s f^{abc} G_\mu^b G_\nu^c \quad (2.19)$$

with  $f^{abc}$  the structure constant of the SU(3) group.

The aforementioned self-coupling of the gluons arises from the term  $-1/4 G_{\mu\nu}^a G^{a\mu\nu}$  in the Lagrangian that leads to triple and quadruple self-couplings.

Another important feature of the strong force is its dependency on the distance between two colour carrying particles  $r$ . Whereas for the electromagnetic force the strength diminishes with increased  $r$  the strong force increases with  $r$ . This allows quarks that are close to each other (i.e. in a nucleon) to move freely, this is known as asymptotic freedom [23, 24]. On the other hand for quarks with increasing distance the force between them also increases until there is enough energy to create a new quark-antiquark pair out of the vacuum. It

is therefore impossible to observe quarks or gluons alone outside hadrons. In cases where quarks are forcefully separated, e.g. at hadron colliders, they radiate gluons which form new quark-antiquark pairs, known as hadronisation. The hadrons are formed in a cone in the direction of flight of the original particle forming so called jets. Jets form an important part for collisions at hadron colliders and need to be simulated carefully.

### 2.1.4 Particle physics at Hadron Colliders

As the proton is not an elementary particle it is not straightforward to calculate the cross section of interactions at hadron colliders.

The proton consists of three valence quarks, two up-quarks, one down-quark, gluons and a sea of quark-antiquark pairs due to quantum fluctuations. For the calculation of cross sections parton distribution functions (PDFs) are used, the partons are the constituents of a proton and the actual particles that collide. The parton distribution function gives the probability of selecting a parton with a momentum fraction  $x$  of the proton momentum. The PDF depends on the scale  $\mu^2$ , the energy at which the proton is probed. The higher the energy the closer the proton is scrutinized. The momentum fraction  $x$  of the various partons has to be determined experimentally. This is done by several collaborations taking into account various available data sets, e.g. electron-proton scattering and providing PDF sets to be used for experimental data analysis.

By employing PDFs a cross section calculation for a process  $pp \rightarrow X$  is given by

$$\sigma_{pp \rightarrow X} = \sum_{ij} \int_0^1 dx_1 \int_0^1 dx_2 \hat{\sigma}_{ij \rightarrow X} f_i(x_1, \mu_F^2) f_j(x_2, \mu_F^2) \quad (2.20)$$

with  $f_{i,j}$  the parton distribution functions of the proton,  $x_{1,2}$  the momentum fractions of the partons and  $\hat{\sigma}$  the cross section of the underlying process (the hard interaction).

The hard interaction is the actual process that produces new particles and is characterized by large momentum transfer. To be able to produce a new particle the total energy of the process must be higher then the QCD binding energy,  $\Lambda_{QCD}$ . The required energies lead to  $p_{T,proton} \gg m_{proton}$  where the proton can be seen as a collection of free partons described in the Feynman parton model. The quadratic energy available for the hard scattering  $\hat{s}$  is given by

$$\hat{s} = x_1 x_2 s \quad (2.21)$$

with  $s$  the total quadratic energy of the protons and  $x_{1,2}$  the momentum fractions of the hard interaction partons. For cases where  $\hat{s} \gg \Lambda_{QCD}$  the cross section can be written as in Eq. 2.20. The cross section  $\hat{\sigma}_{ij \rightarrow X}$  of the hard scatter can then be calculated from Feynman diagrams in varying degrees of precision.

## 2.2 Open questions of the Standard Model

As successful as the Standard Model is, there are still open-ended questions. To solve the problems presented in the following paragraphs, many new theories and extensions of the Standard Model have been postulated.

### 2.2.1 Hierarchy problem

The Higgs mass gains additional contributions through next-to-leading order (NLO) loop corrections as shown in Figure 2.1 that can occur via the Yukawa interactions described in Eq. 2.16.

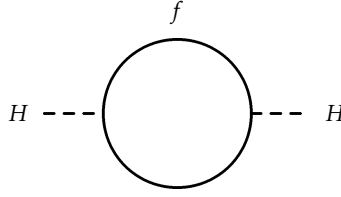


**Figure 2.1:** Feynman diagram of the one-loop corrections to the Higgs mass by fermions .

The observable squared Higgs mass  $m_H^2$  can be parameterized as a “bare” or primary squared mass  $m_{H,bare}^2$  and the part gained through the loop corrections  $\Delta m_H^2$

$$m_H^2 = m_{H,bare}^2 + \Delta m_H^2. \quad (2.22)$$

Fermions contribute as

$$\Delta m_H^2 = -\frac{|\lambda_f|^2}{8\pi^2} \Lambda_{UV}^2 + \mathcal{O}(\ln \Lambda_{UV}) \quad (2.23)$$

to  $m_H^2$ . Here  $\Lambda_{UV}$  is the cutoff scale which is roughly of the order of the reduced Planck scale  $M_{Planck}/2\pi = 2.4 \cdot 10^{18}$  GeV and can be interpreted as the energy scale where new physics (i.e. gravity) must start to play a role and changes the high energy behavior. It is thus a scale until which our known theory could remain valid.  $f$  stands for the involved fermion and  $\lambda_f$  for its Yukawa coupling. Naturally, the largest contributions come from the top quark as it is the heaviest Standard Model fermion. Although the gauge bosons contribute with a positive sign, the effect is too small to balance the fermionic contribution.

By these one-loop corrections, the value of  $\Delta m_H^2$  becomes much too large for the observed particle masses. In the Standard Model one can only solve this problem by tuning  $\Lambda_{UV}$ . As large corrections appear for values of  $\Lambda_{UV} \gg 1$  TeV one would expect new TeV-scale particles to cancel the large corrections to  $\Delta m_H^2$ . Without new physics  $m_H^2$  needs to be severely fine-tuned a solution that is believed rather artificial.

### 2.2.2 Unification of couplings

In analogy to the combined description of the electro-magnetic and weak forces one would like to have a grand unified theory (GUT) which includes the strong force and one day preferably also gravitation. There are several examples of GUTs that have emerged throughout the years [25–27].

For a GUT it would be necessary for the coupling constants to meet at one point around the unification scale of  $\approx 10^{16}$  GeV, but this is not the case in the Standard Model (see Figure 2.2). The measurement of the proton lifetime is the best indicator for GUTs as they predict the decay of the proton. In GUTs, there is an superordinate symmetry e.g. SU(5), which comes with new gauge bosons  $X$  and  $Y$  carrying charge and color. They would couple leptons and quarks, so the proton could decay for example into a pion and a positron. With the current limit of over  $10^{34}$  years, the simplest versions of GUTs are already excluded [8].

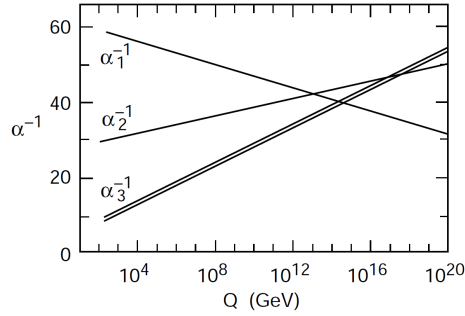


**Figure 2.2:** The evolution of the Standard Model gauge couplings to high energy scales.  $\alpha_1$  is proportional to  $g_2^2$ ,  $\alpha_2$  to  $g_1^2$  and  $\alpha_3$  to  $g_s^2$ .  $\alpha_3$  is given with its experimental error. [28]

### 2.2.3 Dark Matter

Only 5% of the universe is made up of mass and energy we know of. By the measurements of the rotation curves of several galaxies as well as the orbital curves of stars in our galaxy and galaxies in clusters it is confirmed that the known mass is not sufficient to account for the determined velocities [29–31]. So there must be a large amount of mass only interacting weakly (and through gravitation), which has escaped detection until present.

Possible candidates are neutrinos, but they are not massive enough to account for the observed mass. A popular candidate for Dark Matter particles are commonly called WIMPs (weakly interacting massive particles) [12].

A preferred value of the WIMP mass that would accommodate current measurements of the dark matter density is around 100 GeV (heavier WIMP masses are not excluded). So the WIMP mass would be the same order of magnitude as the other heavy Standard Model bosons. Furthermore there are several supersymmetry models that would provide a Dark Matter candidate in the right mass range, this strong motivation of Supersymmetry is known

as 'WIMP miracle'.

In addition the newest results of Planck [32, 33] and WMAP [34, 35] show that the matter and energy content of the universe consists to 26% of Dark Matter and to 69% of Dark Energy. Both are called "dark" as the first does not radiate and the second is simply unknown. The temperature fluctuations of the cosmic microwave background indicate that our universe is flat. Evidence for Dark Energy as the universe is expanding with accelerating speed instead of slowing down and eventually contracting [8].

The 95% of unknown matter and energy are the best arguments for physics beyond the Standard Model. A theory only describing 5% of the universe cannot be the conclusive solution.

### 2.2.4 Gravity

Another aim of an extended Standard Model is the implementation of gravitation as the fourth fundamental force [8]. Because its strength is much below the other fundamental forces it is negligible for short-range interaction. But concerning long-distance, it is the ubiquitous dominant force, which deserves an adequate description by quantum field theory. Its associated gauge boson is already named graviton, yet it has not been discovered.

## 2.3 Supersymmetry

A detailed introduction to Supersymmetry (SUSY) is given for example in [36, 37]. Here only the main features important for this thesis will be introduced. In Section 2.3.1 and 2.3.3 two particular supersymmetric models are described. Both of them are essential for the following chapters.

SUSY could help to find answers for the problems mentioned above in a most natural way. SUSY postulates a superpartner for every fundamental particle in the Standard Model. For every fermion there is a boson and vice versa, which has the same quantum numbers except a differing spin value of  $1/2$ .

SUSY adds therefore fermionic symmetries to the Standard Model and is the extension of the Poincaré symmetry group. The associated super-charges are the generators  $Q_\alpha$  and  $\bar{Q}^{\dot{\alpha}}$  of supersymmetry, 2-component Weyl spinors with a spin index  $\alpha/\dot{\alpha}$  -  $Q_\alpha$  and  $\bar{Q}^{\dot{\alpha}}$  are spin- $\frac{1}{2}$  operators.

The SUSY generating operator  $Q$  acts on a particle state as

$$Q|\text{Boson}\rangle = |\text{Fermion}\rangle, \quad Q|\text{Fermion}\rangle = |\text{Boson}\rangle. \quad (2.24)$$

Supersymmetric theories are usually classified by their number of SUSY generators. The most simple version just possess one copy of  $Q$ , therefore it is denoted "N=1 SUSY". This includes all Supersymmetry models which do not include extra dimensions. The N=1 model with the minimal particle content is called Minimal Supersymmetric Standard Model (MSSM). Table 2.2 shows the postulated particles which are additionally needed in the MSSM.

By implementing SUSY, the coupling constants meet nearly in one point at a scale of order  $\sim 10^{16}$  GeV for the MSSM configuration. Figure 2.3 shows the evolution of the inverse gauge couplings with SUSY [28].

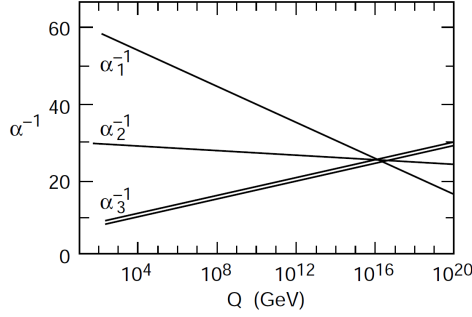


**Figure 2.3:** The evolution of the MSSM gauge couplings to high energy scales, if the SUSY particle masses are of order 1 TeV.  $\alpha_3$  is given with its experimental error. [28]

The fundamental Standard Model particles and their associated superpartners are organized in supermultiplets, which contain both fermions and bosons. All particles of one supermultiplet must have the same mass, electric charge, weak isospin and color degrees of freedom. The superpartner takes part in the same gauge interactions as its Standard Model counterpart. For creating the right supermultiplets, it is important that in each supermultiplet the number of bosonic degrees of freedoms  $n_B$  must equal the number of fermionic degrees of freedom  $n_F$ .

Chiral supermultiplets consist of a single fermion and the corresponding complex scalar field. All Standard Model fermions are arranged in chiral supermultiplets with their superpartner. The superpartner is called scalar fermion or sfermion, e.g. the superpartner of the electron is the selectron.

The other kind of supermultiplet is called gauge supermultiplet and is made up of a spin-1 vector boson and the corresponding spin-1/2 fermion. The gauge supermultiplets contain the Standard Model gauge bosons and their superpartners. For the name of the superpartner a "-ino" is added to the boson's name, e.g. photon and photino.

To implement the Higgs boson, two chiral supermultiplets are necessary to avoid electroweak symmetry inconsistencies. Two chiral supermultiplets are also needed to give mass to both up-type and down-type quarks. The complex scalar Higgs fields are called  $H_u$  and  $H_d$  and consists of both one electric charged and one neutral component. The neutral combination with the lightest mass  $h^0$  can be interpreted as the "known" Standard Model Higgs (see Table 2.2).

Now the solution to the hierarchy problem (see the previous section) is quite simple. Scalar

Name	Spin	$P_R$	Gauge Eigenstates	Mass Eigenstates
Higgs bosons	0	+1	$H_u^0 H_d^0 H_u^+ H_d^-$	$h^0 H^0 A^0 H^\pm$
squarks	0	-1	$\tilde{u}_L \tilde{u}_R \tilde{d}_L \tilde{d}_R$ $\tilde{s}_L \tilde{s}_R \tilde{c}_L \tilde{c}_R$ $\tilde{t}_L \tilde{t}_R \tilde{b}_L \tilde{b}_R$	same same $\tilde{t}_1 \tilde{t}_2 \tilde{b}_1 \tilde{b}_2$
sleptons	0	-1	$\tilde{e}_L \tilde{e}_R \tilde{\nu}_e$ $\tilde{\mu}_L \tilde{\mu}_R \tilde{\nu}_\mu$ $\tilde{\tau}_L \tilde{\tau}_R \tilde{\nu}_\tau$	same same $\tilde{\tau}_1 \tilde{\tau}_2 \tilde{\nu}_\tau$
neutralinos	1/2	-1	$\tilde{B}^0 \tilde{W}^0 \tilde{H}_u^0 \tilde{H}_d^0$	$\tilde{\chi}_1^0 \tilde{\chi}_2^0 \tilde{\chi}_3^0 \tilde{\chi}_4^0$
charginos	1/2	-1	$\tilde{W}^\pm \tilde{H}_u^\pm \tilde{H}_d^\mp$	$\tilde{\chi}_1^\pm \tilde{\chi}_2^\pm$
gluino	1/2	-1	$\tilde{g}$	same
gravitino	3/2	-1	$\tilde{G}$	same

**Table 2.2:** Supersymmetric particles in the MSSM with their gauge and mass eigenstates (adapted from [36] p.78)

bosons contribute to the Higgs mass via

$$\Delta m_H^2 = + \frac{\lambda_S}{16\pi^2} \left[ \Lambda_{UV}^2 - 2m_S^2 \ln(\Lambda_{UV}/m_S) + \dots \right]. \quad (2.25)$$

Compared to Eq. 2.23, it is clear that the contribution of two scalar bosons just cancel the fermion contribution if the coupling strength of the scalar  $\lambda_S$  equals  $|\lambda_f|^2$ . This is the case in the MSSM.

### SUSY-breaking

It was mentioned above that the particles of one supermultiplet have the same mass, despite there has been no discovery of for example two squarks  $\tilde{u}_R, \tilde{u}_L$  with exactly the same mass as the up-quark. Due to its non-discovery, SUSY must be broken.

The way SUSY is broken is called "soft" breaking. The Lagrangian of the MSSM is split up in a SUSY preserving term  $\mathcal{L}_{\text{SUSY}}$ , which contains all gauge and Yukawa interactions and a SUSY-breaking term  $\mathcal{L}_{\text{soft}}$  with positive mass and coupling parameters.

Through the mass terms of the  $\mathcal{L}_{\text{soft}}$  additional NLO corrections to the Higgs mass appear. The corrections are dependent on the largest mass scale  $m_{\text{soft}}$  in  $\mathcal{L}_{\text{soft}}$ :

$$\Delta m_H^2 = + m_{\text{soft}}^2 \left[ \frac{\lambda}{16\pi^2} \ln(\Lambda_{UV}/m_{\text{soft}}) + \dots \right] \quad (2.26)$$

If  $m_{\text{soft}}$  becomes too large, the proposed solution to the hierarchy problem is spoiled. In the case of a reasonable value of  $m_{\text{soft}}$ , the lightest superpartners should have masses around  $\approx 1$  TeV to yield the right Standard Model particle masses.

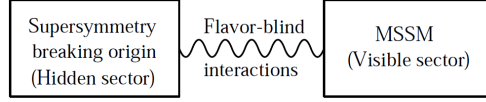


**Figure 2.4:** Illustration of the assumed SUSY-breaking mechanism. [36]

The values of the parameters in the Lagrangian  $\mathcal{L}_{\text{soft}}$  are unknown.

SUSY is broken spontaneously. The symmetry-breaking takes place in a “hidden sector” and is then mediated to the “visible” sector of the MSSM by some kind of interaction as depicted in Figure 2.4. In the MSSM, this interaction has to be flavour-blind to assure universal SUSY-breaking.

It is entirely unknown which kind of interaction plays the role of the symmetry-breaking messenger. There are two main possibilities.

The first possibility is gravitation-mediated SUSY-breaking. For this purpose gravity must be included in the MSSM. The graviton gets a superpartner with spin 3/2, the gravitino. Analogue to gravity, supergravity coupling is suppressed until energies of the Planck scale are reached. As required, supergravity is naturally universal and flavour-blind. The scale at which gravitation-mediated SUSY-breaking occurs is about  $\sim 10^{11}$  GeV.

The other possibility is gauge-mediated SUSY-breaking, where new chiral supermultiplets are introduced for messenger particles. These couple both to the symmetry-breaking sector and the MSSM via  $SU(3) \times SU(2) \times U(1)$  interactions. The scale at which SUSY-breaking occurs is around  $\sim 10^4$  GeV. The LSP is the gravitino for large parts of the parameter space. Gauge-mediated SUSY-breaking also fulfills the condition to be flavour-blind.

The way of SUSY-breaking determines the soft terms  $m_{\text{soft}}$  and has therefore a great influence on the mass spectrum of the MSSM. The general structure of the MSSM is however only slightly affected by choosing a particular breaking mechanism.

### R-parity

R-parity is defined as

$$P_R = (-1)^{3(B-L)+2s} \quad (2.27)$$

where B and L denote the baryon number and the total lepton number respectively and  $s$  is the spin of the particle. In this thesis, only R-parity-conserving MSSM models are considered. R-parity is introduced to accommodate the long lifetime of the proton. This could also be achieved by single B and L conservation, but is thought to be too arbitrary as one already knows that B and L are violated by electroweak effects. All Standard Model particles and the Higgs boson are assigned  $P_R = 1$  and all SUSY particles  $P_R = -1$ .

By this assignment R-parity has some important consequences for the phenomenology.

- Supersymmetric particles must always be produced in pairs (or other even quantities).



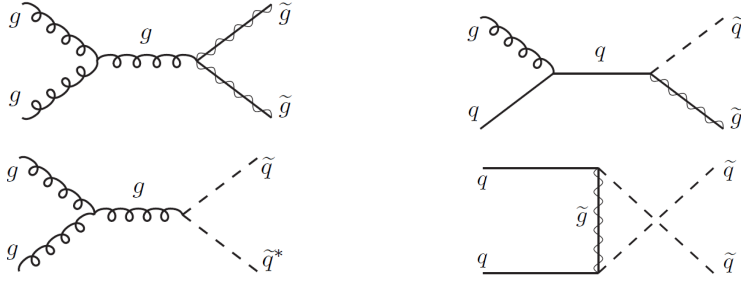


**Figure 2.5:** Example Feynman diagrams for the production of SUSY particles with QCD strength. The time axis goes from the left to the right.

- Each SUSY particle decays to a final state which must contain an odd number of SUSY particles, most naturally the lightest one.
- The lightest supersymmetric particle (LSP) is stable. In most cases the LSP is thought to be electrical neutral, which makes it a only weakly interacting particle with mass of the order  $\sim 100$  GeV. The LSP is therefore an ideal candidate for Dark Matter.

### Mass spectrum

Due to electroweak symmetry-breaking and SUSY-breaking the gauge eigenstates of the superpartners can mix to mass eigenstates if they have the same electric charge,  $R$ -parity and color (see Tab. 2.2).

The wino and the bino mix with the higgsinos to four neutral neutralinos  $\tilde{\chi}_i^0$  and two electrical charged charginos  $\tilde{\chi}_i^\pm$ . The lightest neutralino is often the LSP, especially in gravitation-mediated SUSY-breaking [36].

Due to the very small Yukawa and soft couplings of the first two generations of sfermions, their masses are nearly degenerate. One can therefore also neglect mixing in the first and second generation. This is not the case for the third generation which can have very different mass values from the first two generations. Mixing is also non-negligible, leading to the mixed mass eigenstates  $\tilde{t}_1, \tilde{t}_2, \tilde{b}_1, \tilde{b}_2$  and  $\tilde{\tau}_1$  and  $\tilde{\tau}_2$ .

The gluino  $\tilde{g}$  as a color octet fermion can not mix with any other particle.

### Particle production and decay

SUSY particles can be produced at hadron colliders in collision reactions of electroweak and strong strength. In electroweak processes gauginos can be directly produced in quark-antiquarks annihilations, where the generated Standard Model gauge boson decays to  $\tilde{\chi}_i^\pm/\tilde{\chi}_i^0$ . The strong processes contain besides quark-antiquark annihilation also gluon-gluon fusion, gluon-quark fusion and quark-quark scattering. Figure 2.5 shows some example processes.

As the LHC is a proton-proton collider, the gluon-gluon and gluon-quark fusion processes dominate. This is demonstrated in Fig. 2.6 where the production cross sections for gluino and squark pairs are orders of magnitude larger than for electroweak production. The strong production channels are therefore in the focus of the detector's physics programmes in the early stages of data taking [38]. The electroweak processes become more interesting with larger data sets that counterbalance the low production cross section.

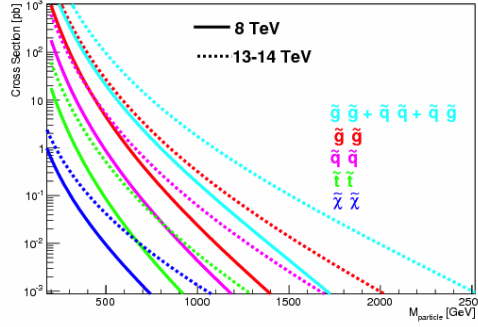


**Figure 2.6:** Cross sections for SUSY particle production, the production cross section for squarks and gluinos is shown for  $\sqrt{s} = 8$  and 13 TeV. The electroweak production cross section is shown for  $\sqrt{s} = 8$  and 14 TeV. [38]

It was already mentioned before that SUSY particles must decay into an odd number of other SUSY particles and Standard Model particles if  $R$ -parity is conserved. Charge and color conservation rules also apply to SUSY particle decays<sup>2</sup>. For the mixed particles their coupling is dependent on their particle content.

Charginos and neutralinos which contain an amount of wino or bino can decay into an  $W^\pm/Z^0$  or the scalar Higgs, together with another chargino or neutralino. They can also decay into any other pair of scalar and fermion. For clear signals in the detector especially the three-body decay of a chargino to a charged lepton plus neutrino and neutralino is important, neutralinos decay into two charged leptons plus neutralino, respectively.

Sleptons always decay into a lepton and a neutralino or chargino.

The dominant decay for squarks is into quark and gluino because it is of the relative strength of the strong force. The electroweak decay into quark and neutralino/chargino is also possible.

As for the gluino, the decay into a squark-quark pair is dominant again, otherwise it can only decay through off-shell squarks leading to  $qq\tilde{\chi}_1^0$  final states.

The most important thing to note is that every decay will lead to a final state containing the LSP - the neutralino  $\tilde{\chi}_1^0$  in most cases.  $\tilde{\chi}_1^0$  interacts only weakly and escapes therefore the detector, leading to missing energy  $E_T^{\text{miss}}$ . The other decay products yield quarks and gluons forming streams of hadrons - the so-called jets - and in some cases leptons. The decay channel without leptons is the most significant as all sparticle pair production contributes

<sup>2</sup> It is always implied in the following that all decay modes have to obey conservation rules.

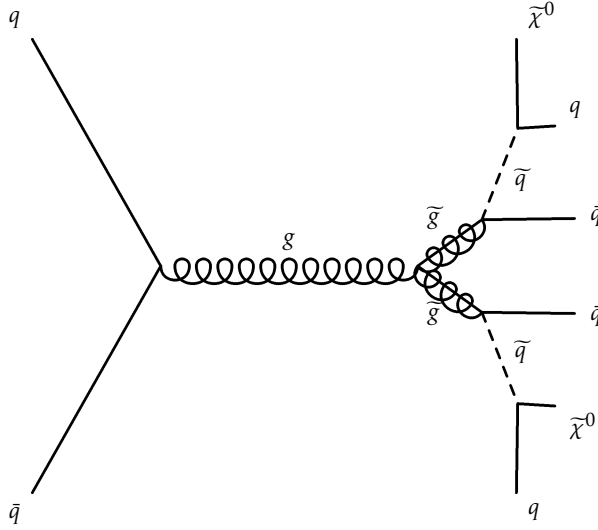


**Figure 2.7:** Feynman diagram of a SUSY cascade decay resulting in jets and missing transverse energy.

to it naturally except slepton pair production. Furthermore, it is also the decay channel prominently featuring in this thesis. Figure 2.7 shows a typical SUSY event.

### 2.3.1 Constrained models

As the breaking mechanism of SUSY is unknown assumptions have to be made to obtain a tangible SUSY model one can study. A popular assumption is that the SUSY breaking is gravity mediated. Examples are minimal supergravity mSUGRA [39] and the constrained cMSSM [40]. mSUGRA was especially popular for early LHC studies as it is especially simple with only five unknown parameters compared to over a hundred in the MSSM, although one has to make several assumptions to accomplish this.

It is required that the soft terms of SUSY-breaking unify at high energies of order of the GUT scale. Together with the gravity mediated SUSY breaking this leaves one parameter for the scalar masses  $m_0$ , one for the gaugino masses  $m_{1/2}$  and one general soft coupling term, the trilinear parameter  $A_0$ , standing for the common values at the GUT scale.

The two remaining parameters are  $\tan \beta$ ,

$$\tan \beta = \frac{\langle H_u \rangle}{\langle H_d \rangle} \quad (2.28)$$

the ratio of the Higgs vacuum expectation values (VEV) and  $\text{sign}(\mu)$ , the sign of the higgsino-mixing parameter.

### 2.3.2 Simplified models

The vast phase space of SUSY models, even of constrained ones as mSUGRA, poses a problem to SUSY searches. Limits on properties as squark and gluino masses vary strongly depending which model is used. ATLAS and CMS have therefore started to employ simplified

models [41]. Simplified models have the advantage that they allow to quantify the reach of search strategies, help with the characterization of any new physics signals and can be used to translate limits to larger models.

Simplified models are characterised by only allowing one sparticle to be produced at the LHC. The remaining sparticles are decoupled by assigning large mass values. In addition to the restricted production process also the decay of the SUSY particles is simplified by often only allowing one decay chain with 100% branching ratio mimicking similar decay chains in the MSSM. Most simplified models have only two free parameters, the mass of the produced sparticle and the mass or the mass difference between sparticles in the decay chain. The resulting models are usually named after the allowed number of decay steps e.g. one-step gluino model ( $\tilde{g} \rightarrow q\bar{q}\tilde{\chi}_2^0 \rightarrow W\tilde{\chi}_1^0$ ).

### 2.3.3 Phenomenological MSSM

The phenomenological MSSM (pMSSM) [42, 43] is a very general SUSY model compared to mSUGRA or other simplified models. There is *no* assumption about the SUSY-breaking mechanism except that the LSP is required to be the lightest Neutralino. So in fact gravitation-mediated SUSY-breaking scenarios are favored, but other breaking scenarios are not excluded. The other assumption is that the first two generations of sfermions are mass degenerated, thus reducing the quantity of mass parameters and the Yukawa couplings. Due to the small Yukawa couplings, the soft couplings of the first and second generation of sfermions are negligible.

In total, 19 parameters are left: 10 sfermion masses  $m_{\tilde{f}}^3$ ; 3 gaugino masses  $M_{1,2,3}$ ; the ratio of the Higgs vacuum expectation values  $\tan\beta$ ; the Higgsino mixing parameter  $\mu$ ; the pseudoscalar Higgs boson mass  $m_A$  and 3 soft coupling terms  $A_{b,t,\tau}$ .

These many parameters give room for a great variety of SUSY models and different mass spectra - leading to different decay patterns and therefore different signals in the detector.

The variety of the pMSSM makes it rather difficult to optimize a search strategy for it. But as it contains all kinds of mass spectra and possible signatures it is a great candidate for broader studies of phase space looking for the most likely neutralino mass for example or for model characteristics that are currently left out by SUSY searches. In studies of the pMSSM often additional experimental constraints are implicitly included to avoid concentrating on already excluded phase space.

### 2.3.4 Experimental constraints

There exist several constraints on SUSY parameters arising from both direct SUSY searches at colliders as well as indirectly from measurements of Standard Model parameters that could deviate if SUSY existed.

The first limits imposed by direct searches come from LEP, where searches were mainly focused on slepton and chargino production via  $Z/\gamma$  production. In the cMSSM combined

---

<sup>3</sup>The sfermion parameters are  $\tilde{Q}_L, \tilde{Q}_3, \tilde{L}_1, \tilde{L}_3, \tilde{u}_1, \tilde{d}_1, \tilde{u}_3, \tilde{d}_3, \tilde{e}_1$  and  $\tilde{e}_3$ .

LEP searches put a limit of 47 GeV on the lightest neutralino and of 92 GeV on the lightest chargino [44, 45]. For light sleptons in the cMSSM masses below 80 GeV to 100 GeV are excluded by DELPHI [46] and ALEPH [47].

For strong production of sparticles  $D\bar{D}$  [48] and CDF [49] set a limit of nearly 400 GeV on squark and gluino masses in the cMSSM. These results were obtained at the Tevatron where proton-anti-protons were collided at a center-of-mass energy of 1.96 TeV. With a much higher center-of-mass energy at the LHC CMS and ATLAS greatly exceed the Tevatron limits, the LHC results will be discussed later in this thesis.

Another constraint comes from the measurement of the Higgs boson mass of 125 GeV. For some models the measured value is in disagreement with the required Higgs boson mass [50]. To not have to completely discard these models workarounds are necessary, e.g. a very heavy stop. SUSY in general narrowly escaped exclusion thanks to radiative corrections to the lightest Higgs mass.

Constraints by astrophysical experiments are mainly placed on the LSP as WIMP candidate. Excesses found by DAMA/LIBRA [51] and CoGent [52] which favor light dark matter and an excess in positrons over electrons in cosmic rays by PAMELA [53] and AMS [54, 55] are ruled out by more recent result by the direct dark matter detection experiments LUX [56] and XENON100 [57].

A strong constraint on SUSY comes from the dark matter relic density. If dark matter is a thermal relic from the early universe, the current observations can be explained by a balance in the annihilation conditions caused by the universes expansion. The dark matter relic density was measured to be  $\Omega_c h^2 = 0.1148 \pm 0.0019$  by WMAP [35] and  $\Omega_c h^2 = 0.1199 \pm 0.0022$  by Planck [33]. Large amounts of SUSY models that result in a too small dark matter annihilation cross section are therefore ruled out.

In general most measurements do not imply a severe constraint on SUSY phase space with exception of the Higgs mass. Though the SUSY phase space can be restricted its large number of free parameters has it so far always left with enough models that comply with all restrictions.

## CHAPTER 3

### The LHC and the ATLAS detector

To study the tiniest of particles requires huge machinery. Stable and controllable conditions are needed to perform precise measurements of elementary particle properties and to search for new physics phenomena. For this purpose particle accelerators produce high energy beams of particles which are set to either collide with each other or with a fixed target. The collision and its products are observed by purpose-built detectors. The detector response for a subset of collision events is recorded for detailed analysis.

The current facility providing this research environment is the Large Hadron Collider (LHC), a circular proton-proton collider located on the border between Switzerland and France at the European Center for Nuclear Research (CERN) near Geneva. This chapter describes the LHC and the ATLAS detector, A Toroidal LHC ApparatuS, a detector designed to observe and measure the particles produced in collisions at the LHC. Their design, configuration and performance is presented.

#### 3.1 The Large Hadron Collider

The Large Hadron Collider [59] is a circular proton-proton collider at CERN and was constructed between 1998 - 2008. The accelerator ring makes use of the tunnel originally built for the Large Electron-Positron collider (LEP) [60], whose operation was stopped in 2000. The ring has a circumference of 26.7 km and is located 170 m underground beneath the French Jura, 45 m underneath lake Geneva level on the Swiss side. The LHC is designed to collide proton beams with a center-of-mass energy of  $\sqrt{s} = 14$  TeV and an instantaneous luminosity of  $10^{34} \text{ cm}^{-2} \text{ s}^{-1}$ . Strict safety protocols due to an incident at the initial start-up of the machine in 2008 limited the LHC operation to a maximum center-of-mass energy of  $\sqrt{s} = 8$  TeV during the first data-taking period between 2010 - 2012 (Run I). Which already made the LHC the most powerful accelerator on earth, a title previously held by the Tevatron [61] located at Fermilab in the US. The Tevatron was colliding protons with anti-protons at a center-of-mass energy of 1.96 TeV, it stopped operating in 2011. For the following data-taking period which started in 2015 (Run II) the LHC center-of-mass energy was increased to  $\sqrt{s} = 13$  TeV.

In addition to proton-proton collisions the LHC also has a heavy-ion program using lead ions with a design energy of 2.76 TeV/nucleon and instantaneous luminosity of  $10^{27} \text{ cm}^{-2} \text{ s}^{-1}$ . The heavy ion collisions are not subject of this thesis.

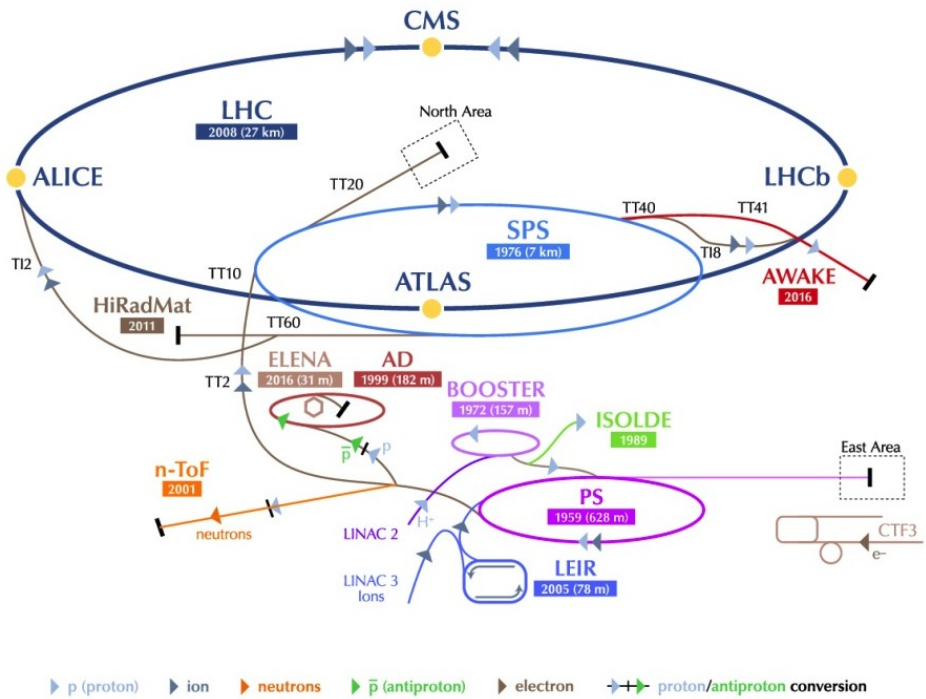


Figure 3.1: Schematic illustration of the LHC with pre-accelerator and experiments ©2016 CERN [58]

### 3.1.1 Experiments at the LHC

There are four main experiments each located at one of the four interaction points along the beam pipe of the LHC where the separately circulating beams collide.

ATLAS [62] and CMS [63] are both multi-purpose detectors designed for high luminosity proton-proton collisions. Their respective interaction points are situated on opposite sides of the ring.

LHCb [64] is designed for the investigation of B-hadron decays. The fourth experiment ALICE [65] is dedicated to observe heavy-ion collisions.

There are also three smaller experiments, TOTEM [66] is aimed at proton elastic scattering at small scattering angles and the total proton-proton cross section, LHCf [67] targets the observation of neutral particles emitted to the very forward region from the collision point. So TOTEM and LHCf are both located near the interaction points of CMS and ATLAS respectively. MoEDAL [68] is dedicated to the search for magnetic monopoles and situated inside the LHCb cavern.

### 3.1.2 Pre-acceleration chain

The protons required for the LHC beams stem from hydrogen atoms stripped of their orbiting electrons. The protons go through several steps before they are injected into the LHC [69], the pre-acceleration chain is shown in Fig. 3.1. In an initial step the protons are accelerated to an energy of  $\sim 50$  MeV in the linear accelerator LINAC2 and injected into the Proton Synchrotron Booster (PSB). In the PSB bunches are formed and filled into the Proton Synchrotron (PS) with a 2-batch filling system at an energy of 1.4 GeV. The PS further accelerates the protons to 25 GeV and performs a multi-splitting of the PSB bunches to ensure the resulting bunch spacing of 25 ns. In the last step in the Super Proton Synchrotron the energy is increased to 450 GeV and the proton bunches are injected into the LHC clockwise and anti-clockwise for the 2 resulting proton beams. The maximum center-of-mass energy reached by the further acceleration by the LHC increased from 7 TeV during the initial start up over 8 TeV in 2011/2012 to 13 TeV in 2015 and 2016.

For the heavy-ion program of the LHC  $\text{Pb}^{29+}$  ions are acquired from a highly purified lead sample heated to  $\sim 500^\circ\text{C}$ . The resulting vapor is ionized by an electron current and accelerated to 4.2 MeV/u (energy per nucleon) in the LINAC3. The ionized lead states are passed through a carbon foil which strips them to  $\text{Pb}^{54+}$  which is accumulated and injected into the Low Energy Ion Ring (LEIR). LEIR increases the energy per nucleon to 72 MeV and injects the beam into the PS. The lead ions are accelerated to 5.9 GeV/u and passed through a foil again, Al foil, that fully strips the ions to  $\text{Pb}^{82+}$  which are further accelerated to 177 GeV/u in the SPS and then injected into the LHC. As for protons the ions are injected both clockwise and anti-clockwise. The LHC accelerates the  $\text{Pb}^{82+}$  beam to its final energy of 2.76 TeV/u.



### 3.1.3 Machine design

The LHC is designed to collide up to 2748 bunches of protons with approximately  $10^{11}$  protons per bunch and a bunch separation of 7 m (corresponding to 25 ns). The particles are kept on track by 1232 dipole magnets, each 14.3 m long and weighing 35 t. The LHC tunnel originates from LEP times and has an internal diameter of only 3.7 m which makes it impossible to have two separate rings of dipole magnets. So a new type of magnet was designed for the LHC, the twin-bore magnet which houses two separate sets of magnet coils and vacuum beam pipes in one cryostat and achieves a maximum magnetic field of 8.3 T at a temperature of 1.9 K.

The bunches are focused by quadropole magnets and accelerated by a 400 MHz superconducting cavity system. Each beam has its individual RF system with eight cavities grouped by four delivering a total of 16 MV accelerating voltage. The two separate RF systems are made possible by an increased distance between the beams from the nominal 194 mm to 420 mm.

The extremely focused proton bunches collide at the four interaction points along the LHC ring with a collision angle of  $290 \mu\text{rad}$ . A measurement for the number of reactions  $N_{event}$  per second at the interaction point is the instantaneous luminosity  $L$ . It is a characteristic variable of a collider and is defined as:

$$\dot{N}_{event} = L \cdot \sigma \quad (3.1)$$

$L$  is only dependent on beam parameters and can be calculated as

$$L = \frac{N_{b1} N_{b2} n_{b2} n_{b1} f_{rev} \gamma_r}{4\pi \epsilon_n \beta^*} F \quad (3.2)$$

with  $N_b$  the number of particles per bunch,  $n_b$  the number of bunches per beam,  $f_{rev}$  the revolution frequency,  $\gamma_r$  the relativistic gamma factor,  $\epsilon_n$  the normalized transverse beam emittance,  $\beta^*$  the  $\beta$ -function at the collision point and  $F$  the geometric luminosity reduction factor arising from the crossing angle of the beams.

The beam emittance gives the phase space ellipse enclosed by the beam particles and needs to be kept especially small due to the dipole's small aperture. The emittance is monitored throughout the pre-acceleration chain and in the LHC by high-resolution beam profile monitors. The  $\beta$ -function gives the optical configuration of the magnets for different powering settings. For normal proton-proton collisions the achieved  $\beta^*$  value in 2016 is 40 cm.

The instantaneous luminosity decreases over time. The main factor for this decrease are the beam collisions which lower the beam intensities and the slow increase of beam emittance. Machine luminosity monitors measure the instantaneous luminosity every second during collisions, the value is averaged over a luminosity block of 60 s. When the luminosity reaches a too low value the beam is dumped and the next fill is prepared. In 2016 the average luminosity life time was 24 h. The average LHC turnaround time from the ramp down of the magnets at the end of the fill to again stable beams with collisions is  $\sim 3$  h (1.15 h theor.). During 2016 the up-time of the LHC was  $\sim 60\%$ .

How many interaction events actually are delivered to the experiments is given by the integrated luminosity:

$$L_{\text{int}} = \int L dt \quad (3.3)$$

Together with the center-of-mass energy the  $L_{\text{int}}$  characterizes a data set. Fig. 3.2 shows the integrated luminosity recorded by ATLAS during 2016 and compared to previous years. The peak instantaneous luminosity reached for each fill in 2016 is shown in Fig. 3.3. The recorded luminosity gives the number of events actually captured by the detector. There is a difference between the delivered luminosity by the LHC and the recorded luminosity by ATLAS. A small difference arises from the time the detector needs to switch to stable beam conditions. During a whole year occasional short-lived problems with subdetectors and the data acquisition system lead to further losses of recorded luminosity.

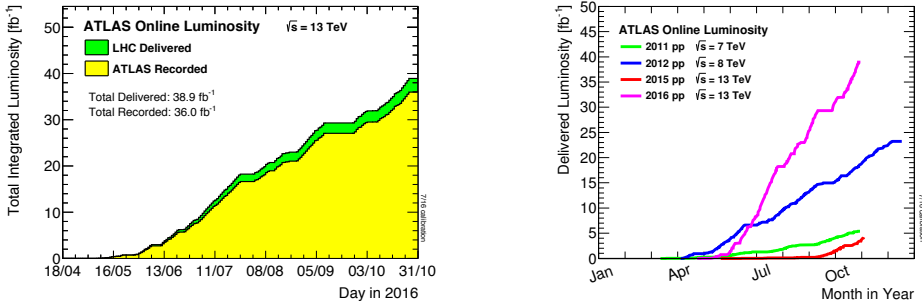


**Figure 3.2:** The left plot shows the cumulative luminosity versus time delivered to (green) and recorded by ATLAS (yellow) during stable beams for p-p collisions at 13 TeV centre-of-mass energy in 2016. In the right plot the cumulative delivered luminosity is shown for the years of 2011 - 2016.

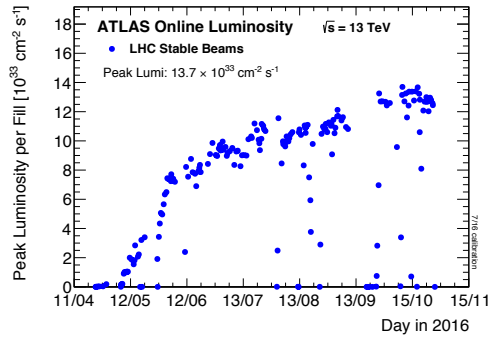


**Figure 3.3:** The peak instantaneous luminosity delivered to ATLAS during stable beams for p-p collisions at 13 TeV centre-of-mass energy is shown for each LHC fill as a function of time in 2016.

Another important parameter is  $\mu$  (or pile-up), the average number of interactions per bunch

crossing:

$$\mu = \frac{L\sigma_{inel.}}{n_b f_{rev}} \quad (3.4)$$

where  $\sigma_{inel.}$  is the total inelastic proton-proton cross section, which is 80 mb for 13 TeV collisions. The bunch luminosity  $\frac{L}{n_b}$  is determined by several independent luminometers part of the ATLAS luminosity system [70]. For the new record peak luminosities up to  $1.2 \times 10^{34} \text{ cm}^{-2} \text{ s}^{-1}$  in 2016 also  $\mu$  increased and ranged between 18 - 39 interaction per crossing for normal p-p data taking. Fig. 3.4 shows the luminosity-weighted average pile-up values for 2016.

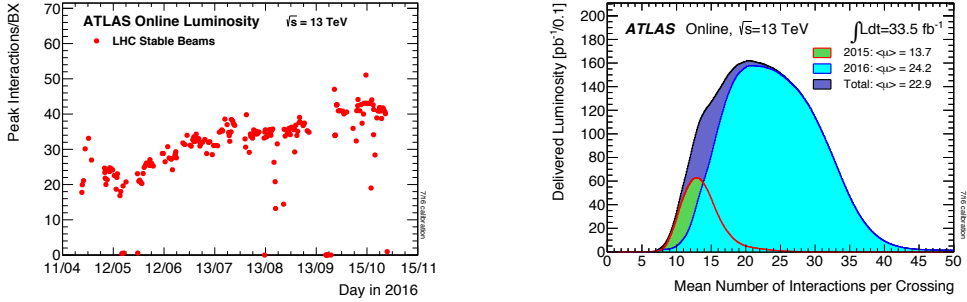


**Figure 3.4:** The peak value for the number of inelastic collisions per beam crossing ( $\mu$ ) during stable beams for p-p collisions at 13 TeV centre-of-mass energy is shown for each fill in 2016 on the left. For comparison on the right the luminosity-weighted distribution of the mean number of interactions per crossing for the 2016 and 2015 p-p collision data is shown.

### Proton-proton collisions

The LHC's peak design luminosity of  $> 1 \times 10^{34} \text{ cm}^{-2} \text{ s}^{-1}$  and center-of-mass energy  $\sqrt{s} = 14 \text{ TeV}$ . The total inelastic proton-proton cross section will be  $\sim 80 \text{ mb}$ . This translates to roughly  $10^9$  interactions per second. Only a small fraction of these events is of interest for physics. Most events will be minimum-bias events with a transverse momentum of only  $\sim 500 \text{ MeV}$ . High transverse momentum final state particles are characteristic for interesting, hard-scattering events from inelastic collisions. The partons in the proton each have a fraction  $x_i$  of the protons collision energy, resulting in a lower effective center-of-mass energy  $\sqrt{\hat{s}} = \sqrt{x_1 x_2} \sqrt{s}$ . Naturally this reduces the energy available to produce heavy particles in the process. The parton fraction of energy increases quickly with the mass of the produced particle. The parton distribution function (PDF) of the proton further diminishes the probability for a high momentum quark-anti-quark interaction, quark-quark interactions are slightly more likely with gluon-gluon interactions the most common ones. The event yields for beyond Standard Model processes with the production of new heavy particles therefore are directly related to these probabilities.

## 3.2 The ATLAS detector

The ATLAS detector [71] is a multi-purpose detector with almost complete coverage of the interaction point. It is 44 m long, has a diameter of 25 m and weighs 7000 t making it the largest detector at the LHC. The physics program of the ATLAS collaboration spans a wide field with focus on the long outstanding discovery of the Higgs boson, searches for supersymmetry and new physics beyond the Standard Model and precision measurements of the top quark and W boson mass and other SM parameters as gauge boson couplings and CP violation.

To accomplish this program the ATLAS design needs to fulfill the following requirements:

- Enclosing the interaction point with a large acceptance in  $\eta$  and nearly full azimuthal angle coverage for an excellent reconstruction of transverse missing momentum and detection of all produced particles.
- Precision tracking in the highly dense environment of the LHC providing high  $p_T$  lepton momentum measurements, efficient charged particle identification and full event reconstruction.
- Great calorimetry in order to identify and measure electrons and photons, complete coverage by the hadronic calorimeter for precise jet and transverse missing momentum measurements.
- Excellent muon spectrometer providing the stand-alone capability to fully reconstruct all muons.
- Outstanding resolution for energy and position measurements also for low  $p_T$  particles important to interesting physics processes.

### 3.2.1 Detector layout

The ATLAS detector is constructed of several layers of sub-detectors each with a specific purpose. The layout of the different components is shown in Fig. 3.5. The Inner Detector (ID) is closest to the beam pipe and provides the high-resolution tracking. It consists of three components, the Pixel detector including also the Insertable B-Layer (IBL), the SemiConductor Tracker (SCT) and the Transition Radiation Tracker (TRT). The Solenoid magnet provides a constant 2 T magnet field for the ID. Surrounding the ID are the electromagnetic Liquid Argon (LAr) calorimeter followed by the hadronic Tile calorimeter, which have the purpose of precise energy measurements of leptons, photons, jets and transverse missing momenta. The sub-detector furthest away from the interaction point is the muon spectrometer (MS) its outer chambers are located at a radius of 11 m. The MS provides high-resolution momentum measurements and identification of muons. The whole detector is surrounded by large air coils of the Toroid magnet.

The combination of all the sub-detectors ensures that all interacting particles are detected and measured and providing a precise reconstruction of missing transverse momenta of non-

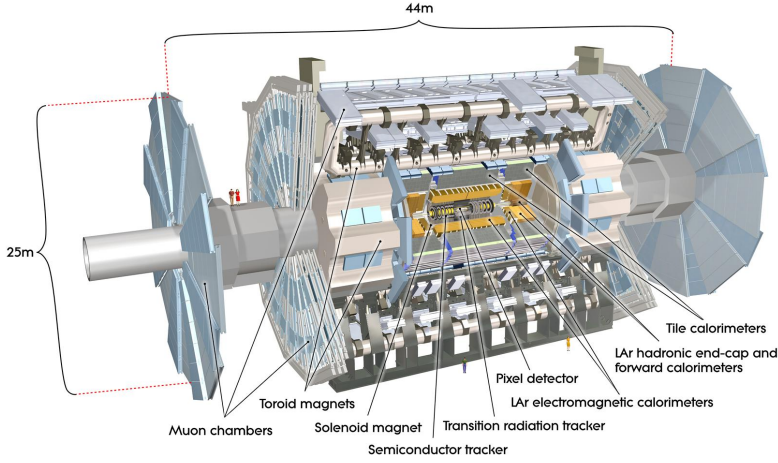


**Figure 3.5:** Schematic view of the ATLAS detector. ATLAS Experiment ©2008 CERN [72]

or only weakly interacting particles that can escape the detector. The ways how different types of particles are detected is shown in Fig. 3.6. Each sub-system will be described in detail in sections 3.2.2-3.2.5.

ATLAS uses a right-handed coordinate system shown in Fig. 3.7 with the x-y-plane perpendicular to the beam-axis, the z-axis, and the x-axis pointing into the center of the LHC. The position of a particle is given by  $\theta$ , the polar angle between a particle and the beam axis and  $\phi$  the azimuthal angle around the beam-axis. Instead of  $\theta$  mostly the pseudorapidity  $\eta$  (3.5) is used.

$$\eta = -\ln \left[ \tan \left( \frac{\theta}{2} \right) \right] \quad (3.5)$$

$\eta$  can take values between  $\infty$  to  $-\infty$ , the value zero corresponds to  $\theta = 90^\circ$ . ATLAS only encloses a  $|\eta|$  values up to a maximum of 4.9

Other parameters commonly used for distance measurements in ATLAS are the transverse impact parameter  $d_0$ , the perpendicular distance to the primary vertex from the point of closest approach of a track, the z-position at closest approach is given by the longitudinal impact parameter  $z_0$ . For the distance between two objects in space  $\Delta R$  is employed:

$$\Delta R = \sqrt{(\Delta\phi)^2 + (\Delta\eta)^2} \quad (3.6)$$

### 3.2.2 Magnet system

The ATLAS magnet system [74] consist of four parts. The central solenoid providing the magnetic field of the inner detector , the barrel toroid and the two end-cap toroids together providing the magnetic field for the muon spectrometer. Fig. 3.8 shows a schematic view of the whole magnet system. All four magnets are cooled by 4.5 K Helium and the coils consists

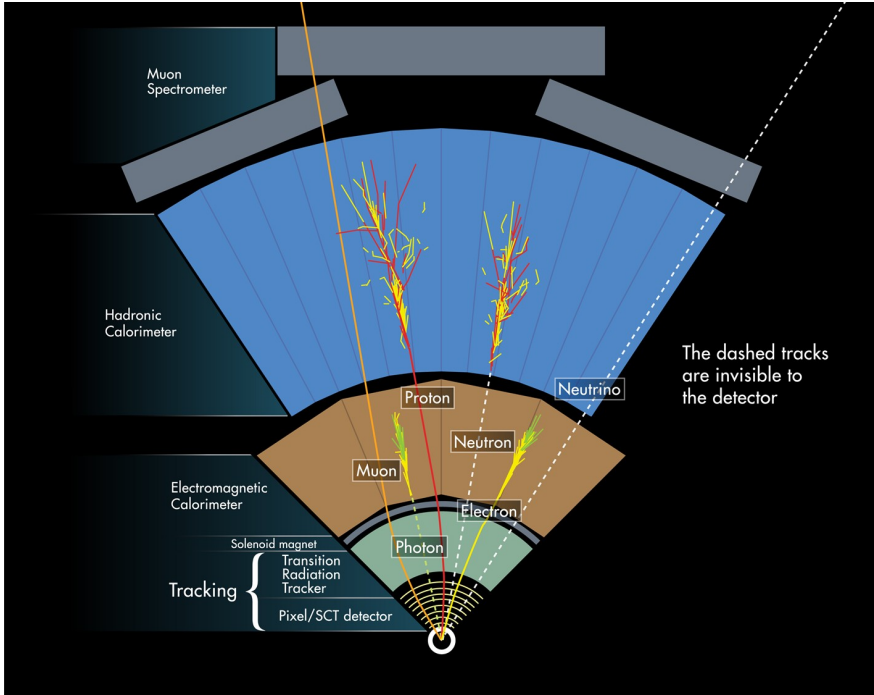


**Figure 3.6:** The detection of different particle types with the ATLAS detector. ATLAS Experiment ©2013 CERN [73]

of flat superconducting NbTi cables with a supporting mantle of Al.

### Central solenoid magnet

The central solenoid is located between the inner detector and the calorimeters. It has an axial length of 5.3 m and an inner diameter of 2.4 m. The single superconducting coil of the solenoid generates an axial symmetric magnetic field of 2 T. The iron in the tile calorimeter functions as reflux yoke and magnetically decouples solenoid and toroid. As the solenoid is located in front of the calorimeter it is essential to minimize its material to not harm the performance of the LAr calorimeter. To achieve this goal the solenoid shares the vacuum vessel with the LAr calorimeter and its material thickness amounts only to 0.64 radiation lengths  $X_0$  [75]. The solenoid is powered by a 8 kA current.

### Toroid magnet

The toroid surrounding the barrel consists of 8 large air-core coils radially arranged around the beam axis, each 26 m long and with a diameter of 20 m. The two end-cap toroids are located at each end of the barrel toroid. They each have a length of 5 m, outer diameter of 10.7 m and are rotated by  $22.5^\circ$  with respect to the barrel to maximize the bending power in the transition region. The bending power  $\int B dl$  of the barrel and end-cap toroids is 2 - 6 Tm and 4 - 8 Tm in the 0 - 1.3 and the 1.6 - 2.7  $|\eta|$  -regions, respectively. Each coil of the toroids

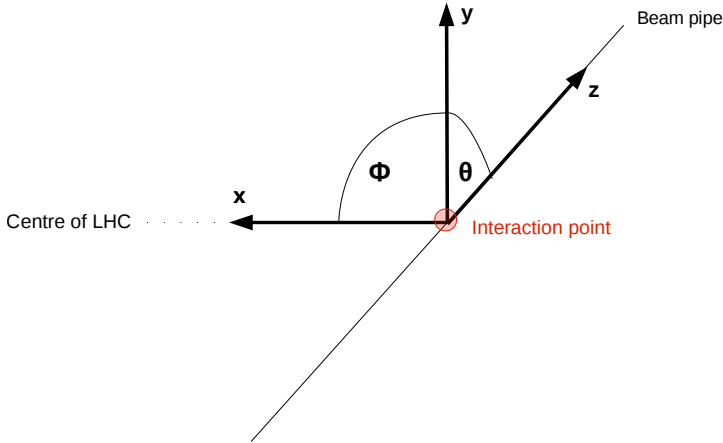


Figure 3.7: Schematic view of the interaction point.

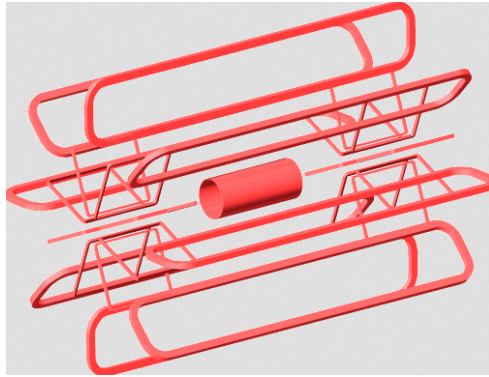


Figure 3.8: Schematic view of the ATLAS magnet system.[74]

is powered by a 20.5 kA current. The end-cap toroids are put on a rail system that allows the opening of the detector.

### 3.2.3 Inner detector

The main purpose of the inner detector[76–78] shown in Fig. 3.9 is high precision tracking of charged particles and vertexing. The ID is contained inside the solenoid, it covers a  $|\eta|$  - range up to 2.5 and is closest to the beam pipe. This poses two challenges, the employed detector technologies need to be radiation hard and need to provide a high spatial resolution in the large track density environment next to the interaction point. Another concern is the material located before the calorimeter, the total amount of interaction length  $X_0$  needs to be minimized. The ID uses three different technologies to achieve this goal, the tracking efficiency for a 500 GeV particle is 0.88. Fig. 3.10 shows a section of the ID configuration in

Run I.

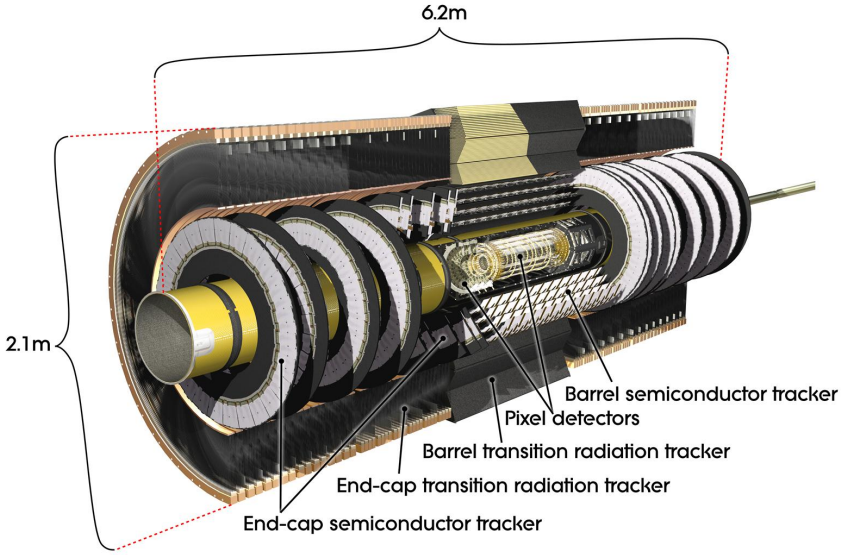


**Figure 3.9:** A schematic view of the ATLAS inner detector. ATLAS Experiment ©2008 CERN[79]

### Pixel and IBL

Pixel detectors are used closest to the interaction point, there are three layers around the beam axis with an inner diameter of 5 - 13 cm with a new fourth layer added for Run II. In addition two end-caps of three concentric discs each are located at a distance of 495 mm, 580 mm and 650 mm from the interaction point.

A single pixel has the dimension of  $50 \times 400 \mu\text{m}^2$  leading to a resolution of  $10 \mu\text{m}$  in the  $R\text{-}\phi$ -plane and  $115 \mu\text{m}$  in the  $z$ -direction. There are 1744 pixel modules that are cooled to  $-5^\circ\text{C} - 10^\circ\text{C}$  to protect them of radiation damage and to reduce the noise level as well.

In the Long Shutdown 1 (LS1) in 2014 the Pixel detector was upgraded with a new Insertable B-Layer (IBL) getting even closer to the beam axis. In the process the beam pipe was also renewed to enable independent repairing of the beam pipe in case of failures.

IBL is crucial for high efficiency  $b$ -tagging at high luminosities as the Pixel detector was optimized for a bit lower luminosities during Run I. It also provides tracking robustness in the case of failures of older Pixel modules. As it is closer to the beam pipe also the precision of the impact parameters will be improved leading to better vertexing.

IBL uses upgraded pixel technology with newly developed chips and readout. The material thickness is only 60% of the radiation length of the existing innermost pixel layer - to fit into the confined space of 12.5 mm between Pixel and beam pipe and also to minimize material in front of the calorimeters.



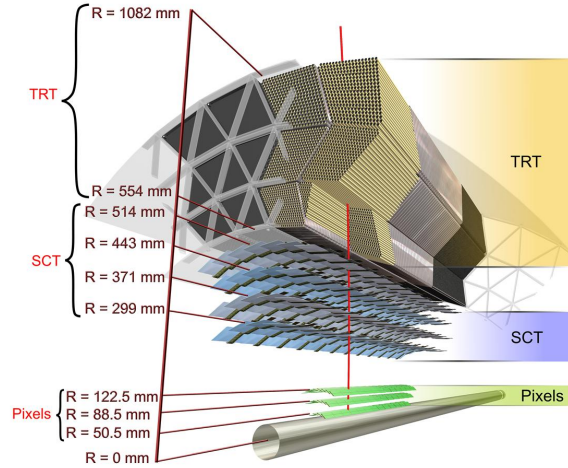


**Figure 3.10:** A detailed view of the ATLAS inner detector before LS1. ATLAS Experiment ©2008 CERN[79]

### Semiconductor Tracker

SCT consists of silicon strips in four layers around the barrel at a inner diameter of 24 - 55 cm. The nine end-cap discs also provide four additional space-point measurements. A silicon strip module is constructed of two layers rotated by 40 mrad to facilitate a z-measurement. Each of the 4088 SCT modules consists of 768 strips, the in-between strip distance is  $80 \mu\text{m}$  providing a resolution of  $17 \mu\text{m}$  in the  $R\text{-}\phi$ -plane and  $580 \mu\text{m}$  in the z-direction. The SCT modules are cooled to the same temperature as Pixel.

### Transition radiation tracker

The TRT uses straw detectors, gas filled tubes, for tracking and electron identification via the transition radiation. There are a total of 370 000 straws arranged in 73 and 160 layers in the barrel and the end-cap, respectively. The large number of straws provides  $\sim 36$  additional space-point measurements.

One straw has a diameter of 4 mm, contains a  $30 \mu\text{m}$  gold-plated W-Re wire and is filled with a radiation hard gas mixture of 70% Xe, 20%  $\text{CO}_2$  and 10%  $\text{CF}_4$ . In the barrel the maximum straw length is 144 cm. The drift time measurement provides two thresholds, a low one for tracking hits and a high one for transition radiation. The spatial resolution per straw is  $170 \mu\text{m}$ .

Each module contains between 329 - 793 straws covering the radial range from 56 - 107 cm in the barrel. The end-cap modules are arranged in 18 discs. Combined the TRT has a resolution of  $50 \mu\text{m}$ , no cooling is required.

### 3.2.4 Calorimeters

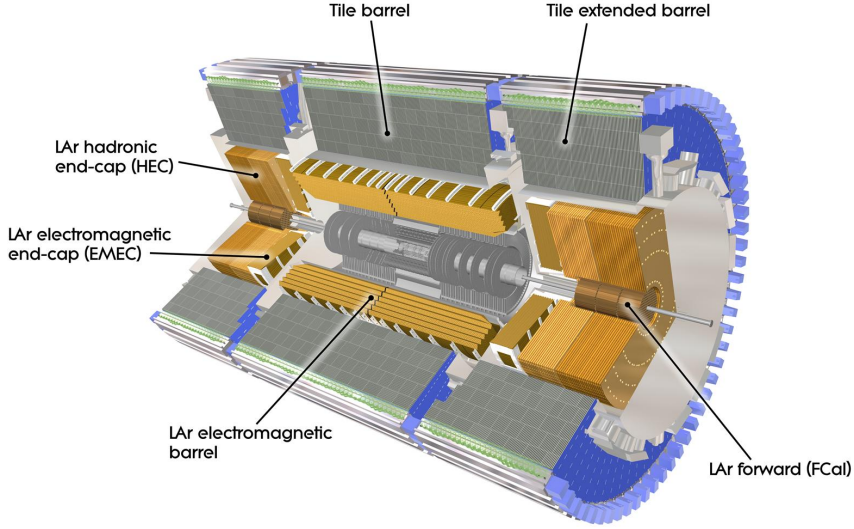


**Figure 3.11:** Overview of the ATLAS calorimeters. ATLASExperiment ©2008 CERN [80]

The calorimeters are composed of three sub-detectors, the electromagnetic (EM), the hadronic and the forward calorimeter. The EM calorimeters covers the range of  $|\eta| < 3.2$  and is designed to measure the energy of electrons and photons. The hadronic calorimeter detects hadrons and hadronically decaying  $\tau$ -leptons and covers  $|\eta|$  up to 4.5. Combined with the forward calorimeter full azimuthal coverage for precise missing transverse energy measurements is provided.

All ATLAS calorimeters are sampling calorimeters where a layer of an active medium and a layer of an absorber material are alternated. The particles coming from the interaction point interact with the matter leading to a particle shower and therefore energy deposition in the calorimeter. To significantly reduce the cost and size most calorimeters do not only contain the active medium but also an absorbing matter.

One of the most important characteristic quantities of a calorimeter is its energy resolution  $\sigma(E)$ . It consists of stochastic  $S$ , noise  $N$  and constant  $C$  terms:

$$\frac{\sigma(E)}{E} = \frac{S}{\sqrt{E}} \oplus \frac{N}{E} \oplus C \quad (3.7)$$

with  $E$  the energy of the particle. Figure 3.11 shows an illustration of the calorimeter system.

#### Electromagnetic calorimeter

The EM calorimeter of ATLAS uses Liquid Argon (LAr) as active material and lead as absorber using an accordion-shaped electrode geometry for high-resolution energy measure-

ments. The EM barrel (ECAL) covers the range  $|\eta| < 1.475$ , the EM end-cap (EMEC) the range  $1.375 < |\eta| < 3.2$  and the transition region ranges between  $|\eta| = 1.37$  and  $|\eta| = 1.52$ . LAr is used because of its radiation-hard properties and its linear response function.

The ECAL and EMEC have a radiation length of  $22 - 33 X_0$  and  $24 - 38 X_0$ , respectively, in order to contain most parts of an electromagnetic shower. To remain as transparent to hadrons as possible to not hamper the hadronic energy resolution the ECAL has only a length of  $1.5 \lambda$  nuclear interaction length. The energy resolution of the ECAL is designed to be  $S = 10\%$ ,  $C = 0.7\%$  and  $N = 400$  MeV.

The ECAL is composed of three layers around the beam pipe. The first layer has the highest granularity with  $\Delta\eta \times \Delta\phi = 0.003 \times 0.1$  and a length of  $4.3 X_0$ . The high granularity is needed to identify electrons and photons from pions. A pion  $\pi^0$  decaying into two photons before the EM calorimeter is leading to two electromagnetic showers with only a small angle between the two, the accordion-shape helps to discriminate between these two close showers and a single shower coming from a primary photon. The second layer is  $16 X_0$  long, the largest fraction of an EM shower is contained in this layer, the granularity is  $\Delta\eta \times \Delta\phi = 0.025 \times 0.025$ . The third layer is used to distinguish between an electromagnetic and a hadronic shower, it has a coarser granularity of  $\Delta\eta \times \Delta\phi = 0.05 \times 0.0245$ .

The EMEC has two co-axial wheels on each side of the interaction point, that consists of 8 wedge-shaped modules each. It also uses the three layer design. The first layer has only strips in  $\eta$  and is  $4.4 X_0$  long, the second and third layer have cells of  $\Delta\eta \times \Delta\phi = 0.025 \times 0.025$  and  $\Delta\eta \times \Delta\phi = 0.05 \times 0.05$ , respectively.

To correct for the lost energy of particles before they reach the ECAL, a presampler of a 1.1 cm active LAr layer is installed in front of the ECAL. The dead material is not evenly distributed in  $\eta$ , the thickness in  $X_0$  varies between 1.8 to 4.3. There is a transition region between barrel and end-cap at  $1.37 < |\eta| < 1.52$  with a worse energy resolution due to additional material. It is named crack region and excluded by physics analyses.

### Hadronic calorimeter

The hadronic calorimeter also consists of a barrel (HCAL) plus barrel extension and two end-caps (HEC) covering a range of  $|\eta| < 1$ ,  $0.8 < |\eta| < 1.7$  and  $1.5 < |\eta| < 3.2$ , respectively. As hadronic showers are composed of more complex interactions (e.g. energy 'vanishing' by providing the binding energy of a nucleus) the energy resolution of a hadronic calorimeter is worse than of an EM one. The ATLAS hadronic barrel calorimeter has a stochastic term of  $S = 50\%$ .

The HCAL is constructed of layers of a 14 mm thick steel absorber and 4 mm scintillator plates. There are 64 modules for each the barrel and its extension arranged in three consecutive layers around the beam pipe. The granularity has values of  $\Delta\eta \times \Delta\phi = 0.1 \times 0.1$  for the two inner layers and  $\Delta\eta \times \Delta\phi = 0.2 \times 0.1$  for the outer layer. The maximum length is  $9.7 \lambda$  at the thickest point at  $\eta = 0$ .

The HEC also uses LAr as active material with copper absorbers. The layout is the same as for the EMEC with 3 concentric wheels segmented in 32 wedges. The range is  $|\eta| < 3.2$  with

a granularity of  $\Delta\eta \times \Delta\phi = 0.1 \times 0.1$  below  $|\eta| = 2.5$  and  $0.2 \times 0.2$  above.

To prevent a hadronic shower leaking through to the muon spectrometer the minimum depth in units of nuclear interaction length in the barrel is  $\lambda = 7.5$  and  $\lambda = 10$  in the end-cap.

### Forward calorimeter

Especially for calorimeters a hermetic coverage in  $\Delta\eta \times \Delta\phi$  is crucial as otherwise no precise measurement of the transverse momentum is possible. The LAr forward calorimeter (FCAL) is challenged by the high flux of particles at a range of  $3.1 < |\eta| < 4.5$ . To be able to contain all particles the three layers of the FCAL are several radiation lengths long. The innermost layer uses a copper absorber, it is  $27.6 X_0$  long and targets the EM shower. The two outer layers have tungsten as absorber material, are  $91.3 X_0$  and  $89.2 X_0$  long and are designed to absorb the hadronic particles.

### 3.2.5 Muon spectrometer

Due to their long lifetime and low energy deposition in the calorimeters high momentum muons are able to traverse the whole detector. The muon spectrometer [81] as shown in Fig. 3.12 provides a stand-alone high precision momentum measurement and trigger for muons based on the magnetic deflection of muon tracks. The configuration of the magnets is such that the bending power is orthogonal to the muon track and at the same time it minimizes multi-scattering. The spectrometer is composed of two independent sub-systems for its two main purposes.

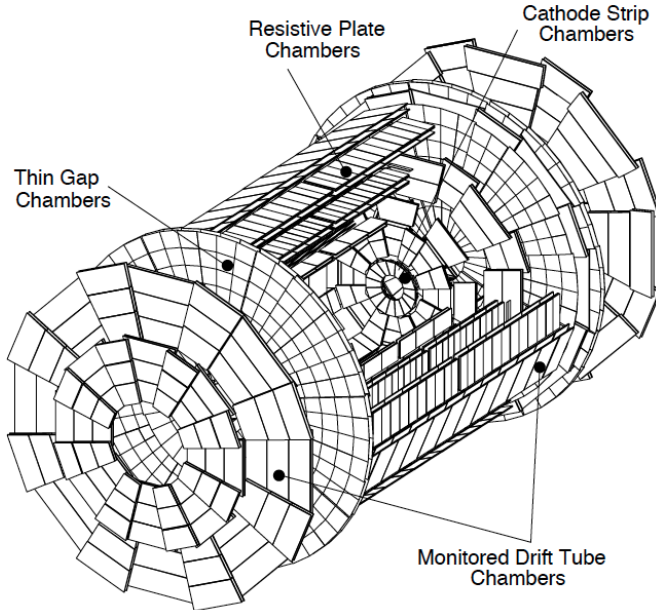


**Figure 3.12:** 3-D view of the muon system with indication where the different chamber technologies are use.[81]

### Tracking system

The high precision tracking system is constructed in a way that a muon always traverses three stations of detection chambers. In the barrel region for  $|\eta| < 1$  there are three cylindrical layers of Monitored Drift Tube (MDT) chambers at a distance of 5, 7.5 and 10 m to the beam tube. Each layer consists of 16 chambers surrounding the interaction point with slightly overlapping chambers ensuring complete coverage. Only a small gap at  $|\eta| = 0$  exists for a service tunnel.

Also the four concentric discs at 7, 10, 14 and 21-23 m from the interaction point in the end-cap region consist of MDT chambers. Only for the innermost ring of the disc closest to the interaction point covering the very forward range of  $2 < |\eta| < 2.7$  Cathode Strip Chambers (CSC) are used as they provide a higher granularity in this especially high flux environment. In the barrel the station arrangement takes the best advantage of the magnet configuration by measuring the bended muon track once at the inner field boundary, once at the field maximum and once at the outermost field boundary.

The MDTs are made of aluminum tubes with a diameter of 30 mm containing a 50  $\mu\text{m}$  W-Re wire and filled with a gas mixture of 93% Ar and 7%  $\text{CO}_2$  pressurized at 3 bar. The single-wire resolution of a MDT is 80  $\mu\text{m}$ , the tubes are combined in  $2 \times 4$  mono-layers for one chamber at the inner station ( $2 \times 3$  for the outer stations) resulting in a resolution of 30  $\mu\text{m}$ . The maximum drift time is 700 ns.

The CSCs are multiwire proportional chambers. The layout consists of a symmetrical cell with the distance between anode to cathode  $d = 2.54$  mm equaling the distance between the anode wires. They are filled with a gas mixture of 30% Ar, 50%  $\text{CO}_2$  and 20%  $\text{CF}_4$ . The muon track coordinate results from the measurement of the charge on the segmented cathode induced by the avalanche arising on the anode wire. The readout spacing of the segmented cathode is 5.08 mm providing a spatial resolution of 60  $\mu\text{m}$ . CSCs have an intrinsically small electron drift time with a time resolution of 7 ns. Other advantages include good two-track resolution and low sensitivity to neutrons destining CSCs for the demanding environment close to the interaction point. The chambers are composed of  $2 \times 4$  layers and slightly tilted to be orthogonal to the muon tracks.

### Muon trigger chambers

The muon trigger system covers a range up to  $|\eta| < 2.4$  and provides three core abilities. The identification of the bunch crossing with a required resolution of 25 ns. A stand-alone trigger for several well-defined  $p_T$  thresholds,  $\sim 5$  GeV for low  $p_T$  and 10 -20 GeV for high  $p_T$  muons. And as third ability the measurement of the second directional coordinate, here a spatial resolution of 5 - 10 mm is sufficient.

Similar to the tracking system it depends on three stations, in the barrel two Resistive Plate Chambers (RPC) are located around the middle MDT station and one before or after the outer MDT station covering the  $|\eta|$ -range up to 1.05. The radial arrangement is chosen in a way that the trigger window area for both low and high  $p_T$  muons is identical. In the end-cap

the trigger is provided by Thin Gap Chambers (TGC) located in the middle stations of MDT chambers ranging between  $1.05 < |\eta| < 2.4$ .

RPCs are gaseous detectors consisting of two parallel resistive bakelite plates separated by a gas gap of 2 mm and filled with tetrafluoroethane with a small mixture of  $\text{SF}_6$  to reduce the operating voltage. The signal from the forming avalanche is read out by capacitive coupling of metal strips on the backside of the plates. The space  $\times$  time resolution is  $1 \text{ cm} \times 1 \text{ ns}$ .

TGCs are similar to CSCs but the distance between the anode wires is larger than between anode and cathode. The gas gap between the cathodes is 2.8 mm, with the anode wires separated by 1.8 mm, and filled with 55%  $\text{CO}_2$  and 45%  $n\text{-C}_5\text{H}_{12}$ . The high operating voltage of 3.1 kV leads to a short drift time and very good time resolution. Depending on the  $|\eta|$  - resolution 4 - 20 wires are combined and read out together.

### 3.2.6 Trigger and data acquisition

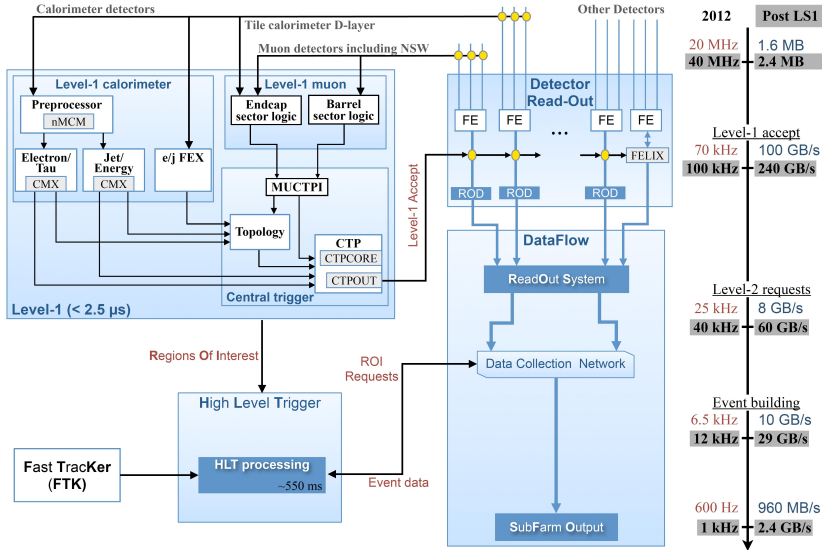


**Figure 3.13:** Overview of the trigger and data acquisition system for Run II. The peak design event (in red) and data rates (in blue) are each given before and after the Long Shutdown 1. [82]

Each second  $10^9$  interactions take place inside ATLAS providing a challenging environment to separate the rare interesting processes from the large amount of background ones. With a bunch spacing of 25 ns the collision rate is 40 MHz whereas the event storage is limited to  $\sim 1$  kHz writing rate corresponding to 2.4 Gb/s. The exercise of selecting events and reducing the rate by a factor of  $10^4$  falls to the trigger and data acquisition system [82]. During the Long Shutdown 1 (LS1) in 2014 the trigger system was upgraded. An overview of the current state is shown in Fig. 3.13 together with a comparison of key parameters to the values in 2012 and 2015 (after LS1).

The ATLAS trigger system originally was a three-level system, but the two higher levels were

merged during LS1. The two existing consecutive levels are the hardware based Level-1 (L1) trigger with access to coarse granularity event information from the calorimeters (L1Calo) and muon spectrometer (L1Muon). At L1 the rate is reduced from 40 MHz to roughly 100 kHz with a latency of  $2.5 \mu\text{s}$ . The second level is the software based High Level Trigger (HLT). The HLT algorithms have access to the full event information and further reduce the rate to the required 1 kHz with a latency of a few seconds.

The Data Acquisition (DAQ) system is responsible for the transport and assembly of event data. This covers read-out of the front-end buffers of the detector electronics to the final storage of events on disk.

### L1 Trigger

The L1 trigger in Run II has three sub-systems: L1Calo, L1Muon and L1Topo. L1Calo and L1Muon have only access to the calorimeter and muon event information respectively, L1Topo which is new and commissioned during Run II has access to both systems and is able to use more complicated algorithms using several Trigger Objects (TOBs) as input.

The Level 1 system consists of built-in custom electronics comparing the incoming signals to 256 programmable items. If the threshold for at least one of the items is met a L1 Accept is issued. This decision is the task of the Central Trigger Processor (CTP). With the L1 Accept the read-out and processing of the event data in the Read-Out Drivers (ROD) is started.

**L1Calo** L1Calo receives input from  $\sim 7200$  analogue trigger towers of the electromagnetic and hadronic calorimeters with a granularity of  $0.1 \times 0.1$  in  $\Delta\eta \times \Delta\phi$ . The input signals are digitized by the PreProcessor (PP) which also identifies the correct Bunch Crossing ID (BCID) of the signal. Further it applies pedestal corrections, noise suppression and energy calibration before transferring the data to the Cluster Processor (CP) and the Jet/Energy-sum Processor (JEP). The CP is responsible for finding electron/photon and  $\tau$  candidates whereas the JEP executes the jet clustering and the calculation of energy sums. Both processors transmit the information about which high  $p_T$  thresholds have been passed and how often (number of hits) to the CTP. Fig. 3.14 shows a schema of L1Calo with the most important processing steps [83].

**L1Muon** The L1Muon system processes information from the muon trigger chambers, the TGCs and RPCs. In total there are over 800 000 input channels. The timing resolution is good enough to allocate the muon candidate to a BCID. A high- $p_T$  muon candidate requires a coincidences of all three RPC stations in the barrel (TGCs in the forward region respectively). For low- $p_T$  muons only the coincidence of the first two stations is required as shown in Fig. 3.15.

**L1Topo** The newly added L1Topological trigger module was commissioned during 2015/2016 and enabled for physics towards the end of 2016 pp data taking. It combines the TOBs from L1Calo and L1Muon and allows to apply topological selection and complex combinations of

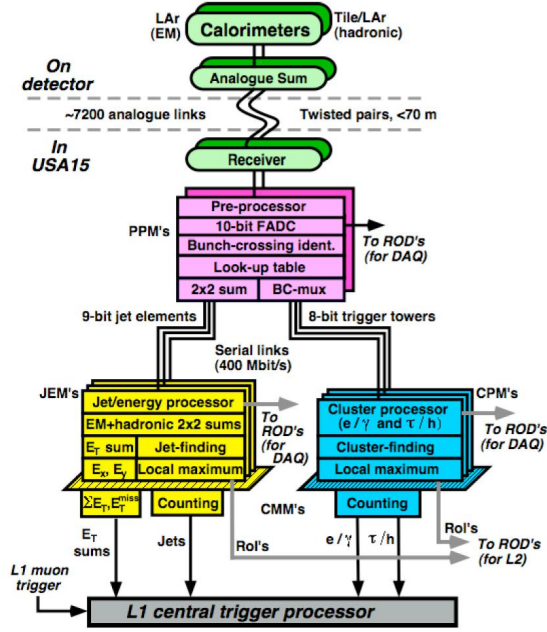


Figure 3.14: Schematic view of L1Calo.

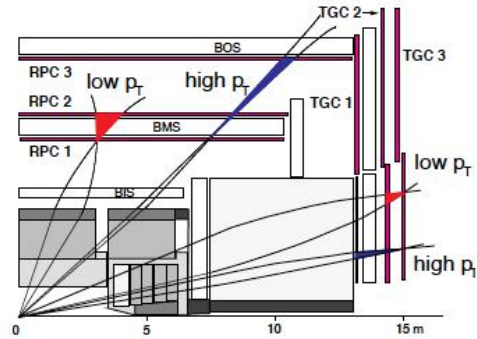


Figure 3.15: Schematic view of L1Muon.



TOBs. The information is transferred via optical fibers [82]. Due to output limitations the L1Muon information is restricted to two muon candidates per octant with three available  $p_T$  thresholds. The output of L1Calo is less limited and the electron/photon, tau, jets and  $E_T^{\text{miss}}$  TOBs all have an energy resolution of 1 GeV. L1Topo is sending its decision to the CTP same as the other Level 1 systems.

### High Level Trigger

In Run I there were two levels on top of the hardware-based on - Level 2 and the Event Filter (EF). L2 was an intermediate step with access to all Front-End Boards of the detector read-out. The EF had access to the complete detector information and enough latency to compute complex algorithms as tracking on a large amount of objects.

For Run II this layout was updated by merging the two levels to the High Level Trigger (HLT). The HLT basically combines the abilities of both L2 and EF, depending on demands it is processing complex algorithms with the whole event information but also ones that only use the Regions of Interest (RoI) as input and are generally faster. The HLT algorithms are designed to be as close as possible to the offline event reconstruction to provide excellent trigger efficiency.

The HLT algorithms are defined to run only if the specified TOBs passed L1 - the L1 seed. The HLT then sends a request for the corresponding data fragments to the ROS. After the event building step the algorithm checks the event against its predefined set of requirements. If an event passes any HLT algorithm's requirements it (the complete detector information) is written out. The sequence of L1 TOB and HLT algorithm is called a trigger chain. The trigger chains are defined in the trigger menu specifically designed for the LHC running conditions. The trigger menu contains over 2000 trigger chains.

### Data Acquisition

The DAQ system handles all the steps to get the data from the read-out of the detector to the final storage on disk. Each sub-detector has its own RODs to process the event fragments from its Front-End Boards (FEB). The processing and feature extraction is started as soon as a L1 accept is issued. From the RODs the data fragments are then send via Read-Out Links (ROL) to the Read-Out System (ROS). For Run II the maximum expected event size is 24 MB, the ROL have each a bandwidth of 200 MB/s. Each ROS consists of several Read-Out Buffers (ROB) to store the data until it receives a request by the HLT. During LS1 there were major upgrades to the DAQ system in order to be able to cope with both higher data request rates and larger event sizes. These two factors largely increase the required throughput rate of the ROS's. Each ROS PC can handle full read-out requests at a rate of 17 kHz. For RoI requests where only the event fragments associated to the corresponding RoI are read-out the rate is 40 kHz.

If an event is accepted by the HLT the data is then written to disk (Tier-0) by the Sub-Farm Outputs (SFO). For the expected 1 kHz HLT accept rate the SFOs need to transfer 2.4 GB of data per second to Tier-0. The maximum available output to storage rate is 3 GB/s. The cap at

2.4 GB/s is motivated by the available disk storage space as well as the offline reconstruction capabilities. The raw data written to Tier-0 is centrally reconstructed, the reconstructed data is then distributed to several grid sites across the globe for permanent storage (Tier-1). The offline reconstruction is very time-intensive. The ensuing backlog on the Tier-0 site needs to be taken into account for deciding the maximum write-out rate.

### 3.2.7 Detector performance

The combined performance of the ATLAS detector depends on the successful operation of its subsystems. During 2016 the data taking efficiency was in total 92.6%, the data taking efficiency by day is shown in Fig. 3.16. The difference between delivered and actual recorded luminosity arises from the time needed to turn on the high voltage of the Pixel, SCT and some of the Muon detectors after the declaration of stable beams by the LHC. It also accounts for deadtimes and temporal problems of individual subdetectors. Fig. 3.16 attests the overall excellent performance of the ATLAS detector in 2016. Chapter 4 gives a more detailed account of the operation and performance of the trigger system.

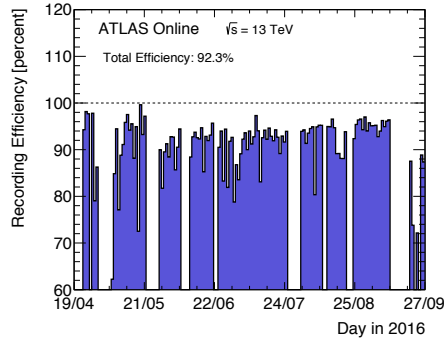


**Figure 3.16:** Shown is the ATLAS data taking efficiency in 2016 by day. The luminosity delivered by the LHC between declaring stable beams and the request for a dump of the beam is the denominator for the efficiency. The numerator is the actual recorded luminosity by ATLAS.



## CHAPTER 4

# Manual for trigger operation

FOR the successful operation of the ATLAS detector it is essential to be able to distinguish interesting hard-scatter events from the rest. Due to design choices and large event sizes at the ATLAS detector it is impossible to directly write-out 40 MHz of events. The necessary selection is done by the trigger system and its operation has therefore an immense impact on the overall data-taking performance.

The successful operation of the trigger system faces several challenges from different sources which are detailed in this chapter. It also describes the procedures in place to minimize any risk of losing data due to a non-working trigger.

### 4.1 Challenges for trigger operation

The main challenge for the trigger is to stay within the bandwidth limitations at both Level 1 and HLT. In general all rate restrictions are handled by the trigger menu which is always tailored to the actual data-taking conditions (see 4.2).

See §3.2.6 Fig. 3.13 for an overview of the TDAQ system including the design peak values for both event and data taking rate. §3.2.6 also describes the data transfer limits of the DAQ system.

**The L1 bandwidth** is nominally 100 kHz due to the detector read-out and event building rate limits [82]. There are circumstances where this rate is further decreased by requirements of the subdetectors. Especially the systems of the ID are put under strain in the high luminosity and high pile-up environment. An example for additional restrictions is the new IBL detector installed for Run II which has a strict read-out rate limit depending on the number of colliding bunches and bunch structure. Fig. 4.1 shows the rate limit of IBL for two different bunch train configurations as function of the number of colliding bunches. As reference the expected L1 rate of the default trigger menu is shown as well. The figure demonstrates that for a low number of colliding bunches further adjustments to the default menu are necessary. If the rate would rise above the limit, IBL would issue a fixed frequency trigger veto corresponding to 100% deadtime. As long as the veto is in place no events can be recorded and the collision data is lost until a rate below the limit can be guaranteed again. Another restriction was imposed by the very high occupancy in layer 2 and the B-layer of the Pixel detector due to high pile-up. The resulting large event fragments cannot be read-out at the nominal L1

accept rate, limiting the L1 bandwidth to 75 kHz in the first half of 2016 data-taking. For  $\mu \geq 45$  the Tile calorimeter starts having problems with the ROL occupancy limiting the L1 read-out request rate to 90 to 95 kHz.

The total L1 bandwidth will be in general only completely exhausted with both high luminosities and high pile-up run conditions starting during the end of 2016 data-taking. From a physics point of view it is not necessary to max out the L1 rate only because of free bandwidth.

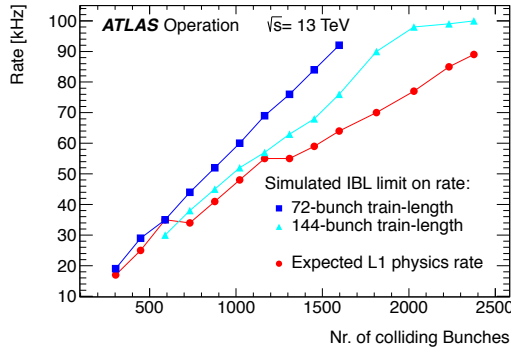


**Figure 4.1:** The simulated L1 rate limit by IBL for two different bunch train configurations (blue/cyan) and the nominal expected L1 rate (red). [84]

**The HLT bandwidth** is limited by the storage and data reprocessing capacities of the ATLAS DAQ system. For Run II the average bandwidth is 1 kHz for physics data, with an event size of  $\sim 1.7$  MB. Algorithms with RoIs as input as well as several detector calibration trigger chains do not require the full event to be built, they run a partial Event Building (EB) which is allowed to have a higher rate as it puts less stress on the read-out and transfer systems. Therefore these chains do not contribute to the 1 kHz bandwidth limit. The pie chart in Fig. 4.2 shows the composition of the data written to disk for a typical run with partial or full EB indicated. The graph on the left shows the size of the main physics stream and the total output of a typical run over time.

Fig. 4.3 shows the average recording rate of physics events per run of pp collisions in 2016. From the point the LHC reached  $\sim 2000$  colliding bunches around June 2016 at least half of the runs had an average recording rate more than 20% above the agreed limit. Causes for this are the high instantaneous luminosity exceeding all expectations and the resulting higher pile-up. To avoid emergency measures resulting in data loss the 1 kHz limit is not a stringent one and can be exceeded for short periods of time in agreement with the ATLAS data preparation management.

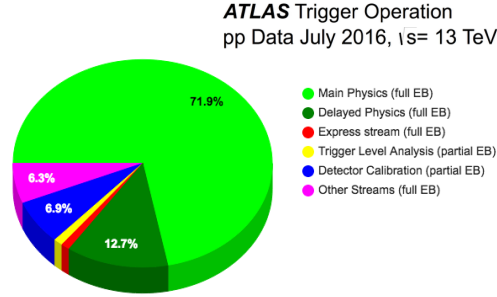
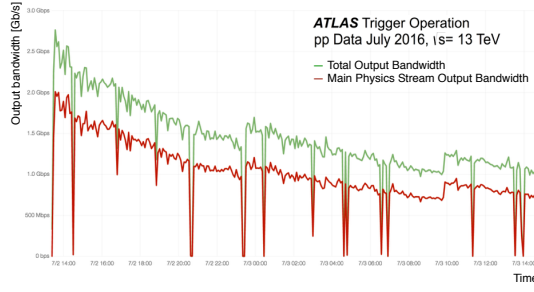


**Figure 4.2:** Shown at the top is the total and main physics stream output bandwidth at the HLT as a function of time throughout one fill taken in July 2016 with a peak luminosity of  $L = 1.02 \times 10^{34} \text{ cm}^{-2} \text{ s}^{-1}$  and a peak pile up of  $\mu = 35$ . The difference between the total and the main physics stream is accounted for by several other streams not shown. They are included at the bottom with their respective percentages of the data writing bandwidth. [84]

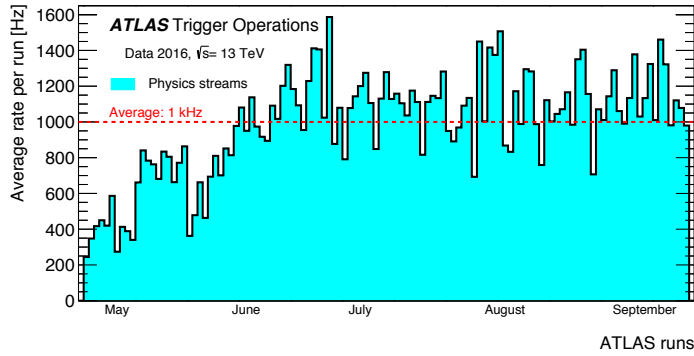


**Figure 4.3:** The average HLT recording rate for each p-p run in 2016. 1.5 kHz is the average rate during the first luminosity blocks, the average of a whole run is around 1 kHz. [84]

**The HLT computing farm** handles the processing of all HLT algorithms. There are 40,000 computer cores to handle the event processing at an input rate of 100 kHz with an average event processing time of 200 ms. The largest percentage of processing time is consumed by tracking algorithms followed by processing calorimeter information and muon information on the third place. For example the b-jet and electron/photon (egamma) slices consume  $\sim 25\%$  and  $22\%$  of all CPU time, both require tracking or calorimeter information. The muon slice uses  $\sim 12\%$ , see Fig. 4.4 for the CPU usage of all slices.

The high pile-up environment translates to longer processing times as the event is much 'busier' than with low pile-up. If there are not enough available cores to handle the incoming requests it leads to the events being queued until the storage capacity of the data transfer system is full - so called "back pressure" - resulting in deadtime and loss of data. Not enough available cores can be caused by a faulty algorithm largely increasing the processing time or prompting the core to be killed. It is therefore important to thoroughly check any HLT software before it is deployed 'online'<sup>1</sup>.

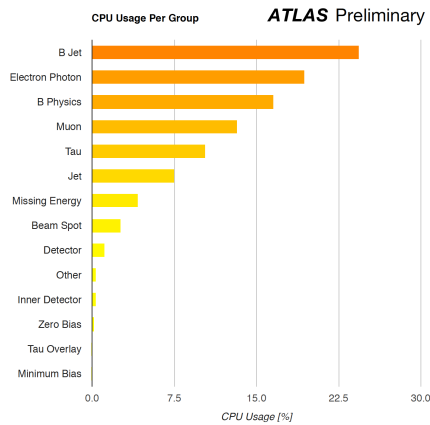


**Figure 4.4:** CPU usage of groupings of chains as a percentage of utilized computing resources.[85]

## 4.2 Menu design

The ATLAS trigger menu for Run II contains approximately 500 L1 and more than 2000 HLT triggers and ensures that the event selection rate stays within all bandwidth limitations. Not all of these triggers are actually used for physics data taking. The trigger menu has to allocate the available bandwidth to different requirements of the ATLAS collaboration. A priority is given to the needs of the ATLAS physics program with its wide range from SM precision measurements over Higgs physics to searches for BSM particles. The input of the physics

<sup>1</sup> The term 'online' refers to the actual computing system of the ATLAS detector which is completely separated from any other computing system used by the ATLAS collaboration and physically located at Point 1 (P1) at CERN. This separation is a measure to safeguard the detector and the data taking granting access only to authorized persons. If access is granted the roles assigned according to one's task further limits the potential of disturbing the system by accident.

groups is therefore vital for a satisfying menu design. One design choice made by the ATLAS collaboration is to give a large portion of bandwidth to generic triggers that can be used by many different analysis groups, e.g. single lepton triggers or low threshold  $E_T^{\text{miss}}$  triggers. In addition there are multi-object triggers with the aim of lower  $p_T$  thresholds by combining two or more constraints and also dedicated triggers only used by one analysis group. Dedicated triggers are allowed a bandwidth of  $\sim 1$  Hz each whereas triggers used by several groups can each aim for a unique rate of  $\sim 10$  Hz or more, the generic triggers like single lepton triggers are allowed a bandwidth in the order of a few hundred Hz each at the HLT level [86].

The different triggers can be grouped by their main purpose:

- **Primary triggers** are used to select events for physics analysis, they are allocated a large fraction of the bandwidth.
- **Support triggers** allow for necessary efficiency and calibration measurements and are also necessary for good monitoring. They typically run at only a low rate in the order of 0.5 Hz.
- **Alternative triggers** are running different online reconstructions either as primary or support selection. Often these are used for commissioning purposes of new trigger algorithms.
- **Backup triggers** are similar to the primary ones but with tighter selections on  $p_T$ , isolation etc. They yield a lower rate and can be used in case the primary trigger rate is too high.
- **Calibration triggers** are used for detector calibrations and normally run prescaled at a high rate. The high rate poses no problem as they only write-out a small part of the detector with the relevant information for the sub-system.

For all single trigger items there are two ways to control the rate. One is to increase the  $p_T$  threshold and/or isolation requirement of a trigger as for example a single electron trigger. The other is to prescale the trigger with a factor  $n$  defined in the trigger menu with prescaling possible at both L1 and HLT. With a prescale only every  $n$ th time the trigger fulfills all requirements the event is actually passed and recorded. The former has the advantage that no additional scaling becomes necessary for the trigger efficiency and it is used for most primary triggers. The latter is normally applied to all the other trigger groups as often low  $p_T$  events are of interest for calibrations. Another possibility to control the rate is to combine several trigger items e.g. a single tau plus a single muon or another lower  $p_T$  tau. It is often used for physics cases where it is important to keep  $p_T$  and or isolation requirements of the primary item as low as possible.

The table in Fig. 4.5 shows a selection of unprescaled primary triggers from the menu designed for  $0.5 \times 10^{34} \text{ cm}^{-2} \text{ s}^{-1}$  in 2015. The total given at the bottom corresponds to all triggers in the menu not only to the ones shown.



Trigger	Typical offline selection	Trigger Selection		Level-1 Peak	HLT Peak
		Level-1 (GeV)	HLT (GeV)	Rate (kHz)	Rate (Hz)
				$L = 5 \times 10^{33} \text{ cm}^{-2}\text{s}^{-1}$	
Single leptons	Single iso $\mu$ , $p_T > 21 \text{ GeV}$	15	20	7	130
	Single $e$ , $p_T > 25 \text{ GeV}$	20	24	18	139
	Single $\mu$ , $p_T > 42 \text{ GeV}$	20	40	5	33
	Single $\tau$ , $p_T > 90 \text{ GeV}$	60	80	2	41
Two leptons	Two $\mu$ 's, each $p_T > 11 \text{ GeV}$	$2 \times 10$	$2 \times 10$	0.8	19
	Two $\mu$ 's, $p_T > 19, 10 \text{ GeV}$	15	18, 8	7	18
	Two loose $e$ 's, each $p_T > 15 \text{ GeV}$	$2 \times 10$	$2 \times 12$	10	5
	One $e$ & one $\mu$ , $p_T > 10, 26 \text{ GeV}$	20 ( $\mu$ )	7, 24	5	1
	One loose $e$ & one $\mu$ , $p_T > 19, 15 \text{ GeV}$	15, 10	17, 14	0.4	2
	Two $\tau$ 's, $p_T > 40, 30 \text{ GeV}$	20, 12	35, 25	2	22
	One $\tau$ , one $\mu$ , $p_T > 30, 15 \text{ GeV}$	12, 10 (+jets)	25, 14	0.5	10
	One $\tau$ , one $e$ , $p_T > 30, 19 \text{ GeV}$	12, 15 (+jets)	25, 17	1	3.9
Three leptons	Three loose $e$ 's, $p_T > 19, 11, 11 \text{ GeV}$	$15, 2 \times 7$	$17, 2 \times 9$	3	< 0.1
	Three $\mu$ 's, each $p_T > 8 \text{ GeV}$	$3 \times 6$	$3 \times 6$	< 0.1	4
	Three $\mu$ 's, $p_T > 19, 2 \times 6 \text{ GeV}$	15	$18, 2 \times 4$	7	2
	Two $\mu$ 's & one $e$ , $p_T > 2 \times 11, 14 \text{ GeV}$	$2 \times 10$ ( $\mu$ 's)	$2 \times 10, 12$	0.8	0.2
	Two loose $e$ 's & one $\mu$ , $p_T > 2 \times 11, 11 \text{ GeV}$	$2 \times 8, 10$	$2 \times 12, 10$	0.3	< 0.1
One photon	one $\gamma$ , $p_T > 125 \text{ GeV}$	22	120	8	20
Two photons	Two loose $\gamma$ 's, $p_T > 40, 30 \text{ GeV}$	$2 \times 15$	35, 25	1.5	12
	Two tight $\gamma$ 's, $p_T > 25, 25 \text{ GeV}$	$2 \times 15$	$2 \times 20$	1.5	7
Single jet	Jet ( $R = 0.4$ ), $p_T > 400 \text{ GeV}$	100	360	0.9	18
	Jet ( $R = 1.0$ ), $p_T > 400 \text{ GeV}$	100	360	0.9	23
$E_{\text{T}}^{\text{miss}}$	$E_{\text{T}}^{\text{miss}} > 180 \text{ GeV}$	50	70	0.7	55
Multi-jets	Four jets, each $p_T > 95 \text{ GeV}$	$3 \times 40$	$4 \times 85$	0.3	20
	Five jets, each $p_T > 70 \text{ GeV}$	$4 \times 20$	$5 \times 60$	0.4	15
	Six jets, each $p_T > 55 \text{ GeV}$	$4 \times 15$	$6 \times 45$	1.0	12
$b$ -jets	One loose $b$ , $p_T > 235 \text{ GeV}$	100	225	0.9	35
	Two medium $b$ 's, $p_T > 160, 60 \text{ GeV}$	100	150, 50	0.9	9
	One $b$ & three jets, each $p_T > 75 \text{ GeV}$	$3 \times 25$	$4 \times 65$	0.9	11
	Two $b$ & two jets, each $p_T > 45 \text{ GeV}$	$3 \times 25$	$4 \times 35$	0.9	9
$b$ -physics	Two $\mu$ 's, $p_T > 6, 4 \text{ GeV}$ plus dedicated $b$ -physics selections	6, 4	6, 4	8	52
Total				70	1400

**Figure 4.5:** A selection of unprescaled primary triggers of the 2015 menu designed for  $0.5 \times 10^{34} \text{ cm}^{-2} \text{ s}^{-1}$ . The total rate includes all triggers not only the ones shown. [86]

To keep the primary triggers stable over longer periods of time the trigger menu is designed for different instantaneous luminosity benchmark points. In 2016 the benchmark points included 0.5, 0.7, 1.0 and  $1.2 \times 10^{34} \text{ cm}^{-2} \text{ s}^{-1}$ . Within a range around the benchmark point the primary triggers will be kept unchanged. To be able to design these benchmark menus that they respect all bandwidth limitations precise rate predictions for all the trigger chains are needed.

#### 4.2.1 Trigger rate predictions

The rate of a trigger chain can be calculated using an unbiased set of data from the probability that the trigger chain passes events of that sample. One way to obtain an unbiased data set would be to use randomly triggered data - zero bias data. A zero bias sample that is statistically powerful enough to predict rates for high- $p_T$  objects would be unreasonably large. The interesting high- $p_T$  objects are produced at a much smaller cross section. To account for this effect the data set for the rate predictions is overweighted in high- $p_T$  events - Enhanced Bias (EB) data.

The EB data is taken with a special set of L1 triggers parallel to the normal data-taking. This set is usually the same for every EB run, but small changes are possible. The chosen L1 triggers cover all possible signatures,  $p_T$  ranges and combinations so that the rates of typical HLT triggers can be predicted [85]. The L1 items are grouped in sets that seed 5 different HLT chains. Each chain targets a specific group of physics signatures. Each L1 set consists of 10 - 30 L1 items collecting event sets labeled: 'high' (objects with especially high  $p_T$ ), 'primary' (including the primary L1 seeds), 'medium' (medium  $p_T$  range), 'low' (low  $p_T$  range) and 'random' (randomly triggered). Only the 'high' and 'primary' L1 sets seed the corresponding HLT chain directly. As the EB data is taken in parallel with normal data taking it needs to work with the L1 triggers and prescales used for physics data. The EB HLT chains with prescaled L1 items are randomly triggered and then take the raw L1 decision into account. As there is no further selection applied at the HLT (except prescales to control the output rate) the data set is only L1 biased. The way the EB data set is taken makes it possible to assign a weight to each event that restores an effective zero bias spectrum. For the rate prediction of a chain the event weight is calculated taking into account the prescales and raw L1 decisions during the EB data taking, luminosity and beam conditions and the decision of the respective trigger chain itself.

The EB data set represents the data-taking and beam conditions (especially pile-up) of the run it was taken in. The trigger performance itself is not linearly dependent on pile-up as the relative  $p_T$  spectrum is changing. It is therefore indispensable to repeat the EB run whenever the data-taking conditions change for accurate predictions. During the data-taking period of 2016 a new EB run was taken approximately every four to six weeks. Normally the EB chains are run for ~an hour at a rate of 300 Hz resulting in an EB data set with roughly one million events.

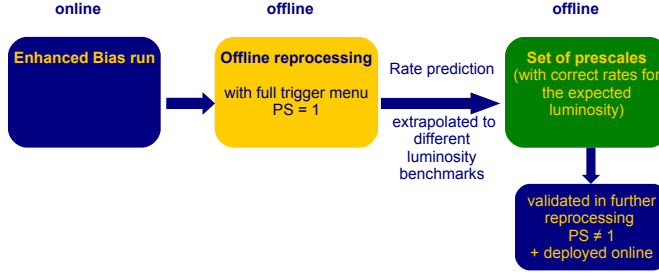


**Figure 4.6:** The schema shows the different steps to obtain the rate predictions.

The schema in Fig. 4.6 shows the steps necessary to determine the rate for a given luminosity. To extract the rate predictions the EB data set is reprocessed with the current trigger software release including the corresponding trigger menu. In a first step all trigger algorithms are run unrescaled to obtain the raw decisions of the trigger. The correct prescales are applied in a later step delivering the rate prediction for each L1 item and HLT algorithm. The procedure also allows to predict unique rates (events accepted by a single trigger chain), rates of combined items and most importantly a scaling to higher luminosities. An EB data set taken at  $0.5 \times 10^{34} \text{ cm}^{-2} \text{ s}^{-1}$  can therefore be used to assign the correct prescales in the benchmark menu for  $1.2 \times 10^{34} \text{ cm}^{-2} \text{ s}^{-1}$ .

### 4.3 Trigger software release

The trigger software release AtlasP1HLT contains all the trigger algorithms, configurations and everything necessary to execute the trigger online including the trigger menu. All software changes must be tested and cross checked thoroughly as any errors in the software can lead to extended data loss. There is a release cycle to allow for testing and at the same time to deploy necessary changes to the software quickly, Fig. 4.7 illustrates the different steps.

The software like trigger algorithms, calibrations and the trigger menu is developed and maintained by the dedicated trigger groups. For new software to be tested it is tagged and the tag is included in the AtlasCAFHLT release, the offline version of the trigger software. The AtlasCAFHLT release is built every night in the general ATLAS software framework. The period for updating AtlasP1HLT is normally one week. If the nightly build of AtlasCAFHLT with the new tags worked fine that version of AtlasCAFHLT is tagged and the current EB data is reprocessed with the new AtlasCAFHLT release. The reprocessing provides a set of the online and offline monitoring histograms for each trigger signature, counts for all L1 and HLT triggers and rate predictions for the included trigger menu. The monitoring histograms and counts are checked by the trigger signature experts with the previous release as reference. All discrepancies are investigated and the new AtlasCAFHLT is only signed off if the changes can be explained reasonably by the new tags. As soon as AtlasCAFHLT is signed off the new

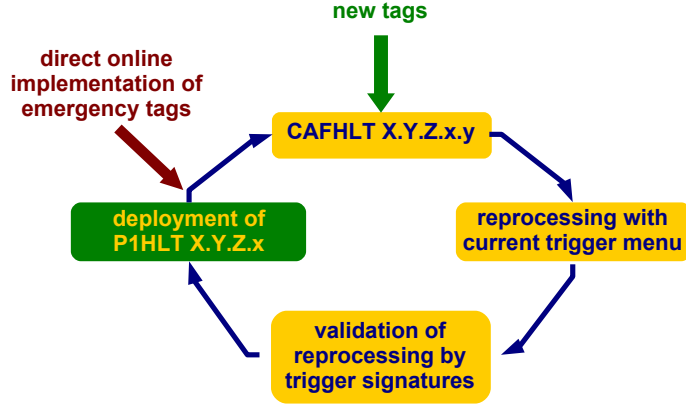


**Figure 4.7:** The different steps in the trigger software release cycle.

tags are swept into the online AtlasP1HLT, creating a new version. The version is built and distributed online on the ATLAS detector computing system. Before the new AtlasP1HLT is actually used for data taking it is tested stand alone on a single computing node with the same environment as the rest of the computing farm. If there are still no problems arising with the new release the switch is made as soon as a run is stopped and there is a short break in data taking. The release is then tested further with the full ATLAS partition. In case there would be problems the release can easily be switched back with a single command and a restart of the ATLAS partition.

In the rare case that a trigger algorithm is running with the wrong calibration or not as expected there is a possibility to deploy a patch directly online without a whole release cycle. For that the tags in the patch need to at least have been included successfully in the nightly AtlasCAFHLT build. The patch is compiled and copied to a dedicated online directory which path is included in the current release by a simple online database update via xml files.

## 4.4 Daily operation

The actual trigger menu to be used by the ATLAS trigger is determined by trigger keys. There is a Super Master Key (SMK) containing the information about the trigger release to be used, a L1 key and a HLT key. The trigger keys are linked via a database to the trigger menu configuration. The database stores the information which L1 items seed which HLT chains, the algorithms the HLT chains execute and their correct order as well as the thresholds and requirements that need to be fulfilled to pass an event. The trigger keys determine the prescales for the different chains, if they are activated at all and in which mode they are running.

During normal operations the LHC announces the beam conditions and bunch configuration for each run in advance. The trigger keys are prepared accordingly for the expected instantaneous luminosity. To make the best use of the available bandwidth a whole set of keys is

prepared in luminosity steps of  $0.5 \times 10^{33} \text{ cm}^{-2} \text{ s}^{-1}$ . As the instantaneous luminosity decreases over time the keys are changed accordingly. The goal is not to always write out the maximum amount of data but to collect the interesting events for the given luminosity and a sufficient amount of monitoring data.

Fig. 4.8 shows the rates for groups of L1 and HLT triggers. The rates for the single groups do not account for any overlap between these groups, the resulting total rate is shown by the black curve. The graph documents how the initial peak rates at the declaration of 'stable beams' decrease with time. When the next luminosity step in trigger keys is reached there is a visible jump in the rates. Fig. 4.9 shows the same but for different HLT streams.

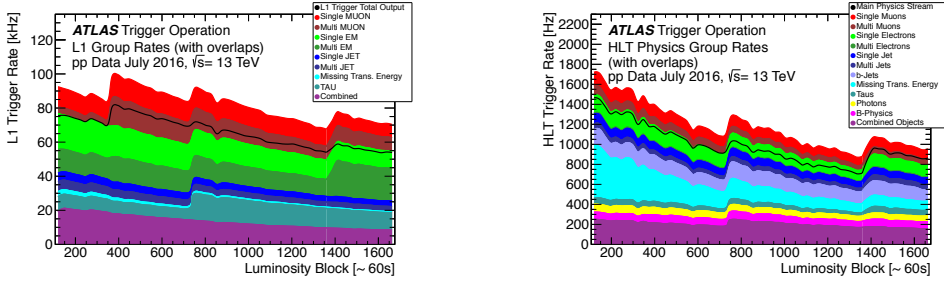


**Figure 4.8:** Exemplary for one p-p run in 2016 the rates of different L1 (left) and HLT (right) groups are shown. The group rates do not account for any overlap, the resulting total physics rate is indicated in black. [84]

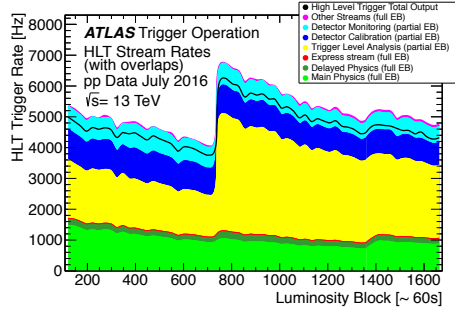


**Figure 4.9:** Exemplary for one p-p run in 2016 the rates of different HLT streams are shown. The total HLT output is indicated in black. [84]

There are several streams at HLT level each stream defines a separate data set, illustrated in Fig. 4.10. The trigger menu defines to which streams an event is written out depending on the triggers passing the event. As the name indicates the 'Main Physics' stream contains the data for physics analysis, the 'express stream' writes out a small amount of representative events for the trigger and detector monitoring. There are also streams for detector calibrations, monitoring and commissioning and a debug stream. Not all streams are automatically

reprocessed offline on the contrary to the 'Main Physics' stream.

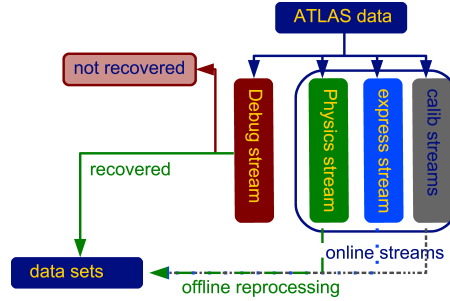


**Figure 4.10:** The schema shows the stream architecture of the ATLAS data output including the debug stream treatment.

The debug stream is especially important for the trigger operations as it contains all events where an HLT algorithm issued an error or could not decide if an event should be passed in the short available time online and there is consequently no trigger decision for the given trigger. For every run the events in the debug stream are analyzed to promptly spot any issues at trigger level and accordingly fix them. If the trigger decision can be recovered by the offline reprocessing the event is included back into the data set. This is often the case especially for algorithms run out of time online as there is no execution time limit in the offline reconstruction.

Apart from the normal data taking trigger operations also prepares the correct configurations for different special runs, e.g. Van der Meer scans. It also assists the detector systems with test setups and with the commissioning of new components as L1Topo.

The efforts of the operation team result in a great data taking efficiency of the ATLAS detector as already shown in sec. 3.2.7.

#### 4.4.1 Possible situations during daily operations

Every possible precaution is taken to ensure a smooth running of the ATLAS trigger. Nevertheless occasionally problems arise that need a quick response to prevent data loss. There is a dedicated team of on call experts whose responsibility is to monitor the daily trigger operations and to take measures in case of problems. The following paragraphs describe common types of problematic situations and how to solve them.

**A too high rate** is one of the most common problems. One can differentiate between an elevated rate that is not immediately causing larger deadtime and a rate high enough (several MHz) resulting in high deadtime, an overloaded DAQ system and/or the IBL fixed frequency veto. In the latter case the cause needs to be found and fixed promptly as it makes data

taking impossible. The former case allows for more time, but the steps are the same. First the source of the high rate needs to be found. There are useful tools displaying the rate of each individual L1 item, HLT chain and stream. When the culprit is found the underlying problem needs to be investigated. Possibilities are that the wrong keys were used, a wrong combination of the L1 and HLT keys with the bunch group configuration or the keys were wrongly generated. Another common reason are hot trigger towers where the subdetector systems need to be alerted to fix or disable the concerned tower. For sudden spikes in rate there is an automated procedure that adapts the keys accordingly (called AutoPrescaler), but this system only reacts after five seconds which is too late for rate spikes in the order of several MHz.

**No or significantly lower rate** of a group of trigger chains points at a problem with a subsystem or wrong algorithm configuration. There is a tool showing live predictions for the most important sets of primary triggers. Thanks to this accurate monitoring problems resulting in lower rate can be spotted quickly. For example a lower rate of the b-jet and electron chains was caused by a timing problem of IBL. These chains require a certain number of hits in the IBL and Pixel detectors. Another case was a too low rate of the primary single electron trigger, in this case the reason was a wrong configuration of the AutoPrescaler labeling the usual 15 kHz at L1 as rate spike. Until a solution was found to update the AutoPrescaler configuration without stopping the run the L1 item with the same  $p_T$  threshold but relaxed isolation requirement was unprescaled as emergency measure.

**A different magnet configuration** requires a set of keys with specifically tailored rules. The goal is to still be able to take data for some physics while taking into account higher rates due to missing magnetic fields. These are only needed in rare cases where either one or both of the Solenoid and Toroid tripped. If the Solenoid is off the muon chains are most affected resulting in much higher rates here the only solution is to not take any collision data. If the Toroid is off it has a lesser effect on rates but it needs to be taken into account by the tracking algorithms. This is done via an automatic flag during the start of the run. In case one or both magnets are off at the start of the run the ATLAS partition needs to be stopped and restarted to reconfigure the HLT algorithms. The magnets are flagged as 'on' as soon as they reach a current slightly higher than their stand-by value. So if the magnets are already ramping back up after a trip a stop and restart of the partition is not needed saving time for data-taking.

**A complete crash of the HLT farm** is one of the worst-case scenarios which makes data-taking impossible. If the error messages automatically broadcasted by the ATLAS partition do not display any clue one needs to look at the log files of the HLT farm. If a single algorithm is the cause the corresponding trigger chains have to be disabled until the bug can be fixed. It usually takes some time to investigate and fix a bug in the trigger software. So disabling the affected chains is necessary to allow data-taking with the remaining chains. It is also possible that there are problems with the database access and the farm already crashes while

configuring the HLT algorithms. Another case is when after a switch to a new AtlasP1HLT release parts of the data necessary for configuration was not synchronized successfully. For both cases communication and help from DAQ and system administrators is necessary.

**High deadtime** can have several causes and usually needs combined investigation by the trigger and DAQ systems. It is not always immediately clear what exactly is causing the deadtime. The HLT can cause high deadtime for example if some algorithms use too much computing time occupying more and more processing units (PUs). This way newly incoming events cannot be processed and data is lost. As an emergency measure these chains need to be prescaled and the timing issue studied and fixed offline. There is also the case where in general not enough PUs are available for the actual data-taking conditions here the only solution is to run with prescales for a higher luminosity reducing the incoming rate. In the long term the problem was resolved by both installing additional PUs and a major effort to slim the time consumption of the HLT algorithms. The rule is that there should be always around 15 000 PUs idle at any moment for smooth operations of the farm. The total number of available PUs is around 40 000.

Generally the first step is always to find the cause of a problem with data-taking followed by finding the best intermediate solution that still allows continuous data-taking. Of course this is not always possible but there is a clear preference to avoid any stop and restart of the ATLAS partition during a run. The most simple stop/start already takes around five minutes - that are five minutes of precious data lost. So a solution at the expense of only one trigger signature or a couple of chains is normally chosen over a stop/start. This makes especially sense if it is not initially clear how long it will take to thoroughly solve the problem in the long term.

#### 4.4.2 Data quality

It is not only important to ensure continuous data-taking but also that the gathered data is of highest quality, meaning usable for physics analysis. To this end a sophisticated system of data-quality monitoring (DQM) tools and checks exists. There are two distinct systems for online and offline monitoring each.

The first line of defense is the online or live monitoring of the trigger. As already mentioned above there are several tools that compare the actual rates to the expected ones for a set of important primary triggers. In addition a large amount of histograms are filled by each HLT chain. For example a single  $E_T^{\text{miss}}$  trigger fills histograms for x-, y- and z-components of the missing energy, the total resulting missing transverse energy, the azimuthal distribution as well as the input from the different calorimeter components. All these histograms are plotted against a reference from a run with similar beam conditions. The histograms can be displayed in the control room and are checked hourly by the trigger shifter to spot any divergences as soon as possible. In parallel to the manual check there is also an automated check with a range of user-defined algorithms, the user in this case are the different trigger signatures. The result of the algorithms for each histogram is displayed as a colour flag, from green 'ev-



everything fine' over yellow 'should be checked' to red 'problem'. This provides a colour code making it easier for the trigger shifter to scan the countless histograms. It also raises a 'red flag' as soon as a deviation occurs as all the flags are weighted and fed into an overall status flag of the HLT. Fig. 4.11 shows the principle of the overall status. If a problem is seen in

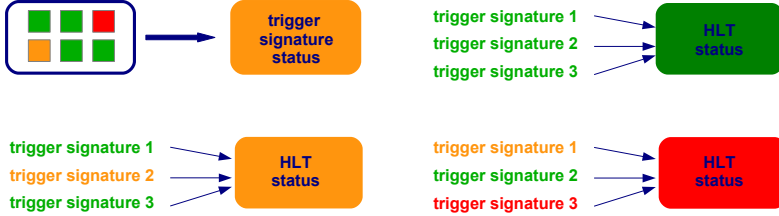


**Figure 4.11:** Schema of the data-quality monitoring framework.

one of the trigger signatures the relevant experts are contacted, each trigger signature has its own rota of experts on call. Thus the problem can be investigated and maybe already solved during the on-going run.

After a run the taken data needs to be signed off as good for physics analysis. For this purpose each trigger signature has a similar range of histograms as online that are filled during the offline reconstruction of the express stream. The small sample of events in the express stream is chosen as sufficient to spot any issues with the data with the advantage of speed. It takes much longer to reconstruct the whole sample written to the physics stream. The offline reconstruction allows to have additional more complex histograms than online. The  $E_T^{\text{miss}}$  trigger signature for example also has histograms displaying the  $E_T^{\text{miss}}$ ,  $\phi$  and other distributions requiring one muon (one electron) in the event for different event characteristics as well as  $\eta - \phi$  maps weighted and unweighted in  $E_T^{\text{miss}}$ . As in the online DQM there is a set of user-defined algorithms checking and flagging the large amount of offline histograms simplifying the sign off procedure.

The on call experts of the trigger signatures are responsible for the daily data-quality sign off. The sign off procedure involves several groups from detector sub-systems to offline reconstruction performance. It is therefore arranged with the use of defects assigned to the data. One has to differentiate between tolerable and intolerable defects. The latter excludes the data from physics analysis while the former indicates minor issues. In general it is possible to assign defects per luminosity block <sup>2</sup> of data which is mainly used by the detector sub-systems. The trigger signatures rather assign defects to the whole run as the monitoring plots are not available per luminosity block. Per default the 'UNCHECKED' defect is set for each DQ sub-group, an intolerable defect. As soon as the data was controlled the responsible expert removes the 'UNCHECKED' defect and sets any other defects, as deemed necessary. One of the most common defects for the calorimeter based trigger signatures (HLT Calo, Jets and  $E_T^{\text{miss}}$ ) is the 'hotspot' defect. A hotspot means a spike in the  $\eta$  and  $\phi$  distribution. A

<sup>2</sup>A luminosity block is 60 seconds long.

hotspot is mostly caused by noisy trigger towers and very low in energy. The 'hotspot' defect is therefore a tolerable defect. There are also cases of high  $p_T$  hotspots caused by hot trigger towers, here communication with the respective L1 trigger experts is advised to exclude any problems in the HLT trigger itself. A serious problem is the misconfiguration of an algorithm, for example once it has happened after an update to the unpacking of calorimeter cells. After the update the HLT Calo algorithms used in the  $E_T^{\text{miss}}$  trigger did not access the third layer of the forward calorimeter component anymore. The information for the  $E_T^{\text{miss}}$  trigger was therefore incomplete. The problem was exacerbated by the omission of the component histograms from the daily data-quality checks and only spotted coincidentally. In the end only a tolerable defect was set as the excluded component has only a very small impact on the overall missing transverse energy. The data-quality checks on the  $E_T^{\text{miss}}$  trigger side were updated accordingly. As the investigation of issues like this can take some time there is a 'unknown' defect that can be set as a placeholder, it is intolerable.

ATLAS pp 25ns run: April-October 2016											
Inner Tracker			Calorimeters		Muon Spectrometer				Magnets		Trigger
Pixel	SCT	TRT	LAr	Tile	MDT	RPC	CSC	TGC	Solenoid	Toroid	L1
98.9	99.9	99.7	99.3	98.9	99.8	99.8	99.9	99.9	99.1	97.2	98.3
Good for physics: 93-95% (33.3-33.9 fb <sup>-1</sup> )											

**Figure 4.12:** Luminosity weighted relative detector uptime and good data quality efficiencies (in %) during stable beam in p-p collisions with 25 ns bunch spacing at  $\sqrt{s}=13$  TeV between April - October 2016, corresponding to an integrated luminosity of 35.9 fb<sup>-1</sup>. The toroid magnet was off for some runs, leading to a loss of 0.7 fb<sup>-1</sup>. Analyses that don't require the toroid magnet can use that data. [87]

The table in Fig. 4.12 shows an overview of the data-quality efficiency for several subsystems in 2016. Overall most of the recorded data is good for physics analysis. Fig. 4.13a shows the percentage of good data compared to the recorded and delivered luminosity on 2015<sup>3</sup>, the corresponding data-quality efficiency table is also shown in Fig. 4.13b. The largest loss of data in 2015 for physics analysis is the part taken with IBL turned off. The data-quality performance of the HLT alone was above 93% and 99% in 2015 and in 2016 respectively.

<sup>3</sup>The plot for 2016 will be available when the final 'good run list' is published.

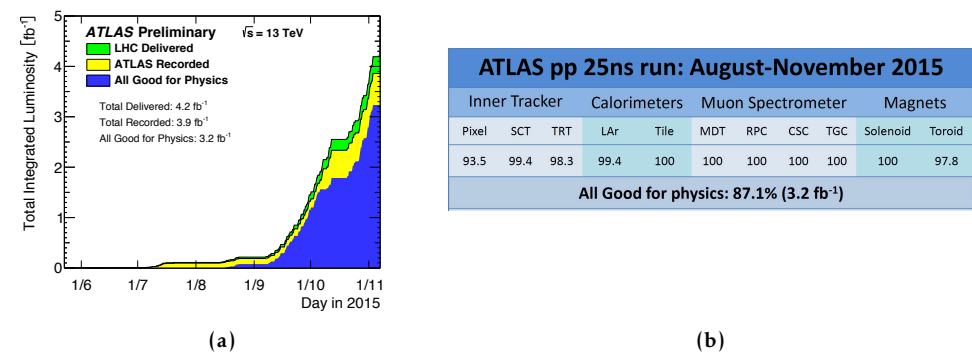


**Figure 4.13:** (a) Cumulative luminosity versus time delivered to ATLAS (green), recorded by ATLAS (yellow), and certified to be good quality data (blue) during stable beams for pp collisions at 13 TeV centre-of-mass energy in 2015.[88] (b) The corresponding luminosity weighted relative detector uptime and good data quality efficiencies (in %) during stable beam in p–p collisions with 25 ns bunch spacing at  $\sqrt{s}=13$  TeV between August - November 2015, corresponding to an integrated luminosity of  $3.7\text{ fb}^{-1}$ . [87]

## CHAPTER 5

# Rethinking transverse missing energy triggers

THE ATLAS detector provides full azimuthal coverage of the interaction point. All interacting particles resulting from the  $p - p$  collision with a transverse momentum larger than zero will therefore be detected. Due to momentum conservation the complete coverage ensures a precise measurement of the transverse missing energy  $\vec{E}_T^{\text{miss}}$ , the most important variable for non- or only weakly interacting particles.

Especially in supersymmetry searches  $E_T^{\text{miss}}$  plays an important role in measuring the transverse energy of the lightest stable sparticle that escapes the detector. So it is of interest to improve the  $E_T^{\text{miss}}$  measurement at all levels from the calorimeters to event reconstruction. This chapter explains the difficulties of triggering on  $E_T^{\text{miss}}$  and describes the effort to improve the detection of transverse missing energy with the new Level 1 Topological trigger. It then focuses on the performance of the  $E_T^{\text{miss}}$  triggers of both Level 1 and HLT during Run II.

### 5.1 Transverse missing energy triggers for Run II

The ATLAS transverse missing energy triggers rely largely on calorimeter information. The electro-magnetic and hadronic calorimeters measure the transverse momentum  $p_T^i$  of all interacting particles. The  $\vec{E}_T^{\text{miss}}$  is then calculated as

$$\vec{E}_T^{\text{miss}} = - \sum_i \vec{p}_T^i \quad (5.1)$$

with the sum running over all interacting particles  $i$ .

With the increased luminosity of the LHC for Run II also the underlying event becomes more busy, resulting in more particles that do not stem from the hard scattering event. These particles with mostly low  $p_T$  impact the resolution of the  $E_T^{\text{miss}}$  measurement, the largest effect is seen in the forward calorimeters. As mentioned in §3.2.6 L1Calo applies several corrections to mitigate the pile-up effects like pedestal corrections, but the L1 MET trigger remains pile-up dependent. This leads to the L1 MET trigger being the main limiting factor on the overall  $E_T^{\text{miss}}$  trigger efficiency.

During the Long Shutdown 1 (LS1) L1Calo conducted several upgrades on hardware and firmware side to conquer the expected increase in pile-up. One of the upgrades is the new Level 1 Topological (L1Topo) module that receives the trigger objects from both L1Calo and L1Muon and allows to apply topological selections as well as for more complex computations already at Level 1.

Another limiting factor is the allowed bandwidth at Level 1 and HLT. During LS1 it was increased to 100 kHz at Level 1 and  $\sim 1$  kHz at HLT to prevent the lowest unprescaled thresholds to raise too much. The higher rate from increased luminosity translates to higher thresholds making it more and more difficult to capture events with only low  $p_T$  particles.

The excellent performance of the LHC foresees an instantaneous luminosity of  $\sim 2 \cdot 10^{-34} \text{ cm}^{-2} \text{ s}^{-1}$  for 2017 high above the design luminosity of  $\sim 1 \cdot 10^{-34} \text{ cm}^{-2} \text{ s}^{-1}$ . This will lead to increased lowest unprescaled thresholds, for the Level 1  $E_T^{\text{miss}}$  trigger it will raise to 60 GeV from the current 50 GeV. So the work on strategies to keep the thresholds of primary trigger items low is an ongoing and never ending effort.

## 5.2 Transverse missing energy trigger at Level 1

At Level 1  $E_T^{\text{miss}}$  is derived from the energy deposits in the complete calorimeter [83]. The actual calculation is done in two steps. First the Jet/Energy-sum Module (JEM) obtains the transverse missing energy components  $E_x$  and  $E_y$  of each jet element by multiplying it with the correct geometrical constants ( $\cos \phi$  and  $\sin \phi$ ). A jet element is composed by  $2 \times 2$  trigger towers translating to a granularity of  $0.2 \times 0.2$  in  $\Delta\eta \times \Delta\phi$ . The JEM also calculates the total scalar  $E_T$  of all jet elements. Each JEM only handles input from trigger towers located in the same quadrant no signed arithmetic is therefore needed. The sums of  $E_x$ ,  $E_y$  and  $E_T$  are then sent to Central Merger Module (CMM) where the summation over all JEMs takes place and the results are compared to various thresholds. The information which thresholds are passed is sent to the CTP.

The jet-finding algorithm is running on the same modules and the L1Calo architecture does not allow for further operations after the jet-finding and energy summation are completed. In Run I it was therefore not possible to apply any pile-up correction to  $E_T^{\text{miss}}$ . The situation changes in Run II with the addition of the L1Topo module.

The L1Topo module receives the Trigger Objects (TOB) of L1Calo and L1Muon as input and can combine these TOBs in any way performing additional algorithms. Fig. 5.1 shows a schema of the L1Topo module. L1Topo receives a jet list containing 64 TOBs and the  $E_T$ ,  $E_x$  and  $E_y$  sums all with an energy resolution of 1 GeV. The TOB lists first need to be sorted, the TOBs with the highest  $p_T$  are then used as input for the L1Topo algorithms.

L1Topo provides therefore the possibility to have a pile-up corrected  $E_T^{\text{miss}}$ , e.g. building  $E_T^{\text{miss}}$  from pile-up corrected jets or modifying the existing  $E_T^{\text{miss}}$  value.

## 5.3 Pile-up corrected $E_T^{\text{miss}}$

The purpose of a pile-up corrected  $E_T^{\text{miss}}$  at Level 1 is to be as close as possible to the hard scatter  $E_T^{\text{miss}}$  value of the event. This would lead automatically to an improved  $E_T^{\text{miss}}$  resolution and better trigger efficiency.

To achieve this a new Kalman filter based algorithm at Level 1 is implemented to subtract pile-up energies and to apply a hadronic energy calibration. The resulting  $E_{T \text{ KF}}^{\text{miss}}$  value has a

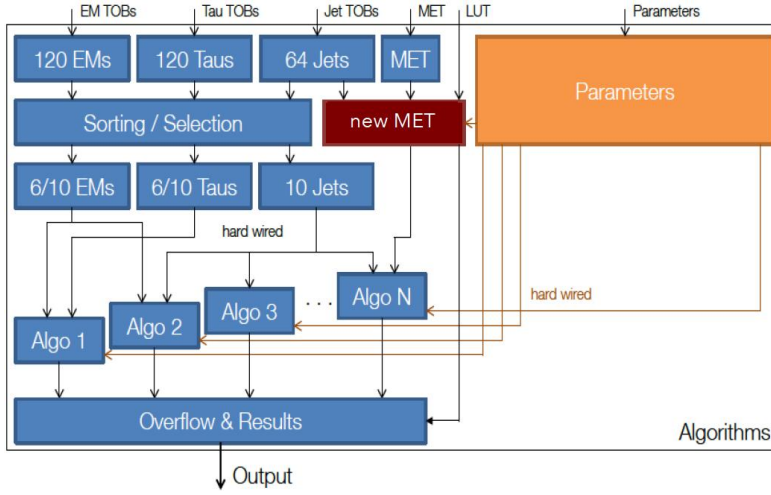


Figure 5.1: L1Topo schema

better correlation with the actual hard scatter transverse momentum. The correction value is calculated from a weighted sum of Level 1 jet TOBs. The weights are optimized using a Kalman filter trained using Monte Carlo events with sizeable pile-up. The resulting correction weights  $w_i$  are stored in a look-up table (LUT) depending on the Level 1 jet  $p_T$  and  $|\eta|$ :

$$\vec{E}_{T \text{ KF}}^{\text{miss}} := \vec{E}_{T \text{ L1}}^{\text{miss}} - \sum_i w_i \times \vec{p}_{T, i\text{-th jet}} \quad (5.2)$$

Fig. 5.2 illustrates the principle of the  $E_{T \text{ KF}}^{\text{miss}}$  calculation.

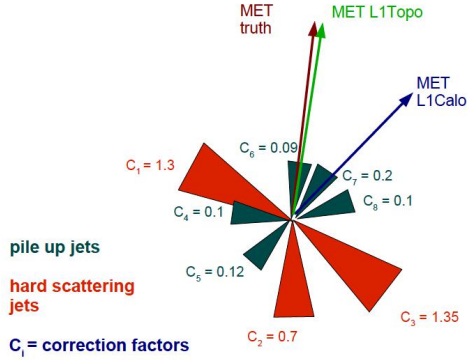


Figure 5.2: Kalman filter schema

### 5.3.1 The Kalman filter technique

The Kalman filter (or linear least square method) is an algorithm that derives the best average value of an unknown variable for each consecutive state by taking into account the previous state. The states correspond to data taken at different points in time or space. By learning from each data point the Kalman filter results in a more precise value than a single measurement. There are many applications of the Kalman filter in signal processing and navigation. It is also widely used in high energy physics, e.g. in the ATLAS muon tracking. The estimated variable  $\widehat{X}_k$  of state  $k$  can be written as

$$\widehat{X}_k = K_k \cdot Z_k + (1 - K_k) \cdot \widehat{X}_{k-1} \quad (5.3)$$

with  $K_k$  the Kalman gain matrix,  $Z_k$  the actual measurement and  $\widehat{X}_{k-1}$  the previous estimation. The Kalman gain matrix contains the covariance matrix of the measurement which can contain off-diagonal values for non-independent states. By only updating the covariance matrix of state  $k$  and leaving both  $\widehat{X}_k$  and  $K_k$  at the previous state values the Kalman filter can also account for noise.

### 5.3.2 Kalman filter $E_T^{\text{miss}}$

To determine the weights of eq. 5.2 the Kalman filter was trained with  $N$  MC events containing true  $E_T^{\text{miss}}$ . The quantity  $Q^2$  to be minimized can be parameterized as

$$Q^2 = \sum_{i=1}^N \left[ \frac{E_{x \text{ truth}}^{\text{miss}}(i) - E_{x \text{ L1}}^{\text{miss}}(i) + \sum_{j=1}^M \sum_{k=1}^{\text{jets}(i)} a_j \cdot E_x(k) \cdot \theta(E_T(j), E_T(k)) \theta(\eta(j), \eta(k))}{\sigma_i} \right]^2 + \sum_{i=1}^N \left[ \frac{E_{y \text{ truth}}^{\text{miss}}(i) - E_{y \text{ L1}}^{\text{miss}}(i) + \sum_{j=1}^M \sum_{k=1}^{\text{jets}(i)} a_j \cdot E_y(k) \cdot \theta(E_T(j), E_T(k)) \theta(\eta(j), \eta(k))}{\sigma_i} \right]^2 \quad (5.4)$$

where  $i$  iterates over the MC events used for training,  $j$  gives the bin of the LUT and  $k$  iterates over the number of jets in the  $i$ th MC event.  $\sigma_i$  is used as a weighting factor to emphasize events with large  $E_T^{\text{miss}}$  or small  $H_T$ . The  $\theta$ -functions determine the correct LUT bin. The LUT has a  $\log_2$  binning in jet  $p_T$  with five bins starting at 8 GeV and the last bin ranging from 128 GeV to 1023 GeV. The  $\eta$ -axis represents the trigger tower geometry with 16 discrete  $|\eta|$  values. Fig. 5.3 shows an example LUT.

The technical details of the Kalman filter training are described in [89]. The LUT was trained with various configurations. The differing conditions are

- the type of signal used in the MC sample

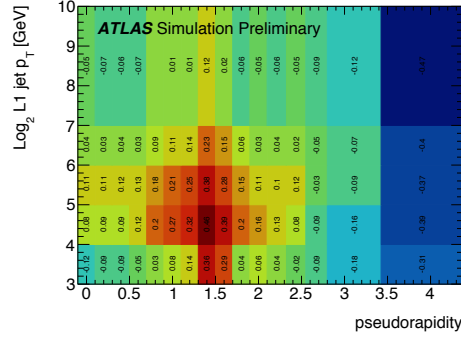


Figure 5.3: An example Look-up Table for the Kalman filter  $E_T^{\text{miss}}$  trigger.

- $t\bar{t}$  or  $ZH \rightarrow \nu\bar{\nu}b\bar{b}$  events
- applying a veto on the first 20 bunch crossings of a run (these have on average much higher pile-up)
- the pre-defined average pile-up number
  - $\mu = 40/60/80$
- the definition of  $\sigma_i$  in eq. 5.4
  - depending on  $E_{T \text{ truth}}^{\text{miss}}$ ,  $E_{T \text{ L1}}^{\text{miss}}$  or  $H_T$

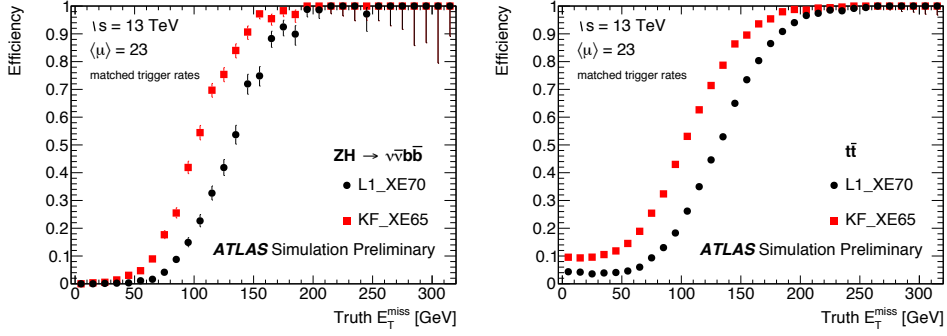
The performance of the different LUT was then studied on the signal samples to obtain the ideal configuration. A minimum bias sample was used to determine the corresponding background rate. As a result a LUT is chosen that is trained on a  $ZH \rightarrow \nu\bar{\nu}b\bar{b}$  with the highest available average pile-up  $\mu = 80$  and a  $\sigma_i(H_T)$ . The signal of  $ZH \rightarrow \nu\bar{\nu}b\bar{b}$  has comparatively low  $E_T^{\text{miss}}$ . Apparently the performance profits from a LUT that is trained on a difficult phase space.

Fig. 5.4 shows the trigger efficiency curves for the  $ZH \rightarrow \nu\bar{\nu}b\bar{b}$  and the  $t\bar{t}$  sample for the  $E_{T \text{ KF}}^{\text{miss}}$  with the best performing LUT and for  $E_{T \text{ L1}}^{\text{miss}}$ . The thresholds for both trigger algorithms are chosen in a way that they correspond to a background rate of  $10^{-4}$ . As the figure shows the  $E_{T \text{ KF}}^{\text{miss}}$  configuration reaches the plateau  $\sim 30$  GeV earlier - a significant improvement.

### 5.3.3 Performance of $E_{T \text{ KF}}^{\text{miss}}$

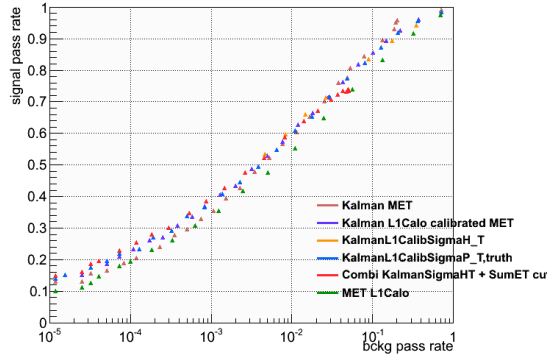
To arrive at the best performing Kalman filter configuration several different configurations were tested on different samples and pile-up conditions. Fig. 5.5 shows the signal efficiency to background rejection of different LUT with different  $\sigma$  definitions and the trigger efficiency for a background rejection of  $10^{-4}$  using a  $ZH \rightarrow \nu\bar{\nu}b\bar{b}$  signal sample and pile-up of 40. The final configuration using  $\sigma_{H_T}$  performs best and reaches the plateau  $\sim 10$  GeV earlier.





**Figure 5.4:** Trigger efficiencies for  $E_{T\text{KF}}^{\text{miss}}$  and  $E_{T\text{L1}}^{\text{miss}}$  compared for the same trigger output rate on a  $ZH \rightarrow \nu\bar{\nu}b\bar{b}$  (left) and a  $t\bar{t}$  (right) sample.

**Eff. of Kalman to Trigger Rate**



**Turn-on curves for bckg reduction rate  $10^{-4}$**

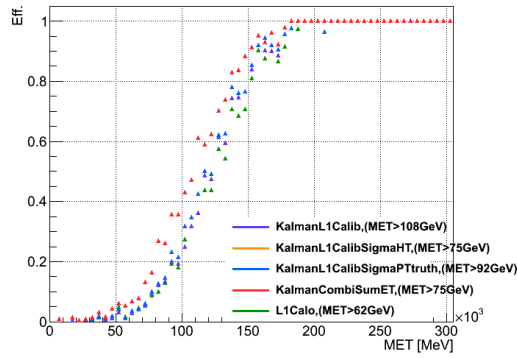


**Figure 5.5:** Performance of different Kalman filter configurations.

The following Fig. 5.6 - 5.9 show the performance of the final configuration of Kalman filter compared to the standard L1 Calo trigger. The samples and pile-up conditions are given in the captions.

Despite promising results the hardware implementation of the Kalman filter  $E_T^{\text{miss}}$  trigger has proven difficult. It is therefore not yet used for physics data taking.

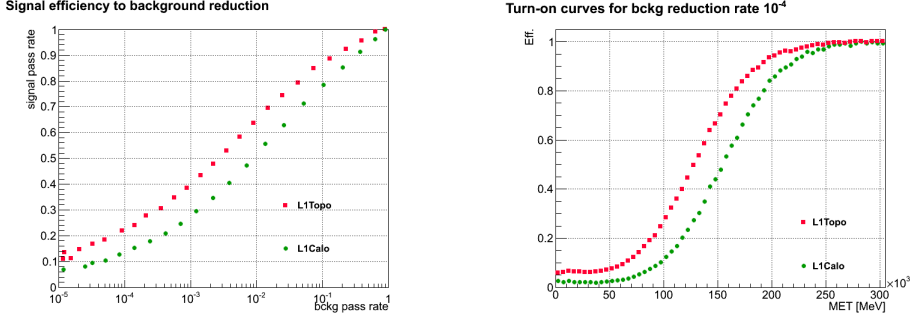


**Figure 5.6:** Performance of Kalman filter  $E_{T \text{ KF}}^{\text{miss}}$  compared to L1Calo  $E_{T \text{ L1}}^{\text{miss}}$ . Shown on a  $t\bar{t}$  sample with  $\mu = 60$

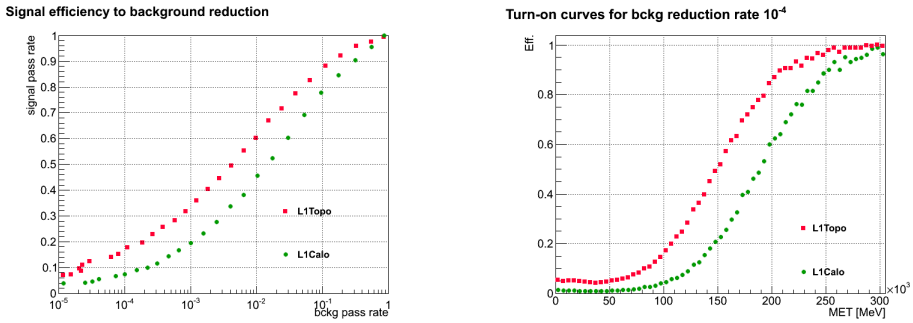


**Figure 5.7:** Performance of Kalman filter  $E_{T \text{ KF}}^{\text{miss}}$  compared to L1Calo  $E_{T \text{ L1}}^{\text{miss}}$ . Shown on a  $t\bar{t}$  sample with  $\mu = 80$

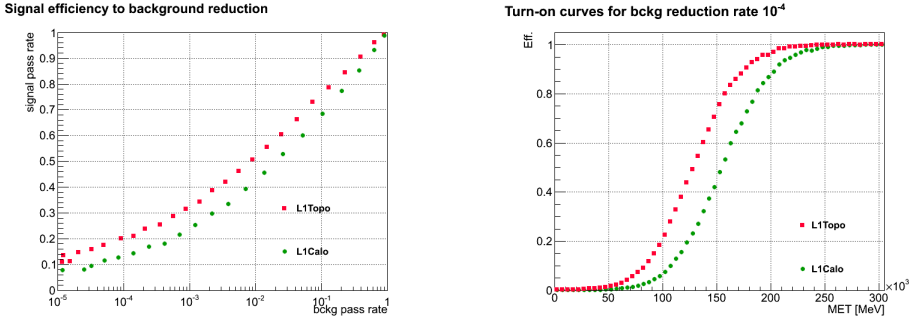


**Figure 5.8:** Performance of Kalman filter  $E_{T\text{KF}}^{\text{miss}}$  compared to L1Calo  $E_{T\text{L1}}^{\text{miss}}$ . Shown on a  $ZH \rightarrow \nu\bar{\nu}b\bar{b}$  sample with  $\mu = 60$

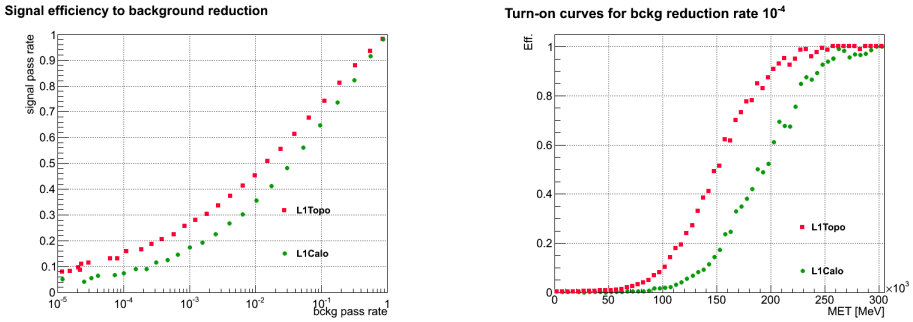


**Figure 5.9:** Performance of Kalman filter  $E_{T\text{KF}}^{\text{miss}}$  compared to L1Calo  $E_{T\text{L1}}^{\text{miss}}$ . Shown on a  $ZH \rightarrow \nu\bar{\nu}b\bar{b}$  sample with  $\mu = 80$

## 5.4 Transverse missing energy trigger at HLT

Until the end of 2011 there was only one  $E_T^{\text{miss}}$  trigger algorithm at EF level which calculates the missing transverse momentum using the full calorimeter granularity of about 188000 cells [90]. A noise cut of  $|E| > 2\sigma$  and  $E > -5\sigma$  is applied on the cell energy, in addition cells marked as *bad* are also excluded. This most basic  $E_T^{\text{miss}}$  algorithm is called 'cell' algorithm. In 2012 a new algorithm was introduced at EF level to run in parallel to the existing one. Instead of using the cells it uses topological information. The calorimeter is clustered up by selecting seed cells with an energy deposit of  $|E| > 4\sigma$  and adjoint cells with  $|E| > 2\sigma$ , where  $\sigma$  is the estimated noise level. Immediate neighbors of the seed cells are also included into the topological object independent of their energy content. The energy content of the cluster is calibrated using so-called local weights, which assign a cluster moment dependent calibration for hadronic particles. This last step could also be dropped corresponding to a electromagnetic calibration what resulted in a slight degradation in performance. A schematic for the "topocluster" algorithm is shown in Fig. 5.10.

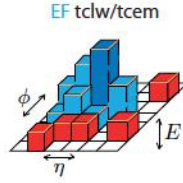


**Figure 5.10:** Schematic view of the topocluster formation. The seed cell is shown in dark blue, adjoint cells in light blue and neighbouring cells in red.

For Run II with the new HLT architecture three more algorithms were added.

**Missing  $H_T$**  The 'mht' algorithm uses the already clustered and calibrated jets provided by the jet trigger algorithms. The currently used calibration is at the hadronic scale. The resulting  $E_T^{\text{miss}}$  is also called  $H_T^{\text{miss}}$ . All jets with a  $p_T$  above 7 GeV are included.

**Topocluster with pile-up subtraction** This algorithm uses the same topoclusters as the "topocluster" algorithm but applies an area-based pile-up correction. The pile-up density is calculated in ten slices of  $\eta$  taking all cells with  $E < 2\sigma$  into account. After the subtraction of the pile-up the topoclusters are then used as input to the  $E_T^{\text{miss}}$  calculation. Fig. 5.11 illustrates the process of the algorithm. Due to the  $\eta$ -dependent correction it is called 'topocl \_pueta'.

**Topocluster with pile-up fit** The third algorithm is also based on topoclusters. It uses a fit to predict the pile-up energy contained in each high- $p_T$  object and calculates  $E_T^{\text{miss}}$  from these corrected objects. The fit is constrained by a combinations of the conditions that the overall pile-up contribution to the resulting  $E_T^{\text{miss}}$  should be zero and the average pile-up

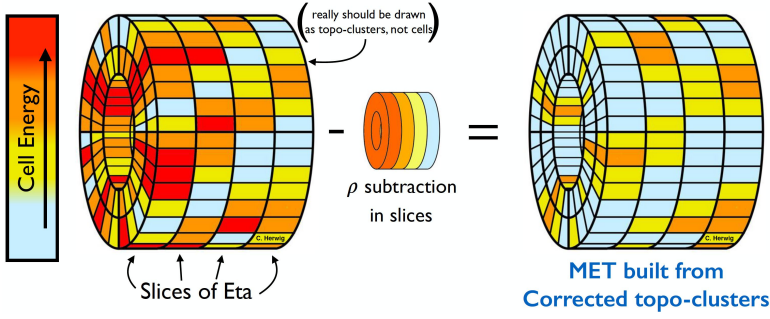


Figure 5.11: Schema for the 'pueta' algorithm. ©2016 C. Herwig

energy density of the event from the low- $p_T$  objects. The relative importance of both constraints can be varied with a covariance matrix.

Fig. 5.12 shows again an illustration of the algorithm. In a first step the algorithm groups clusters into  $0.7 \times 0.7 \Delta\eta - \Delta\phi$  towers, towers with an energy deposit above 45 GeV belong to the high- $p_T$  group. In a second step 4 sets of towers each offset by half a bin in one or both of  $\eta$  and  $\phi$  are compared and the set with the highest resulting  $E_T^{\text{miss}}$  is chosen. This algorithm is called 'topocl\_pufit' accordingly.

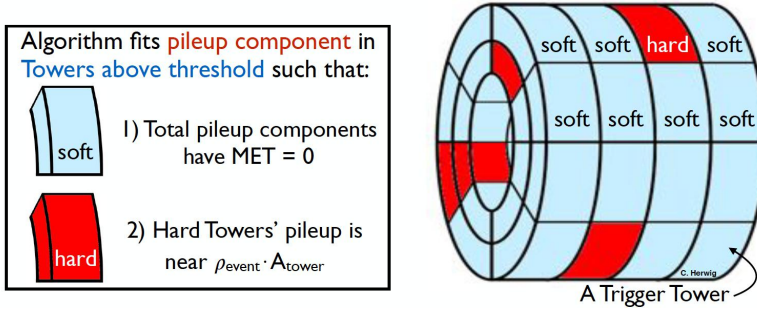


Figure 5.12: Schema for the 'pufit' algorithm. ©2016 C. Herwig

#### 5.4.1 $E_T^{\text{miss}}$ trigger performance

From the beginning of Run II data-taking in 2015 to the end of p-p running in 2016 the  $E_T^{\text{miss}}$  triggers underwent some changes. The new algorithms for Run II, "mht", "topocl\_pueta" and "topocl\_pufit", were running in parallel to the well-proven ones with the "cell" as lowest unprescaled variant. The original configuration had all algorithms always running at the same thresholds as the additional algorithms were expected to add little unique rate on top of the "cell" one.

Fig. 5.13 shows early performance plots of the  $E_T^{\text{miss}}$  algorithms with  $78.7 \text{ pb}^{-1}$  of data taken at 13 TeV in 2015. The top plots show the distributions for  $E_T^{\text{miss}}$  and the sum of  $E_T$  for the different  $E_T^{\text{miss}}$  flavors. The topocluster flavors largely overlay each other. The middle plots

show the turn-on curves for thresholds of 35 GeV (left) and 50 GeV (right). To allow a comparison of the different variants turn-on curves are always shown in the offline reconstructed  $E_T^{\text{miss}}$ . The difference in performance between the default "cell" and the other algorithms is very distinct with "mht" outperforming all others at the same threshold. The bottom plot shows the resolution of  $E_T^{\text{miss}}$  as a function of the offline sum  $E_T$ . The resolution is obtained by a fit of a Gaussian to the  $E_x$  distribution obtained for each bin of the sum  $E_T$  reference.  $E_T^{\text{miss}}$  is very event topology dependent these plots just allow a qualitative comparison of the  $E_T^{\text{miss}}$  variants.

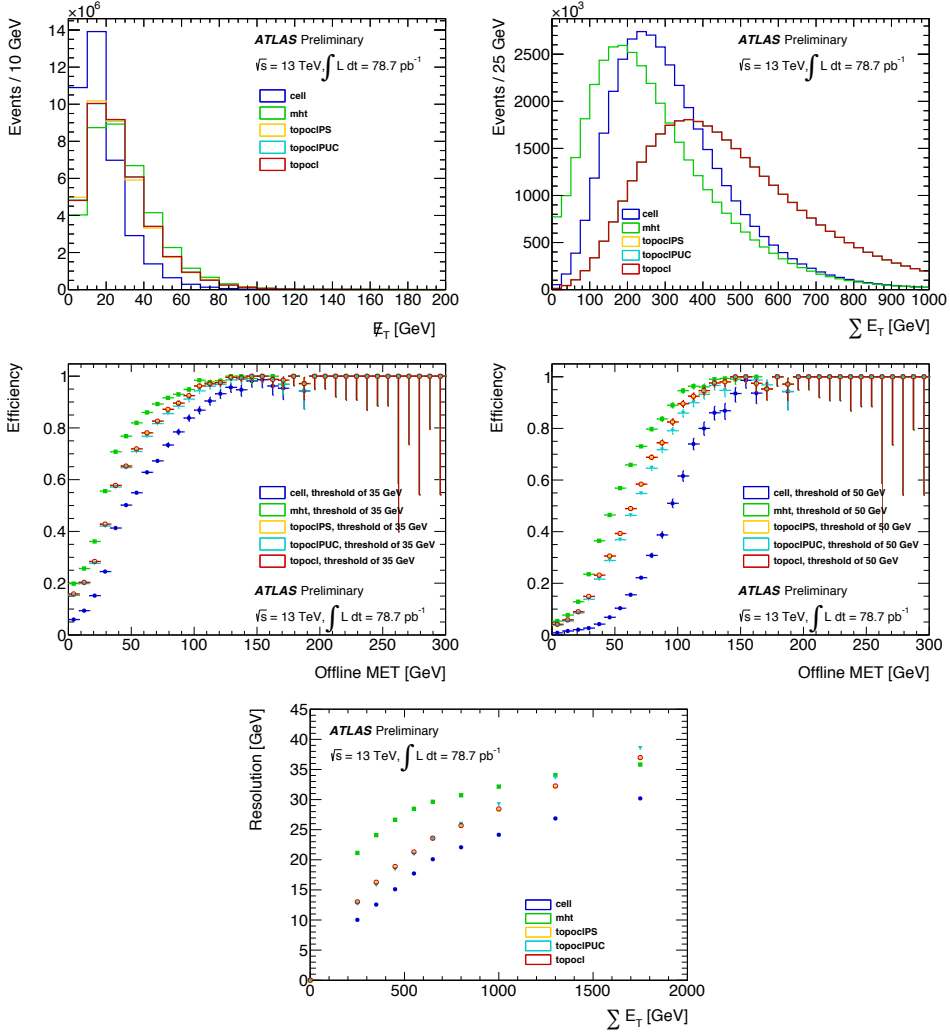
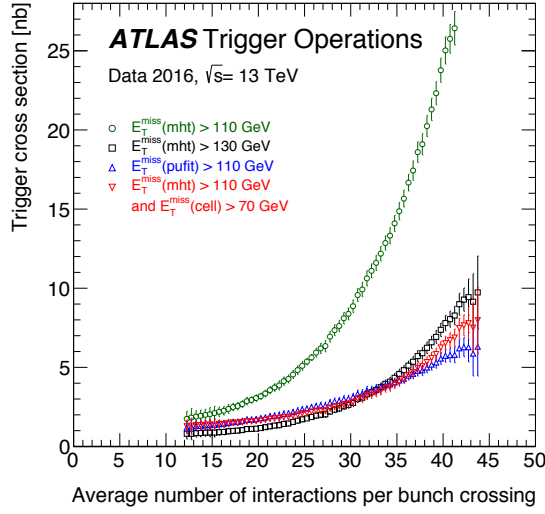


Figure 5.13: Performance of  $E_T^{\text{miss}}$  triggers in early 2015.

Fig. 5.14 shows the performance of the different  $E_T^{\text{miss}}$  trigger variants in 2016 after a re-

calibration of the "topocl\_pufit" algorithm. Now both the "topocl\_pufit" and a combination of the "mht" and "cell" trigger allow to run with continuously lower thresholds opposed to the stand-alone "mht" version which rate increases exponentially with pile-up.



**Figure 5.14:** The trigger cross section as measured by using online rate and luminosity is shown as a function of average number of processes per LHC bunch crossing as measured online, for various missing  $E_T$  triggers. All triggers have an L1  $E_T^{\text{miss}}$  requirement of 50 GeV, measured at the electromagnetic scale.

## CHAPTER 6

### Event reconstruction

To be useful the large amount of event data of the ATLAS detector needs to be reconstructed before it can be analyzed. Every particle interacts with the detector material in a different and therefore characteristic way. This characteristic signature allows to reconstruct and identify the physical objects from the detector response. Charged particles leave a track in the inner detector and can be matched with the energy deposits in the calorimeters or tracks in the muon system. The calorimeter response is characterized as electromagnetic or hadronic interaction and showers of hadronic particles further grouped to jets. Weakly interacting particles leave a trace as missing energy. There are several steps and procedures involved for a successful event reconstruction. They are described together with the corresponding efficiencies in this chapter.

#### 6.1 Tracking and Vertices

Charged particles leave a track in the ID layers which can be reconstructed by dedicated algorithms [91–95]. There are two different approaches: the algorithm can start from hits in the innermost ID layers and follow the track to the outer layers - inside-out tracking, or the algorithm can start from TRT hits on the outside going back to the interaction point - outside-in.

The first one is the default tracking used by ATLAS, it requires the particle to have a  $p_T > 400$  MeV and a lifetime greater than  $3 \times 10^{-11}$  s. Outside-in tracking is mainly useful for decay products originating in a secondary vertex.

For inside-out tracking the algorithm is seeded by three hits in the silicon detectors. The hits are translated into three-dimensional space points and can be located completely in either the Pixel detector or SCT or a mix of both. From the initial three space points the track candidate is formed by adding consecutive space points employing a combinatorial Kalman filter [96].

Track candidates often share space points. To resolve the ambiguity the tracks are ranked by quality according to the numbers of hits and holes they contain. A hole is a space point the fit expected to be there but is missing. The track quality decreases with the number of holes. Shared space points are assigned to the higher quality track and removed from the lower quality track which is then re-fitted. The resolved tracks are then extended into the TRT. The whole overlap process has been greatly improved for Run II by making use of a neural network resulting in efficiency gains for high- $p_T$  tracks of up to 17% [93].



The track reconstruction efficiency depends greatly on the pile-up conditions. With a large amount of available space points 'fake' tracks not associated to a charged particle are more likely under high pile-up conditions. The efficiency also depends on the quality criteria applied on the tracks. In ATLAS two different classifications are used: 'loose' tracks, requiring at least seven silicon hits and allowing two silicon holes (1 Pixel hole) and 'tight primary' tracks, requiring at least nine silicon hits and one hit in the IBL or the next-to-innermost pixel layer. The 'loose' track selection is the default one with highly efficient track reconstruction at the expense of more fake tracks. The 'tight primary' selection targets primary tracks with a high fake track rejection but lower overall efficiency [94]. Fig. 6.1 demonstrates the higher number of fake tracks with the 'loose' selection in dependence of pile-up.

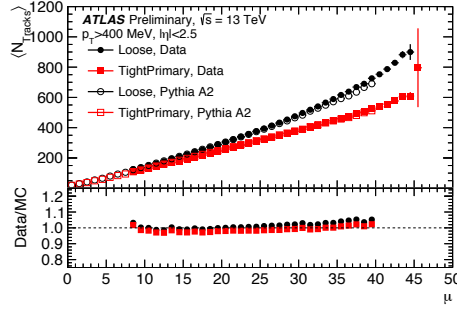


**Figure 6.1:** No. of tracks depending on pile-up and track selection criteria.

After the track reconstruction the origins of the tracks can be determined - the vertices. One can differentiate between 'primary' vertices for an interaction point and 'secondary' vertices indicating a particle decay. The primary vertex reconstruction consists of two steps, the vertex finding and the vertex fitting where the actual coordinates of the vertex are computed.

The vertex finding is an iterative process including all tracks that fulfill the 'tight primary' quality criteria, a vertex requires at least two associated tracks. The seed position for the first vertex is determined as mode of all z-coordinates of tracks at the points of closest approach to the centre of the reconstructed beam spot [97]. Together with the tracks the seed position is used for the iterative vertex fitting. Tracks that can't be associated to the first vertex are used for the finding of the next vertex. Both steps are repeated until there are unassociated tracks left or no new vertex can be found. The vertices are ranked in  $\sum p_T^2$  and the one with the highest value is declared the primary vertex of the event.

As shown in Fig. 6.2, the number of vertices per event is dependent on the pile-up conditions. The number of vertices increases with higher  $\mu$  as pile-up is proportional to the number of interactions. Also shown is the vertex reconstruction efficiency with the number of associated tracks.

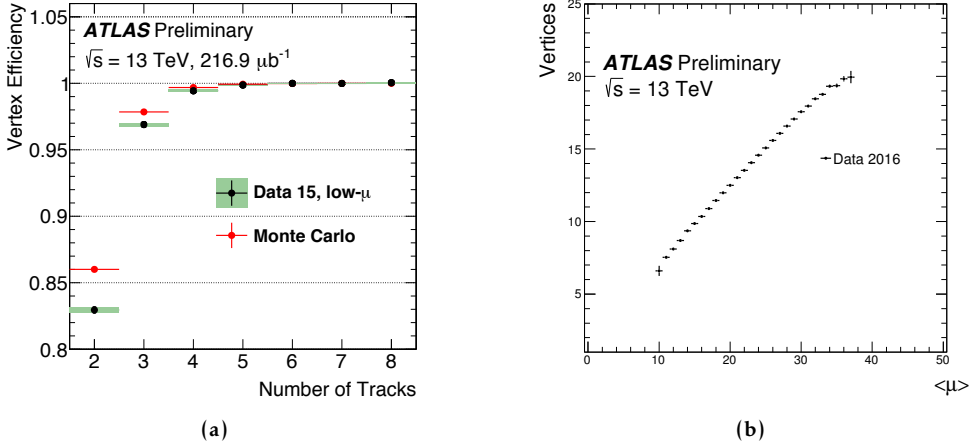


**Figure 6.2:** Vertex reconstruction efficiency to the number of associated tracks (a) and the dependence of the number of vertices per event on pile-up (b).

## 6.2 Jets

Quarks and gluons are not detected as single particles in the detector due to confinement. They form jets instead - collimated sprays of hadronized quarks and gluons. The hadrons usually start decaying in the electro-magnetic calorimeter and the jet is stopped in the hadronic calorimeter. Only calorimeter information is therefore sufficient to be able to reconstruct the jets.

Reconstruction starts from topological clusters, three dimensional clusters of calorimeter cells with energy deposits. A calorimeter cell with a highly significant signal-to-noise ratio forms the seed cell to which directly adjacent and neighbouring cells are added [98]. The cell significance is defined as the ratio of the deposited energy to the average expected noise value. The average expected noise is dependent on both pile-up and the electronic noise and updated for long-term changes in the run conditions, i.e. its value was updated for Run II conditions. Due to the non-compensating calorimeters in ATLAS different cell-significance values for electromagnetic and hadronic clusters are required.

The topological clusters are then used as input to a jet clustering algorithm that groups the clusters iteratively to jets. Commonly used are sequential recombination jet algorithms parameterized by the distance between two objects  $d_{ij}$  and the distance between an object and the beam  $d_{iB}$ :

$$d_{ij} = \min(p_{Ti}^{2p}, p_{Tj}^{2p}) \frac{(y_i - y_j)^2 + (\phi_i - \phi_j)^2}{R^2}, \quad (6.1)$$

$$d_{iB} = p_{Ti}^{2p} \quad (6.2)$$

with  $p_{Ti}$  the transverse momentum,  $y_i$  the rapidity and  $\phi_i$  the azimuth of the object  $i$ .  $R$  and  $p$  are parameters of the algorithms. The algorithm starts with calculating all distances

for cluster  $i$ . In case the smallest distance is between two clusters they are merged and form a new entity, if the distance between the cluster and the beam is the smallest the cluster is called a jet and taken of the list of clusters/entities. This procedure is repeated until no entities are left.

The choice of the parameters  $R$  and  $p$  influences the characteristics of the resulting jet shape.  $p > 1$  results in the  $k_t$ -algorithm,  $p = 0$  in the Cambridge-Aachen algorithm both commonly used in the past. For  $p = -1$  one obtains the anti- $k_T$  algorithm [99], with  $R = 0.4$  the default jet clustering algorithm used in ATLAS in Run II. By choosing a negative value for  $p$  it ensures that soft (low  $p_T$ ) clusters are merged with hard (high  $p_T$ ) clusters before merging among themselves. The resulting jet shapes are therefore not influenced by soft clusters and usually a regular cone shape for hard jets. This is not the case for both  $k_t$  and Cambridge-Aachen. The anti- $k_T$  jet clustering algorithm is implemented in the ATLAS reconstruction software via the FastJet [100, 101] package.

After all jets are reconstructed they are associated to tracks. The associated track information is helpful in distinguishing hard interaction jets from pile-up jets. To this purpose the Jet Vertex Fraction (JVF) is defined as the fraction of the scalar transverse momentum sum of all associated tracks originating from the primary vertex to the scalar  $p_T$  sum of all associated tracks [102]. Pile-up jets have a low JVF whereas jets from the hard interaction have a JVF of one.

### 6.2.1 Jet energy calibration

To be able to calculate a meaningful jet energy the energy deposited in the calorimeter clusters needs to be calibrated first. Without any calibration the jet energy is at the electromagnetic (EM) scale. By applying a local cluster weight (LCW) the topological clusters are divided in electromagnetic and hadronic clusters and their energy corrected accordingly. The energy correction is derived from single pion Monte Carlo simulation, in addition the LCW also takes into account the non-compensating nature of the ATLAS calorimeter, effects of the noise thresholds and losses due to energy deposited in non-instrumented areas of the calorimeters or outside of them. The local cluster weight is used to calibrate the topological clusters before reconstructing any jets.

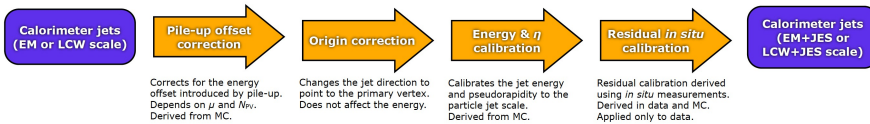


**Figure 6.3:** The schema of the chain of corrections and calibrations for the jet energy scale applied to jets in ATLAS [103].

The jets can be reconstructed from either EM or LCW clusters. In the following the jet energy

is calibrated to ensure that the measured jet energy is equivalent to the energy of the truth jet in Monte Carlo simulation. As shown in 6.3 the Jet Energy Scale (JES) correction consists of several steps. The first step is to correct the energy for the offset introduced by pile-up, both in-time (additional proton interactions in the same event) and out-of-time (collisions in previous and following bunch crossings). This correction is derived from Monte Carlo simulations and depends on the number of reconstructed primary vertices and the average number of interactions. Second the jet direction is corrected to point to its associated primary vertex, this does not affect the jet energy. In a third step the jet energy and pseudo-rapidity are calibrated with transfer functions derived from Monte Carlo. The inverse of the energy transfer function is called jet energy response function:

$$R^{\text{EM(LCW)}} = E_{jet}^{\text{EM(LCW)}} / E_{jet}^{\text{truth}} \quad (6.3)$$

with  $E_{jet}^{\text{truth}}$  the energy of the matched Monte Carlo truth jet and  $E_{jet}^{\text{EM(LCW)}}$  the EM (LCW) corrected energy of the reconstructed jet. The pseudo-rapidity is corrected in the same manner. The last step applies residual in-situ corrections to jets reconstructed from data. The in-situ corrections are derived from the transverse momentum balance between the jet and a well measured reference object like photons and Z-bosons [103]. The jet energy resolution is derived in a similar fashion from the transverse momentum balance in di-jet events [104].

The uncertainty on the jet energy scale and the jet energy resolution are derived by varying the selections used for the data to Monte Carlo comparison. Also the differences seen by using several MC generators are taken into account. The derivation methods are described in detail in [105–107] for the jet energy scale and in [104, 105] for the jet energy resolution. For strong production squark gluino searches these two uncertainties belong to the dominating ones that contribute to the overall systematic uncertainty. Fig 6.4 shows the JES uncertainty in 2015 data to the jet  $p_T$  with fixed  $|\eta|$  and vice versa. It is largest for low  $p_T$  jets with a peak value of 4.5% decreasing to 1% at 200 GeV. It is then relatively stable increasing slightly due to effects from the in-situ calibration up to a  $p_T$  of 2 TeV - the in-situ calibration is only valid up to 2 TeV [108].

### 6.2.2 Heavy flavoured jets

Jets originating from b-hadrons are interesting for data analysis as the mean lifetime of a b-quark is  $\sim 1.5$  ps. The b-hadron can therefore travel some distance in the detector before decaying and will create a secondary or displaced vertex. This vertex can be reconstructed and used to identify the b-jets. b-quarks are produced via the decay of Higgs bosons and top quarks, for both particles the b-quark final state is the dominant one. Due to this fact the LHC is also called ‘b-factory’.

The b-tagging in ATLAS is done by an algorithm based on a multivariate discriminant from a Boosted Decision Tree (BDT). The input for the BDT is generated by further algorithms: an algorithm using the impact parameters (IP2D and IP3D) [109], a secondary vertex finder

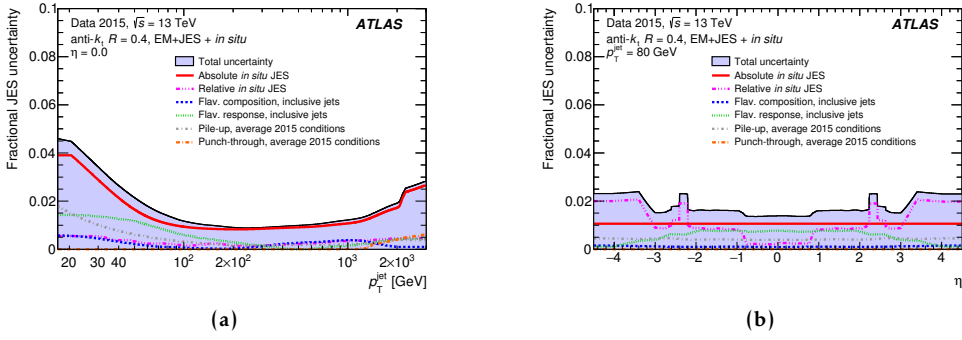


**Figure 6.4:** Combined uncertainty in the JES of fully calibrated jets as a function of (a) jet  $p_T$  at  $\eta = 0$  and (b)  $\eta$  at  $p_T = 80$  GeV in 2015 data [108].

algorithm (SV) [110] and a decay chain multi-vertex algorithm (JetFitter) [109].

The algorithm was re-optimised for Run II as the precision for the secondary vertex increases with the addition of the IBL detector. The algorithm used in 2015 and 2016 is the ‘MV2c10’ [111, 112], it was further optimised for 2016 with actual  $\sqrt{s} = 13$  TeV data. The operating point corresponds to an efficiency of 77%, along with the rejection factors of 134 for light-quark jets and 6 for charm jets [112]. Fig. 6.5 shows the light-flavour jet and c-jet rejection versus the b-tagging efficiency for different configurations in 2015 and 2016.

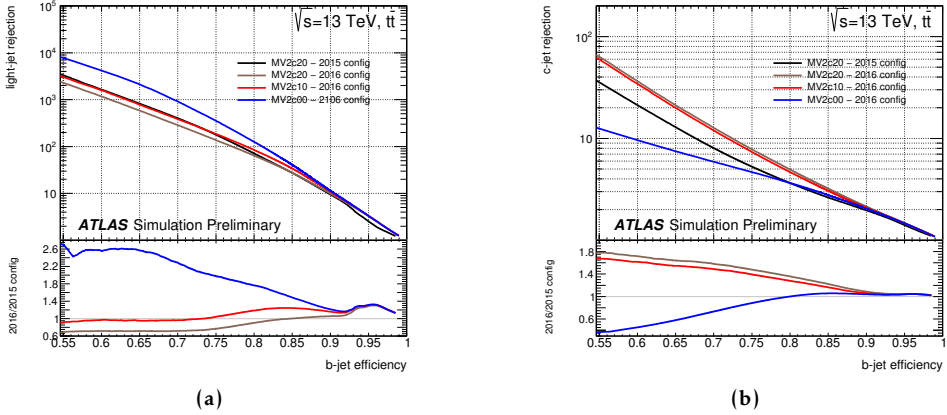


**Figure 6.5:** The rejection efficiency of light-jets (a) and c-jets (b) for different b-tagging algorithms configuration for 2015 and 2016 [112].

### 6.3 Missing transverse energy

Missing transverse energy originates from particles that interact only weakly like neutrinos or only weak-interacting new particles. They do not interact sufficiently with the detector and just leave it unnoticed. As the ATLAS detector encloses the interaction point one can use the transverse missing energy as a measure for the weakly interacting particles. Due to

energy and momentum conservation the weakly interacting particle creates an imbalance in the total measured transverse momentum -  $\vec{E}_T^{\text{miss}}$ .

The transverse missing momentum is calculated based on all energy deposits in the calorimeter. It is the vectorial sum of the transverse momentum of all calibrated calorimeter objects that pass a certain  $p_T$  threshold (for noise reduction) plus a soft term estimating true low  $p_T$  components.

$$E_{x(y)}^{\text{miss}} = E_{x(y)}^{\text{miss}, e} + E_{x(y)}^{\text{miss}, \gamma} + E_{x(y)}^{\text{miss}, \tau} + E_{x(y)}^{\text{miss}, \text{jets}} + E_{x(y)}^{\text{miss}, \mu} + E_{x(y)}^{\text{miss}, \text{soft}}. \quad (6.4)$$

From  $\vec{E}_T^{\text{miss}}$  the absolute value  $E_T^{\text{miss}}$  can be calculated:

$$E_T^{\text{miss}} = \sqrt{E_x^{\text{miss}2} + E_y^{\text{miss}2}}. \quad (6.5)$$

The soft term can be derived either from the calorimeter energy deposits (CST) or from tracks (TST). In Run II the soft term is estimated from tracks in combination with the information about hard objects in the calorimeter [113]. Using the calorimeter energy deposits is very pile-up-prone and not favoured with the 2016 pile-up conditions.

As a measure relying on the whole calorimeter information  $E_T^{\text{miss}}$  is in general very pile-up dependent. Any energy deposits in the calorimeter skew the transverse momentum balance and lead to fake  $E_T^{\text{miss}}$ . This effect increases with the number of pile-up interactions. To suppress pile-up contributions to  $E_T^{\text{miss}}$  a Jet Vertex tagger (JVT) [114] requirement is employed. The JVT test which fraction of tracks associated to a jet originate from the primary vertex. To suppress pile-up jets a high fraction is requested,  $\text{JVT} > 0.59$  is required for all jets with  $p_T < 60$  GeV and  $|\eta| < 2.4$ .

Fig. 6.6 shows the  $E_T^{\text{miss}}$  distribution in  $Z \rightarrow e^+e^-$  events using the track based soft-term for the full 2015 data set and part of the 2016 data set.

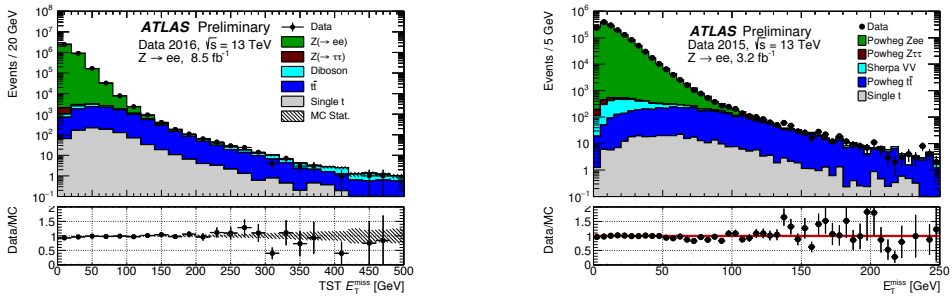


**Figure 6.6:** The  $E_T^{\text{miss}}$  distribution in  $Z \rightarrow e^+e^-$  events using the track based soft-term for the full 2015 data set [115] and part of the 2016 data set [116].

As a measure for the performance of the  $E_T^{\text{miss}}$  measurement often the resolution in  $E_y^{\text{miss}}$  and  $E_x^{\text{miss}}$  is used. The resolution here is defined as the Root Mean Square (RMS) of the distribution. As shown in Fig. 6.7 the TST  $E_T^{\text{miss}}$  is only slightly dependent on the number of primary vertices as the track based method can efficiently determine the tracks coming from

the hard-scatter event. The CST  $E_T^{\text{miss}}$  is much more pile-up dependent [113]. Also shown is the resolution as function of the scalar sum of all transverse energy in the event ( $\sum E_T$ ). It can be seen that the resolution increases with increasing event activity. TST  $E_T^{\text{miss}}$  suffers for high jet multiplicities from its insensitivity to neutral particles, if selecting events with zero jets with  $p_T > 20$  GeV the resolution stays relatively constant [113].

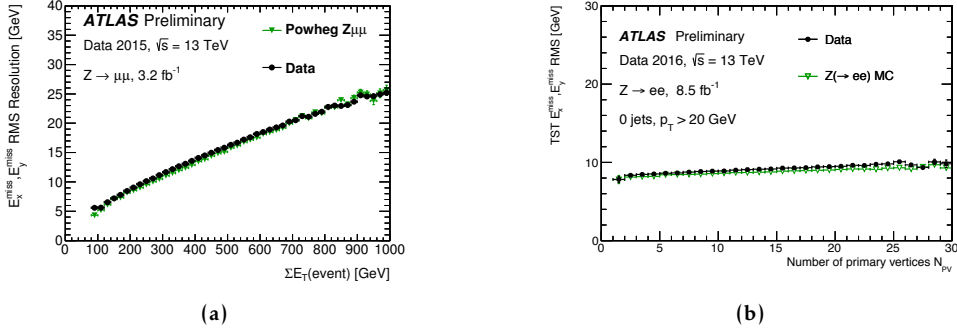


**Figure 6.7:** Shown is (a) the  $E_T^{\text{miss}}$  performance in 2015 data as quantified by the resolution as a function of  $\sum E_T$  of the entire event [115] and (b) the TST  $E_T^{\text{miss}}$  resolution as a function of the number of primary vertices for a selection of Z boson decays to a pair of electrons and requiring no primary-vertex jet activity in the 2016 ATLAS dataset [116] compared to simulation.

## 6.4 Leptons and Photons

### 6.4.1 Electrons

Baseline electron candidates are reconstructed from an isolated electromagnetic calorimeter energy deposit with  $|\eta| < 2.47$  matched to an ID track [117]. The reconstruction takes place in several steps:

1. Seed-cluster reconstruction - a sliding window algorithm searches for electron cluster seeds with a  $p_T > 2.5$  GeV and a window size of  $3 \times 5$  calorimeter towers. The seeds are used as input for the topological cluster algorithm [118] that adds neighbouring cells, the requirements for the neighbouring cells vary with the location in the calorimeter.
2. Track reconstruction - the standard ATLAS track reconstruction as described in § 6.1 modified to allow for an electron hypothesis that allows more energy losses due to bremsstrahlung. The modified reconstruction improves the performance for electrons.
3. Electron specific track fit - the tracks are matched to the topological clusters from the first step by comparing the extrapolated  $\eta - \phi$  location of the track with the center of the cluster. After a first loose match the matched tracks with more than four precision hits are re-fitted taking again into account the effect of bremsstrahlung.
4. Electron candidate reconstruction - the re-fitted tracks are matched with tighter conditions to the clusters, if several tracks are matched the one with the smallest track-

cluster distance and the highest track quality is chosen [119]. A cluster matched to a track is an electron candidate. Clusters without tracks are removed and considered as photons. The electron candidate is re-clustered with a window size of  $3 \times 7$  ( $5 \times 5$ ) in the calorimeter barrel (end-cap) and calibrated to the true electron energy [120].

Not all reconstructed electrons originate from the hard-scatter interaction, major backgrounds are converted photons, heavy-flavour hadron decays and mis-identified jets as well as electrons from pile-up interactions. As a first measure to reduce pile-up an electron is required to come from the primary vertex by selecting only electrons with  $\frac{d_0^{PV}}{\sigma(d_0^{PV})} < 5$  and  $\Delta z_0^{PV} \sin \theta < 0.5$  mm (with  $d_0^{PV}$  and  $z_0^{PV}$  the impact parameters defined in § 3.2.1). Secondly a dedicated electron identification (ID) is developed relying on the electromagnetic shower shape variables, track properties, the track-cluster matching quantities and variables measuring the bremsstrahlung [117].

The electron ID was re-optimised for Run II taking into account the improvements from IBL based on MC with data-driven corrections. The ID algorithm is a multivariate likelihood based method. The algorithm defines three different operation points increasing the background rejection with each step: 'Loose', 'Medium' and 'Tight'. The signal efficiency for electrons with  $E_T > 25$  GeV goes from 78% to 90% increasing with  $E_T$ . Fig. 6.8 shows the identification efficiency versus  $E_T$  for a  $Z \rightarrow ee$  signal and a di-jet background sample.

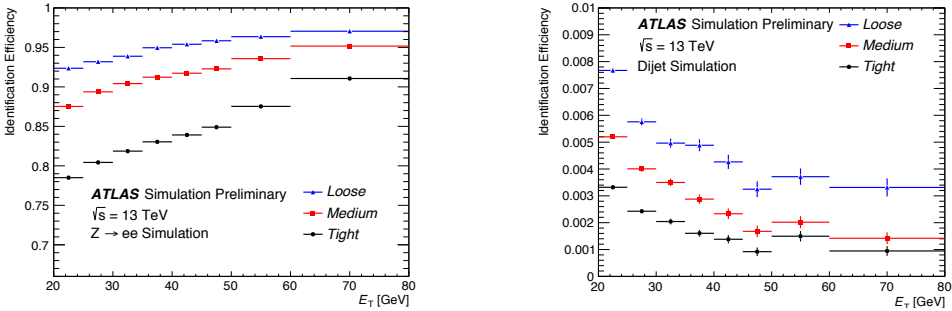


**Figure 6.8:** Electron identification efficiency versus  $E_T$  for a  $Z \rightarrow ee$  signal and a di-jet background sample.

Further the electron is required to be isolated for background rejection. Two discriminating variables exist for the isolation: a calorimeter based one using the clusters in a cone of  $\Delta R = 0.2$  around the electron and a track based one using the tracks around the electron track inside a cone of  $\Delta R = \min(0.2, 10 \text{ GeV}/E_T)$ .

The overall efficiency of the electron selection is then defined as a product of the reconstruction, identification and isolation efficiencies together with the electron trigger efficiency. The efficiencies are measured with the tag-and-probe method in data and MC in a well defined sample as  $Z \rightarrow ee$  or  $J/\Psi \rightarrow ee$  events. One of the electrons is 'tagged' to then measure the efficiency of finding the other. Fig. 6.9 shows the combined reconstruction and identification efficiencies versus  $E_T$  and  $\eta$  for the 2015 data set. The efficiency has dips in  $\eta$  at the points



where there are larger amounts of dead-material. The figures also clearly shows the efficiency increase with increasing transverse energy.

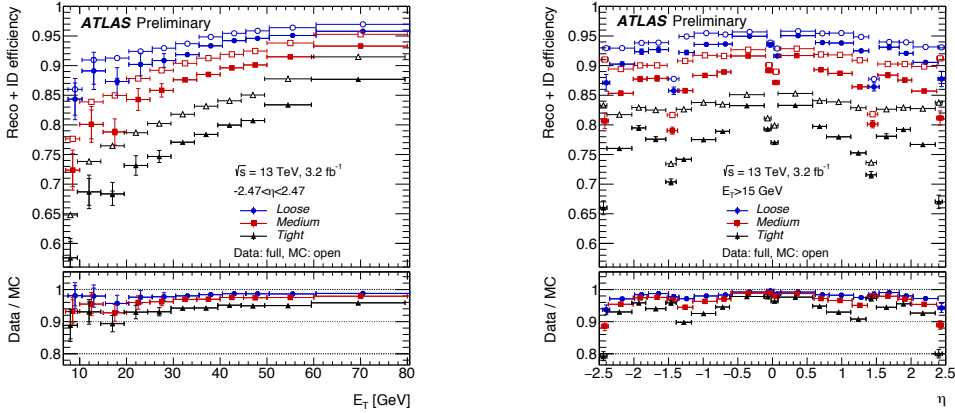


**Figure 6.9:** Combined electron reconstruction and identification efficiencies versus  $E_T$  and  $\eta$  for the 2015 data set.

### 6.4.2 Photons

Photons are reconstructed in a very similar way to the electron reconstruction [121–123]. One distinguishes between prompt, unconverted photons and converted photons converting into two electrons before reaching the electromagnetic calorimeter, both types coming from the hard-scatter interaction.

Electron clusters in the calorimeter that can not be matched to a track are treated as unconverted photon candidates. If a cluster can be matched to one of the two oppositely charged tracks parallel at the place of conversion, it is treated as a converted photon. For photons converting just shortly before the calorimeter the determination if a track pair exists becomes very inefficient. In these cases a single track can be matched to the photon cluster but only if there are no hits in the innermost layer of the pixel detector to avoid mis-identifying electrons as photons.

The same as for electrons identification requirements based on shower shape and energy and track information as well as isolation requirements using calorimeter energy (track transverse momentum) in a cone around the photon cluster (track) are made to help distinguish prompt photons from background. An additional source of true photons are decays of hadrons to photons. Here both the shower shape and energy in the EM and HAD calorimeter are used to discern them from prompt photons and as criteria for the photon identification. Hadrons reconstructed as photons leave a majority of energy in the hadronic calorimeter and the electromagnetic part of the shower tends to be broader [121]. There are two identification operation points: 'Loose' and 'Tight'. Both operations points are tuned separately for unconverted and converted photons in four different  $\eta$  regions.

For the photon identification is measured with three different data-driven methods each tar-

getting slightly different but overlapping  $E_T$  regions:

- Radiative photons - the identification efficiency is measured by selecting a  $Z \rightarrow ll\gamma$  sample and determining the ratio of selected photon candidates to photons passing the 'Tight' ID requirement.
- $e \rightarrow \gamma$  extrapolation - from a large sample of  $Z \rightarrow ee$  events the photon identification efficiency is derived by exploiting the similarities between photon and electron showers with a 'Tag-and-Probe' method. In this case the probe electron that fails isolation and electron identification requirements is used to estimate the photon shower shape.
- Matrix method - in a sample of photons passing the isolation requirements and  $20 \leq E_T \leq 1500$  GeV the track isolation distribution in a cone larger than the default of the isolation criterium is used to differentiate between signal and background photons before and after the 'Tight' identification selection.

As seen in Fig. 6.10 all three methods agree well with each other. The radiative photon method results in larger deviations due to the larger statistical uncertainties of the method. The derived photon identification efficiency increases from 53-64% (47-61%) for unconverted (converted) photons with a  $E_T$  of 10 GeV to 88-92% (96-99%) for a photon  $E_T \geq 100$  GeV.

The methods also agree well with the measurement of the ID efficiency in simulation. They are therefore combined to result in one scale factor depending on the photon  $E_T$  and for four different  $\eta$  regions.

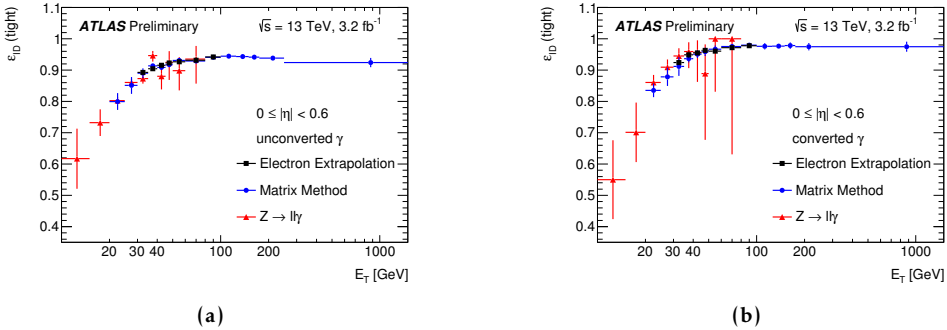


**Figure 6.10:** Identification efficiency for unconverted (a) and converted (b) photons as function of  $E_T$  for the first pseudorapidity interval. [121]

### 6.4.3 Muons

Due to its position on the Bethe-Bloch curve a muon usually leaves only a small fraction of its energy in the calorimeters and reaches the muon system. For the reconstruction of baseline muon candidates both information from the muon spectrometer and the inner tracking detectors are combined as described in [124–126].

The first step is independent reconstruction of tracks in the ID as described in § 6.1 and in the MS. In the MS first track segments are reconstructed from hit patterns with algorithms optimal for each MS subdetector. The track segments are then used as seed for a sequential track finding starting from the middle layer where the most trigger hits are available moving outwards to both sides. For a valid muon track candidate at least two (one high quality) matching segments are required (in the barrel-endcap). The following combined ID-MS reconstruction includes four different types of muons:

- Combined (CB) muons - the muon is reconstructed using both tracks from the ID and the MS in a global fit. Usually this reconstruction uses an outside-in pattern recognition - starting from MS tracks that are extrapolated to the ID and matched to a track there. Inside-out is used as well for completeness.
- Segment-tagged (ST) muons - the muon is reconstructed using an ID track extrapolated to the MS system. If the ID track can be matched to at least one local track segment either in the MDT or CSC chambers it is treated as muon candidate. This type is mostly used for low  $p_T$  muons that only manage to traverse one layer of the MS chambers or traverse a region with low MS acceptance.
- Calorimeter-tagged (CT) muons - the reconstruction of the muon uses an ID track match to a calorimeter cluster that relates to a minimal ionizing particle. This type is only used for muons that hit the region of the MS where there is considerable dead material for cabling and other detector support. It is therefore optimised for the affected region at  $|\eta| < 0.1$  and a muon  $p_T$  between 15 GeV and 100 GeV to intercept the purity loss.
- Extrapolated (ME) muons - the reconstruction of the muon solely uses the MS track, in addition the extrapolation of the track should loosely be compatible with the interaction point. The extrapolation takes into account the estimated energy loss in the calorimeters. This stand-alone method is utilized to extend the MS reach to the region of  $2.5 < |\eta| < 2.7$  without ID coverage.

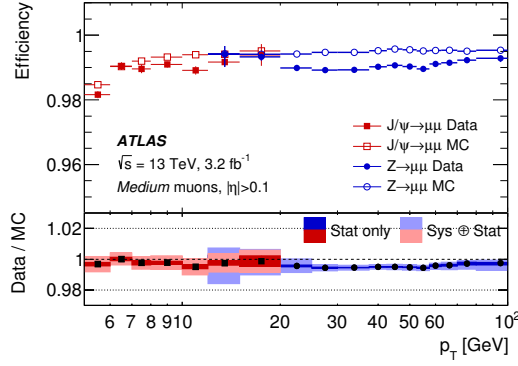
In Run II a reconstruction algorithm is used that combines a statistical combination with a global re-fit of the ID and MS tracks. The algorithm is optimised for Run II conditions and was developed from the two distinct algorithms used in Run I [125].

As seen in the previous sections a dedicated muon identification distinguishes prompt muons from the hard-scatter interaction from background muons from pion and kaon decays. The identification relies on hit and track quality requirements in the ID and MS, the ratio of the charge and momentum  $q/p$  of the muons in the ID and MS and the difference in the measured transverse  $p_T$  in the ID and MS divided by the  $p_T$  of the combined track. Four different identification operation points are defined: 'Loose', 'Medium', 'Tight' and 'high- $p_T$ ' with 'Medium' the default for Run II. The different identifications target different analysis needs. 'Loose' is targeting Higgs boson decays to four leptons by using all muon types, it maximizes the reconstruction efficiency. The default 'Medium' only includes CB and ME muons, it minimizes the systematic uncertainties from muon reconstruction. 'Tight' is designed to provide

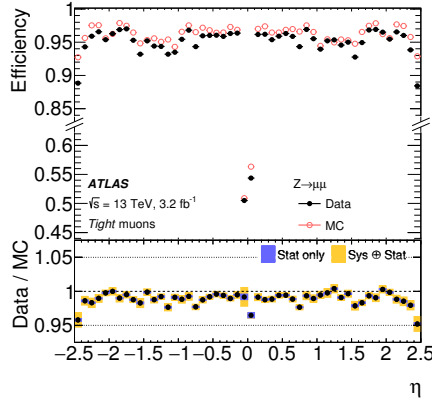
the only high-purity muon on the cost of the reconstruction efficiency, only CB muons are used. The muon-only identification of 'high- $p_T$ ' targets high-mass  $Z'$  and  $W'$  resonances, it requires a CB muon with a  $p_T > 100$  GeV and additional quality requirements that improve the  $p_T$  resolution for high- $p_T$  muons.

The reconstruction efficiency is measured by using the tag-and-probe method in  $Z \rightarrow \mu\mu$  and  $J/\Psi \rightarrow \mu\mu$  samples. Fig. 6.11 shows the resulting efficiencies in the muon  $p_T$  and  $\eta$ , as MC and data do not agree scale factors in  $\eta$  and  $p_T$  are derived to adjust the MC samples. The reconstruction efficiency is above 99% except for very low  $p_T$  muons.

$Z \rightarrow \mu\mu$  and  $J/\Psi \rightarrow \mu\mu$  samples are used as well to study the muon momentum and momentum resolution and to derive correction factors for simulation.



(a)



(b)

**Figure 6.11:** Muon reconstruction efficiency in (a) muon  $p_T$  and in (b)  $\eta$  in 2015 data [124].



## CHAPTER 7

### The MSSM-15 in the light of Run I data

THE data collected during Run I of the LHC resulted in a large amount of new results. Though there was no discovery of any BSM particles the new constraints can be used to analyze the phase space of the phenomenological Minimal Supersymmetric Standard Model (pMSSM). By providing a best-fit point for the model parameters it indicates where to probe the vast phase space next. This chapter describes the use of profile likelihood maps from global fits in the pMSSM to derive preferred values for the masses of supersymmetric particles and dark matter.

Searches for supersymmetry not only strongly restrain the masses of light SUSY particles but also limit a region of phase space that cannot be probed by direct dark matter detection experiments. Including all these experimental constraints in the global fits of the pMSSM gives a best-fit point that roughly corresponds to a squark mass of 2.3 TeV, a gluino mass of 2.1 TeV and a 130 GeV neutralino with a spin-independent scattering cross-section of  $2.4 \times 10^{-10}$  pb. The derived best-fit point is in a range that will be probed with the next generation of multi-ton direct detection experiments and also with the LHC at center-of-mass energy  $\sqrt{s} = 13$  TeV. This study has been jointly conducted with C. Stenge, G. Bertone, G.-J. Besjes, S. Caron, R. Ruiz de Austri and R. Trotta. The complete study is described in [127] whereas this chapter will focus on the implementation and validation of the implemented ATLAS searches. The personal contribution to this work consists of setting up the simulation chain to emulate the ATLAS detector, which includes event simulation, cross section calculations, detector simulation and event reconstruction. Also part of the personal contribution is the implementation of the ATLAS searches included in the paper and the validation of this simulation setup by studying the resulting signal efficiencies compared to ATLAS. This simulation setup was also used for contributions to two other papers.

At the time of the study only 7 TeV results were publicly available. The ATLAS searches for 0-leptons [128] and 3-leptons [129] have therefore been implemented using  $4.7 \text{ fb}^{-1}$  of  $\sqrt{s} = 7$  TeV data.

#### 7.1 Approach to the MSSM-15

In addition to the 19 SM parameters there are 105 unknown Lagrangian parameters, including complex phases, in the minimal supersymmetric standard model. This huge number of free parameters poses a large obstacle to study the MSSM phenomenology. One approach to

significantly reduce the number of parameters is to apply a concrete SUSY breaking mechanism. An example is the constrained MSSM (cMSSM) with universal scalar masses, gaugino masses and the trilinear couplings at a high scale. The cMSSM has been largely used for early searches at the LHC for bench mark models for signal sensitivity optimisation. But it is now severely constrained by the results of SUSY searches with 7 TeV LHC data as well as by direct dark matter searches, such as the XENON100 [57] and LUX [56] experiments. The direct dark matter searches increasingly limit the only region not in conflict with the naturalness of the electroweak breaking due to ever larger SUSY breaking parameters.

To completely avoid the question of natural breaking parameters another approach reduces the MSSM parameters by applying phenomenological constraints, leaving 22 parameters of the phenomenological MSSM (pMSSM) [130]. These 22 parameters include 10 sfermion masses  $m_f^1$ , 3 gaugino masses  $M_{1,2,3}$ , the ratio of the Higgs vacuum expectation values  $\tan\beta$ , the Higgsino mixing parameter  $\mu$ , the pseudoscalar Higgs boson mass  $m_A$ , 3 trilinear coupling terms for the first and second generation  $A_u, A_d, A_e$  and 3 trilinear coupling terms for the third generation sfermions  $A_b, A_t, A_\tau$ . The pMSSM has been studied in the past by either employing random scans [43, 131, 132] or Bayesian methods [133–136]. Random scans appear uniformly distributed in one- and two-dimensional projections. But they have the limitation that for large-dimensional parameter spaces they are highly concentrated in a thin shell of the hypersphere inscribed in the scan box and can thus only explore a tiny fraction of the pMSSM. The Bayesian approach is much more efficient, but the prior dependence of the posterior distribution can be very strong, especially for high-dimensional models such as the pMSSM with a large number of effectively unconstrained parameters.

Here a Bayesian approach is used with a full likelihood function and an algorithm that generates samples from the posterior distribution. Profile likelihood maps are then derived from the results which are in principal independent of the prior, therefore making the approach more statistically robust. The model under study is the MSSM-15, a simplified version of the pMSSM with only 15 free parameters. The 22 free parameters of the pMSSM are further reduced in the MSSM-15 by including the following assumptions: the neutralino is the LSP, the first two generations of sfermions are degenerated, the masses of the right- and left-handed squarks are equal and the bottom and tau trilinear couplings are unified at the GUT scale,  $A_0 \equiv A_b = A_\tau$ . These assumptions retain most relevant phenomenological aspects of the pMSSM in terms of collider and dark matter searches.

All of the input parameters are defined at the SUSY scale  $\sqrt{m_{\tilde{t}_1} m_{\tilde{t}_2}}$ , with the exception of  $A_0$ , which is defined at  $10^{16}$  GeV and run to the SUSY scale using the renormalization group equations. The full list of the parameters and their priors is given in table 7.1.

---

<sup>1</sup>The sfermion parameters are  $\tilde{Q}_L, \tilde{Q}_3, \tilde{L}_1, \tilde{L}_3, \tilde{u}_1, \tilde{d}_1, \tilde{u}_3, \tilde{d}_3, \tilde{e}_1$  and  $\tilde{e}_3$ .

MSSM-15 parameters and priors			
Flat priors		Log priors	
$M_1$ [TeV]	(-5, 5)	$\text{sgn}(M_1) \log  M_1 /\text{GeV}$	(-3.7, 3.7)
$M_2$ [TeV]	(0.1, 5)	$\log M_2/\text{GeV}$	(2, 3.7)
$M_3$ [TeV]	(-5, 5)	$\text{sgn}(M_3) \log  M_3 /\text{GeV}$	(-3.7, 3.7)
$m_L$ [TeV]	(0.1, 10)	$\log m_L/\text{GeV}$	(2, 4)
$m_{L_3}$ [TeV]	(0.1, 10)	$\log m_{L_3}/\text{GeV}$	(2, 4)
$m_{E_3}$ [TeV]	(0.1, 10)	$\log m_{E_3}/\text{GeV}$	(2, 4)
$m_Q$ [TeV]	(0.1, 10)	$\log m_Q/\text{GeV}$	(2, 4)
$m_{Q_3}$ [TeV]	(0.1, 10)	$\log m_{Q_3}/\text{GeV}$	(2, 4)
$m_{U_3}$ [TeV]	(0.1, 10)	$\log m_{U_3}/\text{GeV}$	(2, 4)
$m_{D_3}$ [TeV]	(0.1, 10)	$\log m_{D_3}/\text{GeV}$	(2, 4)
$A_t$ [TeV]	(-10, 10)	$\text{sgn}(A_t) \log  A_t /\text{GeV}$	(-4, 4)
$A_0$ [TeV]	(-10, 10)	$\text{sgn}(A_0) \log  A_0 /\text{GeV}$	(-4, 4)
$\mu$ [TeV]	(-5, 5)	$\text{sgn}(\mu) \log  \mu /\text{GeV}$	(-3.7, 3.7)
$m_A$ [TeV]	(0.01, 5)	$\log m_A/\text{GeV}$	(1, 3.7)
$\tan \beta$	(2, 62)	$\tan \beta$	(2, 62)
$M_t$ [GeV]	(170.6, 175.8)	$M_t$ [GeV]	(170.6, 175.8)

**Table 7.1:** pMSSM parameters and top mass value used for this study and the prior range for the two prior choices adopted in the scans. Flat priors are uniform on the parameter itself (within the ranges indicated), while log priors are uniform in the log of the parameter (within the ranges indicated) except  $\tan \beta$  which is uniform on the parameter itself.

## 7.2 Scanning algorithm

The Bayesian approach is used to sample the MSSM-15 parameter space, in a next step profile likelihood maps are produced from the resulting posterior samples. Without the profile likelihood maps the large dimensionality of the MSSM-15 and the relatively weak constraints imposed by experimental data would lead to a posterior distribution impacted by severe prior-dependent volume effects. These would make the interpretation of the Bayesian posterior problematic.

So only the profile likelihood (PL) for one or two parameters together is used. The profile likelihood is obtained by maximizing the likelihood function over the remaining parameters. For example, for a single parameter of interest  $\theta_i$  the other parameters  $\Psi = \{\theta_1, \dots, \theta_{i-1}, \theta_{i+1}, \dots, \theta_n\}$  are eliminated from the one-dimensional profile likelihood by maximizing over them:

$$\mathcal{L}(\theta_i) = \max_{\Psi} \mathcal{L}(\theta_i, \Psi) = \mathcal{L}(\theta_i, \hat{\Psi}), \quad (7.1)$$

where  $\mathcal{L}(\theta_i, \Psi)$  is the likelihood function. The samples of the MSSM-15 parameter space are distributed according to the posterior pdf, their density in producing profile likelihood maps is overcome by maximizing over the hidden variables. Confidence intervals for the resulting maps are derived from a profile likelihood ratio

$$\lambda(\theta_i) = \frac{\mathcal{L}(\theta_i, \hat{\Psi})}{\mathcal{L}(\hat{\theta}_i, \hat{\Psi})} \quad (7.2)$$

as test statistics. Here  $\hat{\Psi}$  is the conditional maximum likelihood estimate (MLE) of  $\Psi$  with  $\theta_i$  fixed and  $\hat{\theta}_i, \hat{\Psi}$  are the unconditional MLEs. Values of the  $\Delta\chi^2 = -2\ln \lambda(\theta_i)$  corresponding



to 68%, 95% and 99% confidence intervals are obtained from Wilks' theorem [137].

In the described approach, the prior becomes a means of concentrating the scan in certain regions of parameter space. Two different sets of priors are used: a set of flat priors with a uniform distribution for all model parameters and a set of log priors with a logarithmic distribution for all parameters except  $\tan\beta$  which distribution remains uniform. The objective of choosing two different priors is to detect any bias introduced by how the parameter space points are chosen. Flat priors are biased towards large values of the parameters whereas log priors are biased towards low values. The results of the scans are merged afterwards to assure a reliable mapping of the profile likelihood function and thorough scanning of the entire parameter space. The prior ranges are given in table 7.1.

Several instances of MultiNest v2.18 [138, 139] scans are run to compare the different resulting best-fit point and profile likelihood function in order to verify the reliable exploration of the MSSM-15 parameter space and the robustness of our profile likelihood results.

### 7.3 Experimental constraints

The experimental constraints are implemented with a joint likelihood function, whose logarithm takes the following form:

$$\ln \mathcal{L}_{\text{joint}} = \ln \mathcal{L}_{\text{EW}} + \ln \mathcal{L}_{\text{B(D)}} + \ln \mathcal{L}_{g-2} + \ln \mathcal{L}_{\Omega_\chi h^2} + \ln \mathcal{L}_{\text{DD}} + \ln \mathcal{L}_{\text{Higgs}} + \ln \mathcal{L}_{\text{SUSY}}, \quad (7.3)$$

where  $\mathcal{L}_{\text{EW}}$  represents electroweak precision observables,  $\mathcal{L}_{\text{B(D)}}$  B and D physics constraints,  $\mathcal{L}_{g-2}$  measurements of the anomalous magnetic moment of the muon,  $\mathcal{L}_{\Omega_\chi h^2}$  measurements of the cosmological dark matter relic density,  $\mathcal{L}_{\text{DD}}$  direct dark matter detection constraints,  $\mathcal{L}_{\text{Higgs}}$  LHC measurements of the properties of the Higgs boson and  $\mathcal{L}_{\text{SUSY}}$  ATLAS SUSY searches.

Electroweak constraints are taken from the Z-pole measurements at LEP II [140] and include the Z width and the hadronic pole cross section. Not included are constraints from asymmetry parameters as they are found to give a negligible contribution. The B and D physics constraints are taken from the Heavy Flavour Averaging Group including several decay branching fractions, oscillation frequencies and several precision measurements [141]. The constraint on the dark matter relic abundance comes from the Planck measurements [142]. XENON100 provides constraints for direct dark matter detection [57], more recent results from LUX were not included but their impact is expected to be small in this context. To include the XENON100 limits an approximate likelihood function is used.

The results are both shown with and without the constraints from the measured anomalous magnetic momentum of the muon included to evaluate their strong dependence on it. Constraints from the Higgs mass are implemented via a weighted average of ATLAS [143] and CMS [144] measurements. In addition signal strengths for various decay channels from CMS are also included [145–149].

The SUSY searches constraints come from bounds on SUSY masses from LEP II and Tevatron applied via the likelihood and from LHC searches looking for 0-lepton and multi-jets with

missing transverse energy and 3-leptons with missing transverse energy in the ATLAS experiment. These two analyses were chosen to represent the ATLAS SUSY searches covering both direct production of squarks/gluinos and charginos/neutralinos in hadronic and leptonic decay channels with large discovery potential. The ATLAS searches were both conducted with a total integrated luminosity of  $4.7 \text{ fb}^{-1}$  of data at  $\sqrt{s}$  TeV [128, 129]. The details about the likelihood construction and validation of the implementation are given in the next section. All implemented constraints and their values can be found in table 7.2.

	Observable $\mu$	Mean value $\sigma$ (exper.)	Standard deviation $\tau$ (theor.)		Ref.
$W$ mass	$M_W$ [GeV]	80.385	0.015	0.01	[140]
eff. leptonic el.w. mixing angle	$\sin^2 \theta_{\text{eff}}$	0.23153	0.00016	0.00010	[140]
tot. width $Z \Gamma_Z$ [GeV]		2.4952	0.0023	0.001	[140]
had. pole cross sect.	$\sigma_{\text{had}}^0$ [nb]	41.540	0.037	-	[140]
leptonic decay width ratio	$R_l^0$	20.767	0.025	-	[140]
bottom decay width ratio	$R_b^0$	0.21629	0.00066	-	[140]
charm decay width ratio	$R_c^0$	0.1721	0.003	-	[140]
forward-backward asymmetry par.	$\# A_{FB}^{0,l}$	0.0171	0.001	-	[140]
""	$\# A_{FB}^{0,b}$	0.0992	0.0016	-	[140]
""	$\# A_{FB}^{0,c}$	0.0707	0.0035	-	[140]
asymmetry par.	$\# A_l(SLD)$	0.1513	0.0021	-	[140]
""	$\# A_b$	0.923	0.02	-	[140]
""	$\# A_c$	0.670	0.027	-	[140]
discrepancy measurement to SM	$\delta a_\mu^{\text{SUSY}} \times 10^{10}$	28.7	8.0	2.0	[150]
decay branching fract.	$BR(\bar{B} \rightarrow X_s \gamma) \times 10^4$	3.55	0.26	0.30	[141]
ratio meas. oscill. freq. to SM	$R_{\Delta M B_s}$	1.04	0.11	-	[151, 152]
ratio meas. value to SM	$\frac{BR(\bar{B}_u \rightarrow \tau \nu)}{BR(\bar{B}_u \rightarrow \tau \nu)_{SM}}$	1.63	0.54	-	[141]
isospin asym. $B^0$ to $B^+$ decay width	$\Delta_{0-} \times 10^2$	3.1	2.3	1.75	[153–155]
ratio meas. value to SM	$\# \frac{BR(B \rightarrow D \tau \nu)}{BR(B \rightarrow D e \nu)} \times 10^2$	41.6	12.8	3.5	[156]
ratio leptonic/semi-lept. K decays	$\# R_{l23}$	0.999	0.007	-	[157]
integr. forw.-backw. asymmetry	$A_{FB}(B \rightarrow K^* \mu^+ \mu^-)$	-0.18	0.063	0.05	[158]
decay branching fract.	$BR(D_s \rightarrow \tau \nu) \times 10^2$	5.44	0.22	0.1	[141]
""	$\# BR(D_s \rightarrow \mu \nu) \times 10^3$	5.54	0.24	0.2	[141]
""	$\# BR(D \rightarrow \mu \nu) \times 10^4$	3.82	0.33	0.2	[141]
""	$BR(\bar{B}_s \rightarrow \mu^+ \mu^-) \times 10^9$	3.2	1.5	0.38	[159]
constr. dark matter relic abund.	$\Omega_\chi h^2$	0.1186	0.0031	0.012	[142]
Higgs mass	$m_h$ [GeV]	125.66	0.41	2.0	[143, 144]
Higgs signal strength in decay channel	$\dagger \mu_{\gamma\gamma}$	0.78	0.27	15%	[145]
""	$\dagger \mu_{W^+ W^-}$	0.76	0.21	15%	[146]
""	$\dagger \mu_{ZZ}$	0.91	0.27	15%	[147]
""	$\dagger \mu_{b\bar{b}}$	1.3	0.65	15%	[148]
""	$\dagger \mu_{\tau^+ \tau^-}$	1.1	0.4	15%	[149]
		Limit (95% CL)	$\tau$ (theor.)	Ref.	
Sparticle masses		LEP, Tevatron. As in Table 4 of Ref. [160].		[160]	
$\dagger$ 0-lepton SUSY search		ATLAS, $\sqrt{s} = 7$ TeV, $4.7 \text{ fb}^{-1}$		[128]	
$\dagger$ 3-lepton SUSY search		ATLAS, $\sqrt{s} = 7$ TeV, $4.7 \text{ fb}^{-1}$		[129]	
WIMP mass to spin-indep. cross sec.	$m_\chi - \sigma_{\tilde{\chi}_1^0 p}^{\text{SI}}$	XENON100 2012 limits ( $224.6 \times 34 \text{ kg days}$ )		[57]	
WIMP mass to spin-dep. cross sec.	$m_\chi - \sigma_{\tilde{\chi}_1^0 p}^{\text{SD}}$	XENON100 2012 limits ( $224.6 \times 34 \text{ kg days}$ )		[57]	

**Table 7.2:** Summary of experimental constraints used in the likelihood. Upper part: measured observables, modelled with a Gaussian likelihood of mean  $\mu$ , and standard deviation  $(\sigma^2 + \tau^2)^{1/2}$ , where  $\sigma$  is the experimental and  $\tau$  the theoretical uncertainty. Lower part: observables for which only limits currently exist. See text for further information on the explicit form of the likelihood function. Experimental constraints tagged with  $\#$  have been found to contribute an approximately constant value to the log-likelihood and hence have been omitted. Observables tagged with  $\dagger$  are applied via post-processing of the samples.

## 7.4 Implementation of the ATLAS search constraints

To implement the constraints from the ATLAS SUSY searches an approximate approach is used.

The ATLAS 0-lepton analysis [128] has 6 channels which are used to construct between one

and three signal regions with “tight”, “medium” and/or “loose”  $m_{\text{eff}}$ (incl.) selections, giving in total 11 signal regions. The different channels are targeting different SUSY particle production mechanisms. Signal region A is designed for squark-squark production, signal region A’ especially for models with low mass splittings. Signal region B is designed for squark-gluino production and signal regions C-E are constructed for gluino-gluino production with higher jet multiplicities than in the squark-squark case.

The selection criteria for each signal region are shown in table 7.3. Events containing leptons are excluded, hence the name ‘zero lepton’. The selection variables used are the minimum required number of jets and their respective transverse momentum, the missing transverse energy  $E_T^{\text{miss}}$ , the effective mass  $m_{\text{eff}}$  calculated as the scalar sum of all transverse jet momenta larger than 40 GeV and the missing transverse energy, the ratio of  $E_T^{\text{miss}}$  to  $m_{\text{eff}}$  (where  $m_{\text{eff}}$  only includes the required number of jets), the minimum angle between *only the required leading jets* and the missing energy vector  $\Delta\phi(\text{jet}_i, E_T^{\text{miss}})_{\text{min}}$ . For the signal region C-E an additional criterion is applied, a cut on  $\Delta\phi(\text{jet}_i, E_T^{\text{miss}})_{\text{min}}$  including *all jets* with transverse momenta larger than 40 GeV.

The ATLAS 3-lepton analysis [129] consists of 3 signal regions. Signal regions 1a and 1b include a Z-veto, signal region 2 is designed for a on-shell Z boson. All signal regions require exactly three leptons, two of them form the same flavour opposite sign (SFOS) lepton pair. The selection criteria are shown in Table 7.4. The transverse mass  $m_T$  is defined as

$$m_T = \sqrt{2p_T^X E_T^{\text{miss}} \{1 - \cos[\Delta\phi(\vec{p}_T^{\text{miss}}, X)]\}} \quad (7.4)$$

with X the respective particle. For the 3-lepton analysis  $m_T$  is calculated using the missing transverse energy and the third lepton.

### 7.4.1 The likelihood function

The likelihood for each bin in a signal region  $i$  ( $i = 1, \dots, 14$ ) is given by

$$\mathcal{L}_i(n_i|s, b, \theta) = \text{Pois}(n_i|\lambda_s(s, b, \theta)) \times \mathcal{L}_C(\theta), \quad (7.5)$$

where the first factor reflects the Poisson probability of observing a number of events  $n$  in the signal region given the signal (background) expected value  $s$  ( $b$ ) [127]. The Poisson expectation value  $\lambda_s$  also depends on the nuisance parameters  $\theta$  that parameterize systematic uncertainties, such as luminosity or jet energy scale. Those uncertainties are constrained via the likelihood term  $\mathcal{L}_C(\theta)$ , which is taken to be a multivariate Gaussian distribution around the nominal value  $\theta = 0$ , with diagonal covariance matrix entries given by the quoted nominal uncertainties in each of the systematic factors. The Poisson expectation value is written as

$$\lambda_s = s(1 + \Delta_s \theta_s) + b(1 + \Delta_b \theta_b), \quad (7.6)$$

where  $s$  and  $b$  are the nominal values of the signal and background,  $\Delta_s$  and  $\Delta_b$  are their relative uncertainties and  $\theta_s$  and  $\theta_b$  are nuisance parameters, so that  $\theta = \{\theta_s, \theta_b\}$ .

Signal region:	A	A'	B	C	D	E
$E_T^{\text{miss}}$ [GeV]>				160		
1 <sup>st</sup> jet $p_T$ [GeV]>				130		
2 <sup>nd</sup> jet $p_T$ [GeV]>				60		
3 <sup>rd</sup> jet $p_T$ [GeV]>	-	-	60	60	60	60
4 <sup>th</sup> jet $p_T$ [GeV]>	-	-	-	60	60	60
5 <sup>th</sup> jet $p_T$ [GeV]>	-	-	-	-	40	40
6 <sup>th</sup> jet $p_T$ [GeV]>	-	-	-	-	-	40
$\Delta\phi(\text{jet}_i, E_T^{\text{miss}})_{\min} >$	0.4 (i=1,2,(3))			0.4 (i=1,2,3)		
	-	-	-	0.2 (for all jets $p_T > 40$ GeV)		
$E_T^{\text{miss}}/m_{\text{eff}}(\text{Nj}) >$	0.3 (2j)	0.4 (2j)	0.25 (3j)	0.25 (4j)	0.2 (5j)	0.15 (6j)
$m_{\text{eff}}(\text{incl.})$ [TeV] >	1.9/1.4/-	-/1.2/-	1.9/-/-	1.5/1.2/0.9	1.5/-/-	1.4/1.2/0.9

**Table 7.3:** Requirements for the inclusive channels A-E for the ATLAS 0-lepton analysis with an integrated luminosity of  $4.7 \text{ fb}^{-1}$ . For  $m_{\text{eff}}(\text{incl.})$  the limits are given in the order *tight/medium/loose*. The jet  $p_T$  requirements are given for the minimum required number of jets (from [128]).

Signal region:	1a	1b	2
lepton charge, flavour	at least one SFOS pair with $m_{ll} > 20$ GeV		
$E_T^{\text{miss}}$ [GeV]>	75		
$m_{\text{SFOS}}$ [GeV]	< 81.2 or > 101.2		81.2 – 101.2
No. of b-jets	0	0	any
$m_T$ [GeV]	any	> 90	> 90
$p_T$ of all leptons [GeV]>	10	30	10

**Table 7.4:** Requirements for the signal regions 1a, 1b and 2 for the 3-lepton ATLAS analysis with an integrated luminosity of  $4.7 \text{ fb}^{-1}$ . In addition, the number of reconstructed leptons has to be three (from [129]).

The overall uncertainty of the background expectation in the signal region is given by the public ATLAS results. The systematic uncertainty for the signal is further split in uncertainties of the integrated luminosity (which is negligible), the SUSY cross section and the acceptance and efficiency of the detector. The cross-section uncertainty is computed with the NLLFAST2 package [161–165]. The relative uncertainty of the efficiency is obtained via a comparison of the simulation setup signal selection efficiency to the public efficiency maps of the ATLAS analyses also described in the next section.

#### 7.4.2 Simulation of signal efficiency

To study the detector acceptance and efficiency the chain of particle production, detector response and analysis is emulated with the below described setup.

For the same SUSY model points as used in the ATLAS analyses the SUSY kinematical distributions of ten thousand events by Pythia6.4 [166] with the ATLAS MC09 tune [167] are simulated. The parton distribution functions are obtained from the CTEQ6L1 set [168]. The SUSY cross-sections for gluino and squarks production are normalized by NLO K-factors in the strong coupling constant, including the resummation of soft gluon emission at next-to-leading-logarithmic (NLO+NLL) accuracy with NLLFAST2 [161–165]. For the electroweakino production PROSPINO [161, 169] was used which provides a NLO calculation.

For the detector response DELPHES3 [170] is used, a fast detector simulation. DELPHES3 is suitable for multipurpose detectors with the features of a tracking system in a magnetic field, calorimeters and muon system. Other features of the detector response as multiple scattering, photon conversion and bremsstrahlung are more complicated and omitted in favor of computing speed. In addition DELPHES3 assumes that the detector geometry is symmetric, dead material is therefore not taken into account. These assumptions are acceptable for a fast simulation developed for phenomenological studies. The main focus of a fast simulation is a good estimation of the event signature that can be done without large grid computing infrastructure. The precision required for e.g. background modelling is not necessary. Phenomenological studies usually have a high number of both model points and events to compute which make a full simulation not only unnecessary but also infeasible. DELPHES3 is adapted via a detector card that defines several characteristic aspects of the detector and tunes the simulation to the ATLAS detector. Characteristic aspects that can be changed are the coverage of the different sub-detectors and the number and segmentation of the calorimeter towers, energy resolutions for several particles, muon energy smearing, tracking efficiencies as well as parameters of the object reconstructions. An important difference in the object reconstruction is that DELPHES3 relies on the particle identification of the event generator for leptons and photons. There are consequently no fake candidates available for these particles.

For the validation of the event and detector simulations two different ATLAS analyses were implemented - the aforementioned 0- and 3-lepton searches. For both analyses the resulting event selection efficiencies of the simulation setup were cross-checked against the corre-

sponding ATLAS acceptance times efficiency values.

### 7.4.3 Validation of efficiencies

To validate the simulation setup the relative efficiency difference

$$\frac{\Delta\epsilon}{\epsilon} = \frac{(A\epsilon)_{\text{ATLAS}} - (A\epsilon)_{\text{Sim}}}{(A\epsilon)_{\text{ATLAS}}} \quad (7.7)$$

between the simulation setup and the official ATLAS analyses was determined. Here  $(A\epsilon)_{\text{ATLAS}}$  is the acceptance times efficiency of the ATLAS analyses. A negative value of  $\frac{\Delta\epsilon}{\epsilon}$  corresponds to an overestimation of the efficiency by the simulation, a positive value to an underestimation.

For the validation the default ATLAS detector card supplied with DELPHES 3.1 was modified. For both analyses the value of the jet cone parameter  $R$  of the anti- $k_t$  jet algorithm was set to 0.4. For the 3-lepton analysis the lepton efficiencies were increased and the lepton isolation value set to 0.7.

For the ATLAS 0-lepton analysis the validation was done in a cMSSM-grid with  $\tan\beta = 10$ , while  $m_0$  runs from 100 GeV to 4180 GeV,  $m_{1,2}$  from 60 GeV to 750 GeV. The comparison was done for each signal region individually. An example of the results is shown in Figure 7.1, the complete set of results can be found in Appendix 7.A. The minimum value was fixed for all plots due to some large deviations in regions with efficiencies close to zero, as indicated by the color scale. Grid points with values below the minimum are shown in white. For the large areas with value zero in the upper and lower right corner no data points were given by the ATLAS analyses.

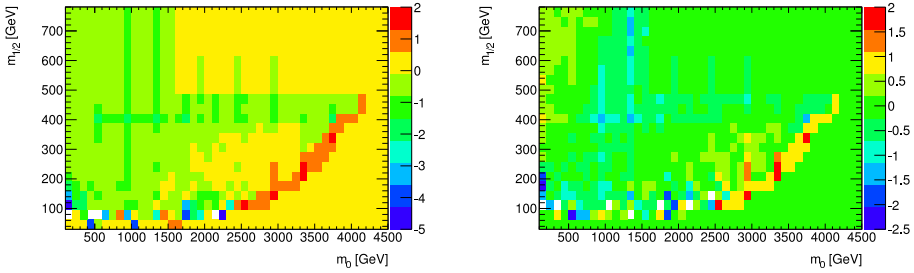


**Figure 7.1:**  $\frac{\Delta\epsilon}{\epsilon}$  of the ATLAS and simulation setups for signal region A *medium* and D of the 0-lepton analysis.

The efficiency of our setup is found to be in agreement with the ATLAS efficiency on the level of 10 – 30% for the 2-, 3- and 4-jet signal regions and for masses of squarks and gluinos around the respective ATLAS limits. These limits are ranging for  $m_{1/2}$  from 200-650 GeV and go up to intermediate  $m_0$  of 1500 GeV. At  $m_{1/2} < 200$  GeV larger deviations occur. Here both the statistical uncertainty of the ATLAS and DELPHES efficiencies are large and the selection efficiencies are small. The signal regions are not intended for SUSY signals at  $m_{1/2} < 200$

GeV and large  $m_0$  and therefore do not contribute to the search for such SUSY signals. The ATLAS analysis always selects the signal region with the largest exclusion potential for each cMSSM model point.

For signal region D-E, a better agreement is observed at low  $m_{1/2}$  and a slightly worse agreement at  $m_0 > 1000$  GeV and  $m_{1/2} > 400$  GeV. Here the DELPHES setup underestimates the efficiency by up to 50 – 70%. The increased differences at larger jet multiplicities are probably due to the “Jet numerical inversion correction” [118] applied by ATLAS which is not implemented into DELPHES3. This correction is applied individually for each jet and leads to a higher jet  $p_T$  and thus to a higher selection efficiency.

In large regions the setup with DELPHES3 underestimates the ATLAS efficiency. There is only the exception of a small region in the  $m_0$ - $m_{1/2}$ -plane (which is already excluded by LEP data [44, 45]), where greater discrepancies between this setup and ATLAS occur.

For the 3-lepton analysis the validation was done for a simplified model where only the masses of the neutralinos, charginos and sleptons are free parameters and the  $\tilde{\chi}_1^\pm$  and  $\tilde{\chi}_2^0$  decay to W and Z bosons. The employed grid has values of 70 GeV to 350 GeV for  $m_{\tilde{\chi}_1^\pm}$  and 0 GeV to 200 GeV for  $m_{\tilde{\chi}_1^0}$ . The results for SR 1 are presented in Figure 7.2. Points with  $m_{\tilde{\chi}_1^\pm} < 103.5$  GeV are excluded by LEP data, the lower right corner is excluded by the constraint that  $m_{\tilde{\chi}_1^\pm}$  must be larger than  $m_{\tilde{\chi}_1^0}$ .

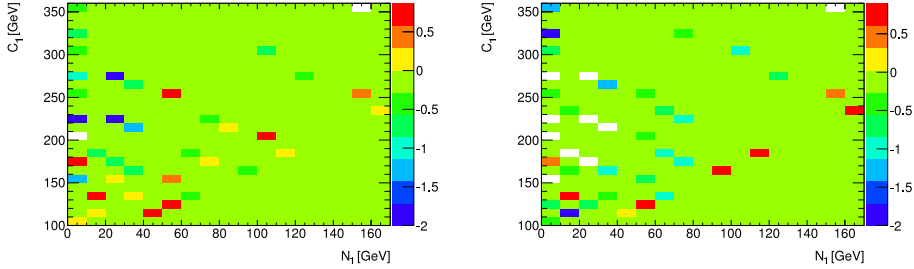


**Figure 7.2:**  $\frac{\Delta\epsilon}{\epsilon}$  of the ATLAS and simulation setups for signal region 1a and 1b of the 3-lepton analysis in the plane of  $N_1 = m_{\tilde{\chi}_1^0}$  and  $C_1 = m_{\tilde{\chi}_1^\pm}$ .

On average the setup is in agreement with the ATLAS efficiency. As for the 0-lepton analysis the ATLAS efficiency in the 3-lepton analysis is rather underestimated. For  $m_{\tilde{\chi}_1^0} < 40$  GeV larger deviations of 50 -70% overestimation occur. Again a region where both the statistical uncertainty of the ATLAS and DELPHES efficiencies are large and the selection efficiencies are small.

As error estimation the mean value of  $\frac{\Delta\epsilon}{\epsilon}$  and its standard deviation were computed for each efficiency bin. Part of the results are presented in Figure 7.3 – 7.4, the complete results can be found in Appendix 7.A. Those values have then been used as estimates for  $\frac{\Delta\epsilon}{\epsilon}$  in the likelihood assuming that the  $\frac{\Delta\epsilon}{\epsilon}$  can be parameterized as a function of the efficiency.

For completeness, the likelihood construction in the cMSSM framework was validated and compared with the results of the ATLAS Collaboration. The  $CL_s$  was computed to estimate



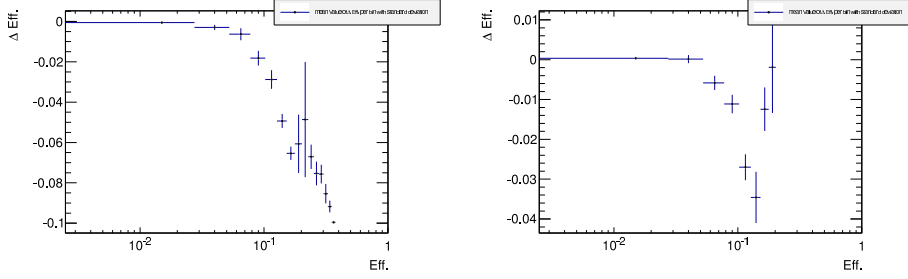


**Figure 7.3:** Mean efficiency value  $\Delta\epsilon$  (denoted as  $\Delta\text{Eff.}$ ) with estimated standard deviation for signal region A *medium* and D of the 0-lepton analysis.

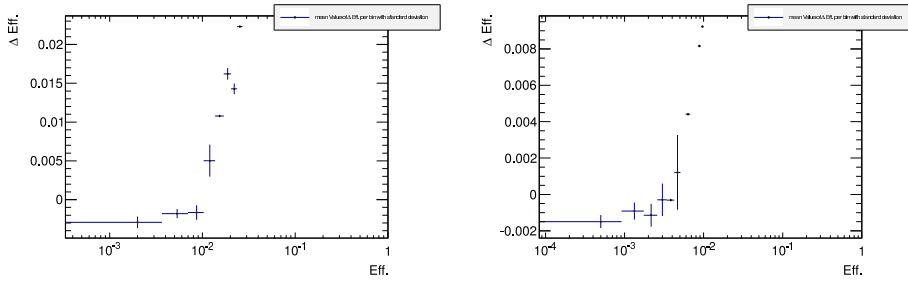


**Figure 7.4:** Mean efficiency value  $\Delta\epsilon$  (denoted as  $\Delta\text{Eff.}$ ) with standard deviation for signal region 1a and 1b of the 3-lepton analysis.

the observed exclusion limits using the prescription outlined in Ref. [171] which uses the concept of Asimov data and Wilk's theorem for its efficient evaluation. The results are shown in Fig. 7.5. The continuous-red line represents our estimated exclusion limits at 95% CL, whereas the region between the dash-dotted gray lines gives the ATLAS Collaboration exclusion limit, accounting for uncertainties in the determination of the SUSY production cross section. The agreement is very satisfactory, indicating that both the signal prediction procedure and the likelihood construction we adopted work remarkably well. Together with the general underestimation of ATLAS efficiencies it is justified to make conclusions based on this setup.

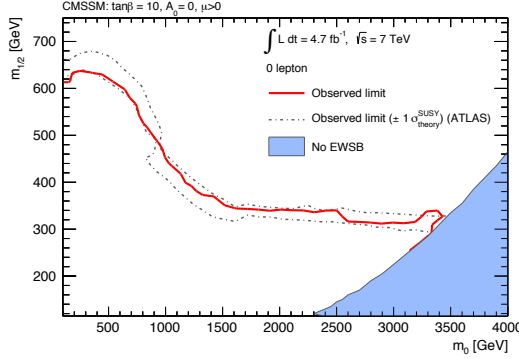


**Figure 7.5:** Shown is the 95% CL observed exclusion limit for the 0-lepton analysis in the cMSSM from our likelihood construction (red line) and the  $CL_s$  method, which is in remarkably good agreement with the ATLAS result [128]. The band limited by the gray dash-dotted lines is the exclusion limit by the ATLAS collaboration, accounting for uncertainties in the SUSY production cross-section.

## 7.5 Results

To derive the best-fit points there are two steps: first the best-fit point is obtained including all experimental constraints except the LHC constraints, the LHC constraints from the SUSY searches and on the Higgs couplings are applied in a second step during the post-processing. The best-fit point is then re-calculated. This procedure allows to determine the impact of the latest LHC results.

The results without the LHC constraints is presented first.

### 7.5.1 Profile likelihood excluding LHC data

The one-dimensional profile likelihoods for several SUSY masses are displayed in Fig. 7.6, the best-fit point is indicated by a cross. The mass of the lightest Higgs boson measured by the LHC can easily be satisfied in the MSSM-15. This is a reflection of the large number of degrees of freedom of the model, which allow to maximize the tree-level contribution to the Higgs mass by pushing  $\tan \beta$  to large values, while at the same time maximizing the leading

1-loop corrections either via heavy stops or maximal stop mixing.

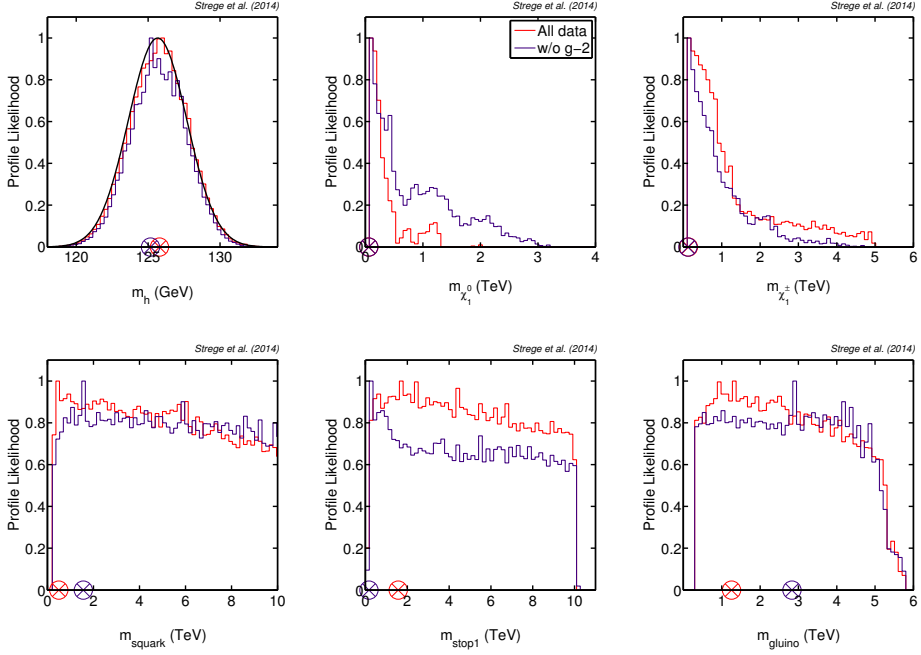


**Figure 7.6:** 1-D profile likelihood global fits results including all data except LHC SUSY searches and Higgs couplings (red) and further excluding the  $g-2$  constraint (purple) for some relevant SUSY quantities. Encircled crosses represent the best-fit points. For quantities constrained in the scan, the likelihood function applied is shown in black. Recall that these analyses does not include null SUSY searches at the LHC (see section 7.5.3).

The LSP neutralino mass is constrained to  $m_{\tilde{\chi}_1^0} < 1.5$  TeV at 99% confidence level for the analysis including all constraints. In contrast, the corresponding profile likelihood for the analysis excluding the  $g-2$  constraint reaches significantly larger masses  $m_{\tilde{\chi}_1^0} \leq 3.0$  TeV. In both cases, the profile likelihood peaks at low values, where the neutralino is bino-like, with an almost identical best fit at  $m_{\tilde{\chi}_1^0} \approx 60$  GeV.

The bump in the neutralino profile likelihood around  $\sim 1$  TeV corresponds to a higgsino-like neutralino (see § 3.5 in [127] for details), and it is more pronounced for the case without  $g-2$ , as expected from the above discussion. The profile likelihood for the analysis excluding the  $g-2$  constraint extends to significantly larger values, showing a small bump at  $m_{\tilde{\chi}_1^0} \sim 2$  TeV that corresponds to a wino-like neutralino.

The profile likelihood for the mass of the lightest chargino stretches to large values, close to the prior boundary around  $\sim 5$  TeV imposed by the prior on the input parameters. Nevertheless, similarly to what was observed for the neutralino mass, small chargino masses are favored. In contrast, the profile likelihood for the average squark mass, the lightest stop mass and the gluino mass are very unconstrained. The shape of the profile likelihood for

these quantities is a direct consequence of the 1D profile likelihood for the corresponding soft masses and  $M_3$ , respectively (see § 3.1.1 in [127]).

### 7.5.2 Dark matter composition

One of the assumptions of the MSSM-15 is that the LSP is the neutralino, it is therefore a prime dark matter candidate. The profile likelihood maps provide the favored neutralino composition in different regions of the MSSM-15 parameter space. The neutralino composition in the plane of neutralino mass vs. spin-independent cross-section is shown in Fig. 7.7, for the analysis including all data (left panel) and when using the Planck relic density constraint as an upper limit (right panel). The neutralino compositions for the analysis excluding the  $g-2$  constraint is qualitatively similar to the case where it is included, hence it is not shown here.

The neutralino is called bino-like if it has a bino mixing fraction of  $b_f > 80\%$ , wino-like

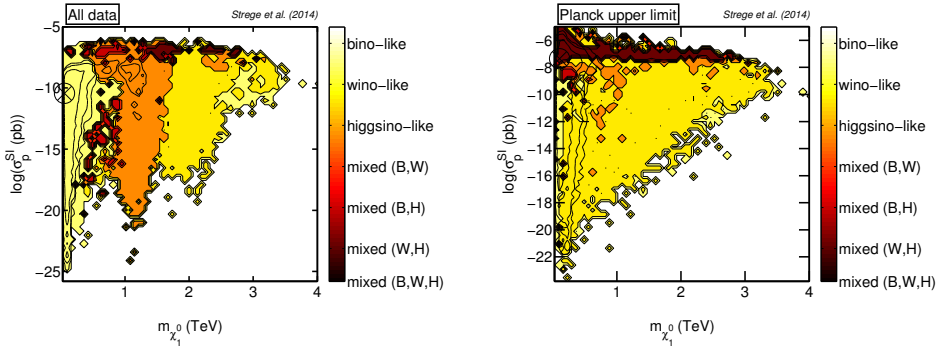


**Figure 7.7:** Composition of the dark matter particle in each bin in the plane of neutralino mass  $m_{\tilde{\chi}_1^0}$  vs. spin-independent cross-section  $\sigma_p^{SI}$  is shown in Fig. 7.7, for the analysis including all data (left) and when using the Planck relic density constraint as an upper limit (right).

for a wino fraction  $w_f > 80\%$  and higgsino-like for a higgsino fraction  $h_f > 80\%$ . A mixed (B,W) neutralino has both a sizeable bino and wino fraction ( $b_f, w_f > 20\%$ ), and similarly for mixed (B,H) and mixed (W,H) neutralinos. Neutralinos that do not fit into any of the above categories are considered mixed (B,W,H) states.

For the analysis including all data (left-hand panel) there are three different dominant dark matter compositions. For low masses,  $m_{\tilde{\chi}_1^0} \lesssim 800$  GeV, the neutralino is bino-like. In this region pole-resonances with Z/h or co-annihilation effects either with light sleptons or higgsinos can provide the right relic density.

In an intermediate mass range of  $0.8 \text{ TeV} \lesssim m_{\tilde{\chi}_1^0} \lesssim 1.6 \text{ TeV}$  the neutralino is higgsino like. For large  $\mu \sim 1 \text{ TeV}$  which leads to  $m_{\tilde{\chi}_1^0} \sim 1 \text{ TeV}$  higgsino like dark matter is favored.

For very large masses  $m_{\tilde{\chi}_1^0} \gtrsim 1.6 \text{ TeV}$  the neutralino becomes predominantly wino-like. To achieve the correct relic density wino-like dark matter requires large wino masses. So a wino-like neutralino is favored at  $m_{\tilde{\chi}_1^0} \gtrsim 2 \text{ TeV}$ .

### 7.5.3 Impact of LHC Higgs properties and ATLAS SUSY searches

The evaluation of the full LHC likelihood is numerically very demanding. The post-processing for all samples is too CPU intensive.

So an intermediate approach is adopted to evaluate the constraining power from LHC searches and Higgs properties. In the so called mini-chains approach, first profile likelihood maps are produced from the full chains for a two-dimensional plane of variables of interest. This leads to approximately  $10^4$  profile likelihood values for each plane. For each of those values, the combined  $\chi^2$  contribution from LHC SUSY searches (0-lepton and 3-lepton) and LHC constraints on the Higgs production cross-sections is computed. The resulting  $\chi^2$  value is added to the combined  $\chi^2$  obtained from the other data.

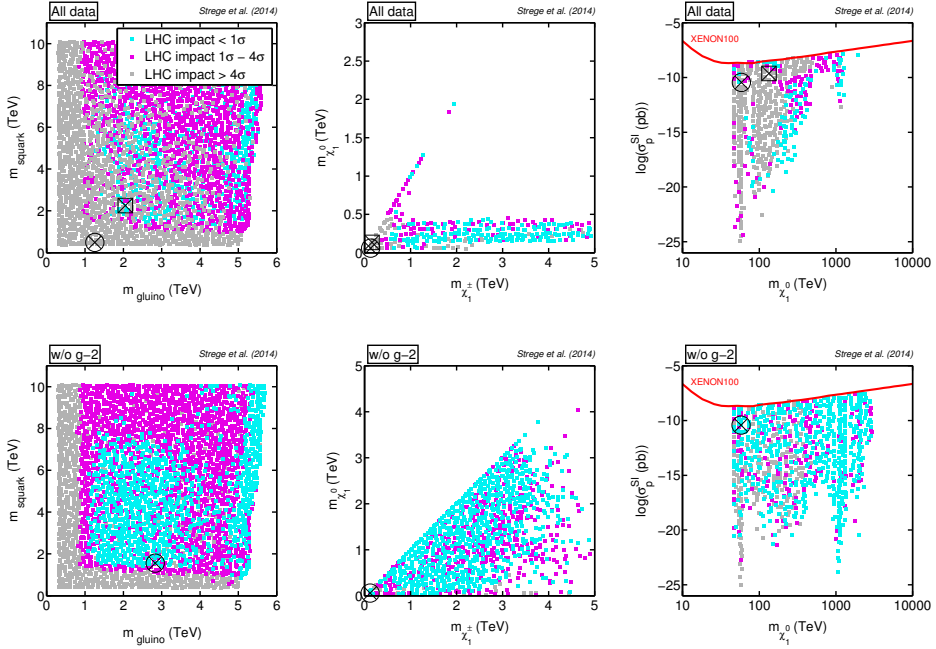
To point out again, this is not a fully consistent statistical approach, and the ensuing maps cannot be interpreted probabilistically as profile likelihood maps (as they full likelihood has not been maximized out in the dimensions not shown). However, it does allow to draw some useful conclusions regarding the impact of the LHC SUSY searches and Higgs properties determination: values that remain viable in the mini-chains would not be ruled out even under a full profile likelihood approach. So this approach gives an indication of the maximal possible constraints coming from the extra LHC data adopted. Furthermore, it allows to investigate whether the best-fit points found with the global fits above remain viable in the light of the LHC data.

Fig. 7.8 shows the LHC impact for both analyses. Bins that are almost unaffected by the LHC constraints (impact  $< 1\sigma$ ) are shown in cyan, bins that are disfavored with a significance  $> 1\sigma$  and  $< 4\sigma$  level are shown in pink, and bins that are ruled out by the LHC (impact  $> 4\sigma$ ) are displayed in grey. Only bins that were included in the 99% CL region before post-processing are shown.

The LHC 0-lepton channel search has a strong impact on the left-hand planes, both for the analysis including and excluding the  $g - 2$  constraint, ruling out gluino and squark masses  $m_{\text{gluino}}, m_{\text{squark}} \lesssim 1$  TeV. Above that, the measurements of the Higgs production cross-sections have a strong impact on the favored regions of the MSSM-15 parameter space. It was verified that in the regions with the largest impact, the Higgs boson decay to  $b\bar{b}$  is very suppressed with respect to the SM prediction and to lesser extend for the  $\tau^+\tau^-$  decay channel. The consequences are too large branching ratios into boson pairs.

The impact of the 3-lepton channel search is rather weak and the 0-lepton channel imposes stronger constraints in the lightest chargino mass vs. lightest neutralino mass plane (central panels).

The impact of the LHC SUSY and Higgs searches in terms of neutralino mass and spin-independent scattering cross-section is shown in the right-hand panels of Fig. 7.8. The main impact of the LHC in this plane is to rule out points at low/intermediate neutralino masses that were previously strongly favored. This is done basically by the 0-lepton channel search which has the biggest impact as mentioned above. Therefore, for small  $m_{\tilde{\chi}_1^0} \lesssim 300$  GeV, the



**Figure 7.8:** Scatter plots from the 2D mini-chains, showing the impact of the LHC (SUSY searches and constraints on the Higgs decay cross-sections) on the chi-square of the best-fit point in each bin. The top (bottom) row shows results for the scans including all data (except the  $g-2$  constraint). The encircled black cross indicates the best-fit point prior to inclusion of the LHC constraints; for the scans including all data, this point is ruled out by the LHC results, hence also the next best-fit point that survives the LHC constraints is shown (cross inscribed in the square). The best-fit point for the analysis excluding  $g-2$  (bottom panels) remains viable after LHC data are included. (Errata: The rightmost plots have a wrong x-axis label, the  $\tilde{\chi}_1^0$  mass is shown in GeV not in TeV.)

LHC is extremely powerful, ruling out cross-sections orders of magnitudes below the reach of future direct detection experiments. For the analysis excluding the  $g - 2$  constraint, a much smaller fraction of points is affected by the LHC, and several points at small  $m_{\tilde{\chi}_1^0}$  are still allowed. This discrepancy is largely a result of the 0-lepton search having less of an impact on the analysis excluding  $g - 2$ , so that low-mass neutralinos are less constrained in this analysis. Note that for  $m_\chi \gtrsim 500$  GeV the MSSM-15 parameter space is largely unaffected by constraints from LHC SUSY searches. The Higgs data interpretation in this plane holds as for the left-hand and central panels in Fig. 7.8.

## 7.6 Conclusions for future searches

The results of a global fit of the MSSM-15 including all available accelerator constraints, constraints from cosmology and also from direct detection experiments have been shown. Here the focus has been on the favored dark matter composition and the impact of the LHC data. The input parameters remain almost unconstrained by current experimental results, but relatively stringent constraints are placed on dark matter related parameters  $M_1, M_2, \mu$ , which are affected by constraints on the relic density and direct detection experiments, and by the requirement that the lightest neutralino is the lightest supersymmetric particle, and therefore tend to prefer small values.

Regarding the SUSY mass spectrum in all considered cases the profile likelihood function for the neutralino LSP mass peaks at small values  $m_{\tilde{\chi}_1^0} \lesssim 100$  GeV. A bino-like neutralino LSP with a mass of  $\approx 60$  GeV is strongly favored, but at lower confidence also higgsino-like dark matter with  $m_{\tilde{\chi}_1^0} \approx 1$  TeV is allowed. In the case where the  $g - 2$  constraint is not included the resulting profile likelihood for the neutralino extends to larger values, pushing the maximum value of the mass from 1.5 to about 3 TeV. The profile likelihood of the squark and gluinos masses on the other hand is almost flat in its parameter range.

Direct detection constraints are found to be complementary to accelerator searches. Whereas upcoming experiments will allow to probe high scattering and annihilation cross-sections, the very long tails in the parameter space extending to extraordinarily small values of the cross-section further strengthen the case for a combined analysis of astroparticle and accelerator data. The next-generation multi-ton experiments will be able to probe the current best-fit point with a spin-independent cross-section of  $2.3 \times 10^{-10}$  pb.

The large parameter space of the MSSM-15 allows for different neutralino compositions. The various allowed compositions were discussed in detail. If the relic density is imposed as an upper limit the favored neutralino composition switches from bino-like to wino-like.

The inclusion of the LHC SUSY searches has a strong impact on the favored parameter space. The employed searches impose stringent constraints in regions of the parameter space corresponding to very low values of  $\sigma_{\tilde{\chi}_1^0 - p}^{\text{SI}}$ , therefore not accessible with astroparticle experiments in any foreseeable future.

The LHC at center-of-mass energy  $\sqrt{s} = 14$  TeV allows to probe the vast SUSY phase space further. The favored regions of the SUSY parameters derived in this study and their phenomenological implications give valuable hints where it is worth looking next.

A similar approach as presented in this chapter was also used for the publication "*Higgs, di-Higgs and tri-Higgs production via SUSY processes at the LHC with 14 TeV*", a research jointly conducted with W. Beenakker, S. Caron, R. Castelijns, M. Lanfermann and M. van Beekveld[172]. We searched the pMSSM for decays of supersymmetric particles via a 125 GeV Higgs boson. As in [127] the pMSSM is further constrained by implementing current measurement data. There are remaining areas of phase space that allow for a high rate of anomalous Higgs, di-Higgs and even tri-Higgs events.

The study selected a set of pMSSM points with an enhanced rate of Higgs production and simulated the ATLAS detector response for these points as described in ¶ 7.4.2. The event numbers the simulation setup yields for each of the signal regions of the implemented ATLAS analyses are scaled to the corresponding integrated luminosity. The scaled numbers are then compared to the model-independent 95% C.L. limits on the number of signal events provided by ATLAS. For [172] three different ATLAS searches were implemented: the 0-lepton search sensitive to squark and gluino production updated to 8 TeV[173], the 3-lepton search for charginos and neutralinos with all 20 bins of signal region SR0 $\tau$  [174] and signal region SR-0l-A of the 3-b-jet search for squarks and gluinos[175]. These three searches were selected to cover a broad range of possible signatures.

More than half of the selected model points are not excluded by the considered ATLAS analyses. A large fraction of not excluded pMSSM model point has remarkably low squark masses due to compressed spectra. This leads to very soft jets from squark decays resulting in the possibility that these points can only be seen by mono-jet searches. The high number of pMSSM model points with compressed spectra results in a larger fraction of model points not excluded by ATLAS analyses than usual.

As the Higgs boson is now discovered and the mass known the study provides a new insight into SUSY plus Higgs and an interesting new search strategy for future SUSY searches at the LHC.



## 7.A Validation results of ATLAS searches implementation

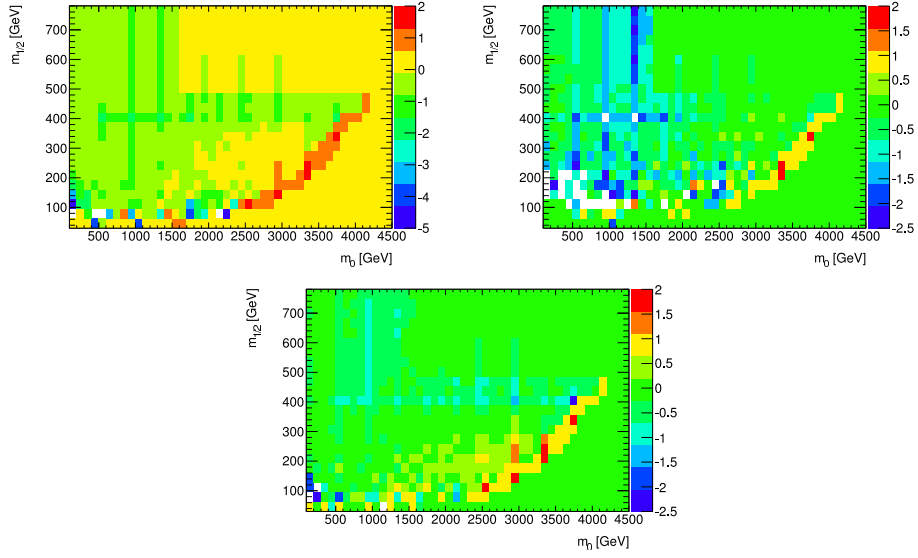


**Figure 7.A.1:**  $\frac{\Delta\epsilon}{\epsilon}$  of the ATLAS and simulation setups for signal region A *medium/loose* and A' of the 0-lepton analysis.

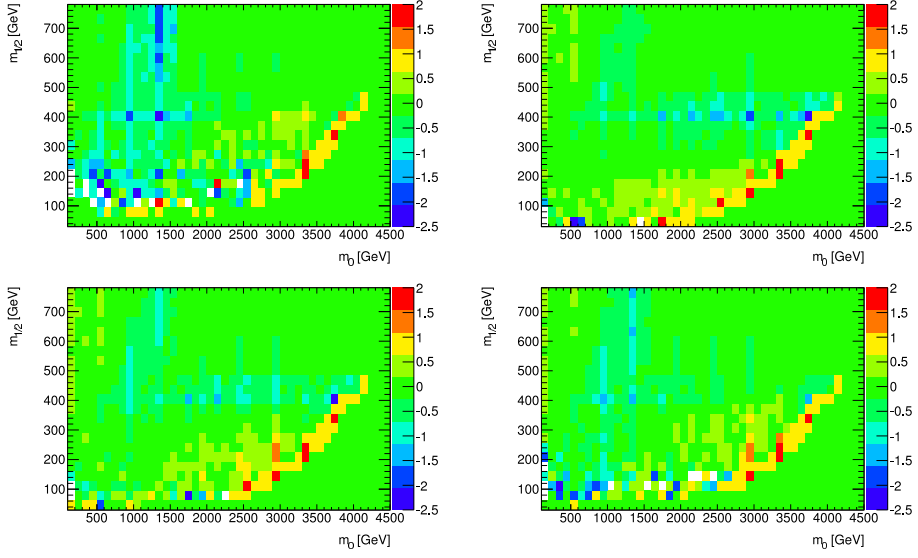


**Figure 7.A.2:**  $\frac{\Delta\epsilon}{\epsilon}$  of the ATLAS and simulation setups for signal region B *tight* and C *loose/medium/tight* of the 0-lepton analysis.

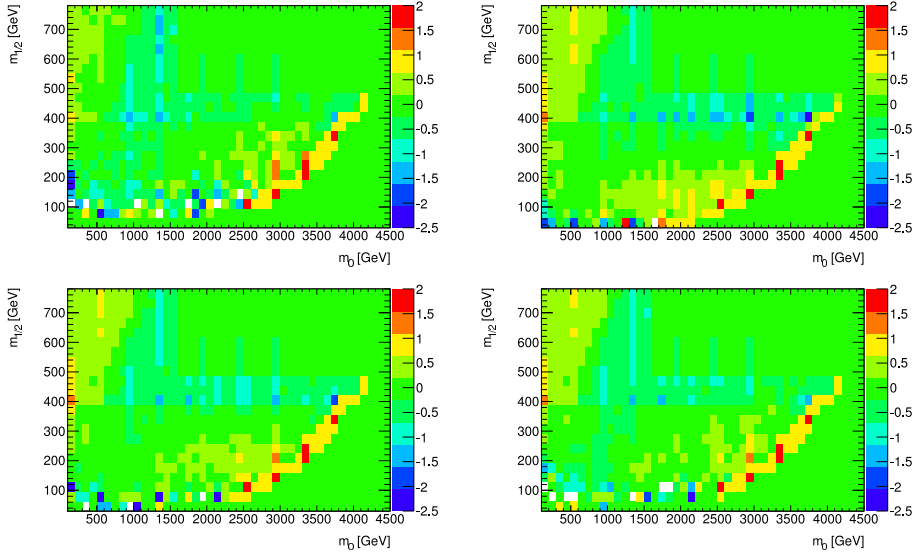


**Figure 7.A.3:**  $\frac{\Delta\epsilon}{\epsilon}$  of the ATLAS and simulation setups for signal region D and E *loose/medium/tight* of the 0-lepton analysis.

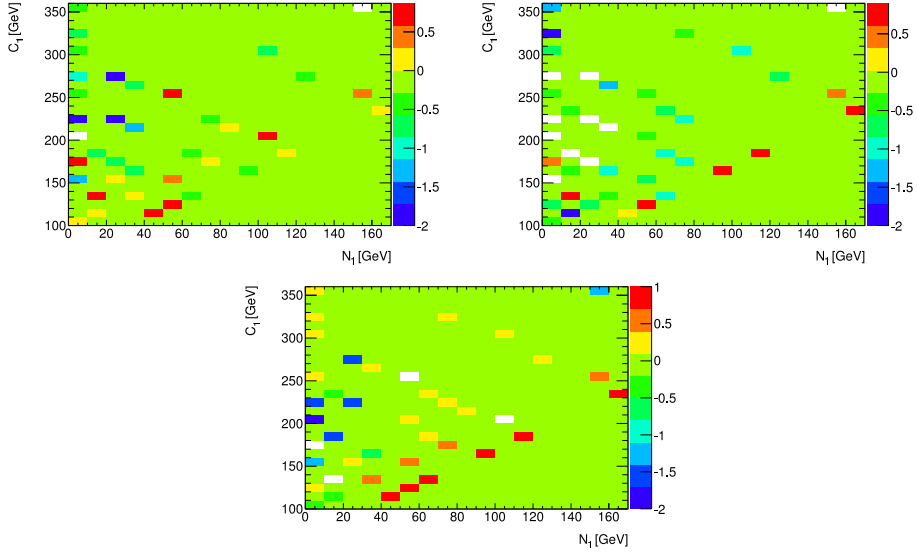


**Figure 7.A.4:**  $\frac{\Delta\epsilon}{\epsilon}$  of the ATLAS and simulation setups for signal region 1a, 1b and 2 of the 3-lepton analysis in the plane of  $N_1 = m_{\tilde{\chi}_1^0}$  and  $C_1 = m_{\tilde{\chi}_1^\pm}$ .

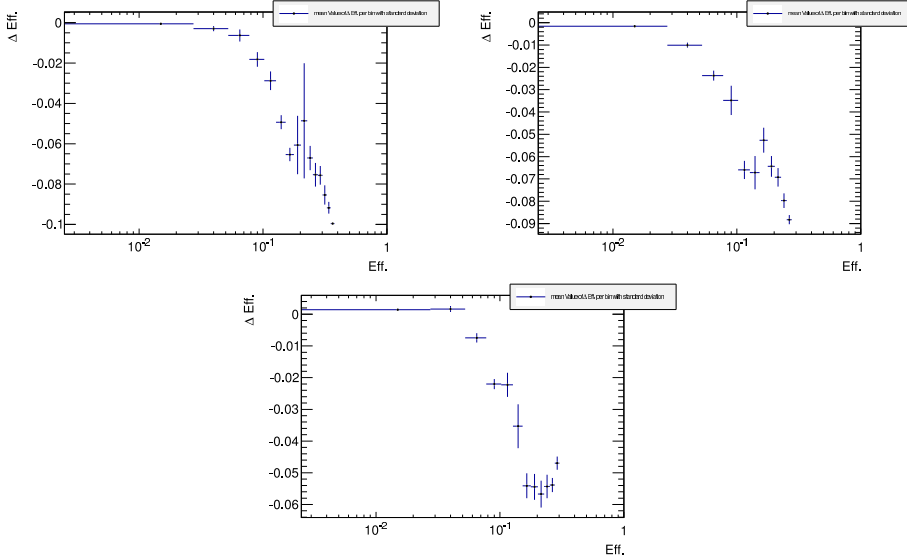


**Figure 7.A.5:** Mean efficiency value  $\Delta\epsilon$  (denoted as  $\Delta\text{Eff.}$ ) with estimated standard deviation for signal region A medium/loose and A' of the 0-lepton analysis.

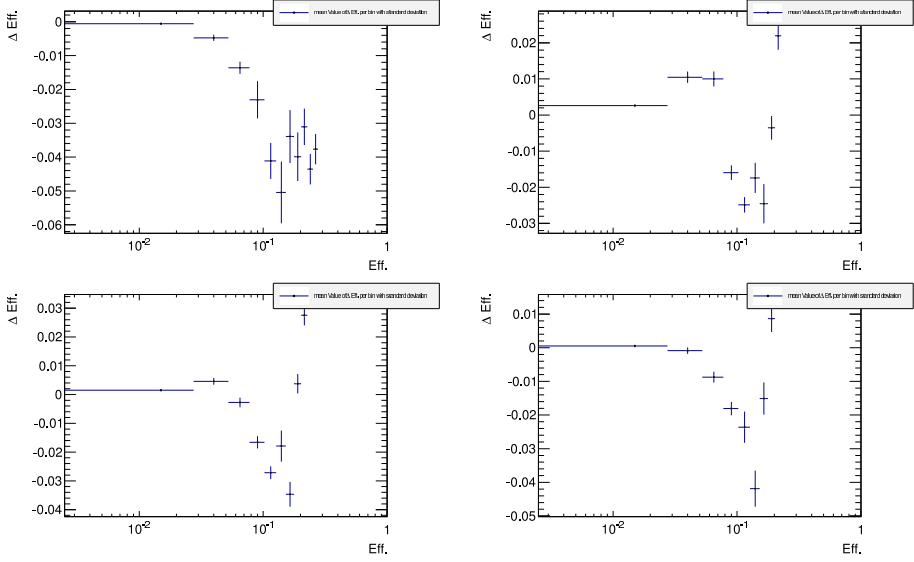


**Figure 7.A.6:** Mean efficiency value  $\Delta\epsilon$  (denoted as  $\Delta\text{Eff.}$ ) with standard deviation for signal region B tight and C loose/medium/tight of the 0-lepton analysis.

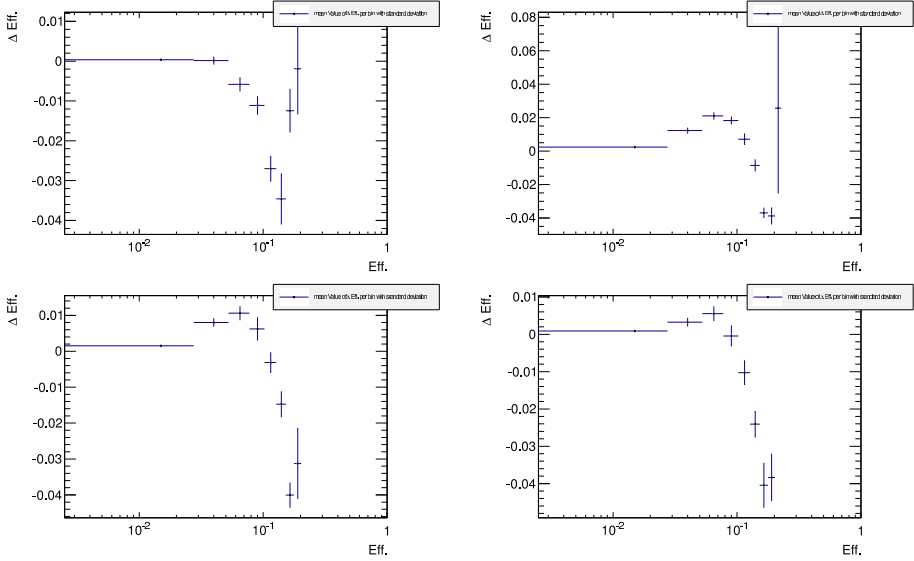


**Figure 7.A.7:** Mean efficiency value  $\Delta\epsilon$  (denoted as  $\Delta\text{Eff.}$ ) with standard deviation for signal region D and E loose/medium/tight of the 0-lepton analysis.

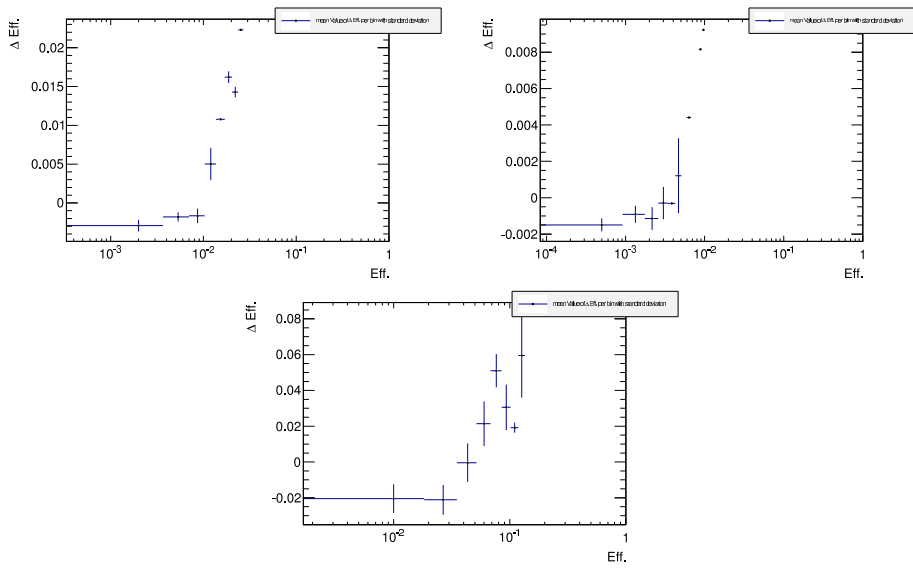


**Figure 7.A.8:** Mean efficiency value  $\Delta \epsilon$  (denoted as  $\Delta \text{Eff.}$ ) with standard deviation for signal region 1a, 1b and 2 of the 3-lepton analysis.

## CHAPTER 8

# Search for supersymmetry with jets and missing transverse energy

**S**UPERSYMMETRY is a popular extension of the Standard Model and includes a good candidate for Dark Matter. It is only logical that there are many teams at both ATLAS and CMS looking for various production and decay channels of SUSY. Along the lines of the previous chapter this thesis concentrates on the strong production of squarks and gluinos decaying to two to six jets, missing transverse energy and no leptons.

The search channel is motivated by the dominance of strong production of particles at the LHC directly linked to the dominance of the strong force (see § 2.3). The large amount of R-parity conserving models leads to decay chains that always end with the lightest  $\tilde{\chi}_i^0$ . As an only weak interacting particle it escapes the detector and results in (large) missing transverse energy. For direct squark/gluino decays the other decay products are quarks leading to jets. For decay chains with more steps via  $\tilde{\chi}_i^\pm$ s plus quark pairs and further to a hadronically decaying  $W^\pm$  and the LSP the final state consists of even more jets.

In addition to jets and  $E_T^{\text{miss}}$  a high  $m_{\text{eff}}$  value is required.  $m_{\text{eff}}$  is the sum over the  $p_T$  of the leading jets and  $E_T^{\text{miss}}$  and is a measure of the total activity in the event [176]. In SUSY events it can be interpreted as a quantifier of the event mass scale. Therefore a high  $m_{\text{eff}}$  selection is chosen to reduce background, as SUSY particles are expected to be heavier than Standard Model particles. This is also true for a high  $E_T^{\text{miss}}$  selection - neutrinos should be much lighter than neutralinos.

The search requirements are general enough that any new physics that results in an undetected escaping particle and jets should be discovered. Together with the increase in center-of-mass energy for Run II it has a very high discovery potential.

The search makes use of several simplified models both for signal sensitivity optimisation and for interpreting the results as limits on SUSY masses.

The work in this chapter was conducted in an analysis team and published in the "Further searches for squarks and gluinos in final states with jets and missing transverse momentum at  $\sqrt{s} = 13$  TeV with the ATLAS detector" [177]. It analyses  $L_{\text{int}} = 13.3 \text{ fb}^{-1}$  of proton-proton collision data taken at the LHC in 2015 and 2016 at  $\sqrt{s} = 13$  TeV and updates previous results [173, 178–183]. The personal contribution to the analysis group effort includes detailed trigger studies (MC validation, data to MC comparison, studies of new trigger chains and their efficiencies, impact of different Level 1 trigger seeds), the studies for a new MC signal grid and request, initial studies for a boosted boson signal region and being part of the team

producing the plots.

The published analysis uses two different search approaches, one using  $m_{\text{eff}}$  to distinguish between signal and background, the other one uses a novel recursive jigsaw reconstruction approach (RJR) [184]. Only the  $m_{\text{eff}}$ -based part will be discussed in this thesis.

## 8.1 Analysis strategy

The presented search is targeting strong production of squarks and gluinos. The signal sensitivity is estimated by using simplified models for squark and gluino pair production. In simplified models all except one particle are decoupled and the decay branching ratios are fixed at 100%. Direct decay chains of the squark have a quark and a  $\tilde{\chi}_i^0$  as final state and of the gluino a quark pair and a  $\tilde{\chi}_i^\pm$ . The resulting signature is two to four jets and missing transverse energy. In case of the one-step decay model for the gluinos via a  $\tilde{\chi}_i^\pm$  there are additional jets in the final state. There also can be additional jets from initial or final state radiation. The search requires therefore two to six jets and vetoes any leptons in the event. The lepton veto is introduced as background rejection measure as well as to avoid overlap with similar searches including leptons.

Though the search is optimised for certain SUSY models it is also able to detect other new physics that would result in the same signature - jets and  $E_T^{\text{miss}}$ . In case a signal is discovered it would require more studies to determine the exact nature of the discovered particle.

To be able to discern a signal event from the abundant Standard Model events all backgrounds for the chosen signal need to be modeled carefully. The lepton veto removes background from processes that result in a final state containing leptons, e.g.  $W \rightarrow \ell \nu$ , remaining backgrounds are for example QCD multijet events and W+jet events.

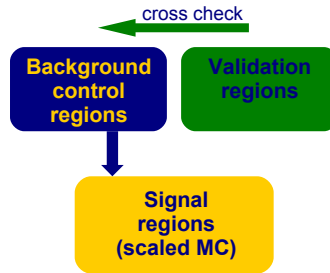


Figure 8.1: Schematic analysis design

Fig. 8.1 is a schematic view of the general analysis design. The underlying principle of this analysis uses a 'cut and count' approach. Relying on the MC simulation of the signal models event selections are defined that target the signal final states. The data and MC samples used for this analysis are described in § 8.2. The signal selections consist of kinematic and

topological thresholds ('cuts') for characteristic event properties. Each set of selection criteria defines a Signal Region (SR). The aim of the selections is to create SRs that include as little as possible to no background events, the SRs used in this analysis are described in § 8.3. The number of events ('count') that remain after the signal selection is applied is compared to the expected number of background events to determine if any excess / new physics events are found.

To know the background contained in the SRs quantitatively and qualitatively for each SR one or more Control Regions (CRs) are designed. The CR is orthogonal in phase space to the SR to avoid any signal contamination and at the same time kinematically close enough to make valid background predictions. To achieve orthogonality typically two or more cuts of the SR are inverted. There can be more than one CR each designed to be enriched in a particular background. Several methods exist how to estimate the background in the SR from the CR, they are described in § 8.4. The estimation for the different background sources from the CR is then used to normalize the Monte Carlo simulation.

To validate the background estimation there are several Validation Regions (VR) in which the estimated background can be compared to the actual data. Again the VR should have no signal contamination but should be in a similar phase space as the SR. For this purpose one of the inverted SR selections is reverted at a time, creating two or more VRs. Only if the background estimation is able to predict the background in the VR the event counts in the SRs are investigated ('unblinding'). Before the validation the SRs are on purpose not studied to avoid biasing the result.

To interpret the data in the SR a likelihood fit is performed to test if the data confirms a background only hypothesis - meaning that there is no excess observed caused by a process beyond the SM. The background-only likelihood fit uses the observed event yields from the CRs as only constraint for each SR. If no excess is observed a model-independent fit is conducted to set limits on the visible BSM cross section in each SR. This fit additionally contains the observed number of events in the SR as input. For the model dependent limits on the squark (gluino) and neutralino masses a model-dependent fit is used including the yield in the SR and also the signal contamination in the CR on top of the model-independent fit. The results from the model-dependent fit of each SR are used to set limits on specific SUSY models. For each point in the model's parameter space the SR with the highest expected signal sensitivity is used. The results of this analysis are given in § 8.5.

## 8.2 Data set and Monte Carlo samples

The data set for this analysis was taken during 2015 and 2016 with the ATLAS detector at the LHC with a center-of-mass energy  $\sqrt{s} = 13$  TeV. During 2015 the peak instantaneous luminosity reached up to  $L = 5.2 \times 10^{33} \text{ cm}^{-2} \text{ s}^{-1}$  with an average pile-up value of  $\langle\mu\rangle = 14$ . The 2016 data set was taken with peak inst. luminosity of  $L = 1.1 \times 10^{34} \text{ cm}^{-2} \text{ s}^{-1}$  with an average pile-up value of  $\langle\mu\rangle = 21$ . ATLAS uses a Good Run List (GRL) to determine for each individual luminosity block if its data quality is sufficient. The GRL takes also beam and detector conditions into account. The resulting integrated luminosity of the combined data



set is  $L_{\text{int}} = 13.3 \text{ fb}^{-1}$  with an uncertainty of  $\pm 2.9\%$ . For an accurate measurement of the delivered integrated luminosity ATLAS performs Van der Meer (VdM) scans once a year, the procedure is comparable to the one detailed in [185] for Run I.

The analysis makes use of detailed Monte Carlo samples for SR optimisation, background estimation and signal sensitivity determination. In general one can differ between signal samples based on theoretical SUSY models and background samples describing the various SM processes. Both are described in the following sections.

### 8.2.1 Signal samples

All supersymmetry signal samples for this analysis are described by simplified models (see also § 2.3.2). As the analysis searches for strong squark/gluino production the models employed are squark- and gluino-pair production where the gluinos and squarks are decoupled respectively. Four different models are studied. One squark-pair production model with the direct decay of the squark to a quark and the LSP ( $\tilde{q} \rightarrow q\tilde{\chi}_1^0$ ), one gluino-pair production model with direct decay of the gluino to a quark-pair and the LSP ( $\tilde{g} \rightarrow q\bar{q}\tilde{\chi}_1^0$ ) and two gluino-pair production models that have a one-step decay. If the gluino decays via a chargino the resulting final state includes quarks,  $W$ s and the LSPs ( $\tilde{g} \rightarrow q\bar{q}W\tilde{\chi}_1^0$ ), the one-step decay via a  $\tilde{\chi}_2^0$  results in a final state with quarks, LSPs and  $Z$ s ( $\tilde{g} \rightarrow q\bar{q}Z\tilde{\chi}_1^0$ ). Fig. 8.2 and Fig. 8.3 show the schematics for the direct and one-step decays.



**Figure 8.2:** Schematic drawing of the decay topology of the direct squark (left) and direct gluino (right) decay models.



**Figure 8.3:** Schematic drawing of the decay topology of the one-step gluino decay models. The left shows the decay via an intermediate  $\tilde{\chi}_1^\pm$ , the right via an intermediate  $\tilde{\chi}_2^0$ .

All signal sample are generated with using MG5\_aMC@NLO 2.2.2 [186] as event generator interfaced to Pythia 8.186 [187] for parton showering. NNPDF2.3LO [188] is used as parton distribution function (PDF) set. The signal cross-sections are calculated at next-to-leading order (NLO) in  $\alpha_s$ , including the resummation of soft gluon emission at NLL accuracy (NLO+NLL) on top [161–165]. For the light-flavour squarks (gluinos) in case of gluino-(squark-) pair production their masses are decoupled and the corresponding cross-sections are evaluated assuming masses of 450 TeV. The detector response is simulated using the fast simulation ATLFast [189] for the calorimeters and the full simulation GEANT4 [190] for all other detector regions.

For each model a grid of model points is generated with the squark (gluino) mass and the  $\tilde{\chi}_1^0$  mass as free parameters. The mass point density is a trade-off of simulation costs and a sufficient number of mass points for SR optimisation and model-dependent limits. For the direct squark grid  $m_{\tilde{q}} = [200, 1600]$  GeV and  $m_{\tilde{\chi}^0} = [0, 600]$  GeV. The mass parameters in the direct gluino grid are  $m_{\tilde{g}} = [200, 2000]$  GeV and  $m_{\tilde{\chi}^0} = [0, 900]$  GeV. For the one step grids with  $W$ s and  $Z$ s in the final state the mass ranges are  $m_{\tilde{g}} = [237, 2025]$  GeV,  $m_{\tilde{\chi}^0} = [60, 985]$  GeV and  $m_{\tilde{g}} = [665, 1745]$  GeV,  $m_{\tilde{\chi}^0} = 1$  GeV respectively. For the decay via a  $\tilde{\chi}_1^\pm$  the intermediate SUSY particle mass is either determined in relation to the gluino and LSP:  $m(\tilde{\chi}_1^\pm) = (m(\tilde{g}) + m(\tilde{\chi}_1^0)) / 2$  or the LSP mass is fixed to 60 GeV.

### 8.2.2 Background samples

The main background sources for this analysis are:  $Z$ +jets,  $\gamma$  + jets,  $W$ +jets, top quark pairs and single top quarks, dibosons and multi-jet production. For each dedicated Monte Carlo simulations are run to obtain the samples used in the background estimation.

For each sample the simulation of the ATLAS detector is done with the full simulation GEANT4.

As a last step for pile-up simulation all events are overlaid with multiple pp collisions. The pile-up interactions are generated with the soft QCD processes of Pythia 8.186 with MSTW2008LO [191] as PDF set and re-weighted to be in agreement with the distribution of the average pile-up observed in data.

Table 8.1 shows an overview of the MC generator and tune, the parton shower generator, the PDF set and the precision of the cross section normalization used for each sample.

Physics process	Generator	cross section normalization	PDF set	Parton shower	Tune
$W \rightarrow \ell \nu$ + jets	SHERPA 2.2.0	NNLO	NNPDF3.0NNLO	SHERPA	SHERPA default
$Z^*/\gamma \rightarrow \ell \ell$ + jets	SHERPA 2.2.0	NNLO	NNPDF3.0NNLO	SHERPA	SHERPA default
$\gamma$ + jets	SHERPA 2.1.1	LO	CT10	SHERPA	SHERPA default
$t\bar{t}$	POWHEG-BOX v2	NNLO + NNLL	CT10	PYTHIA6.428	PERUGIA2012
Single top ( $Wt$ -channel)	POWHEG-BOX v2	NNLO + NNLL	CT10	PYTHIA6.428	PERUGIA2012
Single top ( $s$ -channel)	POWHEG-BOX v2	NLO	CT10	PYTHIA6.428	PERUGIA2012
Single top ( $t$ -channel)	POWHEG-BOX v1	NLO	CT10f4	PYTHIA6.428	PERUGIA2012
$t\bar{t} + W/Z/WW$	MG5_aMC@NLO 2.2.2	NLO	NNPDF2.3LO	PYTHIA8.186	A14
$WW, WZ, ZZ$	SHERPA 2.1.1	NLO	CT10	SHERPA	SHERPA default
Multi-jet	PYTHIA8.186	LO	NNPDF2.3LO	PYTHIA8.186	A14

**Table 8.1:** Configurations of the Monte Carlo generators to simulate the different background samples.

**W/Z/ $\gamma$  + jets** The samples for W + jets and Z + jets are generated using SHERPA 2.2.0 [192] and NNPDF3.0NLO [193] as PDF set whereas the photon + jets sample is generated using SHERPA 2.1.1 [192] and CT10 [194] as PDF set.

**Top** The single-top background is divided in three channels, the W *t*-channel and *s*-channel are both generated with POWHEG-BOX v2 [195] in combination with the CT10 PDF set, the same applies to the  $t\bar{t}$  sample. For the generation of the single-top *t*-channel POWHEG-BOX v1 is used with CT10f4 [194] as PDF set, they both use a four-flavour scheme. For all four samples the event generators are interface with PYTHIA 6.428 [166] for parton shower generation.

$t\bar{t}$  + W/Z/WW processes are generated using MG5\_aMC@NLO 2.2.3 interfaced to Pythia 8.186 for parton shower generation, using NNPDF2.3LO as PDF set.

**Di-boson** The di-boson background samples for WW, WZ and ZZ are generated with SHERPA 2.1.1 using CT10 as PDF set. The samples are normalized to the direct generator cross-sections at LO.

**Multi-jet** The multi-jet background is generated with Pythia 8.186 using the A14 [196] underlying-event tune and the NNPDF2.3LO [188] parton distribution functions.

### 8.3 Event selection and Signal regions

To arrive at the final signal region selection several steps of pre-selection are required. The objects on which the selection is applied have to be well defined, isolation criteria and other object requirements are described in § 8.3.1. In a next step a sub-set of the full data set is created by discarding events that are not interesting for the analysis per se (§ 8.3.2) or do not fulfill additional quality requirements (§ 8.3.2). The definition of the discriminating variables for the final selection and the signal regions are described in § 8.3.3.

#### 8.3.1 Object selection

In addition to the general object reconstruction described in § 6 several additional requirements are applied online like isolation, topological and kinematic that vary between the different types of objects.

**Jets** are reconstructed with the anti- $k_t$  jet algorithm [99] with the jet cone parameter  $R = 0.4$ . Candidate jets have to pass a  $p_T$  threshold of 20 GeV and  $|\eta| < 2.8$ .

**b-jets** are identified with a b-tagging algorithm that was re-optimised for Run-2 conditions - MV2c10 [111, 112]. The working point in use corresponds to a tagging efficiency of 77%. Candidate b-jets have to pass a  $p_T$  threshold of 50 GeV and  $|\eta| < 2.5$ .

**Electrons** that fulfill the baseline requirement must have a  $p_T$  larger than 10 GeV and  $|\eta| < 2.47$ . Additionally they are required to pass the 'Loose' likelihood-based identification criterion [197].

High-purity electrons fulfill in addition the 'Tight' identification criterion, have  $p_T > 27$  GeV,  $|d_0^{PV}|/\sigma(d_0^{PV}) < 5$ ,  $|z_0^{PV} \sin \theta| < 0.5$  mm and pass the isolation requirement of 'GradientLoose' [197]. For a high-purity electron the leading electron needs to have a  $p_T$  larger than 27 GeV.

**Muons** are required to have a  $p_T$  larger than 10 GeV and  $|\eta|$  has to be smaller than 2.7 for baseline muons.

High-purity muons need a  $\eta < 2.47$  and must fulfill similar requirements as high-purity electrons:  $|d_0^{PV}|/\sigma(d_0^{PV}) < 3$ ,  $|z_0^{PV} \sin \theta| < 0.5$  mm and a leading muon with  $p_T > 27$  GeV [124]

**Photons** need to have a  $p_T$  larger than 150 GeV and  $|\eta| < 2.37$ . In addition a candidate must fulfill photon shower shape and electron rejection criteria [123] as well as isolation criteria. Reconstructed photons are only used in the control regions for the Z + jets background (see 8.4).

**Missing transverse energy** The measurement of the missing transverse momentum vector  $\vec{E}_T^{\text{miss}}$  and its magnitude  $E_T^{\text{miss}}$  is based on the calibrated transverse momenta of all electron, muon, photon and jet candidates and all additional tracks originating from the primary vertex [113].

### Overlap removal

When reconstructing an event it can happen that two objects share the same detector objects, e.g. some calorimeter clusters or similar. Most cases where objects overlap are caused by mis-constructions or leptons ending up in jets. To dissolve these ambiguities between candidate jets, leptons and photons a well defined procedure is in place - the overlap removal [198]. The overlap removal takes as input all aforementioned object candidates. Photons are only considered if they are in the event selection, in this case only for certain CR selections. The steps including photons are omitted otherwise (*marked in italics*).

1. If a baseline electron and a baseline muon share the same ID track the electron is discarded and the object reconstructed as muon.
2. *If a baseline photon and a baseline electron are found within  $\Delta R < 0.4$ , the photon is discarded.*
3. *If a baseline photon and a baseline muon are found within  $\Delta R < 0.4$ , the photon is discarded.*
4. If a baseline electron and a jet are found within  $\Delta R < 0.2$  and the jet is not b-tagged with the MV2c10 85% efficiency working point, the object is reconstructed as an electron and the jet is discarded.

5. If a baseline electron and a jet are found within  $\Delta R < 0.4$  and the jet is not flagged as pileup jet ( $p_T < 60$  GeV and  $|\eta| < 2.4$  and JVT  $< 0.59$ ), the object is reconstructed as a jet and the electron is discarded.
6. If a baseline muon and a jet are associated or found within  $\Delta R < 0.2$ , the object is reconstructed as jet if the jet and the muon fulfill either of the following conditions:
  - the number of tracks with  $p_T > 500$  MeV that are associated to the jet is less than three
  - $p_T^{muon}/p_T^{jet} \geq 0.5$  and  $p_T^{muon}/\sum_{injet} p_T^{track} \geq 0.5$
  - the jet is not b-tagged with the MV2c10 85% efficiency working point
7. If a baseline muon and a jet are found within  $\Delta R < \min(0.4, 0.04 + \frac{10\text{GeV}}{p_T^{muon}})$  the muon is discarded if the jet is not flagged as pile-up jet.
8. If a baseline photon and a jet are found within  $\Delta R < 0.4$  the jet is discarded.

### 8.3.2 Event pre-selection

The event pre-selection includes all selections that are applied for all signal regions and not unique to a single SR. These are the trigger selection used to collect the data sample, the event cleaning cuts, cuts to suppress the QCD background, a general lepton veto and a first set of kinematic cuts.

CRs and VRs can have different pre-selections than described here due to the orthogonality requirement.

#### Trigger

The signal events for this analysis are collected by a  $E_T^{\text{miss}}$ -trigger. In the 2015 data set events must pass HLT\_xe70 seeded by L1\_XE50, this means a cut on  $E_T^{\text{miss}}$  of 70 GeV is applied at HLT level. The calibration of trigger and offline  $E_T^{\text{miss}}$  is not identical, as can be seen in Fig. 8.4. The efficiency curve of HLT\_xe70 in offline  $E_T^{\text{miss}}$  only reaches the plateau for  $E_T^{\text{miss}} = 200$  GeV. To ensure that the analysis operates in a region where HLT\_xe70 is fully efficient a corresponding cut is required.

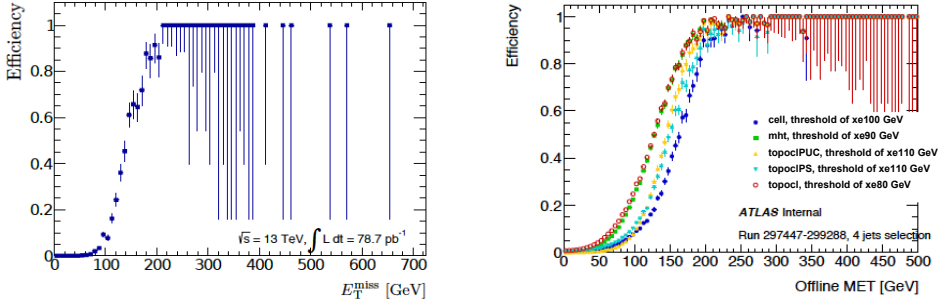
The 2016 data set is selected with HLT\_xe80\_tc\_1cw\_L1XE50 or HLT\_xe100\_mht\_L1XE50 for later runs as it proved more efficient at the same trigger rate. In 2016 the  $E_T^{\text{miss}}$ -trigger is fully efficient at an offline  $E_T^{\text{miss}}$  value of 250 GeV.

Fig. 8.4 shows the existing  $E_T^{\text{miss}}$  trigger variants with efficiency in offline  $E_T^{\text{miss}}$ .

See Appendix 8.C for more detailed trigger studies.

#### Event cleaning

Event cleaning removes undesired effects from non-collision backgrounds (NCB), bad calorimeter regions and fake muons. Non-collision backgrounds are defined as not coming from pp collisions but from cosmic rays or beam-gas remnants. For a better estimation of the NCB



**Figure 8.4:** The trigger efficiency of the  $E_T^{\text{miss}}$ -trigger used for signal event pre-selection in 2015 (left and 2016 (right).)

data is not only taken during pp collisions but already before during ‘Standby’ of the detector with a set of special NCB triggers.

All of the three effects lead to fake  $E_T^{\text{miss}}$  its amount can be reduced with sets of selections tailored to the specific problem.

**Non-collision backgrounds** A first step to reduces non-collision backgrounds is to veto events which have only a reconstructed primary vertex associated with less than two tracks. The energy deposits of NCB processes are reconstructed as jets. Jet properties can therefore be used to discern NCB jets from hard-scatter jets. Events with a ‘LooseBad’ jet with  $p_T > 20$  GeV are rejected. In addition also events containing jets with  $p_T > 100$  GeV and flagged ‘TightBad’ can be discarded [199]. Out-of-time jets also hint at non-collision backgrounds. If the ‘time’ of the both two leading jets is larger than 4 ns the event is rejected. The ‘time’ of a jet is defined as its energy averaged calorimeter cell time.

**Dead calorimeter regions** Dead tile regions were present during 2015 data taking. If a jet is close to a dead tile region it can influence its shape and  $p_T$ . The region is located at  $(0 < \eta < 0.9, \phi = 0.9)$  and  $(-1.6 < \eta < -0.9, \phi = 2.0)$ . Events where a jet is pointing to the dead region has  $p_T > 50$  GeV and  $\Delta\phi(\text{jet}, E_T^{\text{miss}}) < 0.3$  are rejected in the signal region selection. This cut is applied only for the 2015 data set since the problem was fixed for 2016.

**Fake muons** Fake muons are reconstructed muons that do not come from pp collisions. They originate from high hit multiplicities in the muon spectrometer in events where some particles from very energetic jets punch through the calorimeter into the muon system. Other causes are badly measured inner detector tracks in jets wrongly matched to muon spectrometer segments or cosmic muons. Fake muons result in large contributions to fake  $E_T^{\text{miss}}$ , Muon

Events are rejected if there are muons after overlap removal with  $|z_0^{PV}| > 1$  mm or  $|d_0^{PV}| > 0.2$

mm or if

$$\frac{E_T^{\text{miss, Muon}}}{E_T^{\text{miss}}} \cos \Delta\phi(E_T^{\text{miss, Muon}}) > 0.5. \quad (8.1)$$

### Lepton veto

This analysis is solely looking at events with jets and  $E_T^{\text{miss}}$  as tellingly included in the analysis title. It is therefore only logical to veto any events that contain a baseline lepton (electron or muon) after overlap removal for signal selection. The lepton veto also ensures that this analysis is orthogonal to other ATLAS analyses searching for strong production of squarks and gluinos that include leptons in the final state. Furthermore it helps to significantly reduce backgrounds.

### Kinematic selection

The last pre-selection places cuts on  $E_T^{\text{miss}}$  and the jet  $p_T$ . For the complete data set  $E_T^{\text{miss}}$  must be larger than 250 GeV to work on the plateau of the 2016 trigger selection. Events with no jets above  $p_T = 50$  GeV are rejected, an additional requirement is placed on the leading jet  $p_T$ , it must be larger than 200 GeV and sub-leading jet  $p_T > 50$  GeV.

### 8.3.3 Signal regions

Each of the signal region selections is optimised for discovery, meaning that each SR is designed to maximise the significance of rejection of the background-only hypothesis. The thresholds on the variables used to discriminate between signal and background are varied, for each variation the significance is calculated and the signal selection set chosen that has the best significance for an area in the SUSY phase space (corresponding to several signal grid mass points). (A minimum significance of  $3\sigma$  was chosen as discovery reach [198].)

The discriminating variables used in this analysis are defined in the following.

### Discriminating variables

The following variables have properties that allow to distinguish between SUSY signal and background. They are used to design the SRs of this analysis.

$E_T^{\text{miss}}$  is the missing transverse momentum. It is a measure how much energy leaves the detector undetected due to only weakly interacting particles like neutrinos or the LSP. As R-parity conserving SUSY models always include the LSP in the final state one expects to have  $E_T^{\text{miss}}$  though the amount can vary largely with the particular model.

$m_{\text{eff}}$  is defined to be the scalar sum of the transverse momenta of the leading  $N_j$  jets and  $\vec{E}_T^{\text{miss}}$ :

$$m_{\text{eff}} = |\vec{E}_T^{\text{miss}}| + \sum_{\text{jets}} p_T \quad (8.2)$$

$m_{\text{eff}}$  is a good handle on the activity in an event and correlates with the SUSY mass scale. The cut placed on  $m_{\text{eff}}$  for strong SUSY searches is therefore relatively high.  $m_{\text{eff}}$  can be calculated using all jets in the event ( $m_{\text{eff}}(\text{incl.})$ ) or only a sub-set of jets ( $m_{\text{eff}}(N_j)$ ).

$\Delta\phi(\text{jet}_i, E_T^{\text{miss}})_{\min}$  is the minimum azimuthal angle between two objects - in this analysis between a jet and  $E_T^{\text{miss}}$ .  $\Delta\phi(\text{jet}_i, E_T^{\text{miss}})_{\min}$  is a main discriminant against QCD/multijet background. The  $E_T^{\text{miss}}$  in multijet background events is mostly due to mis-measured jets and points therefore in the direction of the jet. This is usually not the case for SUSY events.

$E_T^{\text{miss}}/m_{\text{eff}}$  the fraction of  $E_T^{\text{miss}}$  to  $m_{\text{eff}}$  can be used to distinguish signal from background especially for high mass gluinos. They have a larger  $E_T^{\text{miss}}/m_{\text{eff}}$  value than the SM background.

$E_T^{\text{miss}}/\sqrt{H_T}$  the missing transverse momentum significance is the fraction of  $E_T^{\text{miss}}$  to  $\sqrt{H_T}$ , with  $H_T$  the scalar sum of all jet momenta. In analogue to  $m_{\text{eff}}$  it relates to the jet activity in the event.  $E_T^{\text{miss}}/\sqrt{H_T}$  is the significance of  $E_T^{\text{miss}}$  which is higher in (SUSY) events with large real  $E_T^{\text{miss}}$  and lower for fake  $E_T^{\text{miss}}$ .

**Aplanarity** is defined as  $A = \frac{2}{3}\lambda$  with  $\lambda$  the smallest eigenvalue of the sphericity tensor [200]. For decaying high-mass particles the decay products are rather collimated ('boosted') leading to a 'linear' event shape. For the decay of low-mass particles the event shape as given by  $A$  is more spherical.

**Number of jets** Depending on the SUSY signal model the final state contains more or less jets. For squark-pair production one expects two or more jets, for gluino-pair production at least 4 where the number of jets is increasing with more complex decay chains.

### Signal region selection

Thirteen inclusive signal regions characterized by increasing minimum jet multiplicity from two to six, are defined in Table 8.2: five regions targeting the direct squark models, six regions targeting models with direct gluino decay and for the one-step gluino models there are two regions. Signal regions requiring the same jet-multiplicity are distinguished by increasing the threshold of the  $m_{\text{eff}}(\text{incl.})$  and  $E_T^{\text{miss}}/m_{\text{eff}}$  (or  $E_T^{\text{miss}}/\sqrt{H_T}$ ) requirements. This ensures the sensitivity to various mass differences for each decay mode.

In each region, different thresholds are applied on jet  $p_T$  and on  $\Delta\phi(\text{jet}_i, E_T^{\text{miss}})_{\min}$ . Requirements on  $\Delta\phi(\text{jet}_i, E_T^{\text{miss}})_{\min}$  and  $E_T^{\text{miss}}/m_{\text{eff}}$  are designed to reduce the background from multi-jet processes.

For the 2-jet signal regions which are optimized for direct squark models, the selection requires  $\Delta\phi(\text{jet}_i, E_T^{\text{miss}})_{\min} > 0.8$  for ( $i=(1,2,3)$ ) using only the three leading jets while in signal regions with higher jet multiplicities the requirement  $\Delta\phi(\text{jet}_i, E_T^{\text{miss}})_{\min} > 0.4$  for ( $i=(1,2,3)$ ) is used. For the signal regions requiring at least four, five or six jets in the final state, or



in the case when more than three jets are present in 2-jet or 3-jet signal regions, an additional requirement on  $\Delta\phi(\text{jet}_i, E_T^{\text{miss}})_{\min}$  for ( $i>3$ ) is applied to all jets. Extending the  $\Delta\phi(\text{jet}_i, E_T^{\text{miss}})_{\min}$ -requirement to all jets also in the 2-jet signal regions (different from the 2015 analysis [178]) slightly increases the discovery reach for high squark masses.

In the 2-jet and 3-jet signal regions the requirement on  $E_T^{\text{miss}}/m_{\text{eff}}$  is replaced by a requirement on  $E_T^{\text{miss}}/\sqrt{H_T}$  which is found to lead to enhanced sensitivity to models characterized by  $\widetilde{q}\widetilde{q}$  production. In the other regions with at least four jets in the final state, additional suppression of background processes is based on the aplanarity variable.

Another improvement are individual requirement on  $|\eta|$  of the required jets that help distinguishing signal from background especially for models with  $m_{\widetilde{\chi}^0}$  around 400 GeV. Most signal regions require therefore jets to be more central than the general requirement of  $|\eta| < 2.8$  for all jets in the object selection. This additional requirement has a range of  $|\eta| < 0.8$  to  $|\eta| < 2.0$ .

Targeted signal	$\bar{q}\bar{q}, \bar{q} \rightarrow q \tilde{\chi}_1^0$					
	Meff-2j-800	Meff-2j-1200	Meff-2j-1600	Meff-2j-2000	Meff-3j-1200	
$E_{\text{T}}^{\text{miss}}[\text{GeV}]>$	250					
$1^{st} \text{ jet } p_{\text{T}} [\text{GeV}]>$	200		250			600
$2^{nd} \text{ jet } p_{\text{T}} [\text{GeV}]>$	200		250			50
$3^{rd} \text{ jet } p_{\text{T}} [\text{GeV}]>$	–					50
$ \eta(j_{1,2}) <$	0.8		1.2			–
$\Delta\phi(\text{jet}_{1,2,(3)}, E_{\text{T}}^{\text{miss}})_{\min}>$			0.8			0.4
$\Delta\phi(\text{jet}_{i>3}, E_{\text{T}}^{\text{miss}})_{\min}>$			0.4			0.2
$E_{\text{T}}^{\text{miss}}/\sqrt{H_{\text{T}}}[\text{GeV}^{1/2}]>$	14	16	18	20		16
$m_{\text{eff}}(\text{incl.})[\text{GeV}]>$	800	1200	1600	2000		1200

Targeted signal	$\bar{g}\bar{g}, \bar{g} \rightarrow q\bar{q} \tilde{\chi}_1^0$					
	Meff-4j-1000	Meff-4j-1400	Meff-4j-1800	Meff-4j-2200	Meff-4j-2600	Meff-5j-1400
$E_{\text{T}}^{\text{miss}}[\text{GeV}]>$	250					
$1^{st} \text{ jet } p_{\text{T}} [\text{GeV}]>$			200			500
$4^{th} \text{ jet } p_{\text{T}} [\text{GeV}]>$		100		150		50
$5^{th} \text{ jet } p_{\text{T}} [\text{GeV}]>$			–			50
$ \eta(j_{1,2,3,4}) <$	1.2		2.0			–
$\Delta\phi(\text{jet}_{1,2,(3)}, E_{\text{T}}^{\text{miss}})_{\min}>$			0.4			
$\Delta\phi(\text{jet}_{i>3}, E_{\text{T}}^{\text{miss}})_{\min}>$			0.4			0.2
Aplanarity>			0.04			–
$E_{\text{T}}^{\text{miss}}/m_{\text{eff}}>$	0.25			0.2		0.3
$m_{\text{eff}}(\text{incl.})[\text{GeV}]>$	1000	1400	1800	2200	2600	1400

Targeted signal	$\bar{g}\bar{g}, \bar{g} \rightarrow q\bar{q}W \tilde{\chi}_1^0$	
	Meff-6j-1800	Meff-6j-2200
$E_{\text{T}}^{\text{miss}}[\text{GeV}]>$	250	
$1^{st} \text{ jet } p_{\text{T}} [\text{GeV}]>$	200	
$6^{th} \text{ jet } p_{\text{T}} [\text{GeV}]>$	200	
$ \eta(j_{1\dots 6}) <$	2.0	–
$\Delta\phi(\text{jet}_{1,2,(3)}, E_{\text{T}}^{\text{miss}})_{\min}>$	200	
$\Delta\phi(\text{jet}_{i>3}, E_{\text{T}}^{\text{miss}})_{\min}>$	0.2	
Aplanarity>	0.08	–
$E_{\text{T}}^{\text{miss}}/m_{\text{eff}}>$	0.2	0.15
$m_{\text{eff}}(\text{incl.})[\text{GeV}]>$	1800	2200

**Table 8.2:** The signal selection criteria used in each signal region. In addition the targeted SUSY signal is given.

## 8.4 Backgrounds and Systematics

Depending on the signal it is not always possible to design the signal regions in a way that it contains zero expected background events. Even then the hypothesis of zero background events has to be validated. A proper background estimation is therefore an important part of an analysis.

The following sections describe all considered backgrounds for this analysis and the different methods used to estimate them and project them to the signal regions.

### 8.4.1 Background sources

The main background sources for this analysis are:  $Z/\gamma^* + \text{jets}$ ,  $W + \text{jets}$ , top quark pairs and single top quarks, dibosons and multi-jet production.

**W+jets** background events can enter the signal regions if a muon or electron from the  $W$  decay is mis-identified (due to acceptance/reconstruction efficiency) as a jet or not at all, the real  $E_T^{\text{miss}}$  is provided by the lepton accompanying neutrino. In the case of the  $W$  decaying to a tau lepton the resulting final state is very similar to the signal final state only if the tau decays hadronically.

The cases where **top quark pairs** ( $t\bar{t}$ ) and **single top quark** events enter the signal region are similar to the  $W$ +jets background. For a (anti-)top quark decaying leptonically ( $t \rightarrow b\ell\bar{\nu}_\ell$ ) again the event can look like a signal event if the leptons are not identified or mis-identified as jets. For a hadronic decay ( $t \rightarrow bq\bar{q}'$ ) some of the final state jet energies must be mis-measured leading to fake  $E_T^{\text{miss}}$  in the event. Another possibility is when the top quark is produced in association with a  $W$  or  $Z$  boson which decay provides the required  $E_T^{\text{miss}}$ . The production of top quarks with a Higgs boson is negligible. Top quarks can be both produced as either a  $t\bar{t}$  quark-pair or as a single top.

The largest and irreducible contribution to the  $Z/\gamma^* + \text{jets}$  background comes from  $Z \rightarrow \nu\nu$  decays with real  $E_T^{\text{miss}}$  in the event from the neutrinos. Other small contributions are  $Z/\gamma^* \rightarrow l\bar{l}$  decays in the rare case where both leptons are mis-identified and the jet energy is mis-measured and  $Z/\gamma^* \rightarrow \tau\tau$  decays with hadronically decaying taus - a small contribution as the branching fraction is much smaller than  $Z \rightarrow \nu\nu$ .

Similar to the boson + jet background also events with **diboson** production ( $WW$ ,  $ZZ$ ,  $WZ$ ,  $W\gamma$ ,  $Z\gamma$ ) can resemble a signal event. This is the case if the  $Z$  boson decays into neutrinos for real  $E_T^{\text{miss}}$  and the other boson decays hadronically providing the necessary jets. Also possible are leptonically decaying  $W$  bosons where the leptons are mis-identified. For the diboson background the production is solely estimated with MC simulated data normalized to NLO cross-section predictions.

The **multijet** background (QCD background) arises from jet production where the jet energy is mis-measured resulting in fake  $E_T^{\text{miss}}$ . Another source for the multijet background are semileptonically decaying  $b$  quarks if the lepton is mis-identified. The multijet background is the only one estimated by a fully data-driven method. After applying the selections on  $\Delta\phi(\text{jet}_i, E_T^{\text{miss}})_{\text{min}}$  and  $E_T^{\text{miss}}/m_{\text{eff}}$  the contribution to the signal regions is negligible.

### 8.4.2 Control regions

Except the diboson one all backgrounds are estimated with help of the dedicated CRs for each background and the predictions are cross-checked in validation regions. For each signal region four control regions are defined which are combined for the final background prediction in the SR.

The background in the SR is predicted by the use of Transfer Functions (TF) between the CR and its SR. For the transfer function it is assumed that the ratio of observed events in the CR

$(N_{\text{CR}}^{\text{obs, process}})$  to observed events in the SR ( $N_{\text{SR}}^{\text{obs, process}}$ ) equals the ratio of expected events ( $N_{\text{CR}(\text{SR})}^{\text{exp, process}}$ ). The resulting equation contains the transfer function:

$$N_{\text{SR}}^{\text{est, process}} = N_{\text{CR}}^{\text{obs, process}} \left[ \frac{N_{\text{SR}}^{\text{exp, process}}}{N_{\text{CR}(\text{SR})}^{\text{exp, process}}} \right] = N_{\text{CR}}^{\text{obs, process}} \text{TF}_{\text{CR} \rightarrow \text{SR}} \quad (8.3)$$

where  $N_{\text{SR}}^{\text{est, process}}$  is the SR background estimate for the process. The TFs between CRs used to enable the background estimates to be normalised coherently across all the CRs are defined similarly.

If possible the background in the CR is estimated using a fully data-driven approach. If this is not possible other estimation techniques are semi data-driven (using MC normalized to data in the CR) or fully MC dependent (without the use of a CR).

Tab. 8.3 shows an overview of the selection criteria for each of the four main backgrounds. The details are described in the following sections.

CR	SR background	CR process	CR selection
CR $\gamma$	$Z(\rightarrow \nu\bar{\nu}) + \text{jets}$	$\gamma + \text{jets}$	isolated photon SR with reversed requirements on
CRQ	multi-jet	multi-jet	(I) $\Delta\phi(\text{jet}_i, E_{\text{T}}^{\text{miss}})_{\text{min}}$ and (II) $E_{\text{T}}^{\text{miss}}/m_{\text{eff}}$ or $E_{\text{T}}^{\text{miss}}/\sqrt{H_{\text{T}}}$
CRW	$W(\rightarrow \ell\nu) + \text{jets}$	$W \rightarrow \ell\nu + \text{jets}$	$30 \text{ GeV} < m_{\text{T}}(\ell, E_{\text{T}}^{\text{miss}}) < 100 \text{ GeV}$ b-veto
CRT	$t\bar{t}$ (+EW) and single top	$t\bar{t} \rightarrow b\bar{b}q q' \ell\nu$	$30 \text{ GeV} < m_{\text{T}}(\ell, E_{\text{T}}^{\text{miss}}) < 100 \text{ GeV}$ b-tag

**Table 8.3:** The event selection criteria used in each background control region together with the main targeted background in the SR in each case. Also given is the process that is used to model the corresponding background.

### W+jets and ttbar background

The control regions for CRW and CRT select events that are enriched in  $W(\rightarrow l\nu) + \text{jets}$  and semi-leptonic  $t\bar{t}$  events. The selection requires one lepton (inverting the lepton veto of the SRs),  $E_{\text{T}}^{\text{miss}}$  and a transverse mass  $m_{\text{T}}$  of the lepton and  $E_{\text{T}}^{\text{miss}}$  of  $30 < m_{\text{T}} < 100 \text{ GeV}$ . The  $m_{\text{T}}$  cut ensures selection of leptonically decaying Ws. To distinguish between  $W + \text{jets}$  and  $t\bar{t}$  CRW discards events containing b-tagged jets but CRT requires events with at least one b-tagged jet. The kinematic cuts for the control regions are slightly lower compared to the signal region. For the selected events the required lepton is treated as a jet to mimic a mis-identified lepton and consequently all variables using jets are recomputed, e.g.  $\Delta\phi(\text{jet}_i, E_{\text{T}}^{\text{miss}})_{\text{min}}$ .

### $Z \rightarrow \nu\nu$ background

To estimate the  $Z \rightarrow \nu\nu$  background, events with similar kinematic properties as the signal region are used. Unfortunately selecting  $Z(\rightarrow ll) + \text{jets}$  events results in too low statistics.  $\gamma + \text{jets}$  events are therefore selected for CRY as this process is similar enough with respect to instrumental effects for boosted Z bosons. The Z is expected to be boosted as otherwise not

enough  $E_T^{\text{miss}}$  would be generated to enter the SR. CRY requires a high  $p_T$  photon instead of the  $E_T^{\text{miss}}$  requirement. Following the event selection  $E_T^{\text{miss}}$  is recomputed including the photon as missing transverse energy.

As currently only LO  $\gamma$ +jets cross sections are available a correction factor for the CR events is used to reduce theoretical uncertainties. To derive the correction factor  $\kappa$  an additional CR is defined around the Z mass peak selecting two electrons or muons. The resulting additional CR has very high statistics. The obtained correction factor is  $\kappa = 1.39 \pm 0.05$ . The resulting background estimation for the SR is obtained with

$$N_{\text{SR}}^{\text{est}, Z\nu\nu} = N_{\text{SR}}^{Z\nu\nu, \text{MC}} \frac{N_{\text{CRY}}^{\gamma+\text{jets}, \text{data}}}{N_{\text{CRY}}^{\gamma+\text{jets}, \text{MC}}} \kappa \quad (8.4)$$

### Multijet

For CRQ enriched in QCD jets events the selection uses an inverted and tightened  $\Delta\phi(\text{jet}_i, E_T^{\text{miss}})_{\text{min}}$  cut in addition to a reverted and loosened  $E_T^{\text{miss}}/\sqrt{H_T}$  or  $E_T^{\text{miss}}/m_{\text{eff}}$  (depending on the SR) cut. The multi-jet background in both searches is estimated using a data-driven technique[181], which applies a resolution function to well-measured multi-jet events in order to estimate the impact of jet energy mis-measurement and heavy-flavour semileptonic decays on  $E_T^{\text{miss}}$  and other variables.

As an example, the  $m_{\text{eff}}$  distributions in control regions associated with  $M_{\text{eff}}\text{-}4\text{j-}1000$  selections are shown in Fig. 8.5 and 8.6. In all CRs, the data are consistent with the pre-fit MC background prediction within uncertainties.

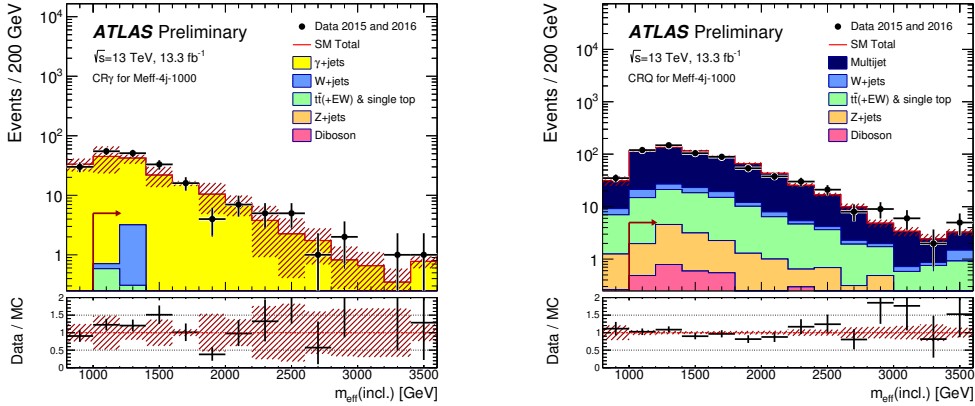


**Figure 8.5:** Exemplary  $m_{\text{eff}}$ -distributions in the control regions  $\text{CR}_\gamma$  (left) and  $\text{CR}_Q$  (right) for signal region  $M_{\text{eff}}\text{-}4\text{j-}1000$ . The arrows indicate the values at which the requirements on  $m_{\text{eff}}$  are applied. The histograms show the pre-fit MC background expectations, normalized to cross-section times integrated luminosity.

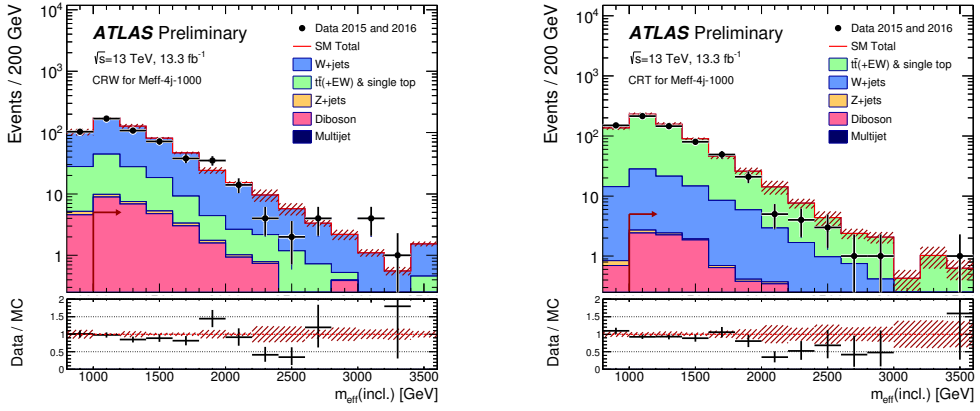


**Figure 8.6:** Exemplary  $m_{\text{eff}}$ -distributions in the control regions CRW (left) and CRT (right) for signal region  $M_{\text{eff}}-4j-1000$ . The arrows indicate the values at which the requirements on  $m_{\text{eff}}$  are applied. The histograms show the pre-fit MC background expectations, normalized to cross-section times integrated luminosity.

### 8.4.3 Validation regions

The background estimation procedure is validated by comparing the numbers of events observed in the VRs to the corresponding SM background expectations obtained from the background-only fits. Several VR samples are selected in both searches, with requirements distinct from those used in the CRs, which maintain a low probability of signal contamination.

The CRY estimates of the  $Z \rightarrow \nu\nu$ +jets background are validated using the samples of  $Z \rightarrow ll$ +jets events selected by requiring high-purity lepton pairs of opposite sign and identical flavour for which the di-lepton invariant mass lies within 25 GeV of the mass of the Z boson. As in CRY in the VRZ regions the leptons are treated as contributing to  $E_T^{\text{miss}}$ .

The CRW and CRT estimates of the  $W$ +jets and top quark background are validated with the same control region selections, but adding back the cut on  $\Delta\phi(\text{jet}_i, E_T^{\text{miss}})_{\text{min}}$ . For each CR two validation regions are defined, one treats the lepton as a jet, recomputing affected variables (VRW and VRT) the other one treats the lepton as missing transverse energy (VRW $\nu$  and VRT $\nu$ ).

The multi-jet background estimation is validated by using the same selections as CRQ but with the original  $E_T^{\text{miss}}/\sqrt{H_T}$  and  $E_T^{\text{miss}}/m_{\text{eff}}$  requirements of the SR (VRQa). The second VR uses the CR selections with a with an intermediate value of  $\Delta\phi(\text{jet}_i, E_T^{\text{miss}})_{\text{min}}$  (VRQb).

Fig. 8.7 shows the differences in each VR between the numbers of observed and expected events expressed as fractions of the one-standard deviation ( $1\sigma$ ) uncertainties on the latter. Most VR observations lie within  $1\sigma$  of the background expectations for both searches, with the largest discrepancy being  $-2.3\sigma$  in VRQa associated with the SR Meff-2j-2000.

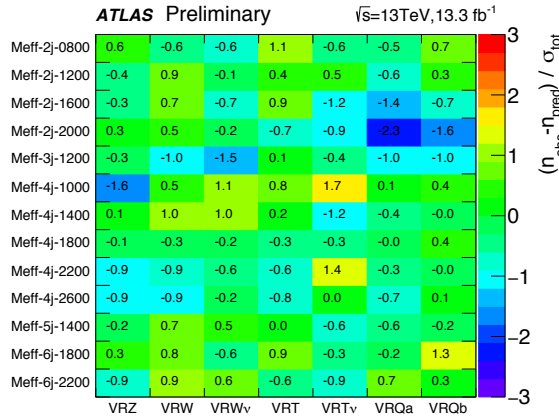


**Figure 8.7:** Differences of the observed to expected background events in each validation region as a fraction of the total uncertainty.

#### 8.4.4 Systematic uncertainties

The expected number of background and signal events can be biased by the systematic uncertainties that arise from the various steps necessary to arrive at the estimation. Sources for systematic uncertainties are the object reconstruction of jets and  $E_T^{\text{miss}}$  for example. The derivation of these uncertainties is described for each object in § 6. Also the uncertainties from the background and signal simulation by Monte Carlo generators and the use of transfer factors influence the final expected number. The systematic uncertainties of all contributing elements is taken into account in the likelihood fit.

Table 8.4 shows the main contributions to the background estimation. The uncertainties of different sources can be correlated and are taken into account where necessary. Here the overall background uncertainty has a range from 8% in Meff-2j-0800 and Meff-4j-1000 up to 43% in Meff-6j-2200 largely due to statistical uncertainties. The percentage is given for the number of total expected background events in the SR.

For the background estimation one of the major contributions arises from the jet energy scale (JES) calibration and jet energy resolution (see § 6) as well as the uncertainty on  $E_T^{\text{miss}}$ . Other large contributions come from the theoretical uncertainties and statistical limitations of the MC samples. The combined uncertainty from JES, JER and  $E_T^{\text{miss}}$  ranges from 1% in 2-jet SRs to 12% in SR Meff-6j-2200.

To estimate the theoretical uncertainties of the background modelling samples for the same background process but generated by different MC generators are compared. This procedure is used for the top quark pair production. Another possibility is to vary the input parameters of the modelling. For W/Z + jets production uncertainties are estimated by increasing and decreasing the renormalization, factorization and resummation scales by a factor of two as well as by increasing and decreasing the nominal Catani-Krauss-Kuhn-Webber (CKKW) [201] matching scale by 10 GeV and 5 GeV, respectively. Uncertainties in diboson production from renormalisation and factorisation scales are estimated by varying the scales in the MC generator and are applied as a uniform 50% for all SRs.

The uncertainties coming from the correction factor  $\kappa$  used in CR $\gamma$  are shown separately in Tab. 8.4, all other statistical and systematic uncertainties are given as a combined value for each SR. For most SRs the contribution from the CR correction factor is around 2%, except in the Meff-2j-0800, Meff-2j-1200 and Meff-2j-2000 SRs where it reaches the maximal value of 4%. The jet-smearing method used for the multi-jet background estimation is accounted for by a uniform 100% resulting in a maximum overall uncertainty contribution of 1%. The impact of the lepton reconstruction and the b-tagging efficiency are found to be negligible.



Channel	Meff-2j-0800	Meff-2j-1200	Meff-2j-1600	Meff-2j-2000	Meff-3j-1200
Total bkg	610	297	121	42	355
Total bkg unc.	$\pm 50$ [8%]	$\pm 29$ [10%]	$\pm 13$ [11%]	$\pm 6$ [14%]	$\pm 33$ [9%]
MC statistics	–	$\pm 3.1$ [1%]	$\pm 1.8$ [1%]	$\pm 1.0$ [2%]	$\pm 4$ [1%]
$\Delta\mu_{Z+\text{jets}}$	$\pm 12$ [2%]	$\pm 8$ [3%]	$\pm 5$ [4%]	$\pm 2.9$ [7%]	$\pm 9$ [3%]
$\Delta\mu_{W+\text{jets}}$	$\pm 9$ [1%]	$\pm 8$ [3%]	$\pm 5$ [4%]	$\pm 2.5$ [6%]	$\pm 8$ [2%]
$\Delta\mu_{\text{Top}}$	$\pm 5$ [1%]	$\pm 3.5$ [1%]	$\pm 2.2$ [2%]	$\pm 0.21$ [1%]	$\pm 7$ [2%]
$\Delta\mu_{\text{Multi-jet}}$	$\pm 0.04$ [0%]	$\pm 0.1$ [0%]	–	–	$\pm 0.03$ [0%]
CR $\gamma$ corr. factor	$\pm 22$ [4%]	$\pm 11$ [4%]	$\pm 4$ [3%]	$\pm 1.5$ [4%]	$\pm 11$ [3%]
Theory Z	$\pm 40$ [7%]	$\pm 22$ [7%]	$\pm 9$ [7%]	$\pm 3.0$ [7%]	$\pm 22$ [6%]
Theory W	$\pm 0.32$ [0%]	$\pm 3.1$ [1%]	$\pm 1.0$ [1%]	$\pm 1.2$ [3%]	$\pm 0.7$ [0%]
Theory Top	$\pm 3.4$ [1%]	$\pm 0.6$ [0%]	$\pm 0.6$ [0%]	$\pm 0.24$ [1%]	$\pm 4$ [1%]
Theory Diboson	$\pm 14$ [2%]	$\pm 8$ [3%]	$\pm 4$ [3%]	$\pm 1.9$ [5%]	$\pm 16$ [5%]
Jet/MET	$\pm 5$ [1%]	$\pm 2.8$ [1%]	$\pm 1.8$ [1%]	$\pm 0.28$ [1%]	$\pm 4$ [1%]
Multi-jet method	$\pm 1.6$ [0%]	$\pm 0.4$ [0%]	–	–	$\pm 0.6$ [0%]

Channel	Meff-4j-1000	Meff-4j-1400	Meff-4j-1800	Meff-4j-2200	Meff-4j-2600	Meff-5j-1400
Total bkg	84	66	27.0	4.8	2.7	68
Total bkg unc.	$\pm 7$ [8%]	$\pm 8$ [12%]	$\pm 3.2$ [12%]	$\pm 1.1$ [23%]	$\pm 0.6$ [22%]	$\pm 9$ [13%]
MC statistics	$\pm 2.6$ [3%]	$\pm 1.8$ [3%]	$\pm 1.1$ [4%]	$\pm 0.35$ [7%]	$\pm 0.32$ [12%]	$\pm 2.3$ [3%]
$\Delta\mu_{Z+\text{jets}}$	$\pm 3.1$ [4%]	$\pm 3.0$ [5%]	$\pm 1.4$ [5%]	$\pm 0.4$ [8%]	$\pm 0.23$ [9%]	$\pm 3.2$ [5%]
$\Delta\mu_{W+\text{jets}}$	$\pm 1.9$ [2%]	$\pm 2.0$ [3%]	$\pm 1.1$ [4%]	$\pm 0.27$ [6%]	$\pm 0.4$ [15%]	$\pm 4$ [6%]
$\Delta\mu_{\text{Top}}$	$\pm 2.6$ [3%]	$\pm 1.6$ [2%]	$\pm 0.9$ [3%]	$\pm 0.16$ [3%]	$\pm 0.11$ [4%]	$\pm 4$ [6%]
$\Delta\mu_{\text{Multi-jet}}$	$\pm 0.03$ [0%]	$\pm 0.02$ [0%]	–	–	–	$\pm 0.02$ [0%]
CR $\gamma$ corr. factor	$\pm 1.9$ [2%]	$\pm 1.9$ [3%]	$\pm 0.7$ [3%]	$\pm 0.13$ [3%]	$\pm 0.06$ [2%]	$\pm 1.6$ [2%]
Theory Z	$\pm 4$ [5%]	$\pm 4$ [6%]	$\pm 1.4$ [5%]	$\pm 0.27$ [6%]	$\pm 0.13$ [5%]	$\pm 3.3$ [5%]
Theory W	$\pm 1.3$ [2%]	$\pm 0.7$ [1%]	$\pm 0.24$ [1%]	$\pm 0.06$ [1%]	$\pm 0.26$ [10%]	$\pm 2.1$ [3%]
Theory Top	$\pm 1.3$ [2%]	$\pm 3.2$ [5%]	$\pm 0.9$ [3%]	$\pm 0.5$ [10%]	$\pm 0.16$ [6%]	$\pm 3.2$ [5%]
Theory Diboson	$\pm 2.1$ [3%]	$\pm 2.8$ [4%]	$\pm 1.5$ [6%]	$\pm 0.4$ [8%]	$\pm 0.06$ [2%]	$\pm 4$ [6%]
Jet/MET	$\pm 2.0$ [2%]	$\pm 1.6$ [2%]	$\pm 0.34$ [1%]	$\pm 0.11$ [2%]	$\pm 0.09$ [3%]	$\pm 0.6$ [1%]
Multi-jet method	$\pm 0.32$ [0%]	$\pm 0.32$ [0%]	–	–	–	$\pm 0.16$ [0%]

Channel	Meff-6j-1800	Meff-6j-2200
Total bkg	5.5	0.82
Total bkg unc.	$\pm 1.0$ [18%]	$\pm 0.35$ [43%]
MC statistics	$\pm 0.6$ [11%]	$\pm 0.16$ [20%]
$\Delta\mu_{Z+\text{jets}}$	$\pm 0.4$ [7%]	$\pm 0.11$ [13%]
$\Delta\mu_{W+\text{jets}}$	$\pm 0.31$ [6%]	$\pm 0.12$ [15%]
$\Delta\mu_{\text{Top}}$	$\pm 0.4$ [7%]	$\pm 0.1$ [12%]
$\Delta\mu_{\text{Multi-jet}}$	–	–
CR $\gamma$ corr. factor	$\pm 0.1$ [2%]	$\pm 0.02$ [2%]
Theory Z	$\pm 0.21$ [4%]	$\pm 0.04$ [5%]
Theory W	$\pm 0.09$ [2%]	$\pm 0.04$ [5%]
Theory Top	$\pm 0.31$ [6%]	$\pm 0.21$ [26%]
Theory Diboson	$\pm 0.5$ [9%]	$\pm 0.07$ [9%]
Jet/MET	$\pm 0.12$ [2%]	$\pm 0.1$ [12%]
Multi-jet method	–	–

**Table 8.4:** An overview of the dominant systematic uncertainties in the background estimates.  $\Delta\mu$  uncertainties are the result of the control region statistical uncertainties and the systematic uncertainties entering a specific control region. In brackets, uncertainties are given relative to the expected total background yield.

The signal uncertainty is estimated by varying different input parameters. These are the renormalisation and factorisation scale, the  $\alpha_s$  scale for initial state radiation, the matching scale to link the MadGraph5 and PYTHIA8 and the A14\_NNPDF tunes for extra jet generation [198]. The last factor has the greatest influence on the overall signal uncertainty.

## 8.5 Results

The overview of the observed events and the SM prediction (from the background estimation fit) in each SR is shown in Fig. 8.8. A good agreement between data and the background prediction is observed. The largest deviation from the background is found in SR Meff-6j-1800 corresponding to a significance of 1.56 standard deviations.

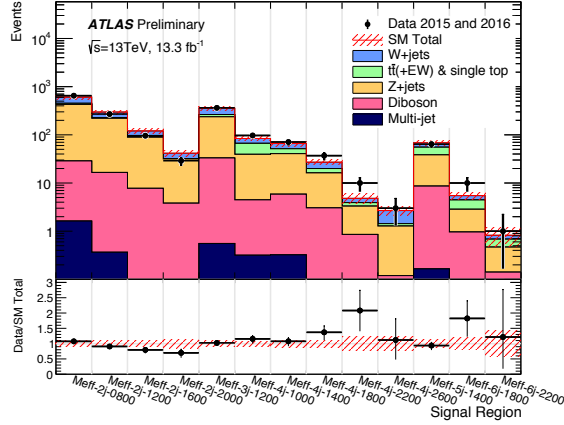


**Figure 8.8:** Comparison of the observed and expected event yields as a function of signal region. The background expectations are those obtained from the background-only fits as in 8.5

Fig. 8.9 - 8.11 show the  $m_{\text{eff}}$  distributions in selected signal regions before the background fit from the CRs with the background the Monte Carlo samples normalised by their theoretical cross-sections. All signal region selections are applied except the  $m_{\text{eff}}$  selection itself. The  $m_{\text{eff}}$  cut is indicated by the red arrows. Also shown are the  $m_{\text{eff}}$  distributions of the respective SUSY benchmark model for that SR. Already in these plots a good agreement between data and background within the theoretical uncertainties is seen.

The detailed numbers for each of the background predictions before and after the background-only fit for every SR are shown in Tab. 8.5. Also shown is the observed number of events in each SR. As no significant excess is observed the last segment of Tab. 8.5 shows the results of the model-independent fit given the number of expected events from the background-only fit: the 95% CL upper limits on the visible cross-section ( $\langle\epsilon\sigma\rangle_{\text{obs}}^{95}$ ), the visible number of signal events ( $S_{\text{obs}}^{95}$ ) and the number of signal events ( $S_{\text{exp}}^{95}$ ) as well as the corresponding p-value  $p_0$ . For the p-value also the number of equivalent Gaussian standard deviations  $Z$  is given.

For each of the simplified SUSY models the results are used to set model-dependent upper limits on the squark/gluino and the  $\tilde{\chi}_1^0$ . The model-dependent fit is done for each signal regions independently, the SR with the best expected sensitivity is chosen for each grid point. Here also the signal regions from the RJR approach are included, for completeness the sig-

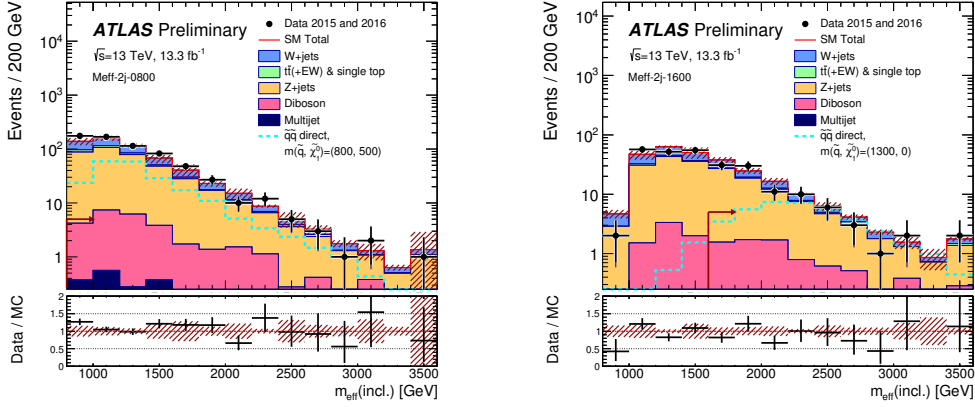


**Figure 8.9:** The observed  $m_{\text{eff}}$  distribution in signal region Meff-2j-0800 (left) and Meff-2j-1600 (right). The arrows indicate the values at which the requirements on  $m_{\text{eff}}$  are applied. The histograms show the pre-fit MC background expectations, normalized to cross-section times integrated luminosity. The red error band indicates the combined experimental, theoretical and MC statistical uncertainties. The distribution of a signal benchmark model is also shown to visualize the expected SUSY signal.

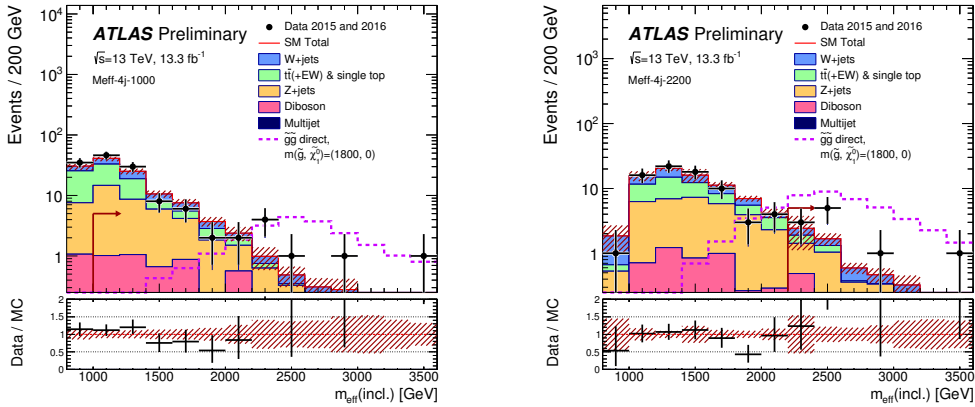


**Figure 8.10:** The observed  $m_{\text{eff}}$  distribution in signal region Meff-4j-1000 (left) and Meff-4j-2200 (right). The arrows indicate the values at which the requirements on  $m_{\text{eff}}$  are applied. The histograms show the pre-fit MC background expectations, normalized to cross-section times integrated luminosity. The red error band indicates the combined experimental, theoretical and MC statistical uncertainties. The distribution of a signal benchmark model is also shown to visualize the expected SUSY signal.

Signal Region	Meff-2j-0800	Meff-2j-1200	Meff-2j-1600	Meff-2j-2000	Meff-3j-1200
MC expected events					
Diboson	27	16	7.8	3.8	35
Z/ $\gamma^*$ +jets	365	183	70	24	219
W+jets	161	73	24	7.7	95
$t\bar{t}$ (+EW) + single top	30	10	3.7	1.5	41
Fitted background events					
Diboson	27 $\pm$ 14	16 $\pm$ 8	8 $\pm$ 4	3.8 $\pm$ 1.9	33 $\pm$ 16
Z/ $\gamma^*$ +jets	400 $\pm$ 50	204 $\pm$ 26	81 $\pm$ 11	28 $\pm$ 5	204 $\pm$ 27
W+jets	154 $\pm$ 11	71 $\pm$ 10	29 $\pm$ 4	9.3 $\pm$ 3.4	91 $\pm$ 8
$t\bar{t}$ (+EW) + single top	23 $\pm$ 5	6 $\pm$ 4	2.5 $\pm$ 2.3	0.7 $\pm$ 0.5	27 $\pm$ 10
Multi-jet	1.6 $\pm$ 1.6	0.4 $\pm$ 0.4	–	–	0.6 $\pm$ 0.6
Total Expected MC	584	283	106	37	387
Total Fitted bkg	610 $\pm$ 50	297 $\pm$ 29	121 $\pm$ 13	42 $\pm$ 6	355 $\pm$ 33
Observed	650	270	96	29	363
$\langle\epsilon\sigma\rangle_{\text{obs}}^{95}$ [fb]	11	3.7	1.4	0.73	6.0
$S_{\text{obs}}^{95}$	146	49	19	9.7	78
$S_{\text{obs}}^{95}$	115 $^{+42}_{-32}$	63 $^{+22}_{-17}$	30 $^{+12}_{-8}$	15.9 $^{+6.5}_{-4.6}$	74 $^{+27}_{-20}$
$p_0$ (Z)	0.23 (0.75)	0.50 (0.00)	0.50 (0.00)	0.50 (0.00)	0.42 (0.21)

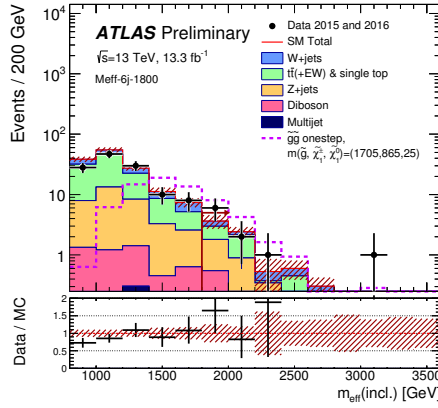
  

Signal Region	Meff-4j-1000	Meff-4j-1400	Meff-4j-1800	Meff-4j-2200	Meff-4j-2600	Meff-5j-1400
MC expected events						
Diboson	4.2	5.5	3.0	0.86	0.12	8.0
Z/ $\gamma^*$ +jets	29	34	14	2.7	1.3	37
W+jets	20	16	6.6	1.4	1.1	23
$t\bar{t}$ (+EW) + single top	31	14	6.7	0.88	0.48	21
Fitted background events						
Diboson	4.2 $\pm$ 2.1	5.5 $\pm$ 2.8	3.0 $\pm$ 1.5	0.9 $\pm$ 0.4	0.12 $\pm$ 0.06	8 $\pm$ 4
Z/ $\gamma^*$ +jets	35 $\pm$ 5	35 $\pm$ 5	13.2 $\pm$ 2.2	2.5 $\pm$ 0.5	1.16 $\pm$ 0.31	30 $\pm$ 5
W+jets	17.4 $\pm$ 2.5	14.7 $\pm$ 2.1	7.0 $\pm$ 1.2	0.89 $\pm$ 0.29	1.3 $\pm$ 0.5	13 $\pm$ 4
$t\bar{t}$ (+EW) + single top	27.2 $\pm$ 3.3	11 $\pm$ 5	3.8 $\pm$ 1.4	0.61 $^{+0.85}_{-0.61}$	0.16 $^{+0.21}_{-0.16}$	17 $\pm$ 6
Multi-jet	0.32 $\pm$ 0.32	0.32 $\pm$ 0.32	–	–	–	0.17 $^{+0.17}_{-0.17}$
Total Expected MC	85	70	31	5.8	3.1	89
Total Fitted bkg	84 $\pm$ 7	66 $\pm$ 8	27.0 $\pm$ 3.2	4.8 $\pm$ 1.1	2.7 $\pm$ 0.6	68 $\pm$ 9
Observed	97	71	37	10	3	64
$\langle\epsilon\sigma\rangle_{\text{obs}}^{95}$ [fb]	2.6	1.9	1.7	0.89	0.38	1.6
$S_{\text{obs}}^{95}$	35	26	22	12	5.1	22
$S_{\text{obs}}^{95}$	24 $^{+10}_{-7}$	23 $^{+8}_{-6}$	14 $^{+6}_{-4}$	7.9 $^{+3.5}_{-2.3}$	4.8 $^{+2.6}_{-1.6}$	24 $^{+9}_{-7}$
$p_0$ (Z)	0.14 (1.06)	0.34 (0.41)	0.06 (1.53)	0.07 (1.50)	0.43 (0.18)	0.50 (0.00)

Signal Region	Meff-6j-1800	Meff-6j-2200
MC expected events		
Diboson	0.96	0.14
Z/ $\gamma^*$ +jets	2.7	0.42
W+jets	1.38	0.29
$t\bar{t}$ (+EW) + single top	2.8	0.42
Fitted background events		
Diboson	1.0 $\pm$ 0.5	0.14 $\pm$ 0.08
Z/ $\gamma^*$ +jets	1.9 $\pm$ 0.5	0.33 $\pm$ 0.13
W+jets	1.04 $\pm$ 0.35	0.14 $\pm$ 0.13
$t\bar{t}$ (+EW) + single top	1.6 $\pm$ 0.5	0.22 $^{+0.26}_{-0.22}$
Multi-jet	–	–
Total Expected MC	8	1.3
Total Fitted bkg	5.5 $\pm$ 1.0	0.82 $\pm$ 0.35
Observed	10	1
$\langle\epsilon\sigma\rangle_{\text{obs}}^{95}$ [fb]	0.83	0.27
$S_{\text{obs}}^{95}$	11	3.5
$S_{\text{obs}}^{95}$	6.5 $^{+3.3}_{-2.1}$	3.3 $^{+2.1}_{-1.3}$
$p_0$ (Z)	0.06 (1.56)	0.43 (0.17)

**Table 8.5:**  $p_0$  and upper limit numbers of events observed in the signal regions compared with the pre-fit and fitted background expectations. For an observed number of events lower than expected, the p-value is truncated at 0.5.



**Figure 8.11:** The observed  $m_{\text{eff}}$  distribution in signal region  $M_{\text{eff}}\text{-}6\text{j-}1800$ . The arrows indicate the values at which the requirements on  $m_{\text{eff}}$  are applied. The histograms show the pre-fit MC background expectations, normalized to cross-section times integrated luminosity. The red error band indicates the combined experimental, theoretical and MC statistical uncertainties. The distribution of a signal benchmark model is also shown to visualize the expected SUSY signal.

nal region selections of the RJR approach can be found in Appendix 8.B . The background estimation for the RJR SRs is very similar to the  $m_{\text{eff}}$  based approach as for both the backgrounds and signal final states are identical. The RJR approach targets mainly compressed SUSY signals and it performs best in the compressed regions of the parameter space.

On the left (right) of Fig. 8.12 limits are shown for the direct decay squark (gluino) models. For the direct-decay squark model the upper 95% CL limit on the light-flavour squark mass region is 1.35 TeV assuming a massless  $\tilde{\chi}_1^0$ . The corresponding limit on the gluino mass is 1.86 TeV, if the  $\tilde{\chi}_1^0$  is massless.

In Fig. 8.13 the model-dependent limit for the one-step gluino decay models is shown. On the left the limit for gluinos decaying via an intermediate  $\tilde{\chi}_1^\pm$  to two quarks, a  $W$  boson and a  $\tilde{\chi}_1^0$  is shown. For a  $\tilde{\chi}_1^0$  mass up to  $\sim 400$  GeV, the lower limit on the gluino mass extends up to 1.83 TeV. On the right the limit for gluinos decaying via an intermediate  $\tilde{\chi}_2^0$  to two quarks, a  $Z$  boson and a  $\tilde{\chi}_1^0$  extends up to gluino masses of 1.9 TeV for  $\tilde{\chi}_2^0$  masses of  $\sim 600$  GeV.



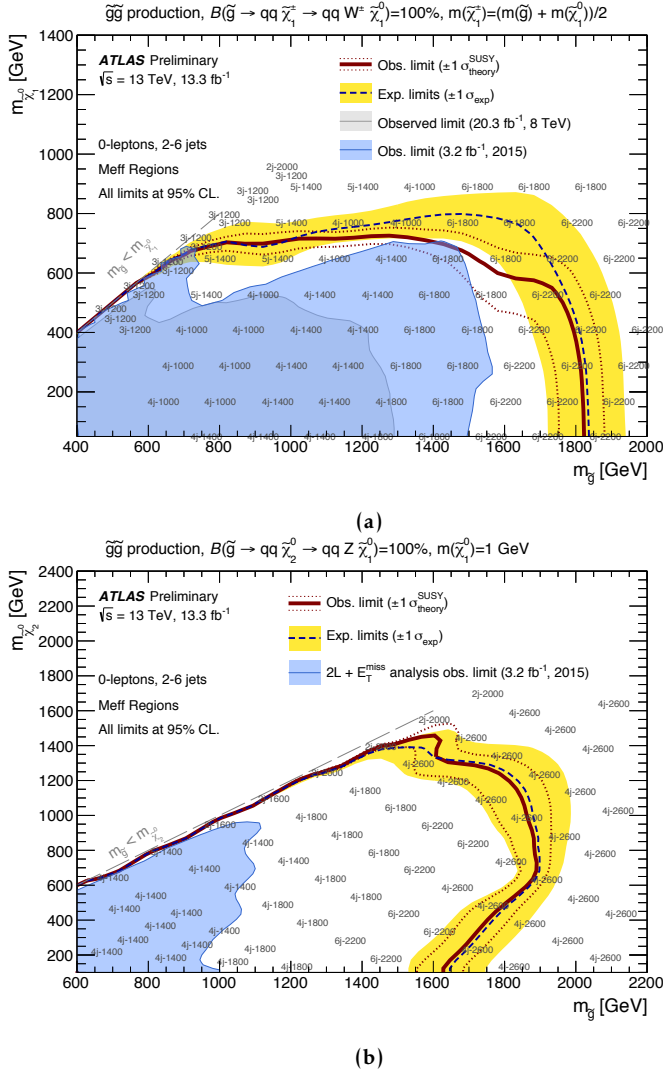


**Figure 8.13:** Exclusion limits for the onestep gluino decay models via a  $\tilde{\chi}_1^\pm$  (a) and via a  $\tilde{\chi}_2^0$  (b). The exclusion limits are obtained by using the signal region with the best expected sensitivity at each point. The signal regions providing the best expected sensitivity at a selection of model points are indicated in the plot together with the expected limits at 95% CL (blue) and their  $1\sigma$  excursions due to experimental and background-only theoretical uncertainties (yellow). The observed limits from this analysis are shown in brown, the ones obtained by the previous ATLAS searches with no leptons, jets and missing transverse momentum is shaded in blue.

## 8.A Boosted boson studies

The short time between the final 2015 publication [178] of this analysis and the described update with the first data in 2016 only allowed for marginal changes and new signal regions based on the existing ones in 2015. Nevertheless there are ongoing studies to improve the sensitivity of the current analysis introducing new supersymmetry signal models with the goal to be included in a later publication of this analysis (then with a larger data set).

An interesting avenue is the extension of the existing simplified one-step decay models. In the current one-step models the gluino is decaying to either the  $W$  or the  $Z$  with a 100% branching ratio (see 8.3). In the new model it is proposed that the gluino can decay into either a  $W$  or a  $Z$ /Higgs boson, allowing decays to a Higgs boson for the first time. The same is proposed for a one-step squark model. The schematic decay for this type of simplified model is shown in Fig. 8.A.1. For certain mass splittings the bosons in the final state can be boosted. This type of model gives therefore a good opportunity to study the use of boson-tagging techniques and fat jets (jets reconstructed with the anti- $k_t$  algorithm and  $R = 1.0$ ).

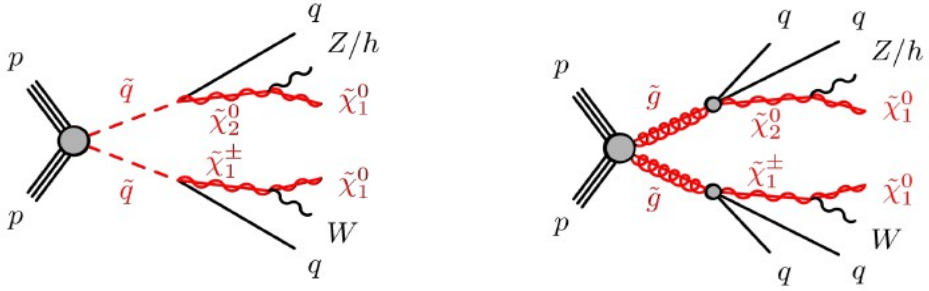


**Figure 8.A.1:** Schematic drawing of the decay topology of the one-step squark and gluino decay models. They show the decay via either an intermediate  $\tilde{\chi}_1^\pm$  or an intermediate  $\tilde{\chi}_2^0$ .

The branching ratios for these new one-step decays are set motivated by possible pMSSM scenarios with similar properties. The branching ratios in the pMSSM scenarios where calculated with SUSY\_HIT [202]. In this study  $m_{\tilde{\chi}_2^0} = m_{\tilde{\chi}_1^\pm}$  is used, the resulting branching ratio for a squark (gluino) decaying to the  $\tilde{\chi}_i^\pm$  is set to 50%, for a squark (gluino) decaying to the  $\tilde{\chi}_2^0$  is therefore also set to 50%. The  $\tilde{\chi}_i^\pm$  decays with a 100% BR to a  $W$  and a  $\tilde{\chi}_1^0$ , the  $\tilde{\chi}_2^0$  decays with a BR of 50% in either a  $Z$  or the  $h$  and a  $\tilde{\chi}_1^0$ .

The properties of the proposed models have been studied in truth studies comparing the most important distributions to the existing one-step models in this analysis. The results are very similar for the gluino and squark models, only the one-step squark model distributions are shown in Fig. 8.A.2 - 8.A.7. Fig. 8.A.2 - 8.A.7 show the comparison of the existing one-step model with 100% BR to  $\tilde{\chi}_1^\pm$  in green, the newly proposed model with decays to both  $W$  and  $Z$ /Higgs in blue. For both models the same mass point was chosen with  $m_{\tilde{q}} = 800$  GeV,  $m_{\tilde{\chi}_2^\pm(\tilde{\chi}_2^0)} = 460$  GeV and  $m_{\tilde{\chi}_1^0} = 60$  GeV.



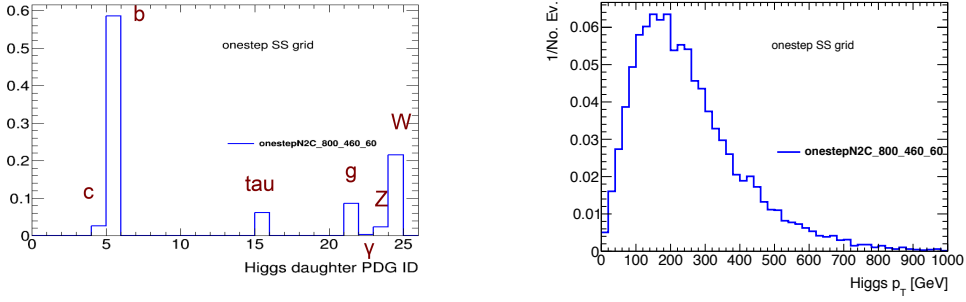


**Figure 8.A.2:** Characteristic Higgs daughters with PDG ID and the characteristic Higgs  $p_T$  distribution in a simplified one-step squark decay model with a decay via  $W/Z/H$  bosons.

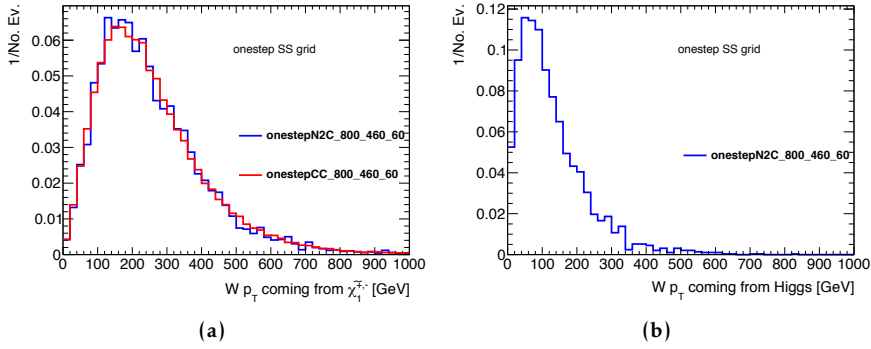


**Figure 8.A.3:** Characteristic  $p_T$  distribution for the W bosons (left) from the decay of a  $\tilde{\chi}_1^\pm$  and (right) from the decay of a Higgs boson in a simplified one-step squark decay model with a decay via  $W/Z/H$  bosons.

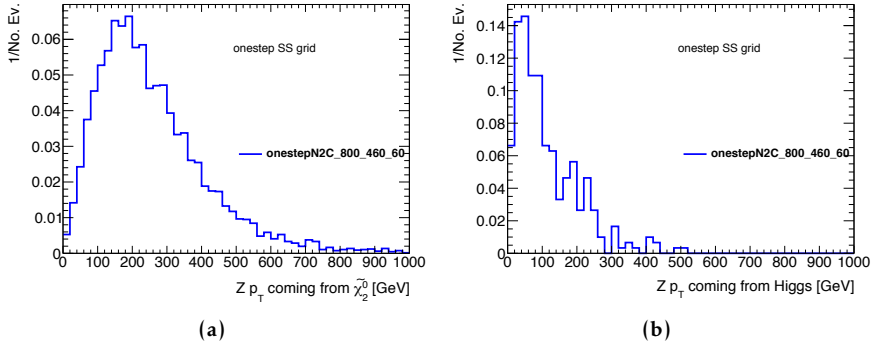


**Figure 8.A.4:** Characteristic  $p_T$  distribution for the Z bosons (left) from the decay of a  $\tilde{\chi}_2^0$  and (right) from the decay of a Higgs boson in a simplified one-step squark decay model with a decay via  $W/Z/H$  bosons.

The W and Z bosons from the  $\tilde{\chi}_1^\pm$  and  $\tilde{\chi}_2^0$  decays respectively both have a similar  $p_T$  spectrum peaking around 200 GeV whereas their  $p_T$  spectrum as expected is much lower if they come from the decay of a Higgs boson. This difference in the  $p_T$  spectra can be used to select signal

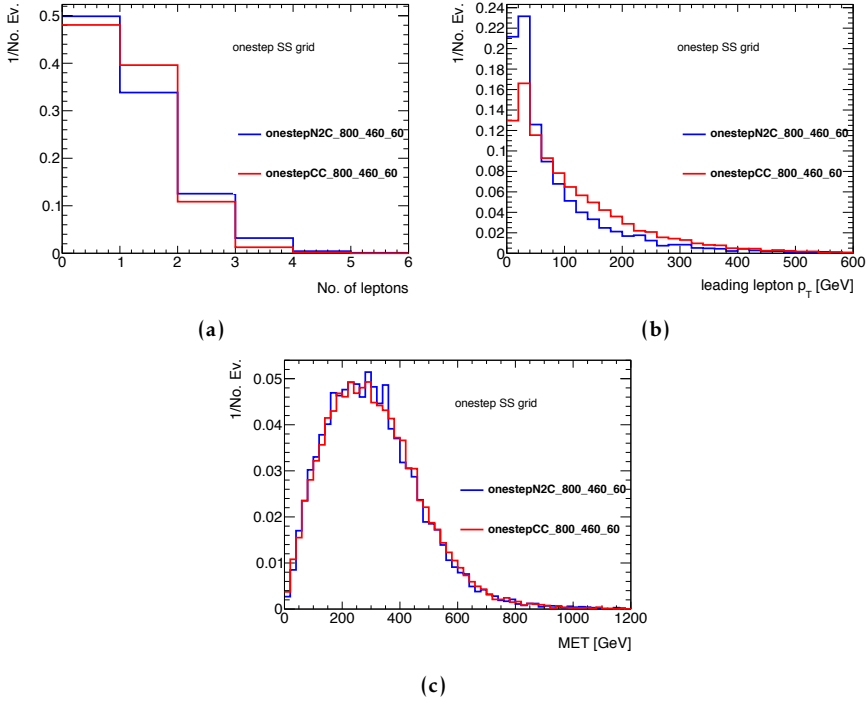


**Figure 8.A.5:** Characteristic distributions of leptons (a – b) and  $E_T^{\text{miss}}$  (c) for a simplified one-step squark decay model with a decay via  $W/Z/H$  bosons compared to the existing one-step squark decay via  $Ws$ .

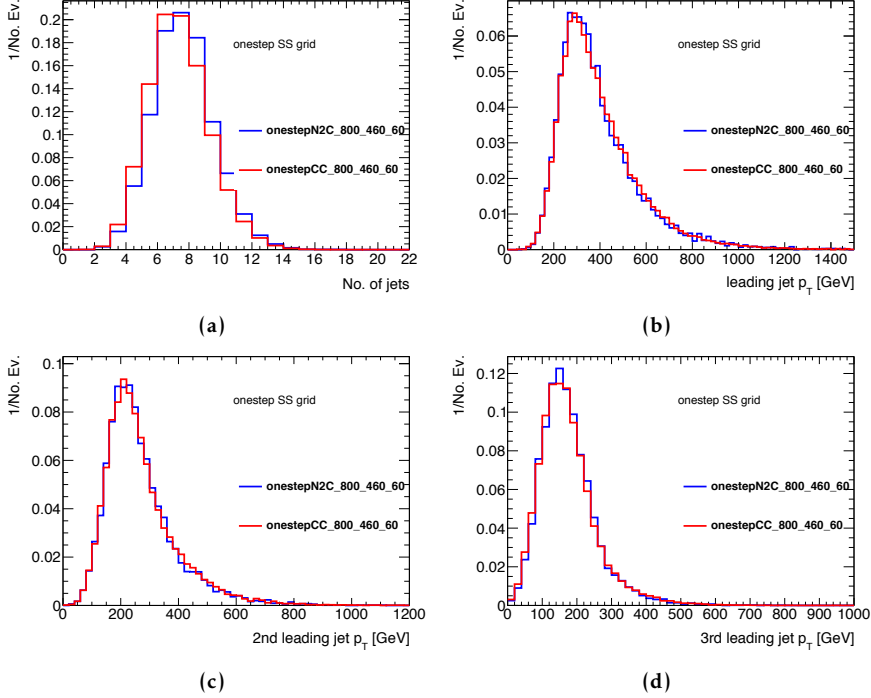


**Figure 8.A.6:** Characteristic distributions of the numbers of jets (a) and the 1st to 3rd leading jet  $p_T$  (b–d) for a simplified one-step squark decay model with a decay via  $W/Z/H$  bosons compared to the existing one-step squark decay via  $W$ s. All jets are reconstructed with the anti- $k_t$  algorithm and  $R=0.4$ .

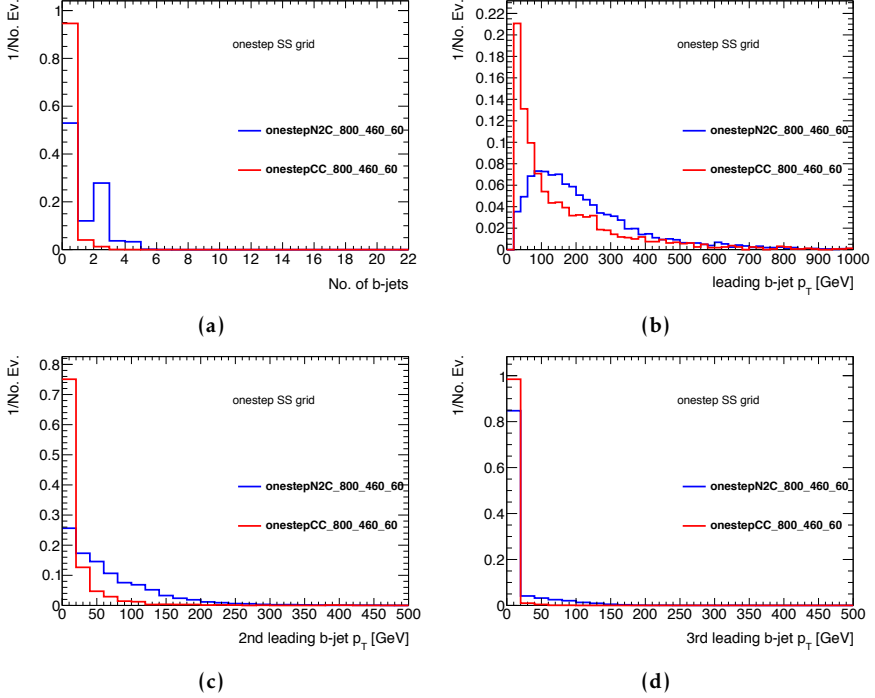


**Figure 8.A.7:** Characteristic distributions of the number of b-jets (a) and 1st to 3rd leading b-jet  $p_T$  (b–d) for a simplified one-step squark decay model with a decay via  $W/Z/H$  bosons compared to the existing one-step squark decay via  $Ws$ . All jets are reconstructed with the anti- $k_T$  algorithm and  $R=0.4$ .

events with boosted boson tagging techniques.

Another main difference in the final state of the simplified model with allowed decays via  $\tilde{\chi}_2^0$  /  $\tilde{\chi}_1^\pm$  is the higher number of b-jets which are in addition also more energetic. This feature raises possibilities for signal regions with b-tagged jets.

These initial studies led to new signal regions for the 2017 Moriond analysis [203] making use of large-R jets for better sensitivity to the boosted topology. With the discovery of the Higgs boson it is important to include it in the signal models and not just ignore it. This way new possibilities open up to enhance signal sensitivity .

## 8.B RJR based signal regions

Tab. 8.B.1 shows the signal region definitions for the analysis part using the Recursive-Jigsaw-Reconstruction (RJR) approach [184]. As the RJR signal regions are included in the final signal dependent fits they are given here for completeness. For further details see [177].

Targeted signal	$\tilde{q}\tilde{q}, \tilde{q} \rightarrow q\tilde{\chi}_1^0$					
Requirement	Signal Region					
	RJR-S1	RJR-S2	RJR-S3			
$H_{1,1}^{\text{PP}}/H_{2,1}^{\text{PP}} \geq$	0.6	0.55	0.5			
$H_{1,1}^{\text{PP}}/H_{2,1}^{\text{PP}} \leq$	0.95	0.96	0.98			
$p_{\text{PP},z}^{\text{lab}} / (p_{\text{PP},z}^{\text{lab}} + H_{T,2,1}^{\text{PP}}) \leq$	0.5	0.55	0.6			
$p_{j2,T}^{\text{PP}}/H_{T,2,1}^{\text{PP}} \geq$	0.16	0.15	0.13			
$\Delta_{\text{QCD}} >$	0.001					
	RJR-S1a	RJR-S1b	RJR-S2a	RJR-S2b	RJR-S3a	RJR-S3b
$H_{T,2,1}^{\text{PP}} [\text{GeV}] >$	1000	1200	1400	1600	1800	2000
$H_{1,1}^{\text{PP}} [\text{GeV}] >$	1000		1400		1600	

Targeted signal	$\tilde{g}\tilde{g}, \tilde{g} \rightarrow q\bar{q}\chi_1^0$					
Requirement	Signal Region					
	RJR-G1		RJR-G2		RJR-G3	
$H_{1,1}^{\text{PP}}/H_{4,1}^{\text{PP}} \geq$	0.35		0.25		0.2	
$H_{T\,4,1}^{\text{PP}}/H_{4,1}^{\text{PP}} \geq$	0.8		0.75		0.65	
$p_{\text{PP},\,z}^{\text{lab}}/(p_{\text{PP},\,z}^{\text{lab}} + H_{T\,4,1}^{\text{PP}}) \leq$	0.5		0.55		0.6	
$\min(p_{j2\,T\,i}^{\text{PP}}/H_{T\,2,1\,i}^{\text{PP}}) \geq$	0.12		0.1		0.08	
$\max(H_{1,\,0}^{\text{P}_i}/H_{2,\,0}^{\text{P}_i}) \leq$	0.95		0.97		0.98	
$ \frac{2}{3}\Delta\phi_{V,P}^{\text{PP}} - \frac{1}{3}\cos\theta_{\text{p}}  \leq$	0.5		-			
$\Delta_{\text{QCD}} >$	0					
	RJR-G1a	RJR-G1b	RJR-G2a	RJR-G2b	RJR-G3a	RJR-G3b
$H_{T\,4,1}^{\text{PP}} [\text{GeV}] >$	1000	1200	1500	1900	2300	2800
$H_{1,1}^{\text{PP}} [\text{GeV}] >$	600		800		900	

Targeted signal	compressed spectra in $\tilde{q}\tilde{q} (\tilde{q} \rightarrow q\tilde{\chi}_1^0); \tilde{g}\tilde{g} (\tilde{g} \rightarrow q\tilde{q}\tilde{\chi}_1^0)$					
Requirement	Signal Region					
	RJR-C1	RJR-C2	RJR-C3	RJR-C4	RJR-C5	
$R_{\text{ISR}} \geq$	0.9	0.85	0.8	0.75	0.70	
$\Delta\phi_{\text{ISR},1} \geq$	3.1	3.07	2.95	2.95	2.95	
$\Delta\phi(\text{jet}_{1,2}, \mathbf{E}_T^{\text{miss}})_{\min} >$	-	-	-	0.4	0.4	
$M_{\text{TS}} [\text{GeV}] \geq$	100	100	200	500	500	
$p_{\text{TS}}^{\text{CM}} [\text{GeV}] \geq$	800	800	600	600	600	
$N_{\text{jet}}^V \geq$	1	1	2	2	3	

**Figure 8.B.1:** Selection criteria and targeted signal model used to define signal regions in the RJR-based search, indicated by the prefix 'RJR'. Each SR is labelled with the targeted SUSY particle or the targeted region of parameter space, such that 'S', 'G' and 'C' denote regions searching for squark-, gluino-pair production, or compressed spectra, respectively.

## 8.C Trigger studies

The following triggers were used in 2015 datasets: SR events are required to pass HLT\_xe70 trigger. For CRW, CRT, CRZ events are required to pass the lowest unscaled single electron or muon trigger, CRY events are required to pass the lowest unscaled single photon trigger.

The following triggers are used in this analysis for 2016: SR events are required to pass HLT\_xe80\_tc\_lcw\_L1XE50 or HLT\_xe100\_mht\_L1XE50 for later runs, CRW, CRT, CRZ events are required to pass the lowest unscaled single electron or muon trigger. CRY events are required to pass the lowest unscaled single photon trigger.

### Trigger efficiencies

Figure 8.C.1 shows the turn-on of the HLT\_xe80\_tc\_lcw\_L1XE50 trigger. To get a sample of events with mostly genuine  $E_T^{\text{miss}}$  to measure the trigger turn-ons, a lowest un-prescaled electron trigger is required in addition to the trigger under study in order to enrich the sample in  $W \rightarrow e\nu$ .

Figure 8.C.2 shows the turn-on of the different  $E_T^{\text{miss}}$  trigger variants on a sample with a signal region like preselection. In addition to the studied trigger four jets are required, the leading jet with a  $p_T > 130$  GeV, the other three with a  $p_T > 50$  GeV. This figure motivates using the topocluster variant with a  $E_T^{\text{miss}}$  threshold of 80 GeV.

For later runs, the performance of HLT\_xe100\_mht\_L1XE50 is also checked. Figure 8.C.5 shows trigger efficiencies measured for data and  $t\bar{t}$  MC. To ensure that trigger efficiency is in plateau,  $E_T^{\text{miss}} > 250$  GeV is required in offline analysis.

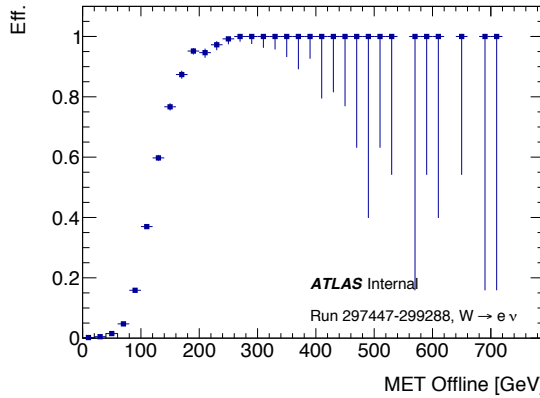
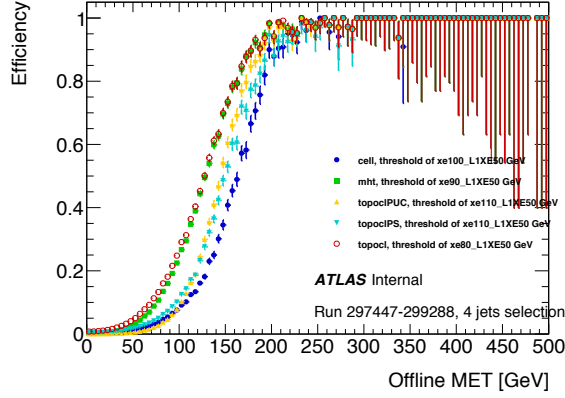
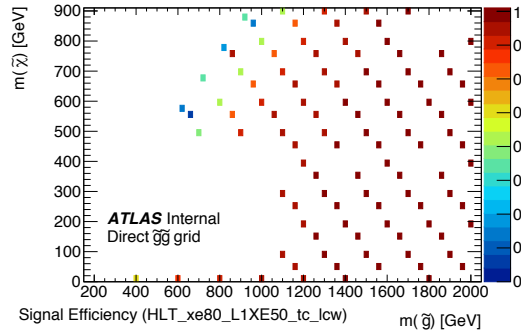


Figure 8.C.1: Trigger turn-on for HLT\_xe80\_tc\_lcw\_L1XE50 for 2016 data.

Figures 8.C.3 and 8.C.4 show the trigger efficiency for the signal samples for the gluino-pair production with direct decay of the gluinos and squark-pair production with direct decay of the squarks without any kinematic cuts.



**Figure 8.C.2:** Trigger turn-on for all  $E_T^{\text{miss}}$  trigger variants for 2016 data.



**Figure 8.C.3:** Trigger efficiencies for HLT\_xe80\_tc\_lcw on signal samples of gluino-pair production with direct decay of the gluinos.

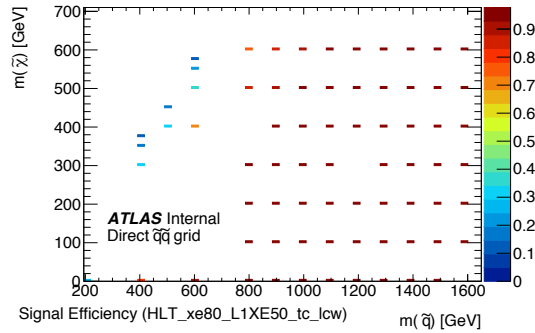


**Figure 8.C.4:** Trigger efficiencies for HLT\_xe80\_tc\_lcw on signal samples of squark-pair production with direct decay of the squarks.



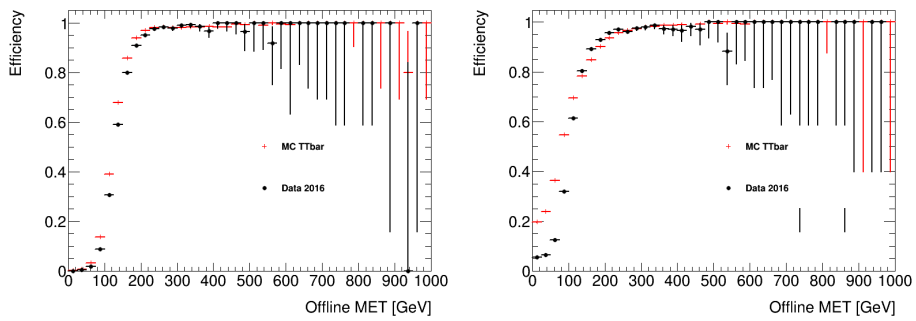


**Figure 8.C.5:** Trigger efficiencies for HLT\_xe100\_mht\_L1XE50 on data and  $t\bar{t}$  MC using electron events (left) and muon events (right).

## CHAPTER 9

### Conclusions

With the start of Run II in 2015, the center-of-mass energy of the LHC was increased to 13 TeV. This increase, together with the large data set accumulated to date, opens new possibilities to explore unknown areas of phase space, testing the Standard Model and searching for Beyond the Standard Model physics.

Unlike the Higgs boson discovery in Run I, Run II has not seen a major discovery yet. The search for squarks and gluinos in final states with jets and  $E_T^{\text{miss}}$  as presented in Chapter 8 is no exception. There were no hints of supersymmetry in the analyzed  $L_{\text{int}} = 13.3 \text{ fb}^{-1}$  of collected data, the search resulted in increased limits for gluino and squark masses to 1.86 TeV and 1.35 TeV respectively (for direct decay models). At the point of writing, the analyzed collected data set increased to  $36.1 \text{ fb}^{-1}$  still without discovery of strong squark/gluino production [203]. Fig. 9.1 shows an overview of the mass limits for various SUSY particles in different models derived by selected ATLAS SUSY searches.

With the ever increasing mass limits, it would be easy to declare that SUSY searches have been to no avail and abandon them, but that would be too simple. SUSY still remains an interesting theory, there are several possible reasons why it is not discovered yet.

One reason could be that squarks and gluinos are just too heavy. If that is the case the full Run II data set available end of 2018 and in the long term Run III provide further opportunities to extend the mass reach. As discussed in Chapter 7 there is no preferred mass value for squarks.

The same case of being too heavy could also apply to the lightest stable particle. As shown in Fig. 9.2 exemplary for the gluino, its mass limits reaches up to 2 TeV for a  $\tilde{\chi}_1^0$  mass around 500 GeV for gluino decays to first and second generation quarks. Models with a gluino decay to tops slightly decrease that limit to 1.85 TeV but with a  $\tilde{\chi}_1^0$  mass around 900 GeV, leaving room for improvement. So far, analyses have been optimized for exclusion reach in the gluino (squark) axis. On the contrary to the gluino/squark mass a LSP mass below 100 GeV is preferred by the MSSM likelihood scans with a maximum value for  $m_{\tilde{\chi}^0}$  of 1.5 TeV if all constraints are included.

However too heavy SUSY particles are opposing one of SUSY's major motivations - the solution to the hierarchy problem. To cancel the contributions of the SM particles to the Higgs mass (see § 2.2) without introducing new superficial fine-tuning the masses of the supersymmetric particles should not be too large. The fine-tuning argument is especially important for the stop with the top quark as the main contributor and for the higgsinos which mass should

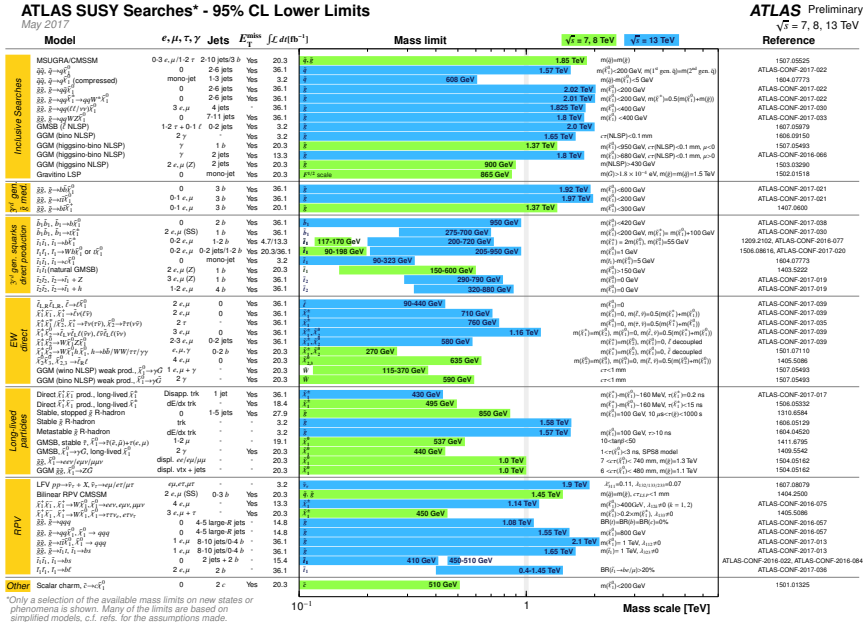


**Figure 9.1:** Mass reach of ATLAS searches for Supersymmetry (May 2017). Only a representative selection of the available results is shown. [204]

be of the same order as the Z boson (no stringent limits have been set for the higgsino mass yet). One could argue that the hierarchy problem and naturalness are rather philosophical problems and therefore not a major constraint for SUSY particle masses. However, without solving the hierarchy problem, SUSY as a theory loses much of its elegance and appeal.

Compressed mass spectra could be another reason why SUSY has not been discovered yet. One speaks of a compressed mass spectra when the mass differences between particles are very small, in this case between the  $\tilde{\chi}_1^0$  and the gluino or squark. Due to the low mass difference, the resulting decay products have a very soft  $p_T$  spectrum. Final states with low  $p_T$  jets and only little  $E_T^{\text{miss}}$  are in general difficult to select and to distinguish from QCD background. This is especially true for the search presented in this thesis as it is optimized for final states with high  $p_T$  jets and large  $E_T^{\text{miss}}$  resulting in low sensitivity to low  $p_T$  final states. As seen in Fig. 8.12 and Fig. 8.13, masses as low as 800 GeV are still allowed for squarks and gluinos for compressed spectra. This is the case despite the already existing efforts of having one or two signal regions more tailored to these type of models and the RJR based analysis part which was designed to be more sensitive to models with small mass differences. To not be blind to SUSY models with compressed spectra is a major challenge for the future and a continuous effort on the ATLAS SUSY community.

Of course all these mass limits are model dependent and favored models change with the time in addition to the trend to become more complex. First Run I limits were given in

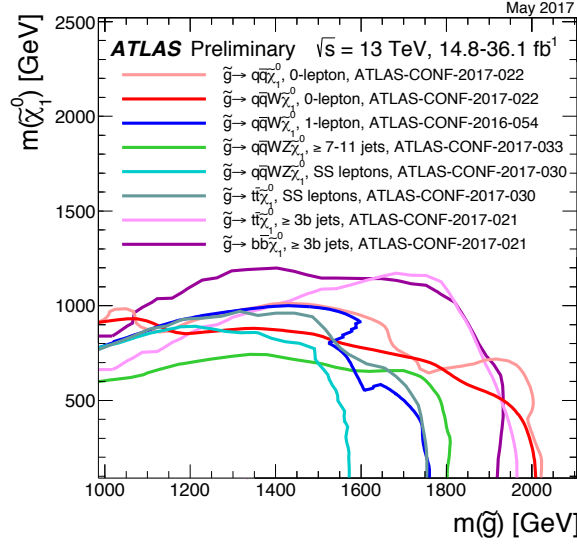


**Figure 9.2:** Exclusion limits at 95% CL for 13 TeV in the (gluino, lightest neutralino) mass plane for different simplified models featuring the decay of the gluino to the lightest neutralino either directly or through a cascade chain featuring other SUSY particles with intermediate mass. For each line, the gluino decay mode is reported in the legend and it is assumed to proceed with 100% branching ratio. The limits might depend on additional assumptions on the mass of the intermediate states, as described in the references provided in the plot.[204]

mSUGRA a SUSY model with only 5 free parameters. By now scans of the pMSSM with its 19 free parameters are no novelty anymore. Their main goal is to identify slices of parameter space that are currently not probed and to give hints as how to possibly improve the existing searches. ATLAS itself conducted a pMSSM scan with the full Run I data set including the constraints from the Run I SUSY searches [205]. This resulted in figures like Fig. 9.3 showing the percentage of excluded model points in the mass range of SUSY particles. It again shows that there are many models left that have relatively high LSP masses.

The current use of simplified models avoids choosing a specific SUSY model but under the assumption of the most simplest decay chain. It is very possible that the SUSY particles do not decay directly to the LSP but via several steps. These longer decay chains often lead to final states with many low  $p_T$  jets where the analysis is less sensitive. The development of signal regions targeting different one-step decay models with more flexibility in the number of particles squarks and gluinos decay to is a first step in further diversifying the range of models.

The SUSY search for squarks and gluinos with jets and  $E_T^{\text{miss}}$  as described in this thesis remains a very strong analysis in the quest to discover strongly produced sparticles. The challenge for the remainder of Run II is to not only further push the squark and gluino mass limits but to also probe difficult parameter space that has been missed so far by new innovative approaches.

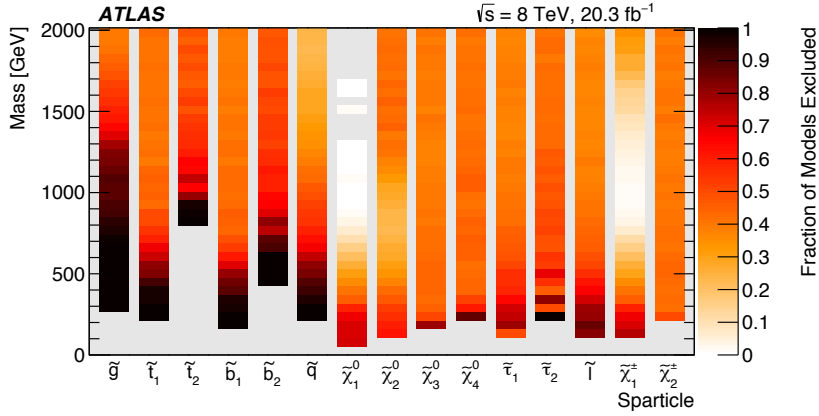


**Figure 9.3:** Each vertical bar is a 1D projection of the fraction of model points excluded, with colour coding representing the fraction of model points excluded for each sparticle. [205]

In the case of very heavy squarks and gluinos it is possible that other lighter SUSY particles are produced first. With the larger statistics available with the Run II data set searches for electro-weak produced sparticles like charginos and higgsinos became interesting. It is here where the increased data set leads to the largest increase in sensitivity.

To explore these more difficult parameter spaces not only the analyses need to innovate to improve their signal sensitivity, it is crucial to start at the beginning of the data selection chain with the trigger. The foreseen LHC conditions with ever more pile-up and instantaneous luminosity make it especially challenging to select the interesting events with a softer  $p_T$  spectrum. Without an efficient trigger analysis improvements are in vain. The search for squarks and gluinos with jets and  $E_T^{\text{miss}}$  in this thesis relies on the  $E_T^{\text{miss}}$  trigger, the raised online threshold between 2015 and 2016 due to run conditions related to a raise on the offline  $E_T^{\text{miss}}$  selection requirement of 50 GeV. The impact of this increase is small for high $p_T$  signal events, the focus of this analysis, but it is larger for more specific signal models with soft  $p_T$  spectra. As shown in Chapter 5 it is possible to improve the current L1  $E_T^{\text{miss}}$  especially under high pile-up conditions. Trigger developments including new hardware/firmware have been proven to take time to become available online. It is therefore important to already develop and improve triggers not only for 'tomorrow' but also for the future (Run III).

Supersymmetry is far from being excluded and ATLAS with its diverse SUSY search program and innovative trigger is well positioned for the coming years of LHC data taking.

## Bibliography

- [1] S. L. Glashow, *Partial Symmetries of Weak Interactions*, *Nucl. Phys.* **22** (1961) 579–588.  
Cited on p. [3](#), [5](#).
- [2] A. Salam, *Weak and Electromagnetic Interactions*, *Conf. Proc.* **C680519** (1968) 367–377.  
Cited on p. [3](#), [5](#).
- [3] S. Weinberg, *A Model of Leptons*, *Phys. Rev. Lett.* **19** (1967) 1264–1266. Cited on p. [3](#), [5](#).
- [4] M. Gell-Mann, *A Schematic Model of Baryons and Mesons*, *Phys. Lett.* **8** (1964) 214–215.  
Cited on p. [3](#), [8](#).
- [5] F. Englert and R. Brout, *Broken symmetry and the mass of gauge vector mesons*,  
*Phys.Rev.Lett.* **13** (1964) 321–323. Cited on p. [3](#), [5](#), [6](#).
- [6] P. W. Higgs, *Broken symmetries and the masses of gauge bosons*, *Phys.Rev.Lett.* **13** (1964)  
508–509. Cited on p. [3](#), [5](#), [6](#).
- [7] G. Zweig, *An SU(3) model for strong interaction symmetry and its breaking. Version 1*,  
CERN-TH-401, 1964. Cited on p. [3](#), [8](#).
- [8] D. Griffiths, *Introduction to Elementary Particles*. WILEY-VCH, Weinheim, second  
revised ed., 2008. Cited on p. [3](#), [5](#), [11](#), [12](#).
- [9] F. Halzen and A. D. Martin, *Quarks and Leptons: An Introductory Course In Modern  
Particle Physics*. Wiley, New York, 1984. Cited on p. [3](#).
- [10] M. E. Peskin and D. V. Schroeder, *An Introduction to quantum field theory*.  
Addison-Wesley, Reading, 1995. Cited on p. [3](#).
- [11] Particle Data Group, C. Patrignani *et. al.*, *Review of Particle Physics*, *Chin. Phys.* **C40**  
(2016), no. 10 100001. Cited on p. [4](#).
- [12] B. Martin, *Nuclear and Particle Physics*. WILEY, Chichester, second ed., 2009. Cited on  
p. [5](#), [11](#).
- [13] G. Guralnik, C. Hagen, and T. Kibble, *Global conservation laws and massless particles*,  
*Phys.Rev.Lett.* **13** (1964) 585–587. Cited on p. [5](#), [6](#).
- [14] ATLAS Collaboration, *Observation of a new particle in the search for the Standard Model  
Higgs boson with the ATLAS detector at the LHC*, *Phys. Lett.* **B716** (2012) 1–29,  
[\[arXiv:1207.7214\]](#). Cited on p. [5](#).

- [15] CMS Collaboration, *Observation of a new boson at a mass of 125 GeV with the CMS experiment at the LHC*, *Phys. Lett.* **B716** (2012) 30–61, [[arXiv:1207.7235](#)]. Cited on p. 5.
- [16] ATLAS Collaboration, CMS Collaboration, *Combined Measurement of the Higgs Boson Mass in  $pp$  Collisions at  $\sqrt{s} = 7$  and 8 TeV with the ATLAS and CMS Experiments*, *Phys. Rev. Lett.* **114** (2015) 191803, [[arXiv:1503.07589](#)]. Cited on p. 5.
- [17] UA1, G. Arnison *et. al.*, *Experimental Observation of Isolated Large Transverse Energy Electrons with Associated Missing Energy at  $s^{1/2} = 540$ -GeV*, *Phys. Lett.* **122B** (1983) 103–116. Cited on p. 5.
- [18] UA2, M. Banner *et. al.*, *Observation of Single Isolated Electrons of High Transverse Momentum in Events with Missing Transverse Energy at the CERN anti- $p$   $p$  Collider*, *Phys. Lett.* **122B** (1983) 476–485. Cited on p. 5.
- [19] UA1, G. Arnison *et. al.*, *Experimental Observation of Lepton Pairs of Invariant Mass Around 95-GeV/ $c^2$  at the CERN SPS Collider*, *Phys. Lett.* **126B** (1983) 398–410. Cited on p. 5.
- [20] UA2, P. Bagnaia *et. al.*, *Evidence for  $Z^0 \rightarrow e^+ e^-$  at the CERN anti- $p$   $p$  Collider*, *Phys. Lett.* **B129** (1983) 130–140. Cited on p. 5.
- [21] N. Cabibbo, *Unitary Symmetry and Leptonic Decays*, *Phys. Rev. Lett.* **10** (1963) 531–533. Cited on p. 8.
- [22] M. Kobayashi and T. Maskawa, *CP Violation in the Renormalizable Theory of Weak Interaction*, *Prog. Theor. Phys.* **49** (1973) 652–657. Cited on p. 8.
- [23] D. J. Gross and F. Wilczek, *Ultraviolet Behavior of Nonabelian Gauge Theories*, *Phys. Rev. Lett.* **30** (1973) 1343–1346. Cited on p. 8.
- [24] H. D. Politzer, *Reliable Perturbative Results for Strong Interactions?*, *Phys. Rev. Lett.* **30** (1973) 1346–1349. Cited on p. 8.
- [25] H. Georgi and S. L. Glashow, *Unity of all elementary-particle forces*, *Phys. Rev. Lett.* **32** (Feb, 1974) 438–441. Cited on p. 11.
- [26] J. C. Pati and A. Salam, *Lepton Number as the Fourth Color*, *Phys. Rev.* **D10** (1974) 275–289. [Erratum: *Phys. Rev.* **D11**, 703(1975)]. Cited on p. 11.
- [27] A. Buras, J. Ellis, M. Gaillard, and D. Nanopoulos, *Aspects of the grand unification of strong, weak and electromagnetic interactions*, *Nuclear Physics B* **135** (1978), no. 1 66 – 92. Cited on p. 11.
- [28] M. E. Peskin, *Beyond the standard model*, [[hep-ph/9705479](#)]. Cited on p. 11, 13, 165.

- [29] F. Zwicky, *Die Rotverschiebung von extragalaktischen Nebeln*, *Helv. Phys. Acta* **6** (1933) 110–127. Cited on p. 11.
- [30] Rubin, V. C. and Ford, W. K. J. and . Thonnard, N., *Rotational properties of 21 SC galaxies with a large range of luminosities and radii, from NGC 4605  $R = 4$  kpc to UGC 2885  $R = 122$  kpc*, *Astrophys. J.* **238** (1980) 471–487. Cited on p. 11.
- [31] T. S. van Albada, J. N. Bahcall, K. Begeman, and R. Sancisi, *The Distribution of Dark Matter in the Spiral Galaxy NGC-3198*, *Astrophys. J.* **295** (1985) 305–313. Cited on p. 11.
- [32] Planck, R. Adam *et. al.*, *Planck 2015 results. I. Overview of products and scientific results*, *Astron. Astrophys.* **594** (2016) A1, [[arXiv:1502.01582](#)]. Cited on p. 12.
- [33] Planck, P. A. R. Ade *et. al.*, *Planck 2015 results. XIII. Cosmological parameters*, *Astron. Astrophys.* **594** (2016) A13, [[arXiv:1502.01589](#)]. Cited on p. 12, 20.
- [34] WMAP, C. L. Bennett *et. al.*, *Nine-Year Wilkinson Microwave Anisotropy Probe (WMAP) Observations: Final Maps and Results*, *Astrophys. J. Suppl.* **208** (2013) 20, [[arXiv:1212.5225](#)]. Cited on p. 12.
- [35] WMAP, G. Hinshaw *et. al.*, *Nine-Year Wilkinson Microwave Anisotropy Probe (WMAP) Observations: Cosmological Parameter Results*, *Astrophys. J. Suppl.* **208** (2013) 19, [[arXiv:1212.5226](#)]. Cited on p. 12, 20.
- [36] S. P. Martin, *A Supersymmetry primer*, [[hep-ph/9709356](#)]. Cited on p. 12, 14, 15, 16, 165, 171.
- [37] I. J. R. Aitchison, *Supersymmetry and the MSSM: An Elementary introduction*, [[hep-ph/0505105](#)]. Cited on p. 12.
- [38] E. Halkiadakis, G. Redlinger, and D. Shih, *Status and Implications of Beyond-the-Standard-Model Searches at the LHC*, *Ann. Rev. Nucl. Part. Sci.* **64** (2014) 319–342, [[arXiv:1411.1427](#)]. Cited on p. 17, 165.
- [39] A. H. Chamseddine, R. L. Arnowitt, and P. Nath, *Locally Supersymmetric Grand Unification*, *Phys. Rev. Lett.* **49** (1982) 970. Cited on p. 18.
- [40] G. L. Kane, C. F. Kolda, L. Roszkowski, and J. D. Wells, *Study of constrained minimal supersymmetry*, *Phys. Rev.* **D49** (1994) 6173–6210, [[hep-ph/9312272](#)]. Cited on p. 18.
- [41] LHC New Physics Working Group, D. Alves, *Simplified Models for LHC New Physics Searches*, *J. Phys.* **G39** (2012) 105005, [[arXiv:1105.2838](#)]. Cited on p. 19.
- [42] MSSM Working Group, A. Djouadi *et. al.*, *The Minimal supersymmetric standard model: Group summary report*, in *GDR (Groupement De Recherche) - Supersymetrie Montpellier, France, April 15-17, 1998*, 1998. [hep-ph/9901246](#). Cited on p. 19.



- [43] C. F. Berger, J. S. Gainer, J. L. Hewett, and T. G. Rizzo, *Supersymmetry Without Prejudice*, *JHEP* **0902** (2009) 023, [[arXiv:0812.0980](#)]. Cited on p. 19, 86.
- [44] LEPSUSYWG, ALEPH, DELPHI, L3 and OPAL experiments, *Combined LEP Chargino Results, up to 208 GeV for low DM*, LEPSUSYWG/02-04.1, CERN, Geneva, 2002. Cited on p. 20, 95.
- [45] LEPSUSYWG, ALEPH, DELPHI, L3 and OPAL experiments, *Combined LEP Chargino Results, up to 208 GeV for large  $m_0$* , LEPSUSYWG/01-03.1, CERN, Geneva, 2001. Cited on p. 20, 95.
- [46] DELPHI, J. Abdallah *et. al.*, *Searches for supersymmetric particles in  $e^+e^-$  collisions up to 208-GeV and interpretation of the results within the MSSM*, *Eur. Phys. J.* **C31** (2003) 421–479, [[hep-ex/0311019](#)]. Cited on p. 20.
- [47] ALEPH, A. Heister *et. al.*, *Absolute lower limits on the masses of selectrons and sneutrinos in the MSSM*, *Phys. Lett.* **B544** (2002) 73–88, [[hep-ex/0207056](#)]. Cited on p. 20.
- [48] D0 Collaboration, V. Abazov *et. al.*, *Search for squarks and gluinos in events with jets and missing transverse energy using  $2.1\text{ fb}^{-1}$  of  $p\bar{p}$  collision data at  $\sqrt{s} = 1.96\text{ TeV}$* , *Phys. Lett.* **B660** (2008) 449–457, [[arXiv:0712.3805](#)]. Cited on p. 20.
- [49] CDF, T. Aaltonen *et. al.*, *Inclusive Search for Squark and Gluino Production in  $p\bar{p}$  Collisions at  $\sqrt{s} = 1.96\text{-TeV}$* , *Phys. Rev. Lett.* **102** (2009) 121801, [[arXiv:0811.2512](#)]. Cited on p. 20.
- [50] A. Arbey, M. Battaglia, A. Djouadi, F. Mahmoudi, and J. Quevillon, *Implications of a 125 GeV Higgs for supersymmetric models*, *Phys. Lett.* **B708** (2012) 162–169, [[arXiv:1112.3028](#)]. Cited on p. 20.
- [51] DAMA, R. Bernabei *et. al.*, *First results from /LIBRA and the combined results with DAMA/NaI*, *Eur. Phys. J.* **C56** (2008) 333–355, [[arXiv:0804.2741](#)]. Cited on p. 20.
- [52] C. E. Aalseth *et. al.*, *Search for an Annual Modulation in a P-type Point Contact Germanium Dark Matter Detector*, *Phys. Rev. Lett.* **107** (2011) 141301, [[arXiv:1106.0650](#)]. Cited on p. 20.
- [53] PAMELA, O. Adriani *et. al.*, *Cosmic-Ray Positron Energy Spectrum Measured by PAMELA*, *Phys. Rev. Lett.* **111** (2013) 081102, [[arXiv:1308.0133](#)]. Cited on p. 20.
- [54] AMS, M. Aguilar *et. al.*, *Electron and Positron Fluxes in Primary Cosmic Rays Measured with the Alpha Magnetic Spectrometer on the International Space Station*, *Phys. Rev. Lett.* **113** (2014) 121102. Cited on p. 20.
- [55] AMS, L. Accardo *et. al.*, *High Statistics Measurement of the Positron Fraction in Primary Cosmic Rays of 0.5 - 500 GeV with the Alpha Magnetic Spectrometer on the International Space Station*, *Phys. Rev. Lett.* **113** (2014) 121101. Cited on p. 20.

- [56] LUX, D. S. Akerib *et. al.*, *First results from the LUX dark matter experiment at the Sanford Underground Research Facility*, *Phys. Rev. Lett.* **112** (2014) 091303, [[arXiv: 1310.8214](#)]. Cited on p. 20, 86.
- [57] XENON100, E. Aprile *et. al.*, *Dark Matter Results from 225 Live Days of XENON100 Data*, *Phys. Rev. Lett.* **109** (2012) 181301, [[arXiv: 1207.5988](#)]. Cited on p. 20, 86, 88, 90.
- [58] C. De Melis, “The CERN accelerator complex. Complexe des accelerateurs du CERN.” <https://cds.cern.ch/record/2119882>, Jan, 2016. Cited on p. 22, 165.
- [59] L. Evans and P. Bryant, *LHC Machine*, *JINST* **3** (2008) S08001. Cited on p. 21.
- [60] LEP, *LEP Design Report: Vol.2. The LEP Main Ring*, CERN-LEP-84-01, 1984. Cited on p. 21.
- [61] TeVI Group, *Design Report Tevatron 1 project*, FERMILAB-DESIGN-1984-01, 1984. Cited on p. 21.
- [62] ATLAS Collaboration, *The ATLAS Experiment at the CERN Large Hadron Collider*, *J. Instrum.* **3** (2008) S08003. 437 p. Cited on p. 23.
- [63] CMS Collaboration, *The CMS experiment at the CERN LHC. The Compact Muon Solenoid experiment*, *J. Instrum.* **3** (2008) S08004. 361 p. Cited on p. 23.
- [64] LHCb Collaboration, A. Alves *et. al.*, *The LHCb Detector at the LHC*, *J. Instrum.* **3** (2008) S08005. Cited on p. 23.
- [65] ALICE Collaboration, K. Aamodt *et. al.*, *The ALICE experiment at the CERN LHC. A Large Ion Collider Experiment*, *J. Instrum.* **3** (2008) S08002. 259 p. Cited on p. 23.
- [66] TOTEM, G. Anelli *et. al.*, *The TOTEM experiment at the CERN Large Hadron Collider*, *JINST* **3** (2008) S08007. Cited on p. 23.
- [67] LHCf, O. Adriani *et. al.*, *The LHCf detector at the CERN Large Hadron Collider*, *JINST* **3** (2008) S08006. Cited on p. 23.
- [68] MoEDAL, J. Pinfold *et. al.*, *Technical Design Report of the MoEDAL Experiment*, . Cited on p. 23.
- [69] M. Benedikt, P. Collier, V. Mertens, J. Poole, and K. Schindl, *LHC Design Report. 3. The LHC injector chain*, . Cited on p. 23.
- [70] ATLAS Collaboration, *Luminosity determination in pp collisions at  $\sqrt{s} = 8$  TeV using the ATLAS detector at the LHC*, [[arXiv: 1608.03953](#)]. Cited on p. 26.
- [71] ATLAS Collaboration, *ATLAS detector and physics performance: Technical Design Report, 1*. Technical Design Report ATLAS. CERN, Geneva, 1999. Cited on p. 27.

- [72] J. Pequenaio, “Computer generated image of the whole ATLAS detector.” <https://cdsweb.cern.ch/record/1095924>, Mar, 2008. Cited on p. 28, 165.
- [73] J. Pequenaio and P. Schaffner, “An computer generated image representing how ATLAS detects particles.” Jan, 2013. Cited on p. 29, 165.
- [74] ATLAS Collaboration, *ATLAS magnet system: Technical design report*, CERN-LHCC-97-18, 1997. Cited on p. 28, 30, 165.
- [75] A. Yamamoto *et. al.*, *The ATLAS central solenoid*, *Nucl. Instrum. Meth.* **A584** (2008) 53–74. Cited on p. 29.
- [76] ATLAS Collaboration, *ATLAS inner detector: Technical Design Report, 1*. Technical Design Report ATLAS. CERN, Geneva, 1997. Cited on p. 30.
- [77] ATLAS Collaboration, S. Haywood, L. Rossi, R. Nickerson, and A. Romaniouk, *ATLAS inner detector: Technical Design Report, 2*. Technical Design Report ATLAS. CERN, Geneva, 1997. Cited on p. 30.
- [78] M. Capeans, G. Darbo, K. Einsweiler, M. Elsing, T. Flick, M. Garcia-Sciveres, C. Gemme, H. Pernegger, O. Rohne, and R. Vuillermet, *ATLAS Insertable B-Layer Technical Design Report*, CERN-LHCC-2010-013. ATLAS-TDR-19, Sep, 2010. Cited on p. 30.
- [79] J. Pequenaio, “Computer generated image of the ATLAS inner detector.” Mar, 2008. Cited on p. 31, 32, 165.
- [80] J. Pequenaio, “Computer Generated image of the ATLAS calorimeter.” Mar, 2008. Cited on p. 33, 166.
- [81] ATLAS Collaboration, *ATLAS muon spectrometer: Technical Design Report*. Technical Design Report ATLAS. CERN, Geneva, 1997. Cited on p. 35, 166.
- [82] ATLAS Collaboration, *Technical Design Report for the Phase-I Upgrade of the ATLAS System*, CERN-LHCC-2013-018. ATLAS-TDR-023, Sep, 2013. Final version presented to December 2013 LHCC. Cited on p. 37, 40, 43, 166.
- [83] R. Achenbach *et. al.*, *The ATLAS level-1 calorimeter trigger*, *JINST* **3** (2008) P03001. Cited on p. 38, 60.
- [84] ATLAS Collaboration, “ATLAS Trigger Operation Public Results.” <https://twiki.cern.ch/twiki/bin/view/AtlasPublic/TriggerOperationPublicResults>. Cited on p. 44, 45, 52, 166.
- [85] ATLAS Collaboration, *Trigger monitoring and rate predictions using Enhanced Bias data from the ATLAS Detector at the LHC*, ATL-DAQ-PUB-2016-002, CERN, Geneva, Oct, 2016. Cited on p. 46, 49, 166.

- [86] ATLAS Collaboration, *2015 start-up trigger menu and initial performance assessment of the ATLAS trigger using Run-2 data*, ATL-DAQ-PUB-2016-001, CERN, Geneva, Mar, 2016. Cited on p. 47, 48, 166.
- [87] ATLAS Collaboration, “ATLAS Data Quality Public Results.” <https://twiki.cern.ch/twiki/bin/view/AtlasPublic/RunStatsPublicResults2010>. Cited on p. 57, 58, 166, 167.
- [88] ATLAS Collaboration, “ATLAS Luminosity Public Results.” <https://twiki.cern.ch/twiki/bin/view/AtlasPublic/LuminosityPublicResultsRun2>. Cited on p. 58, 167.
- [89] J. Schouwenberg, *Kalman filter trained look-up tables for the ATLAS Level-1 Topological Missing Energy Trigger*, Master’s thesis, Radboud University, Nijmegen, Netherlands, 2014. Cited on p. 62.
- [90] ATLAS Collaboration, *The ATLAS transverse-momentum trigger performance at the LHC in 2011*, ATL-CONF-2014-002, CERN, 2014. Cited on p. 67.
- [91] T. Cornelissen, M. Elsing, S. Fleischmann, W. Liebig, and E. Moyse, *Concepts, Design and Implementation of the ATLAS New Tracking (NEWT)*, ATL-SOFT-PUB-2007-007, ATL-COM-SOFT-2007-002, 2007. Cited on p. 71.
- [92] ATLAS Collaboration, *Performance of the ATLAS Inner Detector Track and Vertex Reconstruction in the High Pile-Up LHC Environment*, . Cited on p. 71.
- [93] ATLAS Collaboration, *The Optimization of ATLAS Track Reconstruction in Dense Environments*, ATL-PHYS-PUB-2015-006, CERN, Geneva, Mar, 2015. Cited on p. 71.
- [94] ATLAS Collaboration, *Track Reconstruction Performance of the ATLAS Inner Detector at  $\sqrt{s} = 13$  TeV*, ATL-PHYS-PUB-2015-018, CERN, Geneva, Jul, 2015. Cited on p. 71, 72.
- [95] ATLAS Collaboration, *Early Inner Detector Tracking Performance in the 2015 data at  $\sqrt{s} = 13$  TeV*, ATL-PHYS-PUB-2015-051, CERN, Geneva, Dec, 2015. Cited on p. 71.
- [96] R. Fruhwirth, *Application of Kalman filtering to track and vertex fitting*, *Nucl. Instrum. Meth.* **A262** (1987) 444–450. Cited on p. 71.
- [97] ATLAS Collaboration, *Reconstruction of primary vertices at the ATLAS experiment in Run 1 proton-proton collisions at the LHC*, [[arXiv:1611.10235](https://arxiv.org/abs/1611.10235)]. Cited on p. 72.
- [98] ATLAS Collaboration, *Topological cell clustering in the ATLAS calorimeters and its performance in LHC Run 1*, *Eur. Phys. J.* **C77** (2017) 490, [[arXiv:1603.02934](https://arxiv.org/abs/1603.02934)]. Cited on p. 73.
- [99] M. Cacciari, G. P. Salam, and G. Soyez, *The Anti- $k(t)$  jet clustering algorithm*, *JHEP* **0804** (2008) 063, [[arXiv:0802.1189](https://arxiv.org/abs/0802.1189)]. Cited on p. 74, 114.

- [100] M. Cacciari, G. P. Salam, and G. Soyez, *FastJet User Manual*, *Eur. Phys. J. C* **72** (2012) 1896, [[arXiv:1111.6097](#)]. Cited on p. 74.
- [101] M. Cacciari and G. P. Salam, *Dispelling the  $N^3$  myth for the  $k_t$  jet-finder*, *Phys. Lett. B* **641** (2006) 57–61, [[hep-ph/0512210](#)]. Cited on p. 74.
- [102] ATLAS Collaboration, *Performance of pile-up mitigation techniques for jets in pp collisions at  $\sqrt{s} = 8$  TeV using the ATLAS detector*, *Eur. Phys. J. C* **76** (2016), no. 11 581, [[arXiv:1510.03823](#)]. Cited on p. 74.
- [103] ATLAS Collaboration, *Jet energy measurement and its systematic uncertainty in proton-proton collisions at  $\sqrt{s} = 7$  TeV with the ATLAS detector*, *Eur. Phys. J. C* **75** (2015) 17, [[arXiv:1406.0076](#)]. Cited on p. 74, 75, 167.
- [104] ATLAS Collaboration, *Jet energy resolution in proton-proton collisions at  $\sqrt{s} = 7$  TeV recorded in 2010 with the ATLAS detector*, *Eur. Phys. J. C* **73** (2013), no. 3 2306, [[arXiv:1210.6210](#)]. Cited on p. 75.
- [105] ATLAS Collaboration, *Jet Calibration and Systematic Uncertainties for Jets Reconstructed in the ATLAS Detector at  $\sqrt{s} = 13$  TeV*, ATL-PHYS-PUB-2015-015, CERN, Geneva, Jul, 2015. Cited on p. 75.
- [106] ATLAS Collaboration, *Single hadron response measurement and calorimeter jet energy scale uncertainty with the ATLAS detector at the LHC*, *Eur. Phys. J. C* **73** (2013), no. 3 2305, [[arXiv:1203.1302](#)]. Cited on p. 75.
- [107] ATLAS Collaboration, *Jet energy measurement with the ATLAS detector in proton-proton collisions at  $\sqrt{s} = 7$  TeV*, *Eur. Phys. J. C* **73** (2013), no. 3 2304, [[arXiv:1112.6426](#)]. Cited on p. 75.
- [108] ATLAS Collaboration, *Jet energy scale measurements and their systematic uncertainties in proton-proton collisions at  $\sqrt{s} = 13$  TeV with the ATLAS detector*, *Phys. Rev. D* **96** (2017), no. 7 072002, [[arXiv:1703.09665](#)]. Cited on p. 75, 76, 167.
- [109] *Calibration of the performance of b-tagging for c and light-flavour jets in the 2012 ATLAS data*, ATLAS-CONF-2014-046, CERN, Geneva, Jul, 2014. Cited on p. 75, 76.
- [110] ATLAS Collaboration, *Expected Performance of the ATLAS Experiment - Detector, Trigger and Physics*, [[arXiv:0901.0512](#)]. Cited on p. 76.
- [111] ATLAS Collaboration, *Performance of b-Jet Identification in the ATLAS Experiment*, *JINST* **11** (2016), no. 04 P04008, [[arXiv:1512.01094](#)]. Cited on p. 76, 114.
- [112] ATLAS Collaboration, *Optimisation of the ATLAS b-tagging performance for the 2016 LHC Run*, ATL-PHYS-PUB-2016-012, CERN, Geneva, Jun, 2016. Cited on p. 76, 114, 167.

- [113] ATLAS Collaboration, *Expected performance of missing transverse momentum reconstruction for the ATLAS detector at  $\sqrt{s} = 13$  TeV*, ATL-PHYS-PUB-2015-023, CERN, Geneva, Jul, 2015. Cited on p. 77, 78, 115.
- [114] ATLAS Collaboration, *Tagging and suppression of pileup jets with the ATLAS detector*, ATLAS-CONF-2014-018, CERN, Geneva, May, 2014. Cited on p. 77.
- [115] ATLAS Collaboration, “ATLAS JETM-2016-002 performance public results.” <http://atlas.web.cern.ch/Atlas/GROUPS/PHYSICS/PLOTS/JETM-2016-003/>. Cited on p. 77, 78, 167, 168.
- [116] ATLAS Collaboration, “ATLAS JETM-2016-008 performance public results.” <https://atlas.web.cern.ch/Atlas/GROUPS/PHYSICS/PLOTS/JETM-2016-008/>. Cited on p. 77, 78, 167, 168.
- [117] ATLAS Collaboration, *Electron efficiency measurements with the ATLAS detector using the 2015 LHC proton-proton collision data*, ATLAS-CONF-2016-024, CERN, Geneva, Jun, 2016. Cited on p. 78, 79.
- [118] W. Lampl, S. Laplace, D. Lelas, P. Loch, H. Ma, *et. al.*, *Calorimeter clustering algorithms: Description and performance*, ATL-LARG-PUB-2008-002, ATL-COM-LARG-2008-003, 2008. Cited on p. 78, 95.
- [119] ATLAS Collaboration, *Electron efficiency measurements with the ATLAS detector using the 2012 LHC proton-proton collision data*, ATLAS-CONF-2014-032, CERN, Geneva, Jun, 2014. Cited on p. 79.
- [120] ATLAS Collaboration, *Electron and photon energy calibration with the ATLAS detector using LHC Run 1 data*, *Eur. Phys. J. C* **74** (2014), no. 10 3071, [[arXiv:1407.5063](#)]. Cited on p. 79.
- [121] ATLAS Collaboration, *Photon identification in 2015 ATLAS data*, ATL-PHYS-PUB-2016-014, CERN, Geneva, Aug, 2016. Cited on p. 80, 81, 168.
- [122] ATLAS Collaboration, *Measurement of the photon identification efficiencies with the ATLAS detector using LHC Run-1 data*, *Eur. Phys. J. C* **76** (2016), no. 12 666, [[arXiv:1606.01813](#)]. Cited on p. 80.
- [123] ATLAS Collaboration, *Measurements of the photon identification efficiency with the ATLAS detector using  $4.9\text{ fb}^{-1}$  of  $pp$  collision data collected in 2011*, ATLAS-CONF-2012-123, CERN, Geneva, Aug, 2012. Cited on p. 80, 115.
- [124] ATLAS Collaboration, *Muon reconstruction performance of the ATLAS detector in proton-proton collision data at  $\sqrt{s}=13$  TeV*, *Eur. Phys. J. C* **76** (2016), no. 5 292, [[arXiv:1603.05598](#)]. Cited on p. 81, 83, 115, 168.

- [125] ATLAS Collaboration, *Measurement of the muon reconstruction performance of the ATLAS detector using 2011 and 2012 LHC proton-proton collision data*, *Eur. Phys. J.* **C74** (2014), no. 11 3130, [[arXiv:1407.3935](#)]. Cited on p. 81, 82.
- [126] ATLAS Collaboration, *Muon reconstruction efficiency and momentum resolution of the ATLAS experiment in proton-proton collisions at  $\sqrt{s} = 7$  TeV in 2010*, *Eur. Phys. J.* **C74** (2014), no. 9 3034, [[arXiv:1404.4562](#)]. Cited on p. 81.
- [127] C. Strege, G. Bertone, G. J. Besjes, S. Caron, R. Ruiz de Austri, A. Strubig, and R. Trotta, *Profile likelihood maps of a 15-dimensional MSSM*, *JHEP* **09** (2014) 081, [[arXiv:1405.0622](#)]. Cited on p. 85, 91, 98, 99, 103.
- [128] ATLAS Collaboration, *Search for squarks and gluinos using final states with jets and missing transverse momentum with the ATLAS detector in  $\sqrt{s} = 7$  TeV proton-proton collisions*, ATLAS-CONF-2012-033, CERN, 2012. Cited on p. 85, 89, 90, 92, 97, 168, 171.
- [129] ATLAS Collaboration, *Search for direct production of charginos and neutralinos in events with three leptons and missing transverse momentum in  $\sqrt{s} = 7$  TeV  $pp$  collisions with the ATLAS detector*, *Phys. Lett.* **B718** (2013) 841–859, [[arXiv:1208.3144](#)]. Cited on p. 85, 89, 90, 91, 92, 171.
- [130] A. Djouadi, J.-L. Kneur, and G. Moultaka, *SuSpect: A Fortran code for the supersymmetric and Higgs particle spectrum in the MSSM*, *Comput.Phys.Commun.* **176** (2007) 426–455, [[hep-ph/0211331](#)]. Cited on p. 86.
- [131] A. Arbey, M. Battaglia, and F. Mahmoudi, *Implications of LHC Searches on SUSY Particle Spectra: The pMSSM Parameter Space with Neutralino Dark Matter*, *Eur. Phys. J.* **C72** (2012) 1847, [[arXiv:1110.3726](#)]. Cited on p. 86.
- [132] M. Cahill-Rowley, R. Cotta, A. Drlica-Wagner, S. Funk, J. Hewett, A. Ismail, T. Rizzo, and M. Wood, *Complementarity and Searches for Dark Matter in the pMSSM*, in *Proceedings, Community Summer Study 2013: Snowmass on the Mississippi (CSS2013): Minneapolis, MN, USA, July 29-August 6, 2013*, 2013. [arXiv:1305.6921](#). Cited on p. 86.
- [133] E. A. Baltz, M. Battaglia, M. E. Peskin, and T. Wizansky, *Determination of dark matter properties at high-energy colliders*, *Phys. Rev.* **D74** (2006) 103521, [[hep-ph/0602187](#)]. Cited on p. 86.
- [134] S. S. AbdusSalam, B. C. Allanach, F. Quevedo, F. , and M. Hobson, *Fitting the Phenomenological MSSM*, *Phys. Rev.* **D81** (2010) 095012, [[arXiv:0904.2548](#)]. Cited on p. 86.
- [135] S. S. AbdusSalam, *LHC-7 supersymmetry search interpretation within the phenomenological MSSM*, *Phys. Rev.* **D87** (2013), no. 11 115012, [[arXiv:1211.0999](#)]. Cited on p. 86.

- [136] C. Boehm, P. S. B. Dev, A. Mazumdar, and E. Pukartas, *Naturalness of Light Neutralino Dark Matter in pMSSM after LHC, XENON100 and Planck Data*, *JHEP* **06** (2013) 113, [[arXiv:1303.5386](#)]. Cited on p. 86.
- [137] S. S. Wilks, *The Large-Sample Distribution of the Likelihood Ratio for Testing Composite Hypotheses*, *Annals Math. Statist.* **9** (1938), no. 1 60–62. Cited on p. 88.
- [138] F. Feroz and M. P. Hobson, *Multimodal nested sampling: an efficient and robust alternative to MCMC methods for astronomical data analysis*, *Mon. Not. Roy. Astron. Soc.* **384** (2008) 449, [[arXiv:0704.3704](#)]. Cited on p. 88.
- [139] F. Feroz, M. P. Hobson, and M. Bridges, *MultiNest: an efficient and robust Bayesian inference tool for cosmology and particle physics*, *Mon. Not. Roy. Astron. Soc.* **398** (2009) 1601–1614, [[arXiv:0809.3437](#)]. Cited on p. 88.
- [140] LEP Electroweak Working Group. <http://lepewwg.web.cern.ch/LEPEWWG>. Cited on p. 88, 90.
- [141] Heavy Flavor Averaging Group, Y. Amhis *et. al.*, *Averages of B-Hadron, C-Hadron, and tau-lepton properties as of early 2012*, [[arXiv:1207.1158](#)]. Cited on p. 88, 90.
- [142] Planck, P. A. R. Ade *et. al.*, *Planck 2013 results. XVI. Cosmological parameters*, *Astron. Astrophys.* **571** (2014) A16, [[arXiv:1303.5076](#)]. Cited on p. 88, 90.
- [143] ATLAS Collaboration, *Physics at a High-Luminosity LHC with ATLAS*, ATL-PHYS-PUB-2012-001, 2012. Cited on p. 88, 90.
- [144] CMS Collaboration, *Combination of standard model Higgs boson searches and measurements of the properties of the new boson with a mass near 125 GeV*, CMS-PAS-HIG-12-045, 2012. Cited on p. 88, 90.
- [145] CMS Collaboration, *Updated measurements of the Higgs boson at 125 GeV in the two photon decay channel*, CMS-PAS-HIG-13-001, 2013. Cited on p. 88, 90.
- [146] CMS Collaboration, *Update on the search for the standard model Higgs boson in pp collisions at the LHC decaying to  $W + W$  in the fully leptonic final state*, CMS-PAS-HIG-13-003, 2013. Cited on p. 88, 90.
- [147] CMS Collaboration, *Properties of the Higgs-like boson in the decay  $H$  to  $ZZ$  to  $4l$  in pp collisions at  $\sqrt{s} = 7$  and 8 TeV*, CMS-PAS-HIG-13-002, 2013. Cited on p. 88, 90.
- [148] CMS Collaboration, *Search for the standard model Higgs boson produced in association with  $W$  or  $Z$  bosons, and decaying to bottom quarks for HCP 2012*, CMS-PAS-HIG-12-044, 2012. Cited on p. 88, 90.
- [149] CMS Collaboration, *Search for the Standard-Model Higgs boson decaying to tau pairs in proton-proton collisions at  $\sqrt{s} = 7$  and 8 TeV*, CMS-PAS-HIG-13-004, 2013. Cited on p. 88, 90.



- [150] M. Davier, A. Hoecker, B. Malaescu, and Z. Zhang, *Reevaluation of the Hadronic Contributions to the Muon  $g-2$  and to  $\alpha(MZ)$* , *Eur. Phys. J.* **C71** (2011) 1515, [[arXiv:1010.4180](#)]. [Erratum: *Eur. Phys. J.* **C72**, 1874(2012)]. Cited on p. 90.
- [151] CDF, A. Abulencia *et. al.*, *Observation of  $B_s^0 - \bar{B}_s^0$  Oscillations*, *Phys. Rev. Lett.* **97** (2006) 242003, [[hep-ex/0609040](#)]. Cited on p. 90.
- [152] LHCb, R. Aaij *et. al.*, *Measurement of the  $B_s^0 - \bar{B}_s^0$  oscillation frequency  $\Delta m_s$  in  $B_s^0 \rightarrow D_s^-(3)\pi$  decays*, *Phys. Lett.* **B709** (2012) 177–184, [[arXiv:1112.4311](#)]. Cited on p. 90.
- [153] Belle, M. Nakao *et. al.*, *Measurement of the  $B \rightarrow K^*\gamma$  branching fractions and asymmetries*, *Phys. Rev.* **D69** (2004) 112001, [[hep-ex/0402042](#)]. Cited on p. 90.
- [154] BaBar, B. Aubert *et. al.*, *Measurement of Branching Fractions and CP and Isospin Asymmetries in  $B \rightarrow K^*\gamma$* , in *Proceedings, 34th International Conference on High Energy Physics (ICHEP 2008): Philadelphia, Pennsylvania, July 30-August 5, 2008*, 2008. [arXiv:0808.1915](#). Cited on p. 90.
- [155] Particle Data Group, J. Beringer *et. al.*, *Review of Particle Physics (RPP)*, *Phys. Rev.* **D86** (2012) 010001. Cited on p. 90.
- [156] BaBar, B. Aubert *et. al.*, *Observation of the semileptonic decays  $B \rightarrow D^*\tau^-\bar{\nu}(\tau)$  and evidence for  $B \rightarrow D\tau^-\bar{\nu}(\tau)$* , *Phys. Rev. Lett.* **100** (2008) 021801, [[arXiv:0709.1698](#)]. Cited on p. 90.
- [157] FlaviaNet Working Group on Kaon Decays, M. Antonelli *et. al.*, *An Evaluation of  $|V_{us}|$  and precise tests of the Standard Model from world data on leptonic and semileptonic kaon decays*, *Eur. Phys. J.* **C69** (2010) 399–424, [[arXiv:1005.2323](#)]. Cited on p. 90.
- [158] F. Mahmoudi, S. Neshatpour, and J. Orloff, *Supersymmetric constraints from  $B_s \rightarrow \mu^+\mu^-$  and  $B \rightarrow K^*\mu^+\mu^-$  observables*, *JHEP* **08** (2012) 092, [[arXiv:1205.1845](#)]. Cited on p. 90.
- [159] LHCb, R. Aaij *et. al.*, *First Evidence for the Decay  $B_s^0 \rightarrow \mu^+\mu^-$* , *Phys. Rev. Lett.* **110** (2013), no. 2 021801, [[arXiv:1211.2674](#)]. Cited on p. 90.
- [160] R. Ruiz de Austri, R. Trotta, and L. Roszkowski, *A Markov chain Monte Carlo analysis of the CMSSM*, *JHEP* **05** (2006) 002, [[hep-ph/0602028](#)]. Cited on p. 90.
- [161] W. Beenakker, R. Hopker, M. Spira, and P. Zerwas, *Squark and gluino production at hadron colliders*, *Nucl.Phys.* **B492** (1997) 51–103, [[hep-ph/9610490](#)]. Cited on p. 93, 113.
- [162] A. Kulesza and L. Motyka, *Threshold resummation for squark-antisquark and gluino-pair production at the LHC*, *Phys. Rev. Lett.* **102** (2009) 111802, [[arXiv:0807.2405](#)]. Cited on p. 93, 113.

- [163] A. Kulesza and L. Motyka, *Soft gluon resummation for the production of gluino-gluino and squark-antisquark pairs at the LHC*, *Phys. Rev.* **D80** (2009) 095004, [[arXiv:0905.4749](#)]. Cited on p. 93, 113.
- [164] W. Beenakker, S. Brensing, M. Kramer, A. Kulesza, E. Laenen, and I. Niessen, *Soft-gluon resummation for squark and gluino hadroproduction*, *JHEP* **12** (2009) 041, [[arXiv:0909.4418](#)]. Cited on p. 93, 113.
- [165] W. Beenakker, S. Brensing, M. n. Kramer, A. Kulesza, E. Laenen, L. Motyka, and I. Niessen, *Squark and Gluino Hadroproduction*, *Int. J. Mod. Phys.* **A26** (2011) 2637–2664, [[arXiv:1105.1110](#)]. Cited on p. 93, 113.
- [166] T. Sjostrand, S. Mrenna, and P. Z. Skands, *PYTHIA 6.4 Physics and Manual*, *JHEP* **0605** (2006) 026, [[hep-ph/0603175](#)]. Cited on p. 93, 114.
- [167] ATLAS Collaboration, *ATLAS Monte Carlo tunes for MC09*, ATL-PHYS-PUB-2010-002, ATL-COM-PHYS-2010-033, 2010. Cited on p. 93.
- [168] J. Pumplin, D. R. Stump, J. Huston, H. L. Lai, P. M. Nadolsky, and W. K. Tung, *New generation of parton distributions with uncertainties from global QCD analysis*, *JHEP* **07** (2002) 012, [[hep-ph/0201195](#)]. Cited on p. 93.
- [169] W. Beenakker, M. Klasen, M. Kramer, T. Plehn, M. Spira, and P. M. Zerwas, *The Production of charginos / neutralinos and sleptons at hadron colliders*, *Phys. Rev. Lett.* **83** (1999) 3780–3783, [[hep-ph/9906298](#)]. [Erratum: Phys. Rev. Lett.100,029901(2008)]. Cited on p. 93.
- [170] DELPHES 3, J. de Favereau, C. Delaere, P. Demin, A. Giammanco, V. Lemaître, A. Mertens, and M. Selvaggi, *DELPHES 3, A modular framework for fast simulation of a generic collider experiment*, *JHEP* **02** (2014) 057, [[arXiv:1307.6346](#)]. Cited on p. 93.
- [171] G. Cowan, K. Cranmer, E. Gross, and O. Vitells, *Asymptotic formulae for likelihood-based tests of new physics*, *Eur. Phys. J.* **C71** (2011) 1554, [[arXiv:1007.1727](#)]. [Erratum: Eur. Phys. J.C73,2501(2013)]. Cited on p. 97.
- [172] M. van Beekveld, W. Beenakker, S. Caron, R. Castelijns, M. Lanfermann, and A. Strubig, *Higgs, di-Higgs and tri-Higgs production via SUSY processes at the LHC with 14 TeV*, *JHEP* **05** (2015) 044, [[arXiv:1501.02145](#)]. Cited on p. 103.
- [173] ATLAS Collaboration, *Search for squarks and gluinos with the ATLAS detector in final states with jets and missing transverse momentum using  $\sqrt{s} = 8$  TeV proton–proton collision data*, *JHEP* **09** (2014) 176, [[arXiv:1405.7875](#)]. Cited on p. 103, 109.
- [174] ATLAS Collaboration, *Search for direct production of charginos and neutralinos in events with three leptons and missing transverse momentum in  $\sqrt{s} = 8$  TeV pp collisions with the ATLAS detector*, *JHEP* **04** (2014) 169, [[arXiv:1402.7029](#)]. Cited on p. 103.

- [175] ATLAS Collaboration, *Search for strong production of supersymmetric particles in final states with missing transverse momentum and at least three  $b$ -jets at  $\sqrt{s}=8$  TeV proton-proton collisions with the ATLAS detector*, *JHEP* **10** (2014) 024, [[arXiv:1407.0600](#)]. Cited on p. 103.
- [176] ATLAS Collaboration, *Expected performance of the ATLAS experiment: detector, trigger and physics*. CERN, Geneva, 2009. Cited on p. 109.
- [177] ATLAS Collaboration, *Further searches for squarks and gluinos in final states with jets and missing transverse momentum at  $\sqrt{s}=13$  TeV with the ATLAS detector*, ATLAS-CONF-2016-078, CERN, Geneva, Aug, 2016. Cited on p. 109, 133, 141, 170.
- [178] ATLAS Collaboration, *Search for squarks and gluinos in final states with jets and missing transverse momentum at  $\sqrt{s}=13$  TeV with the ATLAS detector*, *Eur. Phys. J.* **C76** (2016), no. 7 392, [[arXiv:1605.03814](#)]. Cited on p. 109, 120, 135.
- [179] ATLAS Collaboration, *Search for squarks and gluinos with the ATLAS detector in final states with jets and missing transverse momentum and  $20.3\text{ fb}^{-1}$  of  $\sqrt{s}=8$  TeV proton-proton collision data*, ATLAS-CONF-2013-047, CERN, Geneva, 2013. Cited on p. 109.
- [180] ATLAS Collaboration, *Search for squarks and gluinos with the ATLAS detector using final states with jets and missing transverse momentum and  $5.8\text{ fb}^{-1}$  of  $\sqrt{s}=8$  TeV proton-proton collision data*, ATLAS-CONF-2012-109, CERN, Geneva, 2012. Cited on p. 109.
- [181] ATLAS Collaboration, *Search for squarks and gluinos with the ATLAS detector in final states with jets and missing transverse momentum using  $4.7\text{ fb}^{-1}$  of  $\sqrt{s}=7$  TeV proton-proton collision data*, *Phys. Rev.* **D87** (2013), no. 1 012008, [[arXiv:1208.0949](#)]. Cited on p. 109, 124.
- [182] ATLAS Collaboration, *Search for squarks and gluinos using final states with jets and missing transverse momentum with the ATLAS detector in  $\sqrt{s}=7$  TeV proton-proton collisions*, *Phys. Lett.* **B710** (2012) 67–85, [[arXiv:1109.6572](#)]. Cited on p. 109.
- [183] ATLAS Collaboration, *Search for squarks and gluinos using final states with jets and missing transverse momentum with the ATLAS detector in  $\sqrt{s}=7$  TeV proton-proton collisions*, *Phys.Lett.* **B701** (2011) 186–203, [[arXiv:1102.5290](#)]. Cited on p. 109.
- [184] P. Jackson, C. Rogan, and M. Santoni, *Sparticles in motion: Analyzing compressed SUSY scenarios with a new method of event reconstruction*, *Phys. Rev.* **D95** (2017), no. 3 035031, [[arXiv:1607.08307](#)]. Cited on p. 110, 141.
- [185] ATLAS Collaboration, *Luminosity determination in  $pp$  collisions at  $\sqrt{s}=8$  TeV using the ATLAS detector at the LHC*, [[arXiv:1608.03953](#)]. Cited on p. 112.

- [186] J. Alwall, R. Frederix, S. Frixione, V. Hirschi, F. Maltoni, O. Mattelaer, H. S. Shao, T. Stelzer, P. Torrielli, and M. Zaro, *The automated computation of tree-level and next-to-leading order differential cross sections, and their matching to parton shower simulations*, *JHEP* **07** (2014) 079, [[arXiv:1405.0301](#)]. Cited on p. 113.
- [187] T. Sjostrand, S. Ask, J. R. Christiansen, R. Corke, N. Desai, P. Ilten, S. Mrenna, S. Prestel, C. O. Rasmussen, and P. Z. Skands, *An Introduction to PYTHIA 8.2*, *Comput. Phys. Commun.* **191** (2015) 159–177, [[arXiv:1410.3012](#)]. Cited on p. 113.
- [188] R. D. Ball *et. al.*, *Parton distributions with LHC data*, *Nucl. Phys.* **B867** (2013) 244–289, [[arXiv:1207.1303](#)]. Cited on p. 113, 114.
- [189] ATLAS Collaboration, *The simulation principle and performance of the ATLAS fast calorimeter simulation FastCaloSim*, ATL-PHYS-PUB-2010-013, CERN, Geneva, Oct, 2010. Cited on p. 113.
- [190] S. Agostinelli *et. al.*, *Geant4 - a simulation toolkit*, *Nuclear Instruments and Methods in Physics Research Section A: Accelerators, Spectrometers, Detectors and Associated Equipment* **506** (2003), no. 3 250 – 303. Cited on p. 113.
- [191] A. D. Martin, W. J. Stirling, R. S. Thorne, and G. Watt, *Parton distributions for the LHC*, *Eur. Phys. J.* **C63** (2009) 189–285, [[arXiv:0901.0002](#)]. Cited on p. 113.
- [192] T. Gleisberg, S. Hoeche, F. Krauss, M. Schonherr, S. Schumann, F. Siegert, and J. Winter, *Event generation with SHERPA 1.1*, *JHEP* **02** (2009) 007, [[arXiv:0811.4622](#)]. Cited on p. 114.
- [193] NNPDF, R. D. Ball *et. al.*, *Parton distributions for the LHC Run II*, *JHEP* **04** (2015) 040, [[arXiv:1410.8849](#)]. Cited on p. 114.
- [194] H.-L. Lai, M. Guzzi, J. Huston, Z. Li, P. M. Nadolsky, J. Pumplin, and C. P. Yuan, *New parton distributions for collider physics*, *Phys. Rev.* **D82** (2010) 074024, [[arXiv:1007.2241](#)]. Cited on p. 114.
- [195] S. Alioli, P. Nason, C. Oleari, and E. Re, *A general framework for implementing NLO calculations in shower Monte Carlo programs: the POWHEG BOX*, *JHEP* **06** (2010) 043, [[arXiv:1002.2581](#)]. Cited on p. 114.
- [196] ATLAS Collaboration, *Summary of ATLAS Pythia 8 tunes*, ATL-PHYS-PUB-2012-003, CERN, Geneva, Aug, 2012. Cited on p. 114.
- [197] ATLAS Collaboration, *Electron identification measurements in ATLAS using  $\sqrt{s} = 13$  TeV data with 50 ns bunch spacing*, ATL-PHYS-PUB-2015-041, CERN, Geneva, Sep, 2015. Cited on p. 115.
- [198] B. Abeloos, S. Adachi, G.-J. Besjes, D. Bullock, G. Conti, O. Dale, I. Deigaard, L. Dufлот, L. Heelan, S. Henrot-Versille, M. Hodgkinson, P. Jackson, L. Lee,

- N. Makovec, J. Mamuzic, H. J. Moss, Y. Nakahama, B. Petersen, A. Petridis, C. S. Rogan, M. Ronzani, Z. Rurikova, R. Smith, M. Vranjes Milosavljevic, T. Yamanaka, T. J. Khoo, Y. Sano, A. Farbin, A. Strubig, M. White, E. Tolley, and A. Qureshi, *Search for squarks and gluinos with the ATLAS detector in final states with jets and missing transverse momentum at  $\sqrt{s} = 13$  TeV: supporting documentation for ICHEP 2016*, ATL-COM-PHYS-2016-488, CERN, Geneva, May, 2016. Cited on p. 115, 118, 128.
- [199] ATLAS Collaboration, *Selection of jets produced in 13TeV proton-proton collisions with the ATLAS detector*, ATLAS-CONF-2015-029, CERN, Geneva, Jul, 2015. Cited on p. 117.
- [200] C. Chen, *New approach to identifying boosted hadronically-decaying particle using jet substructure in its center-of-mass frame*, *Phys. Rev.* **D85** (2012) 034007, [[arXiv:1112.2567](#)]. Cited on p. 119.
- [201] S. Catani, F. Krauss, R. Kuhn, and B. R. Webber, *QCD matrix elements + parton showers*, *JHEP* **11** (2001) 063, [[hep-ph/0109231](#)]. Cited on p. 127.
- [202] A. Djouadi, M. M. Muhlleitner, and M. Spira, *Decays of supersymmetric particles: The Program SUSY-HIT (SUSpect-SdecaY-Hdecay-InTerface)*, *Acta Phys. Polon.* **B38** (2007) 635–644, [[hep-ph/0609292](#)]. Cited on p. 135.
- [203] ATLAS Collaboration, *Search for squarks and gluinos in final states with jets and missing transverse momentum using  $36\text{ fb}^{-1}$  of  $\sqrt{s}=13$  TeV pp collision data with the ATLAS detector*, [[arXiv:1712.02332](#)]. Cited on p. 140, 145.
- [204] ATLAS Collaboration, “ATLAS Supersymmetry Combined Summary Public Results.” <https://atlas.web.cern.ch/Atlas/GROUPS/PHYSICS/CombinedSummaryPlots/SUSY/>. Cited on p. 146, 147, 170.
- [205] ATLAS Collaboration, *Summary of the ATLAS experiment’s sensitivity to supersymmetry after LHC Run 1 - interpreted in the phenomenological MSSM*, *JHEP* **10** (2015) 134, [[arXiv:1508.06608](#)]. Cited on p. 147, 148, 170.

## List of Figures

2.1	Feynman diagram of the one-loop corrections to the Higgs mass by fermions . . . . .	10
2.2	The evolution of the Standard Model gauge couplings to high energy scales. $\alpha_1$ is proportional to $g_2^2$ , $\alpha_2$ to $g_1^2$ and $\alpha_3$ to $g_s^2$ . $\alpha_3$ is given with its experimental error. [28] . . .	11
2.3	The evolution of the MSSM gauge couplings to high energy scales, if the SUSY particle masses are of order 1 TeV. $\alpha_3$ is given with its experimental error. [28] . . . . .	13
2.4	Illustration of the assumed SUSY-breaking mechanism. [36] . . . . .	15
2.5	Example Feynman diagrams for the production of SUSY particles with QCD strength. The time axis goes from the left to the right. . . . .	16
2.6	Cross sections for SUSY particle production, the production cross section for squarks and gluinos is shown for $\sqrt{s} = 8$ and 13 TeV. The electroweak production cross section is shown for $\sqrt{s} = 8$ and 14 TeV. [38] . . . . .	17
2.7	Feynman diagram of a SUSY cascade decay resulting in jets and missing transverse energy. 18	
3.1	Schematic illustration of the LHC with pre-accelerator and experiments ©2016 CERN [58] . . . . .	22
3.2	The left plot shows the cumulative luminosity versus time delivered to (green) and recorded by ATLAS (yellow) during stable beams for p-p collisions at 13 TeV centre-of-mass energy in 2016. In the right plot the cumulative delivered luminosity is shown for the years of 2011 - 2016. . . . .	25
3.3	The peak instantaneous luminosity delivered to ATLAS during stable beams for p-p collisions at 13 TeV centre-of-mass energy is shown for each LHC fill as a function of time in 2016. . . . .	25
3.4	The peak value for the number of inelastic collisions per beam crossing ( $\mu$ ) during stable beams for p-p collisions at 13 TeV centre-of-mass energy is shown for each fill in 2016 on the left. For comparison on the right the luminosity-weighted distribution of the mean number of interactions per crossing for the 2016 and 2015 p-p collision data is shown. . . . .	26
3.5	Schematic view of the ATLAS detector. ATLAS Experiment ©2008 CERN [72] . . . . .	28
3.6	The detection of different particle types with the ATLAS detector. ATLAS Experiment ©2013 CERN [73] . . . . .	29
3.7	Schematic view of the interaction point. . . . .	30
3.8	Schematic view of the ATLAS magnet system.[74] . . . . .	30
3.9	A schematic view of the ATLAS inner detector. ATLAS Experiment ©2008 CERN[79] . .	31
3.10	A detailed view of the ATLAS inner detector before LS1. ATLAS Experiment ©2008 CERN[79] . . . . .	32

3.11 Overview of the ATLAS calorimeters. ATLASExperiment ©2008 CERN [80] . . . . .	33
3.12 3-D view of the muon system with indication where the different chamber technologies are use.[81] . . . . .	35
3.13 Overview of the trigger and data acquisition system for Run II. The peak design event (in red) and data rates (in blue) are each given before and after the Long Shutdown 1. [82]	37
3.14 Schematic view of L1Calo. . . . .	39
3.15 Schematic view of L1Muon. . . . .	39
3.16 Shown is the ATLAS data taking efficiency in 2016 by day. The luminosity delivered by the LHC between declaring stable beams and the request for a dump of the beam is the denominator for the efficiency. The numerator is the actual recorded luminosity by ATLAS. . . . .	41
4.1 The simulated L1 rate limit by IBL for two different bunch train configurations (blue/cyan) and the nominal expected L1 rate (red). [84] . . . . .	44
4.2 Shown at the top is the total and main physics stream output bandwidth at the HLT as a function of time throughout one fill taken in July 2016 with a peak luminosity of $L = 1.02 \times 10^{34} \text{ cm}^{-2} \text{ s}^{-1}$ and a peak pile up of $\mu = 35$ . The difference between the total and the main physics stream is accounted for by several other streams not shown. They are included at the bottom with their respective percentages of the data writing bandwidth. [84] . . . . .	45
4.3 The average HLT recording rate for each p-p run in 2016. 1.5 kHz is the average rate during the first luminosity blocks, the average of a whole run is around 1 kHz. [84] . . .	45
4.4 CPU usage of groupings of chains as a percentage of utilized computing resources.[85] .	46
4.5 A selection of unprescaled primary triggers of the 2015 menu designed for $0.5 \times 10^{34}$ $\text{cm}^{-2} \text{ s}^{-1}$ . The total rate includes all triggers not only the ones shown. [86] . . . . .	48
4.6 The schema shows the different steps to obtain the rate predictions. . . . .	50
4.7 The different steps in the trigger software release cycle. . . . .	51
4.8 Exemplary for one p-p run in 2016 the rates of different L1 (left) and HLT (right) groups are shown. The group rates do not account for any overlap, the resulting total physics rate is indicated in black. [84] . . . . .	52
4.9 Exemplary for one p-p run in 2016 the rates of different HLT streams are shown. The total HLT output is indicated in black. [84] . . . . .	52
4.10 The schema shows the stream architecture of the ATLAS data output including the de- bug stream treatment. . . . .	53
4.11 Schema of the data-quality monitoring framework. . . . .	56
4.12 Luminosity weighted relative detector uptime and good data quality efficiencies (in %) during stable beam in p-p collisions with 25 ns bunch spacing at $\sqrt{s} = 13 \text{ TeV}$ between April - October 2016, corresponding to an integrated luminosity of $35.9 \text{ fb}^{-1}$ . The toroid magnet was off for some runs, leading to a loss of $0.7 \text{ fb}^{-1}$ . Analyses that don't require the toroid magnet can use that data. [87] . . . . .	57

4.13 (a) Cumulative luminosity versus time delivered to ATLAS (green), recorded by ATLAS (yellow), and certified to be good quality data (blue) during stable beams for pp collisions at 13 TeV centre-of-mass energy in 2015.[88] (b) The corresponding luminosity weighted relative detector uptime and good data quality efficiencies (in %) during stable beam in p-p collisions with 25 ns bunch spacing at $\sqrt{s}=13$ TeV between August - November 2015, corresponding to an integrated luminosity of $3.7 \text{ fb}^{-1}$ . [87]	58
5.1 L1Topo schema	61
5.2 Kalman filter schema	61
5.3 An example Look-up Table for the Kalman filter $E_T^{\text{miss}}$ trigger.	63
5.4 Trigger efficiencies for $E_{T \text{ KF}}^{\text{miss}}$ and $E_{T \text{ L1}}^{\text{miss}}$ compared for the same trigger output rate on a $ZH \rightarrow \nu \bar{\nu} b \bar{b}$ (left) and a $t \bar{t}$ (right) sample.	64
5.5 Performance of different Kalman filter configurations.	64
5.6 Performance of Kalman filter $E_{T \text{ KF}}^{\text{miss}}$ compared to L1Calo $E_{T \text{ L1}}^{\text{miss}}$ . Shown on a $t \bar{t}$ sample with $\mu = 60$	65
5.7 Performance of Kalman filter $E_{T \text{ KF}}^{\text{miss}}$ compared to L1Calo $E_{T \text{ L1}}^{\text{miss}}$ . Shown on a $t \bar{t}$ sample with $\mu = 80$	65
5.8 Performance of Kalman filter $E_{T \text{ KF}}^{\text{miss}}$ compared to L1Calo $E_{T \text{ L1}}^{\text{miss}}$ . Shown on a $ZH \rightarrow \nu \bar{\nu} b \bar{b}$ sample with $\mu = 60$	66
5.9 Performance of Kalman filter $E_{T \text{ KF}}^{\text{miss}}$ compared to L1Calo $E_{T \text{ L1}}^{\text{miss}}$ . Shown on a $ZH \rightarrow \nu \bar{\nu} b \bar{b}$ sample with $\mu = 80$	66
5.10 Schematic view of the topocluster formation. The seed cell is shown in dark blue, adjoint cells in light blue and neighbouring cells in red.	67
5.11 Schema for the 'pueta' algorithm. ©2016 C. Herwig	68
5.12 Schema for the 'pufit' algorithm. ©2016 C. Herwig	68
5.13 Performance of $E_T^{\text{miss}}$ triggers in early 2015.	69
5.14 The trigger cross section as measured by using online rate and luminosity is shown as a function of average number of processes per LHC bunch crossing as measured online, for various missing $E_T$ triggers. All triggers have an L1 ETmiss requirement of 50 GeV, measured at the electromagnetic scale.	70
6.1 No. of tracks depending on pile-up and track selection criteria.	72
6.2 Vertex reconstruction efficiency to the number of associated tracks (a) and the dependence of the number of vertices per event on pile-up (b).	73
6.3 The schema of the chain of corrections and calibrations for the jet energy scale applied to jets in ATLAS [103].	74
6.4 Combined uncertainty in the JES of fully calibrated jets as a function of (a) jet $p_T$ at $\eta = 0$ and (b) $\eta$ at $p_T = 80$ GeV in 2015 data [108].	76
6.5 The rejection efficiency of light-jets (a) and c-jets (b) for different b-tagging algorithms configuration for 2015 and 2016 [112].	76
6.6 The $E_T^{\text{miss}}$ distribution in $Z \rightarrow e^+e^-$ events using the track based soft-term for the full 2015 data set [115] and part of the 2016 data set [116].	77



6.7	Shown is (a) the $E_T^{\text{miss}}$ performance in 2015 data as quantified by the resolution as a function of $\sum E_T$ of the entire event [115] and (b) the TST $E_T^{\text{miss}}$ resolution as a function of the number of primary vertices for a selection of Z boson decays to a pair of electrons and requiring no primary-vertex jet activity in the 2016 ATLAS dataset [116] compared to simulation. . . . .	78
6.8	Electron identification efficiency versus $E_T$ for a $Z \rightarrow ee$ signal and a di-jet background sample. . . . .	79
6.9	Combined electron reconstruction and identification efficiencies versus $E_T$ and $\eta$ for the 2015 data set. . . . .	80
6.10	Identification efficiency for unconverted (a) and converted (b) photons as function of $E_T$ for the first pseudorapidity intervall. [121] . . . . .	81
6.11	Muon reconstruction efficiency in (a) muon $p_T$ and in (b) $\eta$ in 2015 data [124]. . . . .	83
7.1	$\frac{\Delta\epsilon}{\epsilon}$ of the ATLAS and simulation setups for signal region A <i>medium</i> and D of the 0-lepton analysis. . . . .	94
7.2	$\frac{\Delta\epsilon}{\epsilon}$ of the ATLAS and simulation setups for signal region 1a and 1b of the 3-lepton analysis in the plane of $N_1 = m_{\tilde{\chi}_1^0}$ and $C_1 = m_{\tilde{\chi}_1^\pm}$ . . . . .	95
7.3	Mean efficiency value $\Delta\epsilon$ (denoted as $\Delta\text{Eff.}$ ) with estimated standard deviation for signal region A <i>medium</i> and D of the 0-lepton analysis. . . . .	96
7.4	Mean efficiency value $\Delta\epsilon$ (denoted as $\Delta\text{Eff.}$ ) with standard deviation for signal region 1a and 1b of the 3-lepton analysis. . . . .	96
7.5	Shown is the 95% CL observed exclusion limit for the 0-lepton analysis in the cMSSM from our likelihood construction (red line) and the $\text{CL}_s$ method, which is in remarkably good agreement with the ATLAS result [128]. The band limited by the gray dash-dotted lines is the exclusion limit by the ATLAS collaboration, accounting for uncertainties in the SUSY production cross-section. . . . .	97
7.6	1-D profile likelihood global fits results including all data except LHC SUSY searches and Higgs couplings (red) and further excluding the $g-2$ constraint (purple) for some relevant SUSY quantities. Encircled crosses represent the best-fit points. For quantities constrained in the scan, the likelihood function applied is shown in black. Recall that these analyses does not include null SUSY searches at the LHC (see section 7.5.3). . . . .	98
7.7	Composition of the dark matter particle in each bin in the plane of neutralino mass $m_{\tilde{\chi}_1^0}$ vs. spin-independent cross-section $\sigma_p^{\text{SI}}$ is shown in Fig. 7.7, for the analysis including all data (left) and when using the Planck relic density constraint as an upper limit (right). . . . .	99

7.8	Scatter plots from the 2D mini-chains, showing the impact of the LHC (SUSY searches and constraints on the Higgs decay cross-sections) on the chi-square of the best-fit point in each bin. The top (bottom) row shows results for the scans including all data (except the $g-2$ constraint). The encircled black cross indicates the best-fit point prior to inclusion of the LHC constraints; for the scans including all data, this point is ruled out by the LHC results, hence also the next best-fit point that survives the LHC constraints is shown (cross inscribed in the square). The best-fit point for the analysis excluding $g-2$ (bottom panels) remains viable after LHC data are included. (Errata: The rightmost plots have a wrong x-axis label, the $\tilde{\chi}_1^0$ mass is shown in GeV not in TeV.) . . . . .	101
8.1	Schematic analysis design . . . . .	110
8.2	Schematic drawing of the decay topology of the direct squark (left) and direct gluino (right) decay models. . . . .	112
8.3	Schematic drawing of the decay topology of the one-step gluino decay models. The left shows the decay via an intermediate $\tilde{\chi}_1^\pm$ , the right via an intermediate $\tilde{\chi}_2^0$ . . . . .	112
8.4	The trigger efficiency of the $E_T^{\text{miss}}$ -trigger used for signal event pre-selection in 2015 (left and 2016 (right).) . . . . .	117
8.5	Exemplary $m_{\text{eff}}$ -distributions in the control regions CR $\gamma$ (left) and CRQ (right) for signal region Meff-4j-1000. The arrows indicate the values at which the requirements on $m_{\text{eff}}$ are applied. The histograms show the pre-fit MC background expectations, normalized to cross-section times integrated luminosity. . . . .	124
8.6	Exemplary $m_{\text{eff}}$ -distributions in the control regions CRW (left) and CRT (right) for signal region Meff-4j-1000. The arrows indicate the values at which the requirements on $m_{\text{eff}}$ are applied. The histograms show the pre-fit MC background expectations, normalized to cross-section times integrated luminosity. . . . .	125
8.7	Differences of the observed to expected background events in each validation region as a fraction of the total uncertainty. . . . .	126
8.8	Comparison of the observed and expected event yields as a function of signal region. The background expectations are those obtained from the background-only fits as in 8.5 . . . . .	129
8.9	The observed $m_{\text{eff}}$ distribution in signal region Meff-2j-0800 (left) and Meff-2j-1600 (right). The arrows indicate the values at which the requirements on $m_{\text{eff}}$ are applied. The histograms show the pre-fit MC background expectations, normalized to cross-section times integrated luminosity. The red error band indicates the combined experimental, theoretical and MC statistical uncertainties. The distribution of a signal benchmark model is also shown to visualize the expected SUSY signal. . . . .	130
8.10	The observed $m_{\text{eff}}$ distribution in signal region Meff-4j-1000 (left) and Meff-4j-2200 (right). The arrows indicate the values at which the requirements on $m_{\text{eff}}$ are applied. The histograms show the pre-fit MC background expectations, normalized to cross-section times integrated luminosity. The red error band indicates the combined experimental, theoretical and MC statistical uncertainties. The distribution of a signal benchmark model is also shown to visualize the expected SUSY signal. . . . .	130

8.11	The observed $m_{\text{eff}}$ distribution in signal region Meff-6j-1800. The arrows indicate the values at which the requirements on $m_{\text{eff}}$ are applied. The histograms show the pre-fit MC background expectations, normalized to cross-section times integrated luminosity. The red error band indicates the combined experimental, theoretical and MC statistical uncertainties. The distribution of a signal benchmark model is also shown to visualize the expected SUSY signal. . . . .	132
8.12	Exclusion limits for the direct squark decay model (a) and the direct gluino decay model (b). The exclusion limits are obtained by using the signal region with the best expected sensitivity at each point. The signal regions providing the best expected sensitivity at a selection of model points are indicated in the plot together with the expected limits at 95% CL (blue) and their $1\sigma$ excursions due to experimental and background-only theoretical uncertainties (yellow). The observed limits from this analysis are shown in brown, the ones obtained by the previous ATLAS searches with no leptons, jets and missing transverse momentum is shaded in blue. [177] . . . . .	133
8.13	Exclusion limits for the onestep gluino decay models via a $\tilde{\chi}_i^\pm$ (a) and via a $\tilde{\chi}_2^0$ (b). The exclusion limits are obtained by using the signal region with the best expected sensitivity at each point. The signal regions providing the best expected sensitivity at a selection of model points are indicated in the plot together with the expected limits at 95% CL (blue) and their $1\sigma$ excursions due to experimental and background-only theoretical uncertainties (yellow). The observed limits from this analysis are shown in brown, the ones obtained by the previous ATLAS searches with no leptons, jets and missing transverse momentum is shaded in blue. . . . .	134
9.1	Mass reach of ATLAS searches for Supersymmetry (May 2017). Only a representative selection of the available results is shown. [204] . . . . .	146
9.2	Exclusion limits at 95% CL for 13 TeV in the (gluino, lightest neutralino) mass plane for different simplified models featuring the decay of the gluino to the lightest neutralino either directly or through a cascade chain featuring other SUSY particles with intermediate mass. For each line, the gluino decay mode is reported in the legend and it is assumed to proceed with 100% branching ratio. The limits might depend on additional assumptions on the mass of the intermediate states, as described in the references provided in the plot.[204] . . . . .	147
9.3	Each vertical bar is a 1D projection of the fraction of model points excluded, with colour coding representing the fraction of model points excluded for each sparticle. [205] . . .	148

# List of Tables

2.1	Particle content of the Standard Model (the corresponding anti-particles are unlisted). $R, L$ indicate the values for right- and lefthanded particles. $Y$ is the hypercharge. . . . .	4
2.2	Supersymmetric particles in the MSSM with their gauge and mass eigenstates (adapted from [36] p.78) . . . . .	14
7.1	pMSSM parameters and top mass value used for this study and the prior range for the two prior choices adopted in the scans. Flat priors are uniform on the parameter itself (within the ranges indicated), while log priors are uniform in the log of the parameter (within the ranges indicated) except $\tan\beta$ which is uniform on the parameter itself. . . .	87
7.2	Summary of experimental constraints used in the likelihood. Upper part: measured observables, modelled with a Gaussian likelihood of mean $\mu$ , and standard deviation $(\sigma^2 + \tau^2)^{1/2}$ , where $\sigma$ is the experimental and $\tau$ the theoretical uncertainty. Lower part: observables for which only limits currently exist. See text for further information on the explicit form of the likelihood function. Experimental constraints tagged with # have been found to contribute an approximately constant value to the log-likelihood and hence have been omitted. Observables tagged with $^\dagger$ are applied via post-processing of the samples. . . . .	90
7.3	Requirements for the inclusive channels A-E for the ATLAS 0-lepton analysis with an integrated luminosity of $4.7 \text{ fb}^{-1}$ . For $m_{\text{eff}}(\text{incl.})$ the limits are given in the order <i>tight/medium/loose</i> . The jet $p_T$ requirements are given for the minimum required number of jets (from [128]). . . . .	92
7.4	Requirements for the signal regions 1a, 1b and 2 for the 3-lepton ATLAS analysis with an integrated luminosity of $4.7 \text{ fb}^{-1}$ . In addition, the number of reconstructed leptons has to be three (from [129]). . . . .	92
8.1	Configurations of the Monte Carlo generators to simulate the different background samples. . . . .	113
8.2	The signal selection criteria used in each signal region. In addition the targeted SUSY signal is given. . . . .	121
8.3	The event selection criteria used in each background control region together with the main targeted background in the SR in each case. Also given is the process that is used to model the corresponding background. . . . .	123

8.4 An overview of the dominant systematic uncertainties in the background estimates.  $\Delta\mu$  uncertainties are the result of the control region statistical uncertainties and the systematic uncertainties entering a specific control region. In brackets, uncertainties are given relative to the expected total background yield. . . . . 128

8.5  $p_0$  and upper limit numbers of events observed in the signal regions compared with the pre-fit and fitted background expectations. For an observed number of events lower than expected, the p-value is truncated at 0.5. . . . . 131

## Summary

**I**N this thesis a search for supersymmetric particles with the ATLAS detector at the LHC was presented. No deviation from the Standard Model was observed. The presented search relies on transverse missing energy triggers for which an improvement using a Kalman filter is described. In addition fits of the phenomenological minimal supersymmetric Standard Model are performed using preceding results of the search. The fits allow to identify regions of interest for further supersymmetry searches and their improvement.

The Standard Model of particle physics is a most powerful description of the underlying principles of particle physics. Despite its success there are still some unresolved questions like the 'unnaturally' large fine-tuning necessary to obtain the Higgs mass and the fact that only 4.9% of our universe consist of matter known to us. Some of these questions could be answered by Supersymmetry, an extension of the Standard Model that proposes a superpartner with a spin difference of one half for each elementary particle. With the assumption that R-parity is preserved the lightest supersymmetric particle is a promising candidate for dark matter.

Searches for Supersymmetry can be conducted with the help of large particle colliders as the LHC and all-purpose detectors as ATLAS. The high center-of-mass energy of the proton collisions renders the production of much heavier new particles possible. Both the LHC and the ATLAS detector are described in this thesis together with the detector performance and event reconstruction.

The ATLAS detector produces large amounts of data every second during the p-p collisions. Due to hardware and storage space limitations it is not possible to write out every event. The trigger system deciding on which events are interesting enough to write to disk is therefore essential for taking meaningful data. The challenges of a successful trigger operation are discussed. One of them is the high number of interactions apart from the hard-scatter. Missing transverse energy triggers are especially affected by high pile-up as they aim to measure the energies of particles that leave the detector undetected. Due to the non-interacting nature of the lightest supersymmetric particle missing transverse energy trigger play an important role for Supersymmetry searches. This thesis describes a new method of pile-up mitigation for the Level-1 missing transverse energy trigger. By employing a Kalman filter corrections to each jet's energy can be obtained, downgrading the contributions of jets from pile-up interactions to the overall energy calculation.

For a more general survey of the supersymmetric parameter space the publicly available results of several experiments have been used for fits of the MSSM-15, a 15 parameter version of the phenomenological MSSM. Data from direct dark matter detection experiments, *B*- and *D*- physics experiments, LEP and Tevatron has been included in the fits as well as already

available LHC results and astrophysical constraints on the relic dark matter density. The best fit results in the most likely values in the MSSM-15 parameter space which correspond to a squark mass of 2.3 TeV, a gluino mass of 2.1 TeV, a neutralino mass of 130 GeV and a spin-independent cross section of  $2.4 \times 10^{-10}$  pb. The best fit point can be well probed with future LHC runs.

The supersymmetry search in this thesis targets strong production of squarks and gluinos by requiring 2 - 6 jets, large missing transverse energy and no leptons in the final state. The squarks and gluinos decay to quarks and a neutralino, the lightest supersymmetric particle. This decay chain results in at least 2 jets, more for a decay via intermediate particles, and the neutralino leaves the detector unseen contribution to the transverse missing energy. The search consists of thirteen inclusive signal regions characterized by increasing minimum jet multiplicity and varying requirements on the effective mass of the event. Each signal region is accompanied by 4 control region for the estimation of the four main backgrounds  $Z/\gamma^* + \text{jets}$ ,  $W + \text{jets}$ , top quark pairs and single top quarks and multi-jet production. In none of the signal regions any significant deviation from the Standard Model was observed. The results are interpreted as model-independent cross section limits as well as model-dependent mass exclusion limits. For the exclusion limits simplified models are used which give a specific production mode and decay chain rather than a specific set of model parameters. For a massless neutralino directly decaying squarks are excluded up to a mass of 1.35 TeV, directly decaying gluinos up to masses of 1.86 TeV. For gluinos decaying via an intermediate particle masses below 1.83 TeV and 1.9 TeV are excluded for a decay via charginos and neutralinos respectively.

So far it was not possible to observe Supersymmetry but this does not mean that Supersymmetry is a disproved theory not even a less attractive one. Supersymmetric particles could be just produced with a cross section too low to be detected with the current LHC's center-of-mass energy. The dataset that will be collected during Run II until the end of 2018 is already large enough that searches are sensitive to electroweak production of supersymmetric particles. Together with the future runs of the LHC this opens a new window to probe for physics beyond the Standard Model.

## Samenvatting

**I**N dit proefschrift werd een zoektocht naar supersymmetrische deeltjes met de ATLAS detector bij de LHC voorgesteld. Er werd geen afwijking van het Standaardmodel waargenomen. De gepresenteerde zoektocht gebruikt ontbrekende transversale energie ( $E_T^{\text{miss}}$ ) triggers, waarvoor ook een verbetering met behulp van een Kalman-filter wordt beschreven. Bovendien worden fits van het fenomenologische minimale supersymmetrische Standaardmodel (fMSSM) uitgevoerd met behulp van eerdere resultaten van de zoektocht. De fits maken het mogelijk om interessante regio's te identificeren voor toekomstige supersymmetriezoektochten en de verbetering daarvan.

Het Standaardmodel van deeltjesfysica is een zeer krachtige beschrijving van de onderliggende principes van de deeltjesfysica. Ondanks het succes van dit model, zijn er nog steeds enkele onopgeloste vragen zoals de 'onnatuurlijk' grote 'fine-tuning' die nodig is om de Higgsmassa te verkrijgen en het feit dat slechts 4.9% van ons universum uit gekende materie bestaat. Sommige van deze vragen kunnen worden beantwoord door Supersymmetrie, een uitbreiding van het Standaardmodel dat voor elk elementair deeltje een superpartner voorstelt met een spinverschil van  $1/2$ . Onder de aanname dat R-pariteit behouden blijft, is het lichtste supersymmetrische deeltje een veelbelovende kandidaat voor donkere materie. Zoektochten naar Supersymmetrie kunnen worden uitgevoerd met behulp van grote deeltjesvernellers als de LHC en multifunctionele detectoren als ATLAS. De hoge massamiddelpuntsenergie van de protonbotsingen maakt de productie van veel zwaardere nieuwe deeltjes mogelijk. Zowel de LHC als de ATLAS detector worden in dit proefschrift beschreven, samen met de detectorperformance en de eventsreconstructie. De ATLAS detector produceert elke seconde grote hoeveelheden gegevens tijdens de p-p botsingen. Vanwege beperkingen in hardware en opslagruimte is het niet mogelijk om elke event weg te schrijven. Het trigger-systeem dat beslist welke events interessant genoeg zijn om op te slaan, is daarom essentieel voor het opnemen van betekenisvolle gegevens. De uitdagingen van succesvolle triggeroperatie worden besproken. Eén daarvan is het hoge aantal interacties bovenop de harde botsing – de pile-up interacties.  $E_T^{\text{miss}}$  triggers zijn gevoelig aan pile-up omdat ze erop gericht zijn de energieën te meten van deeltjes die de detector ongedetecteerd verlaten. Vanwege het niet-interagerende karakter van het lichtste supersymmetrische deeltje speelt de  $E_T^{\text{miss}}$  trigger een belangrijke rol in supersymmetrische zoektochten. Dit proefschrift beschrijft een nieuwe methode voor de mitigatie van pile-up bij de level-1 ontbrekende transversale energie trigger. Door het gebruik van een Kalman-filter kunnen correcties op de energie van elke jet worden verkregen, waardoor de bijdrage van de pile-up jets aan de totale energiesom lager wordt.

Voor een meer algemeen overzicht van de supersymmetrische parameterruimte zijn de open-



baar beschikbare resultaten van verschillende experimenten gebruikt voor de fits van het MSSM-15, een 15-parameterversie van het fenomenologische MSSM. Gegevens van directe detectie-experimenten met donkere materie,  $B$ - en  $D$ - fysica-experimenten, LEP, en Tevatron zijn opgenomen in de fits, evenals reeds beschikbare LHC resultaten en astrofysische limieten voor de dichtheid van donkere materie. De beste fit resulteert in de meest waarschijnlijke waarden in de MSSM-15 parameterruimte; deze komen overeen met een squark massa van 2.3 TeV, een gluino massa van 2.1 TeV, een neutralino massa van 130 GeV en een spinonafhankelijke werkzame doorsnede van  $2.4 \times 10^{-10}$  pb. Het beste fit punt kan verder worden onderzocht in toekomstige LHC runs.

De supersymmetriezoektocht in dit proefschrift richt zich op sterke productie van squarks en gluino's, in de aanwezigheid van twee tot zes jets, hoge ontbrekende transversale energie en zonder leptonen in de eindtoestand. De squarks en gluino's vervallen tot quarks en een neutralino, het lichtste supersymmetrische deeltje. Deze vervalketen resulteert in ten minste twee jets, meer in het geval van een verval via intermediaire deeltjes, en het neutralino verlaat de detector ongezien en draagt bij aan de  $E_T^{\text{miss}}$ . De zoektocht bestaat uit dertien inclusieve signaalregio's die worden gekenmerkt door een toenemende minimum jetmultipliciteit en variërende eisen voor de effectieve massa van het event. Elke signaalregio wordt vergezeld door vier controleregio's voor de schatting van de vier belangrijkste achtergronden  $Z / \gamma^* + \text{jets}$ ,  $W + \text{jets}$ , top-quark-paren en single top-quarks, en multijetproductie. In geen van de signaalregio's werd enige significante afwijking van het Standaardmodel waargenomen. De resultaten worden geïnterpreteerd als modelonafhankelijke limieten voor de werkzame doorsnede en de massa. Voor de uitsluitingslimieten worden vereenvoudigde modellen gebruikt die een specifieke productiemodus en vervalketen geven in plaats van een specifieke reeks modelparameters. Voor een massaloos neutralino zijn onmiddellijk vervallende squarks uitgesloten tot een massa van 1.35 TeV en onmiddellijk vervallende gluino's tot massas van 1.86 TeV. Voor gluino's die vervallen via een intermediaire deeltje worden gluinomassa's onder de 1.83 TeV (1.9 TeV) uitgesloten, voor een verval via chargino's (neutralino's).

Tot nu toe was het niet mogelijk om Supersymmetrie waar te nemen, maar dit betekent niet dat Supersymmetrie een minder aantrekkelijke of weerlegde theorie is. Supersymmetrische deeltjes kunnen met een net te lage doorsnede worden geproduceerd om te worden gedetecteerd met de huidige LHC. De dataset die tijdens Run II tot eind 2018 zal worden verzameld, is al groot genoeg dat zoektochten gevoelig zijn voor elektrozwakke productie van supersymmetrische deeltjes. Samen met de toekomstige runs van de LHC opent dit nieuwe mogelijkheden om te peilen naar fysica voorbij het Standaardmodel.

## Curriculum vitae

Antonia Hanna Strübig was born in Hamburg on the 14th December 1985. After graduating from Freies Gymnasium in Bern in 2004 she spent one year in Tainan, Taiwan as a volunteer for International Cultural Youth Exchange (ICYE) .

In 2005 she enrolled in the diploma course of physics at Albert-Ludwigs-Universität Freiburg with minor subjects of meteorology and astrophysics. One year of her studies was spent as exchange student at Nanjing University, China. In 2009 she received a scholarship from German Academic Exchange Service (DAAD) for a three months internship at National Centre for Theoretical Sciences at National Cheng Kung University in Tainan, Taiwan. She obtained her diploma in physics in 2012. The work for her diploma thesis *Study of phenomenological models with the ATLAS experiment* was conducted in the group of Prof. Dr. Gregor Herten. Following the graduation she participated in the South Korean Summer School funded by the DAAD as a research assistant at the Konkuk University Next Generation Solar Cells Institute in Seoul, South Korea.

In December 2012 the author started as a graduate student in the department of Experimental High Energy Physics at Radboud University, Nijmegen under the supervision of Prof. Nicolo de Groot and Dr. Sascha Caron. The work during her graduate studies is summarized in this thesis. One year of the graduate program was spent at CERN from January 2015 to February 2016. She also took on responsibilities in teaching at Radboud University for advanced particle physics courses and second year laboratory courses.



## Acknowledgements

**A**FTER SPENDING FOUR YEARS (not counting the tiny bit it took writing this) being part of Nikhef and especially the Nikhef Nijmegen group there are several people I would like to mention. It is a long time and you meet many people, I am sorry if I forgot somebody.

First and foremost my thanks goes to my promoter Olya for accepting me as her first official PhD student and the necessary patience. Your never wavering optimism motivated me throughout the writing process. And to my supervisor Sascha who gave me the opportunity to start in the Nijmegen ATLAS group. It was not always easy but your enthusiasm for Supersymmetry is catching. Thank you for the continued guidance and useful discussions throughout the years since starting my master thesis back in Freiburg. I could always count on you for an honest opinion. And apologies that I did not manage to keep my thesis shorter, making you read more than hundred pages.

Thank you also to Nicolo, Alan, Gerhard, Hella, Paul and Wim for agreeing to be on my defense committee, the helpful comments and taking part in my graduation.

The atmosphere in the HEF group in Nijmegen was always welcoming and relaxed. At any time there was somebody for coffee break, discuss physics or life and to join for Dutch lunch or borrel. Thank you to the whole group, Annelies, Gemma, Marjo, Gertie, Nicolo, Frank, Charles, Sijbrand, Cristina, Magda, Lucia, Thijs, Giuseppe and Fabrizia and in particular to Guus, Stefan and Stefan for your continuous effort to make me speak Dutch. Thank you Veronica, Snezana, for all the Serbian lunches at CERN, Jeroen, for getting a coffee machine for our office and Vince for trying your best to keep the plants alive and proof reading parts of this thesis, also for all sharing an office with me over the time.

The main topic of this thesis is Supersymmetry without leptons and I would like to thank the Nikhef team working on this during my time, Marija, Geert Jan and Ingrid as well as everybody I worked with: Yu, Nicola, Manfredi, Judita, Takashi and Laurent.

A special thanks goes to the Trigger Operations group at CERN. Working with you is still my favourite part of the job despite the sleepless nights in the control room and various emergencies. Stress makes for a great team. In no particular order thanks to Alex, Martin, Catrin, Mark, Elisabetta, Emma, Arantxa, Moritz, Savanna, Merve, Tim, Michael, Daniele, Joerg, Heather, Lidija, Kate, Aparajita, Sebastien and Anna. I am very happy that I can continue to work with most of you.

The time spent at CERN was enjoyable thanks to Matteo, Ruchi, Remco, Wouter, Marie, Dominik, Tim and Loan. Thank you, Lydia, for the great evenings trying out recipes. And special thanks to Sara for continuous coffee break support in my last year as well as helping with translating my summary.

To my paranympths, Nena and Luca, who agreed to stand in front together with me, I hope

## *Acknowledgements*

you have your sabres ready at any moment. Thank you, Nena, for being the friend I can always count on and the many great weekends spent in Freiburg and other places since I moved away. And thanks to Luca, for your upbeat view on life making various Nikhef activities more enjoyable, it is much less fun to have cappuccino after lunch without you.

A big thanks goes to Laura, my sister, who helped designing the cover and understands how hard it can be to actually sit down and write. And Thömu, thank you for your helpful comments on my design choices.

Zuletzt ein grosser Dank an meine Familie, vorallem an meine Eltern, ihr habt mich immer unterstützt und ohne euch würde ich heute nicht hier stehen.